Imperial College London

THESIS

A Fluid Solid Interaction Model of Lubricated Soft Contacts with Application to Windscreen Wipers

Author: **Qian Wang**

Supervisors: Prof. Daniele Dini

Dr. Tom Reddyhoff

A report submitted in fulfilment of the requirements

for the degree of Doctor of Philosophy

in the

Tribology group

Department of Mechanical Engineering

April 2019

DECLARATION OF ORIGINALITY

I, QIAN WANG, declare that this thesis titled, "A Fluid Solid Interaction Model of Lubricated Soft Contacts with Application to Windscreen Wipers" and the work presented in it are my own.

I confirm that:

- This work was done wholly or mainly while in candidature for a research degree at the Imperial College of London.
- Where I have consulted the published work of others, this is always clearly attributed.
- Where I have quoted from the work of others, the source is always given. With the exception of such quotations, this thesis is entirely my own work.
- I have acknowledged all main sources of help.
- Where the thesis is based on work done by myself jointly with others, I have made clear exactly what was done by others and what I have contributed myself.

Signed:

Date: 17/04/2019

COPYRIGHT DECLARATION

Signed:

Date: 17/04/2019

Abstract

Developing reliable Fluid-Solid-Interaction models are important for understanding the tribological behaviour in compliant contacts in lubricated conditions. This is particularly important for applications such as seals and windscreen wipers, which play a significant role in *e.g.* the automobile industry. This thesis presents a thorough modelling and computational solution framework aimed at the numerical simulation of a wiper blade sliding against glass in a wide range of lubrication regimes in steady-state conditions. Three modules each containing a unique algorithm are demonstrated to handle the coupling between the fluid flow and the solid deformation and capture the transition between different lubrication regimes.

Whilst the hydrodynamic pressure is obtained by solving the Reynolds equation with Finite Difference method and Gauss-Seidel iterative scheme, the interaction between asperities can be described using analytical formulations based on Persson's theory or the boundary element method (BEM) which solves the contact problem deterministically. As the latter provides more flexibility dealing with any given rough surfaces (measured or computer generated), it is employed here together with the Fast Fourier Transform (FFT) technique and the Conjugate Gradient (CG) iterative method to determine the variation of the real contact areas and the interfacial separation with respect to the applied load. These relations are represented as fitted functions and act as solid solvers in the presented FSI model. The effect of the thermodynamic correction, the continuum correction, the fractal correction and the surface property Hurst exponent, which usually affects the accuracy of the numerical analysis, are assessed in a systematic manner to provide general guidance for the employment of the BEM.

Elastic deformation, which is critical in determining the film thickness, is calculated by means of an innovative Reduced Stiffness Method, which is based on the finite element method and model condensation techniques. This approach has been validated for both linearly elastic and non-linearly elastic (hyper-elastic and viscoelastic) materials in static and sliding conditions. Depending whether the contact behaviour is associated with small or large strain deformations, the initial stiffness matrix or the deformed stiffness matrix can be extracted from the finite element model at a certain state and incorporated into the FSI model to account for the finite deformation of compliant solids due to geometric and material nonlinearity, respectively.

The proposed model has been compared with experimental measurements and has shown a good agreement in terms of friction prediction for elastomer specimens of triangular cross-section. For real wiper blades, simulations have shown that the accuracy of model predictions is sensitive to quantities such as the roughness, the input configuration and the reduced stiffness matrix employed, which are evaluated regarding their relative importance. Suggestions on how to obtain improved performance and further investigations aimed at clarifying the behaviour of these complex systems in different scenarios have also been proposed.

Acknowledgement

I would like to thank my supervisor, Prof Daniele Dini, for his continous and extraordinary support and patience throughout my PhD. Not only he provide guidance in reseach, he is also mentored me with life experiences.

Special thanks to Dr Tom Reddyhoff for offering me this remarkable oppotunatiy in the first place and for his encouragement every step of the way.

I would also like to express my sincere thanks to Alessandra, Sorin, Debashis, Stefano, Yasunori, Joanna, Pawel, Francisco, Jia and all the other members of the Imperial College Tribology group. Thank you for making this journey pleasant and unforgetable, I will always cherish these memories. Special thank you to Mrs. Chrissy Stevens for all the help with many administrative matters.

Furthmore, I would like to thank everyone at Bosch who sponsored my PhD and provided technical support whenever I needed it.

Finally, my deepst gratitude to my families who love me and support me unconditionally when it matted most. Thank you!

Contents

List of figures

List of tables

Nomenclatures

Latin symbols

a	Hertzian contact area [m^2]
A	real contact area [m^2]
A_0	nominal contact area [m^2]
$C(q)$	radial averaged PSD [m^4]
C_{1D+}	one-dimensional (1D) PSD [m^3]
C_g	global damping matrix
C_r	reduced damping matrix
C_{10}	material parameter for hyper-elastic materials
D_f	fractal dimension
D_{ij}^{kl}	influence coefficient matrix (2D)
D_1	material parameter for hyper-elastic materials
E_r	reduced elastic modulus [Pa]
E	elastic modulus [Pa]
E_0	instantaneous elastic modulus [Pa]
E'	in-phase response, denoted as the storage modulus [Pa]
E''	the out-of-phase component, denoted as loss modulus [Pa]
E^*	complex modulus
E_∞	long-term elastic modulus [Pa]
EK_{ij}	equivalent influence coefficient matrix to K_r^0
EK_{ij}^d	equivalent influence coefficient matrix to K_r^d
F_n	current load [N]
F_f	friction force [N]
ΔF	load increment [N]
G_0	initial shear modulus [Pa]
h_a	average roughness [m]
h_{rms}	root-mean-square roughness
h'_{rms}	root-mean-square gradient
H_c	central film thickness [m]
H_{min}	minimum film thickness [m]
H	Hurst exponent
k	ellipticity parameter
K_{ij}	influence coefficient (1D)
K_g	global stiffness matrix
K_r	reduced stiffness matrix
K_0	bulk modulus [Pa]
K_r^0	initial stiffness matrix
K_r^d	deformed stiffness matrix
L	length of a rough surface [m]
M_g	global mass matrix

M_r	reduced mass matrix
N	number of nodes in the computing domain
p_f	hydrodynamic pressure [Pa]
p_s	solid pressure [Pa]
p_{total}	total pressure [Pa]
p_{s0}^d	pressure associated with u_0^d [Pa]
q	wavevector [m^{-1}]
q_L	cut-off wavevector [m^{-1}]
q_r	roll-off wavevector [m^{-1}]
q_s	upper cut-off wavevector [m^{-1}]
R	effective radius of curvature [m]
u	separation [m]
u_0	undeformed profile [m]
u_c	central separation [m]
u_0^d	deformed profile [m]
U	relative sliding speed in x direction [m/s]
$\bar{U}$	dimensionless speed parameter
U_{el}	elastic energy
v	velocity [m/s]
V	relative sliding speed in y direction [m/s]
w	deformation [m]
Δw	nodal displacement from stage B to stage C [m]
W	applied normal load [N]
$\bar{W}$	dimensionless load parameter
x_{in}	inlet of the calculation domain
x_{end}	outlet of the calculation domain
Δx	grid spacing

Greek symbols

α_l	relaxation factor
α_f	relaxation factor for fluid in BML
α_s	relaxation factor for solid in BML/MEHL module
α_u	relaxation factor for deformation in BML/MEHL module
α_c	relaxation factor for central separation in MEHL
α_{fs}	relaxation factor for Fredholm solver in MEHL
α_{eqv}	equivalence coefficient
ε	strain
ε_g	difference error of deformed geometries
ε_W	convergence criterion for load
ε_f	fluid convergence error
ε_u	separation convergence error

ε_{fs}	Fredholm solver convergence error
ζ	magnification
η	Lubricant viscosity [Pa·s]
κ	proportionality coefficient
λ	wavelength [m]
λ_r	roll-off wavelength [m]
λ_L	largest wavelength [m]
λ_s	smallest wavelength [m]
μ	friction coefficient
ρ	Lubricant density [kg/m^3]
σ	stress [Pa]
σ_s	shear stress derived from asperity shearing [Pa]
σ_f	shear stress derived from flow shearing [Pa]
σ_{total}	total shear stress [Pa]
σ_1	shear strength [Pa]
υ	Poisson's ratio

1 INTRODUCTION

1.1 Background

Lubricated soft contacts, or lubricated compliant contacts, refer to systems where one or both contacting bodies have a low elastic modulus in the presence of fluid. Numerous examples can be found in engineering applications, such as elastomeric seals, tyres, *etc*, as well as in biological systems, *e.g.* synovial joints, contact lenses, and human skin contacts. Despite its widespread application and increasing interest in research, understanding of the interaction mechanism between fluid and solids in compliant contacts, particularly using numerical tools to make accurate simulations, lags behind that of stiff contacts. The main challenge is in dealing with the strong coupling between the lubricant behaviour and the deformable body and the complex pattern of deformation and operating conditions. For example, surface roughness plays an important role in determining the contact behaviour and the transitions between lubrication regimes. Moreover, the response of solid bodies is marked by the nonlinear time-dependent stress-strain constitutive laws. Other properties, including surface energy and interface strength, increase the difficulty to obtain an accurate description of the phenomena under investigation. Most of the existing studies presented in the literature focus only on one or two of aforementioned issues.

Among all kinds of soft materials under investigation, elastomers, or rubbers, are the most common given their practical relevance. A typical example is the windscreen wipers in the automobile industry. The main purpose of wiper blades is to wipe away rain, dust or other contamination that may obstruct drivers' view, which means a minimum film is usually preferred in the interface for good "wipe ability". However, if the fluid film is much lower than or in the same order of magnitude as the surface roughness, the boundary lubrication or the mixed lubrication will occur, resulting in high friction and potentially a reduced lifetime of the wiper. Such trade-off between the film thickness and the friction is one of the main challenges faced in the wiper blade industries, for whom the goal is to find an optimum combination of materials, surface properties and operating conditions so that a balance could be achieved. Another phenomenon associated with the mixed presence of

liquid and contact between asperities is the friction induced vibration which produces disturbing noise during wiping. This kind of noise usually occurs when friction quickly drops with sliding speed and was found associated with the geometry, the stiffness, and the surface property of the wiper blade [1]. Thus, understanding the contact mechanism and being able to simulate the behaviour of windscreen wipers have significant implications on ensuring driving safety, enhancing economic efficiency and improving ride comfortability.

Experimental investigations of wiper blade systems have made significant progress over the years. In the previous PhD project collaborated with Bosch, experimental studies have performed to shed some light on the mechanism of friction and lubrication in these particular configurations. However, modelling the lubrication and performance of windscreen wipers in existing literatures is limited to simplified cases where the geometry of the wiper blade is approximated as a cylinder or a roll-shaped specimen [2]. Despite the numerical convenience, such approximation overlooks the impact of the unique profile of the wiper blade. To date, only few studies have been performed to consider the rough contact, the material nonlinearity and the finite deformation of a soft contact system all at the same time [3, 4]. Existing approaches accounting for one or two of these aspects requires considerable computational expenses with significant mathematical complexity, making it difficult to apply in the industrial test or design. Therefore, a comprehensive model that can be easily implemented is needed.

1.2 Research objectives

As the continuation of the previous experiment-based study on the same general topic, this project aims to develop a fluid-solid-interaction model which can capture the interfacial behaviour of real windscreen wipers in steady-state sliding motion and make predictions for a wide range of contact operating conditions. Specifically,

- Appropriate algorithms need to be developed to solve the fluid flow, the contact

pressure (if there is contact between asperities) and the deformation of solid body. The algorithm should be able to handle the level of coupling between the fluid pressure and the deformation, which usually depends on the lubricating conditions.

- As the surface roughness plays an important role in determining the transition from the boundary lubrication regime to the EHL regime, it is necessary to gain a better understanding of the rough contact mechanism. Particularly, in order to incorporate the effect of roughness into the FSI model, the relations between the load and separation, and the relations between the contact area and the pressure, should be investigated for real rough surfaces.

- The large deformation usually observed in compliant contact systems needs be captured accurately. As such deformation is often associated with the strong nonlinearity due to the material properties and the geometry. The strain response of hyper-elastic or viscoelastic materials and the unique configuration of the wiper blades are to be considered for a better prediction of the behaviour of the compliant solids.

Overall, this research is to provide accurate and efficient predictive tools for the estimation of frictional behaviour and lubricating performance in rough soft contacts. Particularly for the windscreen wiper system, this model can be used to optimize design and recommend operation conditions for improved performance.

1.3 Thesis outline

This thesis is organized in the following way:

Chapter 2 provides a literature review, which highlights the most relevant work undertaken in this area of research to date and is a crucial step to ensure existing knowledge is built

upon. After a description of various numerical approaches developed for modelling the fluid-solid interaction especially in the mixed lubrication regime, studies on rough contact mechanics are thoroughly reviewed, followed by a comprehensive demonstration of friction mechanism of elastomers for a better understanding of the tribological behaviour.

Chapter 3 presents the governing equations of the FSI model as well as relevant mathematical formulations for a classical line contact based on the half-space assumption and the approximation of linear elasticity. Three algorithms are developed accounting for interaction behaviour in different lubrication regimes and benchmarked against an existing numerical simulation. The effect of roughness and elastic modulus are assessed in this initial stage to gain some insights into the lubrication mechanism.

Chapter 4 focuses on the study of contact mechanics between rough surfaces. Persson's theory and the boundary element method are described and evaluated regarding their performance of predicting true contact area and interfacial separation. By using computer generated rough surfaces, the influence of the roughness properties on interacting behaviour is assessed qualitatively.

Chapter 5 introduces the reduced stiffness method for calculating the finite deformation of soft materials. After explaining the limitation of the classical theory of elasticity, this new approach is validated by the finite element method for various materials from linearly elastic to hyper-elastic and viscoelastic, alongside with the characterization of material response.

Chapter 6 modifies the original FSI model by incorporating the effect of roughness and the finite deformation solved by the previous boundary element method and the reduced stiffness method respectively. To validate its capability of predicting friction, experiments are also carried out between an elastomer specimen and a glass slide, where small strain deformations are encountered.

Chapter 7 extends the FSI model to a more advanced version which can account for large deformations particularly for the application of windscreen wiper system. Based on the concept of linearization, the reduced stiffness method is updated so that the main algorithm can be adapted accordingly to capture the steady-state behaviour of the system. Given the complexity, influential factors are evaluated to provide reference value for future use.

Chapter 8 summaries the conclusions and achievements of the current research and suggests a range of open questions to be investigated going forward.

2 LITERATURE REVIEW

2.1 Introduction

Dealing with Fluid-Solid Interaction (FSI) in soft contacts requires a multiphysics coupling strategy that combines models that describe the interaction between fluid dynamics and structural mechanics in a lubricated contact where one or both bodies are compliant. This class of problems is characterized by interactions between a deformable moving structure and surrounding fluid flow. Such phenomena can be found in a number of industrial applications and biological systems, such as seals, windscreen wipers, synthetic joints, *etc*. Thus, developing reliable models is of great significance in understanding the interaction mechanism between fluid and structures and optimizing the design and performance of industrial products.

Modelling FSI in the contact mechanics context usually involves solving the Reynolds equations for fluid flow as well as the solid mechanics equations for the deformation of a solid body. There are a variety of appropriate modelling approaches available. However, accurate simulation of the real-world soft contacts is not yet fully achieved as such systems can be too complex to be described in all aspects. One challenge is to incorporate the effect of roughness as it directly determines which lubrication regime the system operates in and how solid bodies interacts with each other. Moreover, soft materials have low elastic moduli, which leads to large deformations associated with geometric nonlinearity. Additional complication arises when considering rubber-like materials, for which the stress-strain behaviour is highly non-linear and time-dependent.

In this chapter, the state-of-the-art research of theories, technologies and methodologies addressing the aforementioned issues is reviewed. Firstly, approaches that are commonly employed to solve fluid-solid interactions under fully flooded and partially lubricated conditions are presented in section 2.2, aiming to understand the algorithm required for solving the coupling between fluid flow, asperity contact and elastic deformation. In section 2.3, analytical theories and numerical methods developed for rough contact mechanics in

dry conditions are reviewed in detail to gain knowledge about how asperity interactions are handled and what advantages and limitations of the different existing methods are. Finally, studies on tribological behaviours of rubber-like materials are described in section 2.4, focusing on friction mechanisms and film measurements. In particular, research into windscreen wipers is discussed as an important application in the context of the present work.

2.2 Numerical models of Fluid-Solid-Interaction

This section surveys the most relevant approaches of simulating fluid solid interaction in soft contacts, starting with models developed for full film elasto-hydrodynamic lubrication. As contacting bodies are completely separated by the lubricant, the main concern is to calculate the fluid flow and the structural deformation. Subsequently, regarding the capability and applicability of methodologies capable of accounting for asperity contacts, several algorithms for solving mixed lubrication problems are examined.

2.2.1 Model Elasto-hydrodynamic lubrication

Elasto-hydrodynamic lubrication (EHL) in compliant contacts differs from the traditional EHL in two perspectives. First, the deflection of the solid is much larger due to the low elastic modulus. Second, the pressure built-up in the contact is relatively low, insufficient to cause change in the lubricant's viscosity. For these reasons, such lubrication systems are usually categorised as iso-viscous EHL(I-EHL).

The theoretical study of I-EHL has a long history [5], nearly the same as experimental studies. Initially, methods applied to EHL problems in steel-steel contacts were also used for I-EHL, which means the Reynolds equation governing the hydrodynamic flow and the elasticity equation governing the structural deformation were solved in an iterative loop.

Concretely, starting from a given pressure distribution, a compatible film profile is found by solving the elasticity equation, after which the pressure distribution is corrected by solving the Reynolds equation before a new profile is calculated. This process is repeated until a certain convergence is met. Despite the numerical convenience, such iteration often encounters convergence issues due to the strong coupling between low pressure and large deformation.

In order to overcome this problem, Herrebrugh [5] proposed an integral type of equation to solve the coupling between the Reynolds equation and the elasticity equation simultaneously. By applying this method to line contacts, where side leakage is neglected, Herrebrugh observed no pressure spike even at high loads.

I-EHL on point contacts was initially investigated by Biswas and Snidle [6], who used the elasticity equation to obtain detailed shape information under lightly loaded conditions. Under high loads, where convergence becomes an issue, they adopted the assumption from Baglin and Archard's approach [7], in which a tilted-pad shaped film thickness was used to resemble the film thickness under the Hertzian pressure distribution.

Following their original work on hard EHL [8], Hamrock and Dowson provided a more systematic methodology to assess soft lubrication problems by calculating the pressure as the sum of Hertzian pressure and a pressure difference. A better convergence was achieved, and this method was applied to generate the most well-known equations for predicting central and minimum film thickness, H_c and H_{min} respectively, in elliptical contacts for materials of low elastic moduli [9, 10]:

$$H_{min} = 7.43(1 - 0.85e^{-0.31k})\bar{U}^{0.65}\bar{W}^{-0.21} \qquad \textit{Equation 2-1}$$

$$H_c = 7.32(1 - 0.72e^{-0.28k})\bar{U}^{0.64}\bar{W}^{-0.22} \qquad \textit{Equation 2-2}$$

where $\bar{U}$ is the dimensionless speed parameter

$$\bar{U} = \frac{\eta v}{E_r R}$$

and $\bar{W}$ is the dimensionless load parameter

$$\bar{W} = \frac{W}{E_r R^2}$$

with η, E_r and R being the viscosity, reduced elastic modulus and effective radius of curvature respectively, v and W are the velocity and the applied normal load, and k is the ellipticity parameter.

The study of I-EHL has progressed significantly over the years and has been extended to various conditions. Hooke [11, 12] investigated the film thickness in soft, highly deformed, non-steady motion contacts. Dowson and Yao [13] used an efficient Newton successive-over-relaxation approach to solve the EHL of soft-layered solids. Hook and Huang [14] performed pioneering work considering the influence of viscoelasticity of solids on pressure and film thickness. Nikas *et al.* [15] developed a numerical model to improve the performance of rotary vane seals in both steady-state and transient conditions.

While the above studies can accurately predict the tribological behaviour in I-EHL, in many practical cases, the existence of roughness prevents the occurrence of full film lubrication conditions. To incorporate the interaction of asperities in the partial lubrication, three methods are commonly explored, which are reviewed in the following subsections.

2.2.2 Stochastic methods for modelling mixed lubrication

Stochastic methods use statistical parameters to account for the influence of surface roughness when the Reynolds equation is solved. First proposed by Christensen [16], this method was applied to deal with hydrodynamic lubrication problems between bearing

surfaces with different directional roughness. The elastic deformation was not considered until a decade later, when, in 1978, Lebeck extended this approach to seal applications [17].

The most well-known approach to solve the mixed lubrication problems was proposed by Patir and Cheng through their average flow model [18, 19], also known as PC's model. In this model, the classical Reynolds equation is modified by introducing flow factors which are derived from the simulation of flow between asperities. While the average Reynolds equation accounts for the hydrodynamic behaviour, a simplified stochastic contact model is employed to handle the asperity contact, which takes into consideration more statistical properties of a rough surface than a simple root-mean-square (RMS) value. Results were later confirmed by Elrod's study [20] where the multi-asperity analysis was employed.

Many researchers extended the PC's model for different applications by either modifying the calculation of flow factors or further modifying the Reynolds equation. To name a few, Tripp [21] overcame the difficulty in extracting the ensemble average of flow factors by introducing a Green function allowing the pressure to be related to the roughness. Letalleur *et al.* [22] used this model to study the surfaces with sinusoidal waviness. Harp and Saland [23, 24] proposed an "universal Reynolds equation" that accounts for both inter-asperity cavitation and macroscopic cavitation. Kim and Cho [25] enhanced the roughness characterization by introducing skewness and kurtosis of the roughness distribution.

Although being mathematically simple and efficient, the stochastic method only demonstrates the global trend of lubrication performance and transition, predicting mean values of pressure and film thickness. More detailed information such as the pressure distribution and localized maximum/minimum values, which are critical for lubrication breakdown and surface failures, are not fully resolved. Moreover, due to the lack of proper consideration of the asperity deformation and interaction, which leads to overestimation of film thickness, especially in the mixed and boundary lubrication regime, the stochastic method is intrinsically more suitable for problems characterised by large contact areas,

which is typical of conformal contacts.

2.2.3 Deterministic methods for modelling mixed lubrication

Compared with stochastic methods, the deterministic method exhibits great advantages not only in providing local information but also in modelling the engineering contacts using measured rough surfaces directly. This method is often applied to small contact areas where the region can be meshed with roughness-level elements so that the influence of every single asperity can be considered. The classical Reynolds equation and contact models can then be employed on a very fine mesh to calculate the real contact area and the evolution of the lubricant film.

Several early deterministic studies were carried out by Lubrecht [26], Kweh *et al.*[27] and others. However, these initial investigations are limited in simple roughness profiles such as sinusoidal waves due to the restricted computational power available at the time of investigation. Ai and Cheng [28] and Chang [29] offered additional contribution to the research topic, providing an extended model capable to account for the transient analysis and the two-dimensional rough topography obtained from either experimental measurements or synthetic generation.

The initial attempts to solve mixed lubrication problems using deterministic methods were made by Jiang [30], who calculated the hydrodynamic pressure and the contact pressure on separate domains. At the edge of the asperity contact, a boundary condition was set to ensure continuity, *i.e.* the lubricant pressure equals to a non-zero contact pressure on the asperity contact boundary. This model was further improved by Hu and Zhu [31, 32] to study mixed lubricated counter-formal contacts. They proposed a unified Reynolds equation which can be used in both lubricated and contact regions, thus eliminating the need for additional boundary conditions at the interfaces between fluid and contact nodes.

When the fluid film approached zero, the Reynolds equation switched to its reduced form, where an equivalent solution of elasticity equation was given. Various types of roughness were tested, and the transition from full-film and mixed lubrication regime down to boundary lubrication or even dry contact were captured.

Based on Hu and Zhu's model, a three-dimensional model for line contact were developed by Ren *et al*.[33]. This is particularly important in mechanical transmissions and gears, where line contacts are encountered. While the macro-contact geometry was simplified as two dimensional, the effect of roughness and topography were simulated in a three-dimensional model. Results were compared with PC's stochastic solutions and the same trend was found.

Deterministic methods were applied to compliant contacts as well. For example, Shi and Salant [34] presented a mixed soft lubrication model to simulate the lift-off process of rotary lip seals. Three equations, *i.e.* the Reynolds equation, the mass conservation equation and the elasticity equation, were employed so that inter-asperity cavitation was also taken into consideration. Minet *et al*. [35] focused on a different type of seal, the mechanical face seal, for which a deterministic model combining the Reynolds equation and the Hertzian asperity contact model was used. An interesting finding in their study was that the friction results showed sometimes high variability when different surfaces are considered, even though they are statistically equivalent.

In order to capture the detailed information for each asperity, deterministic models are usually quite demanding in terms of mesh density, algorithmic development, and computational power, and are time-consuming in general. Although efforts were made to accelerate the calculation by employing the multi-level multi-integration (MLMI) technique [36] or Fast Fourier Transform (FFT) based methods [37] to solve the asperity deformation, deterministic methods are still considered computationally expensive in many cases.

2.2.4 Two-scale methods for modelling mixed lubrication

Another common technique for modelling mixed lubrication problems is a two-scale approach, also known as a macro-micro scale approach, where the fluid flow is solved in a macro-scale, whereas the asperity-asperity interaction is considered on a micro-scale.

Wang and others [38, 39] initially applied this method to counter-formal contacts. While the asperity interaction was solved deterministically and transposed to the macro-scale using a contact-embedment method, PC's average flow model was employed to account for the influence of roughness on lubricant. The results were compared with Zhu and Hu's deterministic model [31] and good agreement was found when the average film thickness and the RMS value were in the same order of magnitude. However, in regions where solid contacts is dominant, the macro-micro approach tends to overestimate the pressure due to the direct superposition of asperity obtained from an offline contact simulation and the hydrodynamic pressure from the average flow analysis.

The two-scale approach was widely adopted to handle the mixed lubrication problems in soft contacts as well. Persson and Scaraggi [2] proposed a two-scale approach to capture the transition from boundary lubrication regime to EHL regime in lightly loaded conditions. The classical Reynolds equation and Persson's rough contact theory were used to describe the behaviour of fluid flow and solid interactions respectively. Straightforward as it seems, this approach was based on the small displacement assumption and only valid for ball-on-disc geometries where the contact scale is much larger than the asperity scale. The authors observed that for small scale contacts, the asperities may be completely flattened because of the high pressure and the influence of asperity deformation cannot be neglected. Thus, Scaraggi and Carbone [40] extended the above model by introducing a threshold for length scales. The roughness larger than the threshold was treated by a deterministic method, while the effect of roughness with shorter wavelength was incorporated through flow

factors. The main advantage of this new method was to address the complex contact problems between multiscale asperities with a significantly reduced computational effort, enabling a general application in engineering field.

In addition to Persson's theory, Greenwood and Williamson's roughness model was also used to handle asperity contacts in two-scale approaches [41-43]. Masjedi and Khonsari [41, 42] employed this model with the modified Reynolds equation to study the mixed lubrication problems in soft contacts. Stribeck curves were generated and compared with Scaraggi's results [43], a good agreement between the two studies being observed.

Another interesting development in the two-scale approach is the homogenisation technique. The introduction of homogenisation decouples the flow problem into two separate issues: a homogenised problem where the global geometry is considered at the macro-scale and a local problem where individual asperity is accounted for at the micro-scale. Reynolds equation was consequently reformulated with coefficients of the homogenised problem based on the solution of the local problems. Early implementation of homogenization in flow problems were performed employing direct numerical methods. Kane *et al*. [44] and Almqvist *et al*. [45] applied this technique to both incompressible and compressible problems, respectively, and compared the results with deterministic solutions. Good agreement was found, but the homogenisation approach showed significantly improved computing efficiency.

Since homogenisation allowed the calculation to account for both the direction and amplitude of roughness, which traditional stochastic methods lack, it was later employed in conjunction with the flow factor method to capture the full picture of lubrication between rough surfaces. Sahlin *et al*. [46, 47] calculated the flow factor for rough surfaces in compressible hydrodynamic lubrication using homogenized technique. The method not only allowed the flow factor to be obtained for any arbitrary geometry, but also separate the hydrodynamic effect of local roughness from that of the global geometry. With rough

topography as the only input, the flow factors can be determined rapidly without truncation of local solution to avoid the overestimation of the pressures, as in Harp and Salant's study [23].

As shown by Meng and co-workers [48], the limitation of the method described above [2, 46] is that the elastic deformation resulting from asperity interactions were entirely neglected, which could cause non-negligible errors when the separation approaches the root-mean-square roughness value, especially for compliant contacts. To address this, Scaraggi *et al*. [49, 50] applied the homogenised approach to capture the transition from boundary lubrication regime to elasto-hydrodynamic lubrication regime. While the flow factors were calculated by a homogenised technique to account for the effect of roughness on lubrication, the asperity-asperity contact was characterised by Persson's theory which make it particularly accurate for soft materials.

To briefly summarise, three types of numerical methods are commonly used to solve the mixed lubrication problems. Stochastic approaches, represented by the famous PC's flow factor equation, are often employed to make general predictions at a global scale, whereas the deterministic solution provides detailed information but with a much higher computing cost. The macro-micro approaches provide a comprehensive and efficient alternative and can be easily accommodated depending on the scale level of interest.

2.3 Rough contact mechanics

Contact mechanics has been studied for more than a century and is of great interest in many research fields. The Hertzian theory, the cornerstone of the contact mechanics, described the behaviour of elastic solids with smooth surfaces in frictionless contacts. Based on the following approximations:

1. Surfaces are infinitely large half-spaces.

2. Pressure profile is parabolic (which means that the shape of the bodies in contact can also be approximated well with parabolic shapes, e.g. sphere, ellipsoid or cylinder).
3. All the assumptions of the classical theory of elasticity apply (small strain, homogeneous material etc.).

the Hertzian theory predicted that, when two spheres (Young's modulus E_1, E_2, Poisson ratio v_1, v_2, and radius R_1, R_2) are squeezed together, the contact area a and the external force W follow the relation [51]:

$$W = \frac{4E'a^3}{3R} \qquad \textit{Equation 2-3}$$

where R is the reduced radius $1/R = 1/R_1+1/R_2$, and E_r is the reduced modulus $1/E_r = (1-v_1^2)/E_1+(1-v_2^2)/E_2$.

Building on the Hertzian theory, Johnson *et al.* [52] proposed the JKR theory to consider the adhesion in the contact. The adhesion force F_{adh}, also known as the pull-off force, were expressed as a result of free surface energy γ:

$$F_{adh} = -\frac{3}{2}\pi R\Delta\gamma \qquad \textit{Equation 2-4}$$

where $\Delta\gamma$ is called the "work of adhesion" per unit area required to separate the two bodies. Up to date, Hertzian theory and JKR theory are still widely employed to provide fundamental information in engineering design as well as in scientific research. For an overview of historical and more recent advances in this area, the readers are referred to [53-55].

More recent studies focused on the contact mechanism between rough surfaces which involves the physical quantities such as the real contact area, the interfacial separation between solids, the stress distribution and the contact stiffness. When two bodies are squeezed together, they will not make contact everywhere in the nominal contact area but

only on a few asperity spots. These areas of real contact will directly influence a large number of physical properties such as heat transfer, adhesion, friction and wear between solids in stationary or sliding contacts. Furthermore, the separation in the non-contact regions is also crucial given its relevance to seals and optical properties of composite systems, *e.g.* the optical interference between glass lenses. Thus, it is important to understand the effect of roughness on these phenomena using accurate mechanical models.

One of the fundamental issues in solving contact problems is to analyse the rough surface properly using characterization tools. This is especially critical for measured rough surfaces whose roughness information may be compromised by the limitations and artefacts of the measuring techniques [56-58]. In order to accurately characterise the multi-scale nature of the roughness, research showed that prior knowledge of those artefacts, such as the stylus tip geometry and measuring mode (contact or non-contact), are necessary[59]. In addition, post-processing is also helpful in terms of extracting useful roughness information from the raw data. These will be further discussed in Chapter 3 where more details of characterisation and representation of roughness are discussed. In the following sections, reverent studies on rough contact mechanics including analytical theories and deterministic simulations are reviewed, with particular emphasis placed on the evolution of real contact area and the load-separation relations.

2.3.1 Analytical theories

Analytical studies of rough contact problems use the statistical representation of rough surfaces to predict tribological behaviour of the system. The most well-known theories can be categorised into two classes: multi-asperity contact theories and Persson's theory.

One of the early works in multi-asperity contact theories was carried out by Archard [60], who proposed a model based on the assumption that each asperity at scale n is replaced by many asperities at a higher scale. This permits an "uncoupling" of scales in the calculations

of the redistribution of the pressure from one scale to the next, smaller one. Based on this idea, the most famous work on multi-asperity contact theories was presented by Greenwood and Williamson [61] in 1966. In their model (the GW model), roughness was modelled as an ensemble of identical spherical asperities with equal radii and with randomly distributed heights. By applying Hertzian theory to each asperity, the relations between the separation between the mean planes of the rough surface and the real contact area and the load were obtained, and the essential physics of the contact mechanics in partial contact were captured. Since then, this model has been employed and improved by many researchers. For instance, Ciavarella refined GW's model by introducing the interaction between Hertzian micro-asperity contacts [62, 63], whereby the contact behaviour from low load to intermediate load were accounted for more accurately. Another example would be Fuller and Tabor's work [64] where the GW theory was extended to consider adhesive rough contacts by combining it with the JKR model.

Since the GW model assumed all the asperity peaks have the same radius, a nonlinear relation between the true contact area and the resultant force under small loads were predicted, which was found to be linear in experiments. With the development of random process theory, Bush, Gibson and Thomas [65] proposed a model (the BGT model) where the asperity curvature depended on heights, thus truly realising the multiscale nature of most rough surfaces. Hertzian theory was subsequently applied to each asperity, and the dependence of pressure and contact area as function of the separation were obtained. Although this resulted in an asymptotic linearity between the real area of contact and the nominal load, such relation only held true for very low and sometimes even unrealistic squeezing pressures [66].

Because they are relatively simple and computationally cheap, multi-asperity contact models are widely used to describe the contact behaviour between rough surfaces. However, it should be borne in mind that they are limited in small contact areas for the following reasons: (i) The roughness representations in the original models were rather idealized with

either identical radii or a few different bumps and the hierarchical, fractal-like nature of real surfaces was somewhat overlooked; (ii) Coupling between deformation of asperities was neglected in the classical models, which could lead to qualitatively wrong results. Although the incorporation of the inter-asperity deformation was attempted in [63], the long-range elastic interaction still cannot be cut off without considerable loss in accuracy.

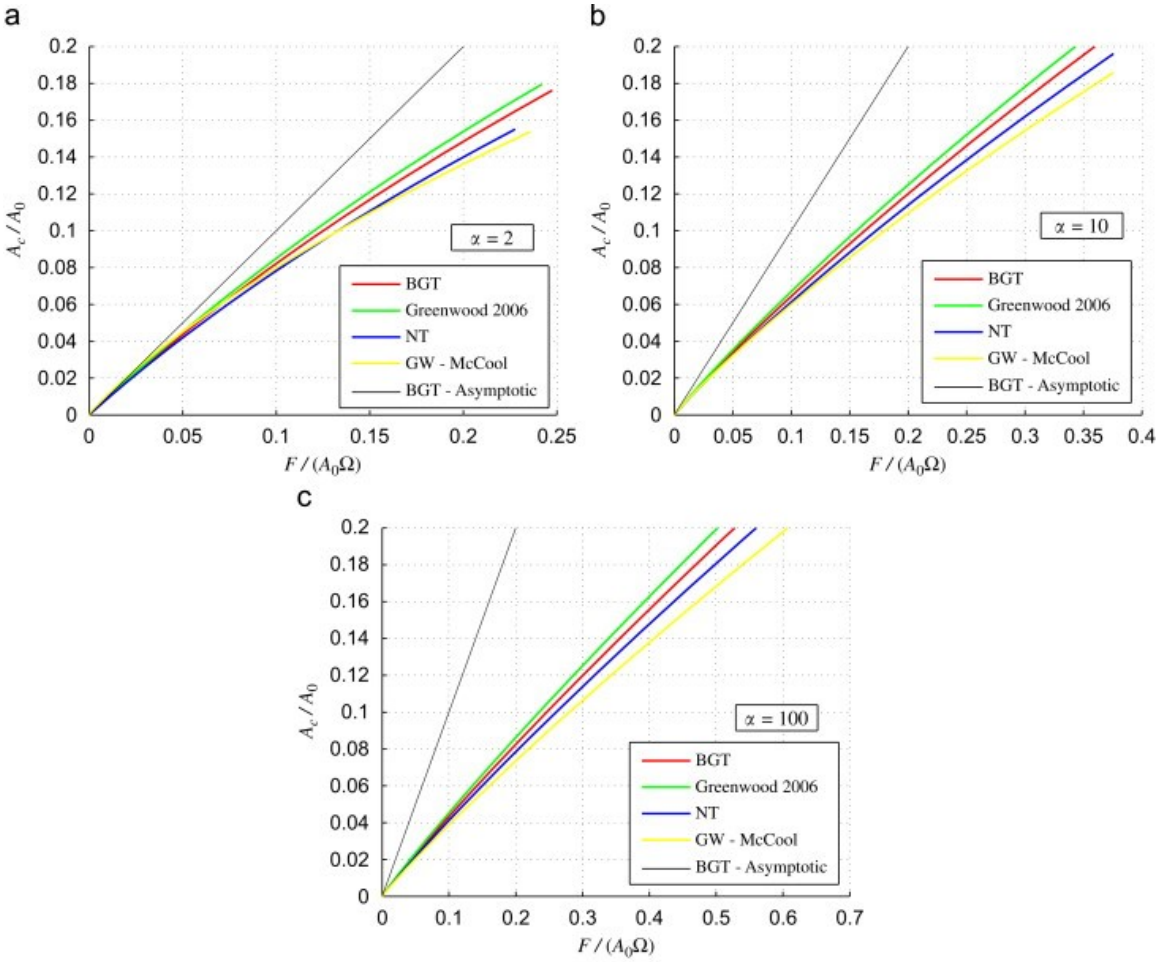

Figure 2-1 Contact area ratio A_c/A_0 obtained by multi-asperity theories, as a function of the non-dimensional load $F/(A_0\Omega)$ for surfaces with different power spectral breadth parameters α_{PSD}. Details refers to [66]. Copyright with permission from [66].

Another analytical model proposed by Persson (Persson's theory) studied the contact mechanics between rough surfaces from a different perspective. In his initial investigations [67], a rubber block was assumed sliding against a randomly rough rigid surface, for which a diffusion-like equation was used to describe the stress distribution between rough

surfaces as a function of observation scale and coordinates. If the surface was observed at a low magnification, the surface appeared smooth and a complete contact was preserved. With the increasing magnification, more asperities could be detected, resulting in smaller true contact areas, as shown in Figure 2-2. By introducing a boundary condition, *i.e.* the probability of stress distribution is zero when the pressure reaches zero, Persson extended this theory to contacts where asperities partially interact [68, 69]. Thus, contact area evolution from zero to full contact can be captured and the comparisons between theoretical predictions and experiments showed good agreement [69, 70]. Details of the roughness representation and the derivation of Persson's theory can be found in Chapter 4.

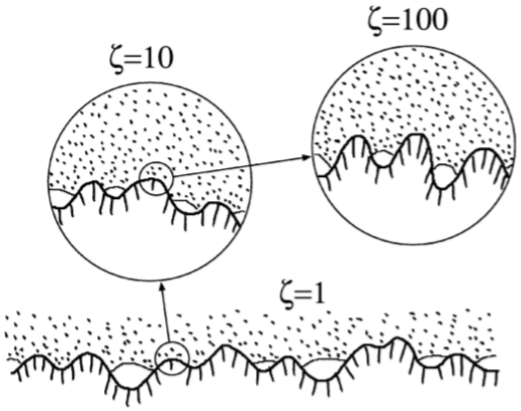

Figure 2-2 Magnifying a contact region with the magnification ξ one observes smaller length scale roughness and the surface "looks the same" as before.[67]

Many numerical simulations were carried out to assess Persson's model and its prediction of contact areas. Results have demonstrated a general good agreement with numerical results, with the model showing less fidelity in partial contacts [71-74] due to the approximations made in Persson's theory. In [75], Manner and Greenwood raised questions about the boundary conditions employed and derived a simpler form for Persson's diffusion equation. Dapp *et al*. [76] checked the diffusion coefficient using high-resolution numerical simulations and found that although error caused by individual assumptions can be mostly cancelled out, this cancellation cannot be guaranteed in all situations and guidelines ought to be provided.

Contrary to the real contact area, studies of the interfacial separation based on Persson's

theory started from partial contacts. The work done by external pressure to deform the surface was considered equal to the elastic energy stored in the contact area. Persson and Yang [73, 77] employed a corrective function to link the elastic energy equation for small loads to high loads where full contacts occur, whereby the analytical expressions for relations between interfacial separation and resultant average pressure can be derived with approximations. However, it was not clear which form of corrective functions should be used or how the corrective coefficients change with surface properties, which often led to discrepancies between this theory and numerical simulations for predictions at complete contact cases [78-81].

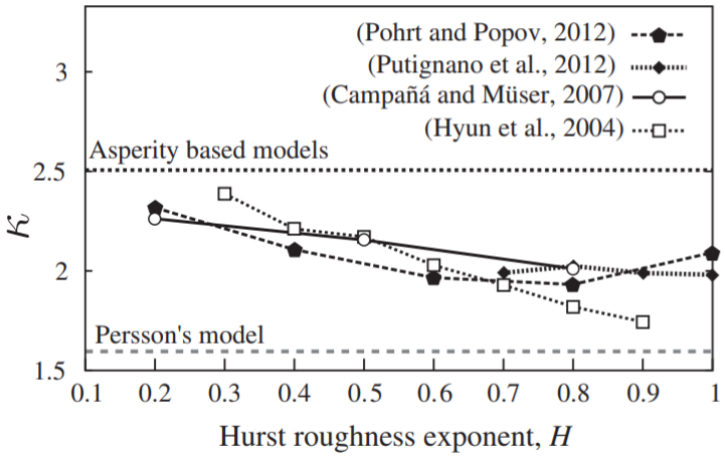

Figure 2-3 κ value obtained in analytical theories and numerical studies. Copyright with permission from Ref [82].

Although both multi-asperity theories and Persson's theory demonstrate qualitatively comparable predictions to some extent, for instance, they both show an asymptotic linear contact area evolution for small loads and an exponential relation between separation and load, these two theories differ drastically if details are pursued. The proportionality coefficient κ, which is introduced to correlate the contact area with pressure and a product of the effective elastic modulus and the RMS gradient, is approximately 1.6 using Persson's theory and around 2.5 in BGT's model [83]. Most numerical analyses predicted this value to be within this range, which is discussed in next section, as shown in Figure 2-3. In a close examination of the multi-asperity theories (GW model, GW improved version, and

BGT) and Persson's model, Carbone and Bottiglione [66] found that the latter can predict the linear increase of true contact area up to about 10-15% of nominal one, making it a preferable choice in cases characterised by physically reasonable loads and contact areas. Not much validation of load-separation relation on real rough surfaces has been performed expect for the work presented in Refs. [84] and [85]. Lorenz and co-workers conducted experiments pressing a silicon rubber block against different types of road surfaces under controlled displacements. Measurement of load and separation were compared with those obtained from the BGT model and Persson's theory. It was shown that the load-separation relation followed an exponential function, agreeing better with Persson's prediction than the BGT model.

2.3.2 Numerical simulations

Apart from analytical theories, different methodologies relying on numerical simulations have also been developed to study the mechanical interactions between rough surfaces. As the calculation is carried out on measured or synthetic (computer generated) surfaces with limited statistical information, such as the cut-off wavevectors (the frequency of wavelength), the Hurst exponent, the RMS roughness *etc*., much research has been focused on model validity, computational efficiency as well as the effect of surface properties on contact mechanics. Three categories of numerical methods are commonly found in the investigation of rough contact mechanics: the finite element method (FEM), the boundary element method (BEM) and molecular dynamics (MD) simulations.

FEM is a well-known numerical tool for solving the contact problems, by which the constitutive behaviour of materials can be described using infinitesimal or finite strain formulations. Hyun *et al*. [86] initially applied this method to analyse the frictionless, non-adhesive contacts between self-affine fractal surfaces of which the roughness was incorporated down to the discretization scale. A wide range of parameters such as the roughness amplitude, the roughness exponent and Poisson's ratio were tested when

observation was made on the variation of real contact areas and the average load carried by the rough surfaces investigated. A linear relation between them was found when the contact area ratio was less than 5~10%, with the proportionality coefficient κ falling between the prediction of BGT model $\kappa = (2\pi)^{1/2}$ and Persson's theory $\kappa = (8/\pi)^{1/2}$. Although this value barely changed with RMS roughness and only slightly decreased with higher Hurst exponents, it appeared to be very sensitive to the largest wavelength considered [87]. In addition, larger-scale cut-off wavevectors could mitigate the localization of the contact zones, resulting in larger contact areas.

FEM was also used to solve rough contact problems for viscoelastic materials. Wriggers and Reinelt [88] proposed a finite element model where the rough surface was decomposed into a limited number of harmonic functions with different wavelengths and amplitudes. The effects of hysteresis and adhesion were considered and a fair agreement in comparison with experiments was obtained. However, due to the extremely high computational efforts required, they were only able to capture a small range of roughness.

Although FEM is advantageous for its effectiveness and versatility especially for nonlinear constitutive material models, when the deformation is much smaller than the dimension of contacting bodies, the use of BEM is preferred given that only the surface needs be discretized. Instead of calculating the deformation for all elements of a three-dimensional body, BEM only concerns the displacement (and stress) on the grid nodes of two-dimensional surfaces, therefore improves the computational efficiency significantly.

One challenge in solving rough contact problems with BEM was the calculation of deformation. Polonsky and Keer [89] proposed a boundary element method where the linear system of equations was solved by a conjugate gradient method and the deflection was determined by a multi-level multi-summation (MLMS) technique. This approach was compared with a Fast Fourier Transform (FFT) algorithm, and both showed significant improvement in computing speed [90]. While the FFT was more suitable for periodic

surfaces, the MLMS was more efficient in concentrated contact problems.

Early attempts to solve rough contact problems using BEM were carried out by Webster and Sayles[91], who showed that certain assumptions about the nature of real rough surfaces used in the random process theory can be relaxed by the deterministic approach. The topography was obtained using a mapping technique proposed by Webster et al.[92], which provides good visual images and quantitative information that can be used for further analysis.

More recent studies using the BEM was given by Putignano *et al.* [71], who developed a numerical model on a non-uniform adaptive mesh to evaluate the elastic contact solution between rough surfaces. Refinement of mesh was made where the stress and strain gradient increased, thus improved the efficiency and accuracy significantly. This model was subsequently employed to investigate influence of roughness properties on contacting behaviour. For small squeezing pressure, a linear relation between the real contact area and pressure were found, with the proportionality coefficient 2 which is between Persson and BGT predictions [93]. Such relations were lost when asperities with large curvature were brought into contact under high loads. They also demonstrated that even though the ratio of true contact area to dimensionless pressure varied for different Hurst exponents, the proportionality coefficient was affected by the RMS gradient rather than the Hurst exponent. In a following study [94], a similar discovery for the cut-off wavelength was found, *i.e.* the influence of the cut-off wavevector on the contact area ratio was indeed through the RMS gradient. The same conclusion held true in the non-linear range of contact area evolution as well. They argued that literatures [86, 95] predicting otherwise may be due to a lack of refinement in the mesh points in the contact region.

The effect of cut-off wavevector on the real contact area was also investigated by Yastrebov *et al.* [74] who employed a FFT filtering algorithm [96] to construct rough surfaces and a spectral based BEM [97] to handle contact problems. They suggested that to construct

representative rough surfaces, the specimen size must be much larger than the longest wavelength. If the domain size was equal to the longest wavelength, the rough surface considered might be non-Gaussian, which could lead to the clustering of contact zones and consequently a larger contact area. This phenomenon was often referred to as the "finite size effect" and confirmed in many studies [86, 93, 94].

Furthermore, they pointed out that the Nayak's parameter characterizing the breadth of the surface spectrum played a significant role in representing the statistical properties of rough surfaces. The Nayak's parameter is a dimensionless combination of the zeroth, second and fourth moments of the roughness distribution and can change the contact area drastically [95]. While many studies focused on the effect of the upper cut-off wavevectors and the Hurst exponent on the evolution of the contact area, Yastrebov *et al*. showed that these properties did not act independently, but implicitly through the Nayak's parameter [82]. When the surface was spectrally rich, the Nayak's parameter changed drastically with the Hurst exponent, and the higher the Nayak's parameter, the smaller the contact area [98]. These results agreed with multi-asperity models but contradicted Persson's theory, which, as the authors suggested, may be because the latter did not consider the Nayak's parameter in deducing the diffusion equation, and thus is only valid when the Nayak's parameter is high.

Papangelo *et al*. [80] also employed the BEM to study the load-separation curve for contacts between self-affine rough surfaces. The "finite size effect" was evaluated for the relation between the resultant average pressure and the mean interfacial separation, and comparisons with multi-asperity theories and Persson's model were performed. It was found that Persson's theory agreed with numerical simulation better in the intermediate pressure but required significant corrective factors. Multi-asperity theories, on the other hand, were more appropriate for large separations as the interaction between asperity deformation was not considered.

It is worth mentioning at this point that a method of dimensionality reduction was proposed by Pohrt and Popov [99, 100] to reduce the computational time by projecting a three-dimensional contact problem to an equivalent two-dimensional one. They employed this method to particularly study the contact stiffness between self-affine fractal rough surfaces and compared results with the BEM. The contact stiffness followed a power law with the applied force, which can be expressed as a function of the Hurst exponent, agreeing with the BEM qualitatively but not quantitatively.

Another mainstream approach for solving contact problems numerically is based on molecular dynamics. Campana and Muser [101] proposed a Green's function molecular dynamics (GFMD) where a semi-infinite, harmonic solid was replaced with a single layer of atom, which is more computationally efficient. Both real surfaces and artificially generated surfaces were considered in their simulation, and the results have shown that the probability distribution of contact stress had Gaussian tails for randomly generated rough surfaces but exponential ones for experimentally determined topographies [72]. However, the true contact area was not affected significantly by this difference, with the approximated proportionality coefficient κ around 2, in between Persson's theory and BGT model.

To understand the relation between the contact area, interfacial separation, stress distribution and load for soft materials, such as rubber, Yang and Persson [73] presented a numerical study using a multiscale molecular dynamics approach to simulate the transition from small to full contact. The outcomes were consistent with Persson's theory qualitatively. However, the interpolation function used to predict the interfacial separation for a given load were in several different forms and did not have a universal implication.

Further investigate on soft rough contact mechanics was carried out by Almqvist *et al.* [81] who confirmed that while the real contact area was proportional to the squeezing pressure under small loads, the interfacial separation depended logarithmically on the applied force.

Three numerical methods, the BEM, the GFMD and the smart-block classical MD were used in their study. Despite the good agreement achieved in comparison with Persson's prediction for high loads, the rather small system size used in their calculations resulted in the "finite size effect" for large separations.

This "finite size effect" was also investigated by Pastewka *et al.* [79] who applied the GFMD to study the contact stiffness which was found to be linear with the squeezing pressure over a large range of loading conditions, unlike the power-law trend presented by Pohrt and Popov [100]. The authors believed that the latter was likely due to the finite size of the contact. They stated that this power law region will vanish in the thermodynamic limit, *i.e.* when the system is considerably larger than longest wavelength.

As more and more research showed that the interfacial properties were determined by not a single, but a few parameters combined, Prodanov *et al.* [78] performed a systematic study on the effect of thermodynamic correction, fractal correction and continuum correction on the relative contact area and the mean gap. The quantities were defined as the ratio of system size over the largest wavelength, the ratio of smallest wavelength over the largest wavelength, and the smallest wavelength over discretisation resolution, respectively. The numerical simulation employed a GFMD method and was compared with Persson's theory. Although no universal rules were concluded, this study provided valuable reference for contact mechanics between self-affine fractal surfaces. With regards to contact area, it was found that the influence of the continuum and fractal correction were more substantial. To achieve the asymptotic convergence, a fine discretization was required for systems with small Hurst exponent while a small range of wavelength was needed for those with larger Hurst exponent. In terms of the mean gap, criteria varied drastically with the system as well. For those with large Hurst exponent and under low pressure, the effect of finite size and discretization were less significant as long as the roughness spectrum spanned over a large range of wavelengths. On the other hand, if the system had a small Hurst exponent and was under high pressure, the grid size was required to be much smaller than the smallest

wavelength. Furthermore, the dimensionless representation of the pressure was suggested to involve the RMS gradient in addition to the reduced elastic modulus, which was also adopted in [82, 87].

In summary, with the increasing speed and memory capacity of modern computers, numerical tools have become a viable alternative to theoretical analysis as they provide more exact results in terms of stress distribution and deformed profiles. The FEM is more versatile and accessible for general research but can be computationally expensive. The BEM is easy to implement and efficient under reasonable assumptions. The MD methods also requires significant computing resources and is usually reserved for system of relatively small sizes. Therefore, despite the numerous studies performed the tremendous progress made in this area, there is still much to be done to have a better understanding of the mechanics and to solve target problems. In Chapter 4, more details of Persson's theory and the BEM, which are adopted in this thesis, will be discussed.

2.4 Tribological behaviour of elastomers

Among all compliant contacts, rubbers, or elastomers, are the most common materials given the wide application in practice, *e.g.* the tire/road contact, windscreen wiper and seals. This section reviews studies on the tribological behaviour of rubbers to understand their friction mechanism. Friction of elastomers strongly depends on load, sliding velocity, temperature, surface roughness and the viscoelastic property of the material. A general expression of the origins of elastomer friction in lubricated contacts can be given as:

$$F_f = F_{hysteresis} + F_{adhesion} + F_{viscous} + F_{cohesion}$$

$F_{hysteresis}$ is the hysteresis component resulting from the energy dissipation through bulk deformation. It is closely related to the viscoelastic response of elastomers and can be affected by many parameters such as sliding velocity, temperature, load and roughness.

$F_{adhesion}$ is the adhesion term due to the intermolecular interaction between surfaces and is often influenced by the surface roughness.

$F_{cohesion}$ is usually considered when abrasion, crack initiation or wear occurs, which is associated with the existence of sharp asperities.

$F_{viscous}$ is the contribution of lubricant which arises when there is viscous shear of fluid at the interface.

In the following, studies on the friction mechanism of rubber in dry and lubricated contacts, including experimental measurements, techniques as well as theories, are reviewed to establish a more comprehensive understanding of the rubber friction.

2.4.1 Friction mechanism of elastomers in dry contacts

On dry contacts and when low shear forces occur, *i.e.* no contribution from lubrication and wear, the friction is considered to mainly originate from adhesion and hysteresis, which can be significantly affected by the modification on surfaces. Due to the complex nature of the material property, friction of elastomers can be further influenced by load, velocity and temperature.

Early studies were carried out by Schallamach [102] who experimented with rubber hemispheres sliding on a glass track and revealed the load dependence of rubber friction. He also found that the rubber friction was a rate process by investigating the influence of velocity and temperature [103]. A following study by Grosch [104] demonstrated that the velocity- and temperature- dependency was in fact a result of the viscoelastic response of rubber. This was later confirmed by Barquins [105] who measured the sliding friction between a rubber specimen and hard surfaces. However, it was worth mentioning that Barquins' initial results did not repeat Grosch's data because the former used optically

smooth surfaces while the latter employed abraded rubber to avoid stick-slip. This further implied the important role of surface finish on friction mechanism.

Generally, on smooth surfaces, adhesion is the main contribution to rubber friction. In the investigation of static adhesion, Johnson, Kendal and Roberts examined the adhesion between an optically smooth rubber sphere and an optically smooth flat surface. An increased contact area was found even in an unloaded condition due to the high elasticity of rubber. They described this adhesive behaviour as an intermolecular process at the interface depending on the surface energy and provided an analytical formula to calculate the contact area, known as the Johnson-Kendal-Roberts (JKR) theory [106]. A similar study was carried out by Robert and Thomas [107] who dropped a small steel ball on a rubber surface and found that the steel ball rebounded from a dusted surface but adhered to the clean surface, thus confirming the formation of intermolecular bonds.

When the surfaces are in dynamic motion, the intermolecular bonds experience a formation-breakage process due to the relative displacement between surfaces. The polymer chain repeatedly attaches to the moving counterpart, stretches, detaches, relaxes and reattaches, seen in Figure 2-4. The energy dissipated during the cyclic peeling and unpeeling forms the origin of friction, and this wave of detachment discovered by Schallamach was known as the Schallamach wave[108]. Theoretical investigations on this friction mechanism can be found in the study by Persson and Volokitin [109].

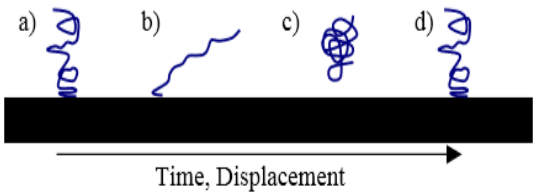

Figure 2-4 The stick-slip transition of a single rubber chain when relative displacement occurs. The rubber chain goes through four stages: a) sticking to the surface, b) stretching with increasing time, c) detaching from the surface and relaxing, d) reattaching to the surface. [108]

The instability caused by Schallamach waves transforms to a stick-slip motion at high velocity. When in contact, no relative motion occurs at the interface (stick-stage), whereas in the second stage (slip-stage), relative sliding at the interface occurs and a critical shear deformation is met. Friction in stick-slip motions alters periodically due to the detachment and reattachment of contact surfaces and represents as a jigsaw wave. A heavy stick-slip motion may evoke the slider to move up and down, as is shown schematically in Figure 2-5, and cause severe problems such as noise and instability of the mechanical system.

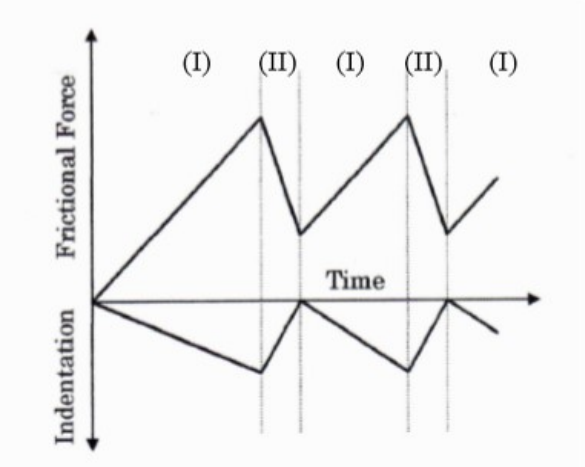

Figure 2-5 The slider is displaced vertically while horizontally sliding on a rubber block. The change in indentation correlates to a change in frictional force during the stick-phase (I) and slip-phase (II) [110]

On rough surfaces, roughness affects the frictional behaviour in two aspects. On one hand, roughness reduces the real contact area and hence reduces the level of adhesion. For example, the actual contact area was only ~1% of the nominal contact area on a tire road contact, in which case the adhesive contribution was considered to be negligible [67, 111]. On the other hand, the micro-indentation of asperities into rubber causes the energy loss due to viscoelastic deformation, which is characterized as hysteresis. This means the majority contribution to the sliding friction for rough surfaces is derived from the time-dependent deformation of the rubber and closely associated with its viscoelastic nature.

The experimental evidence of the mechanism mentioned above can be found in Fuller and

Tabor's study [112] where optically smooth rubber spheres and hard roughened surfaces were used. Adhesion was measured through the pull-off force, and results showed that even rough surfaces with RMS value 1 μm were able to reduce the adhesion to a very small fraction of that for smooth surfaces (by nearly 20%). In addition, this trend was more marked for rubber with higher modulus but only affected by the radius of rubber ball marginally.

More recent theories for interpreting this phenomenon was developed by Persson. In his early studies of rubber friction [113], he suggested that the hysteric contribution was associated with the long-wavelength surface roughness and the adhesion with short-wavelength roughness. For rough surfaces, a large fraction of friction was attributed to the energy "dissipation" caused by internal friction of the rubber (previously known as hysteresis). This was confirmed by Grosch's research where the material response was closely associated with the roughness scale and the velocity [104], and by the work of Barquins and Roberts which revealed the dependency of friction on temperature and velocity [114]. The adhesion component, which plays an important role when the surface is clean, was initially considered insignificant for rough surfaces.

Interestingly, Le Gal *et al*. [115] and Lorenz *et al*. [116] showed that, on very rough surfaces such as tire road contacts, in addition to the viscoelastic deformation, there was a considerable contribution to the rubber friction from shearing process in the contact area (adhesive contribution). This process was conceived to arise from rubber molecules undergoing bonding-stretching-debonding cycles as demonstrated by Schallamach. The magnitude of the frictional shear stress depended on the velocity and the temperature, typically in the order of a few MPa, measured by Rowe *et al.* [117]. Thus, the effect of adhesion cannot be overlooked for rough contacts, especially when high friction at low velocities was observed [116].

2.4.2 Friction mechanism of elastomers in lubricated contacts

With lubricant present, the frictional behaviour of elastomers is complicated even further because the formation of the fluid film affects how the solid is deformed and introduces additional frictional shear due to the fluid flow. In some applications, lubricants are used to lower interface friction and avoid or reduce wear. In other cases, *e.g.* sealing, fluid film is undesirable and should be kept to its minimum.

The general evolution of friction on rough surfaces (since most surfaces can be considered rough to a certain extent) in different lubricated conditions can be illustrated in a Stribeck curve in Figure 2-6, which plots the variation of friction against the Hersey number (the product of velocity and viscosity of the lubricant), usually denoted as $U \times \eta$.

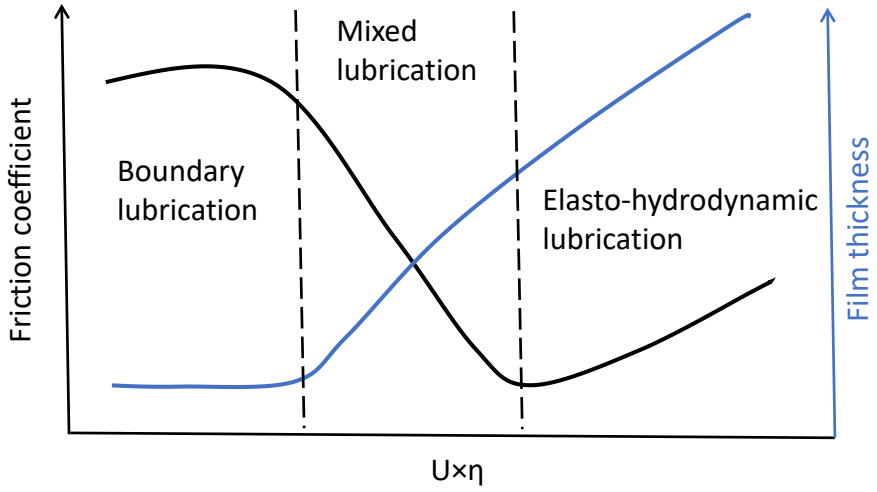

Figure 2-6 A typical Stribeck curve and film thickness variation in different lubrication regimes.

When the Hersey number is low, there is little fluid to form a film in the contact, and the majority of load is supported by asperity contacts. This is known as the boundary lubrication regime where friction is normally high and dominated by the shearing process between solids. With more fluid entrained into the contact and sharing the load, friction undergoes a remarkable fall due to the reduction of contact patches; this is named as the

mixed lubrication regime. As the amount of fluid grows such that solids are fully separated by the film, there will be no asperity contacts and the fluid will be carrying all the applied load. At this stage, the EHL regime, friction will reach its minimum and gradually rise as the shearing from fluid component increases.

Back to the 1950s, Denny [118] already demonstrated the load dependence of rubber friction in lubricated conditions, as a result of the elastic deformation of surface asperities. More experiments were carried out by Greenwood and Tabor [119] and Sabey [120] who measured the friction on the contact where a steel ball or cone slid over a well lubricated rubber plate. It was observed that both the hard ball and cone gave the same friction in lubricated conditions, indicating that the major origin of friction was the hysteresis.

To observe the transition of friction from boundary lubrication to EHL, Vicente and co-workers [121, 122] conducted a series of experiments using various solutions of different viscosities. Both sliding and rolling friction were measured between an elastomer plate and a steel ball on a mini-traction machine (MTM). They found that while the sliding friction curves resembled Stribeck curves, the rolling friction curve had a broadly constant value in the boundary and the mixed lubrication regimes, with friction increased with the Hersey number in the EHL regime. The origin of these two friction types was explained as follows: the sliding friction was primarily contributed by the adhesion at low $U\times\eta$ and the Couette flow at high $U\times\eta$; the rolling friction, on the other hand, originated from the elastic hysteresis, which was independent of $U\times\eta$, and Poiseuille flow at high $U\times\eta$. In this way, they clearly showed that in the EHL regime where roughness did not play an important role, the friction mainly resulted from two different types of flow. They further derived regression equations to predict the friction from the Couette and Poiseuille component in the soft EHL [121], which was later verified by Myant *et al.* [123].

As the friction mechanism in the boundary and mixed lubrication regimes remained unclear, Bongaerts *et al.* [124] carried out more studies to investigate the effect of roughness and

hydrophobicity. In their experiments, the contact consisted of a ball and a disk both made from polydimethylsiloxane (PDMS). Full Stribeck curves were obtained for different surface roughness and surface energy using the same method in Vicente *et al.*[121]. According to their results, the main influence of the increased roughness was to shift the transition point between the mixed lubrication regime and the EHL regime to larger values of $U\times\eta$, especially for hydrophobic surfaces, as shown in Figure 2-7(a). In addition, the roughness affected the boundary friction more significantly, with lower friction for rougher surfaces. The hydrophobic character of the surfaces also had a notable impact on the boundary and mixed lubrication. Aqueous lubricant experience enhanced the entrainment for hydrophilic substrates, which resulted in friction within these two regimes were one order of magnitude lower for hydrophilic surfaces than the hydrophobic ones, seen in Figure 2-7(b).

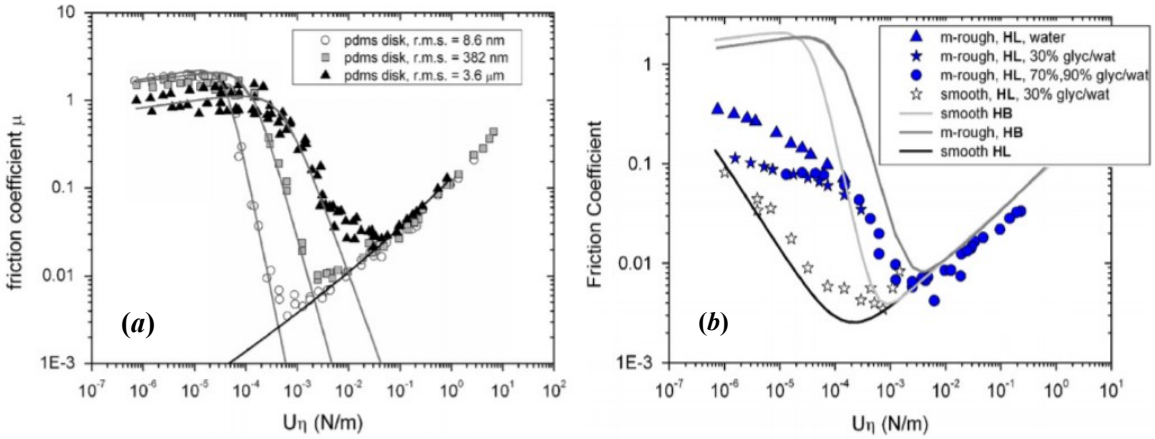

Figure 2-7 (a). Stribeck curves for three different values of roughness of the disk. (b). Stribeck curves for disks with different roughness and hydrophilicity.[121]

The effect of topography is not limited in rough or very rough surfaces. Mofidi *et al.* [125] showed that even for seemingly smooth surfaces, there might exist short wavelength roughness which made predominant contributions to rubber friction. Normally, rubber friction on perfectly smooth surfaces is believed to be caused by periodic cycles of peeling or rapid slips of rubber molecules, in other words, adhesion. However, in their study, a well-polished steel cylinder was used to slide on a rubber substrate in eleven different

lubricant oils with very different viscosities, and nearly the same friction curves were found. This indicated that the main contribution was from the pulsating deformation (hysteresis) of the rubber, even in lubricated conditions, which was very important for applications such as wiper blades, where smooth hard surfaces are involved.

In addition to friction, another quantity of great practical interest in lubricated soft contacts is the film thickness. This is crucial in applications which aims to keep the liquid film as thin as possible. Furthermore, the ratio of film thickness over RMS roughness, denoted as the lambda ratio, is often used to identify the lubrication regimes and related tribological behaviours. Conventionally, lambda ratio greater than 10 indicates that the influence of roughness is negligible, and the system is in full-film regime, while the lubrication at low values of lambda ratio (<1) corresponds to the boundary lubrication [126].

Theoretical predictions of the film thickness, which can be obtained either by analytical equations or an FSI simulation, have been described in the previous sections. In order to verify those predictions, experimental techniques were also developed significantly over the years. However, measuring the film thickness on compliant contacts is not an easy task because the surfaces are usually rough and poorly reflective, which makes the direct interferometric observation impossible. In 1969, Robert and Swales [127] overcame this obstacle by depositing an anti-reflection coating onto the surface and measured the film thickness between a cylindrical rubber surface and a glass plate down to 2 μm.

Since then, the optical interferometry method has been much improved and applied to various cases. For example, the behaviour of the artificially-roughened ball surface was studied using the optical interferometry method in rolling and sliding motions by Kanteta and Cameron [128]; Guangteng *et al*. [129] used an ultrathin film interferometry to measure the very thin film and combined it with an image mapping to study the influence of roughness on film thickness; Myant *et al.* [130] employed a monochromatic two-beam interferometry method to obtain the film thickness map between an elastomer and a plain

glass.

Other techniques for measuring film thickness in lubricated compliant contacts were also developed. Bongaerts *et al.* [131] presented an experimental setup which combined friction measurement with confocal Raman microscopy on the fluid film. For elastomer-glass contacts employed, they were able to obtain the thickness of full film directly without the need for reflective surfaces. However, the observation of fluid film in the mixed regime was still very challenging.

Recently, a laser-induced fluorescence (LIF) technique was proved to be effective in viewing the contact between elastomers. For a particular dye and concentration, the film thickness map can be converted by the proportional fluorescence intensity which captured by a fluorescence microscopy using a simple calibration. Myant *et al.* [132] managed to adopt this technique to obtain the film thickness data for a sliding contact between a PDMS and a glass under both fully flooded and starved conditions. Fowell *et al*. [133] also employed this method to the film thickness in compliant contacts and used material of which the geometry was more representative of that found in the elastomeric seals. Compared with other techniques, LIF was not only fast but also avoided the use of any reflective coatings.

Another newly developed method was proposed by Dwyer-Joyce and co-workers [134-136]. They introduced an ultrasonic reflection technique to measure the film thickness in the EHL regime. By connecting the ultrasonic transducer to a pulse-receiver (UPR), the voltage pulses were reflected from the lubricant layer, and the film thickness can be predicted from the frequency of the ultrasonic wave, the density, the speed of sound and the reflection coefficient. Although this method can be applied to non-transparent materials in dry, static and dynamic contact conditions, the spatial resolution is limited and may affect the accuracy of measurement.

2.4.3 Applications of elastomer friction

Compliant contacts are commonly seen in biological systems including contact lenses [137], synovial joints [138], tongue palate contacts [139, 140] and so on. Studies on the underlying tribological mechanisms closely involve with our daily activities such as shaving, brushing, eating, *etc*. More importantly, bio-tribology plays a significant implication in medical interventions in terms of diagnoses and artificial replacements. Comparing to engineering contacts, biological systems usually have lower friction due to the hydrodynamic effect and the biphasic nature of the soft tissues.

In the technological field, elastomers are more widely used because of their unique frictional properties as well as chemical resistance. Typical examples are tire/road contacts [141-143], seals [144-146], wiper blades/windscreen systems [3, 147] and shoe/floor contacts [148-150]. Depending on specific areas, desirable tribological behaviours vary from case to case. For instance, high friction is crucial between shoe sole and floor to keep one from slipping. Likewise, the braking system usually needs high frictional resistance. Seals and windscreen wipers, on the contrary, require not only minimum film but also low friction to avoid noise or wear. The rest of this section will focus on the application of wiper blade systems and review the most relevant studies performed.

Windscreen wipers are crucial components in car manufacturing and immediately affect the level of comfort and safety during driving. The main purpose of windscreen wipers is to wipe away any rain and dust that obstruct driver's vision. In principle, wipers are to remove the water (in rainy cases) and leave as little film as possible. However, increasing the pressing force blindly may lead to substantial friction and wear, reducing the lifetime of wiper blades.

In general, the tribological behaviour of windscreen wipers complies with the friction law of elastomers. In other words, the dry friction originates from the adhesive attraction due

to molecular bonding and energy dissipation through bulk deformation, while in more frequent conditions where fluid exists, the resistance of fluid film against shearing gives additional source for friction. Koenen *et al*.[151] and Bodai *et al.* [3] measured both dry and wet friction using commercial wiper blades and glass discs. The reduction effect of water on friction was remarkable in both studies. However, in wet conditions, Bodai *et al.* [3] showed that the friction force was very sensitive to the normal force, especially at low speed. This was because in the boundary lubrication regime, the asperity contact was covered with a very thin water film which affected the formation of adhesion bonds. In this regime, the friction was found to be proportional to the shear strength of boundary layer and the real contact area. Since the shear strength depended on many parameters, such as the surface coating, the material, *etc*., its value might change drastically in the boundary lubrication regime and can only be determined from measurements, which explained the increased boundary friction in their experiments.

As the main purpose of wiper blade is to remove water and other contamination from the glass, it is also of great importance to investigate the film thickness associated with the wiping quality. Normally, the water film remains invisible as long as its thickness is less than 600 *nm*. Deleau *et al*. [152] observed film around 200 nm in the intermediate speed and more than 200 *nm* at higher speed using an interferometric technique. However, instead of real wiper blades, the rubber specimen employed was a semi-cylinder with small radius to facilitate the measurement. In a previous project collaborated with Bosch [1], attempts were made to measure the film thickness between a commercial wiper blade and a glass using and LIF. The fluid film was found to be between 200 nm and 1 μm for the applied load from 9 N/m to 25 N/m. Below 200 nm, the film was difficult to detect due to the limitation of calibration. Using an optimised LIF set-up with a relatively high signal-to-noise ratio, Fowell *et al. [133]* was able to achieve a lower limit of measurement between 50 ~ 100 nm.

Another common issue for wiper blade system is the instability associated with friction-

induced-vibration, known as the squeal. This noise can be also noticed when braking a disc or stopping tires on wet ground. Koenen *et al.* [151] used a microphone to capture the noise between a real wiper blade and a glass and, found that a very thin water film in the contact induced the stick-slip phenomena and enhanced the squeal of frequency between 500 to 1000 Hz. By varying velocity, normal load, wetting conditions and material, Deleau *et al*. [152] revealed that this instability particularly occurred in a certain velocity range where a negative slope of friction was observed, and the emission of noise was actually independent of load. Such phenomenon was explained by Le Rouzic *et al*.[153] who utilised a mathematical model to analyse the stability for a single degree-of-freedom system based on the first Lyapunov method. According to their model, it was more likely to experience instability when the negative gradient of the friction-versus-velocity curve was steep. Therefore, it was suggested that modifying the contact surface by either choosing an appropriate coating or optimizing the roughness can, at least in theory, improve the situation. Surface treatment can shift the transition to a different speed but can also impact the friction. From a study of Reddyhoff *et al.* [154], the noise was detected at frequencies in close proximity with the eigen-frequencies of the wiper blade, which depended on the material property and the specimen geometry. Thus, it was possible to eliminate the vibration by using a finite element simulation to predict and control the natural frequency modes of the wiper blade.

2.5 Summary

This chapter provides an overview of experimental and theoretical studies on Fluid-Solid Interaction on rough compliant contacts. Given the broad topic, this chapter focuses on three most relevant aspects: the modelling algorithm for the FSI simulation, the rough contact mechanics and the frictional behaviour of elastomers. Some conclusions are drawn below.

- Numerical simulations for FSI can be categorized as stochastic models,

deterministic models and two-scale approaches. Normally, it is difficult to calculate the flow factors in a stochastic method (such as the PC's model) and computationally expensive to develop a deterministic one. Hence, a two-scale approach is often preferred to make accurate predictions with reasonable computing speed. In the majority of cases, researchers developed algorithms to solve the coupling between the fluid flow and the elastic deformation in the Reynolds equation for the mixed lubrication. Despite the general success and wide applications, these algorithms can only capture a small section of the Stribeck curve. It is worth considering more flexible models or algorithms so that the interaction between fluid and solid in the boundary lubrication regime and the EHL regime can be described as well and a full transition region can be obtained.

- Both analytical theories and numerical simulations have been well improved for solving the contact problems between rough surfaces. Given the mathematical convenience, the former is more commonly found in the FSI models to determine the contact pressure. However, this method strongly depends on the comprehensiveness of the statistical properties of rough surfaces, which are difficult to obtain using measured surfaces due to the limited resolution and dimension in the measurement.

- Large deformation in the modelling of FSI for soft contacts are often calculated using the elasticity equation with a very low elastic modulus, which lacks accuracy as the half-space assumption may no longer apply. More reliable approaches involves fine-meshed and well-defined FE model and usually leads to the demand for increasing computational power. Although recent studies have shown that it is possible to the deformation for viscoelastic solids using BEM, the materials considered is rather simple with only a few relaxation terms [155]. Determining the large deformation for realistic nonlinear materials with high accuracy and efficiency remains challenging.

- While great progress has been made to understand the friction mechanism of elastomers experimentally, studies on simulations are relatively less given the complexity of the model considered. Especially in the application of windscreen wipers, there is little study on numerically describe the FSI behaviour with the consideration of roughness, material nonlinearity and geometric nonlinearity at the same time.

3 BASIC FLUID-SOLID-INTERACTION ALGORITHMS

3.1 Introduction

In this chapter, the main structure of the proposed Fluid-Solid Interaction (FSI) model for soft rough contacts and relevant mathematical formulations is described. A classical line contact, investigating a half cylinder sliding against a substrate is used here to demonstrate the development of the FSI model; however, algorithms can be easily extended to account for three-dimensional problems and more complex geometries.

First, a contact model is established to represent real physical systems. Subsequently, governing equations which are employed to describe the contact behaviour, including the fluid flow, the asperity interaction and the elastic deformation, are introduced and discussed, together with the corresponding numerical treatments. After that, three modules of the FSI model, each containing an algorithm for different lubrication regimes, are illustrated in detail in section 3.4. The proposed model is then tested and benchmarked using other existing numerical models in section 3.5, where the pressure distribution and separation results are compared. Following the successful validation of the proposed method, Stribeck curves are generated to describe the behaviour of soft contacts in the full range of lubricating conditions, and the effect of elastic modulus and surface roughness on the evolution of friction and minimum separation between solid surfaces are discussed.

3.2 Problem description

The contact system between a real windscreen wiper and a glass in lubricated conditions is complex and can be affected by various physical quantities, such as the roughness of the surface, the viscoelastic properties of the material, the rheological response of the lubricant, and the unique configuration used for industrial application. To resolve this complicated problem, let us start by focusing on the contact region and studying a simplified case of an elastic half cylinder with radius R sliding against a rigid substrate in lubricated conditions, as shown in Figure 3-1; all the elastic deformation is accommodated by the cylinder and

not the lower body. The radius R is considered much larger than the contact area thus the assumption of half-space applies. Figure 3-1 also shows the coordinate system with the x-axis being the sliding direction and $x = 0$ corresponding to the position of the cylinder axis. The length of the cylinder is much larger than the radius so that the problem can be considered in first approximation to be two-dimensional and the side leakage is neglected.

The half cylinder has elastic modulus E and Poisson ratio υ and is pressed against the rigid substrate by a normal force W whose line of action is orthogonal to the contact interface and passes through the cylinder axis. While the lower substrate is completely smooth, the surface of the elastic solid is rough and can be characterized as a self-affine fractal, *i.e.* the surface "looks the same" as the observation is magnified. The viscosity of lubricant is denoted as η and the sliding velocity is v.

Given that the applied load is supported not only by the lubricant but also the contact between asperities, a full description of the fluid-solid interaction depends on the fluid pressure, the solid pressure and the interfacial separation between the two surfaces, which are governed by the equations presented in the next section.

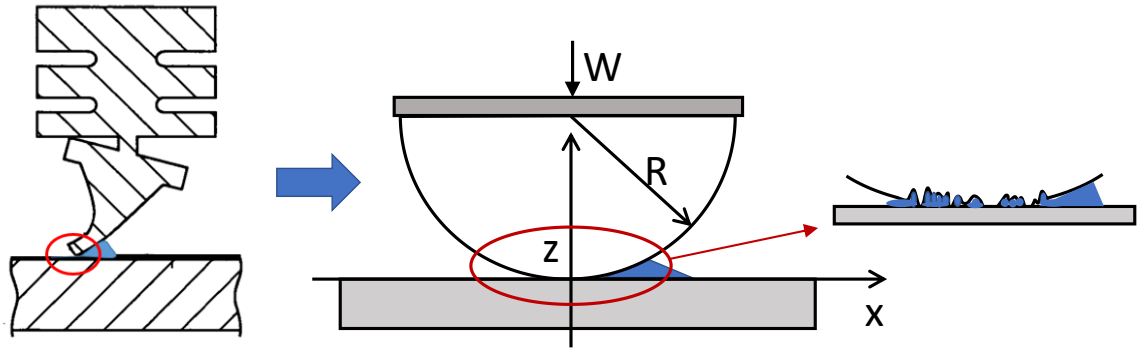

Figure 3-1 Simplification of the problem and the schematic view of the one-dimensional contact model of a half elastic cylinder with rough surface sliding on the flat rigid substrate.

3.3 Governing equations

3.3.1 Fluid flow

The hydrodynamic pressure distribution, denoted as p_f, in a lubricant film, whose thickness is denoted by u, is governed by the Reynolds equation which can be derived from a combination of the Navier-Stokes and continuity equations under the assumptions that:

(1) Body forces are negligible,
(2) Pressure is constant through the thickness of the lubricant film,
(3) Velocity and shear stress gradients are only significant through the thickness of the lubricant film,
(4) Inertia and surface tension forces are negligible compared with viscous forces,
(5) The lubricant flow is Newtonian with low laminar flow,
(6) No slip occurs at the boundary surfaces.

A general Reynolds equation (for 3D contacts) takes the form:

$$\frac{\partial}{\partial x}\left[\frac{\rho u^3}{\eta}\frac{\partial p_f}{\partial x}\right]+\frac{\partial}{\partial y}\left[\frac{\rho u^3}{\eta}\frac{\partial p_f}{\partial y}\right]=6\left\{v_x\frac{\partial}{\partial x}(\rho u)+v_y\frac{\partial}{\partial y}(\rho u)+2\frac{d}{dt}(\rho u)\right\} \quad \textit{Equation 3-1}$$

where η_0 and ρ are fluid viscosity and density respectively, $v_x=(v_{x1}+v_{x2})/2$ and $v_y=(v_{y1}+v_{y2})/2$ are relative sliding speed in x and y (out-of-plane) direction (the subscript 1 and 2 represents the upper and lower body, respectively). In this work, since a two-dimensional problem is considered with no side leakage, $\partial p/\partial y = 0$, $v_y = 0$ and $v_x = v$. In addition, constant viscosity and density of the lubricant, *i.e.* constant η and ρ, are assumed for the study of soft contacts. Thus, in the steady-state condition, can be reduced to an incompressible, iso-viscous, and iso-thermal form:

$$\frac{\partial}{\partial x}\left(\frac{u^3}{6v\eta}\frac{\partial p_f}{\partial x}\right)=\frac{\partial u}{\partial x} \quad \textit{Equation 3-2}$$

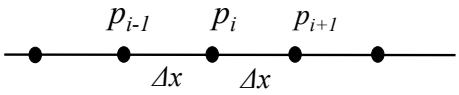

Figure 3-2 Discretisation of calculation domain for one-dimensional problems.

To solve hydrodynamic pressure from Equation 3.2, one common way is to apply the Finite Difference Method (FDM), which discretizes the differential equation in a mesh grid, as seen in Figure 3-2. There are several schemes available to approximate the partial derivative of the pressure at each node from Taylor's series expansion. Typical ones are the first order forward difference scheme:

$$\left(\frac{\partial p_f}{\partial x}\right)_i = \frac{p_{f_{i+1}} - p_{f_i}}{\Delta x} \qquad \textit{Equation 3-3}$$

the first order backward difference scheme:

$$\left(\frac{\partial p_f}{\partial x}\right)_i = \frac{p_{f_i} - p_{f_{i-1}}}{\Delta x} \qquad \textit{Equation 3-4}$$

and the intermediate difference scheme expressed as:

$$\left(\frac{\partial p_f}{\partial x}\right)_i = \frac{p_{f_{i+1}} - p_{f_{i-1}}}{2\Delta x} \qquad \textit{Equation 3-5}$$

or

$$\left(\frac{\partial p_f}{dx}\right)_i = \frac{p_{f_{i+1/2}} - p_{f_{i-1/2}}}{\Delta x} \qquad \textit{Equation 3-6}$$

In this thesis, the last one is employed to provide the best approximations.

Applying FDM on a finer mesh tends to result in more accurate solutions; however, it should be borne in mind that this accuracy also comes with an (potentially significant) increase of computational time. It is also possible to adopt a non-uniform mesh as in several studies to accelerate the computation [156]. Nevertheless, in this thesis, a uniform grid is employed for solving the Reynolds equation for convenience.

The discretised form of Equation 3.2 can be rewritten as:

$$\frac{\psi_{i-i/2}\cdot p_{f_{i-1}}-(\psi_{i-1/2}+\psi_{i+1/2})\cdot p_{f_i}+\psi_{i+1/2}\cdot p_{f_{i+1}}}{\Delta x^2}=\frac{u_{i+1}-u_{i-1}}{\Delta x} \qquad \textit{Equation 3-7}$$

where

$$\psi=\frac{u^3}{6v\eta}$$

$$\psi_{i\pm1/2,j}=\frac{1}{2}(\psi_{i,j}+\psi_{i\pm1,j})$$

$$\Delta x=x_i-x_{i-1}$$

and calculated with boundary conditions which are given as:

$$p_{f_i}=0 \;\; at \;\; x_i=x_{in}$$

$$p_{f_i}=0 \; at \; x_i=x_{end}$$

For a typical EHL system in Figure 3-1, the calculation domain $x \in [x_{in}, x_{end}]$ is often defined as [-4×a, 1.5×a] (a being the Hertzian contact area calculated for equivalent dry contact conditions [51]). However, for soft contacts characterised by relatively significant deformations, in order to guarantee a fully flooded condition, it is necessary to use a much larger domain to avoid the influence of remote boundaries on predicted pressure distributions.

Pressures directly calculated from the above equations often have negative values, which physically means the fluid film would break and the resulting cavity would form there. This phenomenon is referred as lubrication cavitation and can be handled by a number of mass-conservation cavitation models [157, 158]. Here, Gumbel's model, *i.e.* only the pressure greater than or equal to zero is admitted [159], was employed for its simplicity. Although this does not strictly enforce the mass-conservation principle of fluid flow, studies have shown that cavitation has very little impact on calculation of friction [2].

For a given separation u, the hydrodynamic pressure in Equation 3-7 can be calculated by the Gauss Seidel (GS) iterative method. At each iteration step, the pressure is updated by:

$$\tilde{p_f}_i^{\,l} = \frac{1}{\psi_{1-1/2}+\psi_{1+1/2}}\left(\Delta x(u_{i-1}-u_{i+1}) + \psi_{i-1/2}{p_f}_{i-1}^{\,l} + \psi_{1+1/2}{p_f}_{i+1}^{\,l-1}\right) \quad \textit{Equation 3-8}$$

where the superscript l indicates the l-th iteration, and corrected by the successive under-relaxation scheme for the next iteration:

$${p_f}^{l} = {p_f}^{l-1} + \alpha_l(\widetilde{p_f}^{\,l} - {p_f}^{l-1}) \quad \textit{Equation 3-9}$$

where α_l is the relaxation factor, until the criterion based on the residual ε_f is met:

$$\frac{\sqrt{\left(\Sigma_{i=1,N}\left({p_f}_i^{\,l}-{p_f}_i^{\,l-1}\right)^2\right)/N}}{\Sigma_{i=1,N}\left|{p_f}_i^{\,l-1}\right|} < \varepsilon_f \quad \textit{Equation 3-10}$$

where N is the number of nodes in the computing domain. This form of residual calculation will be used throughout the thesis to check convergence of pressure (or separation for which p_f is replaced with u).

3.3.2 Solid pressure

In real applications, all surfaces have roughness, which covers a wide range of scale from centimetres to nanometres; this cannot be neglected when investigating soft contacts as it plays a significant role in influencing frictional behaviours, especially in the boundary and mixed lubrication regimes. Rough contact mechanics, particularly for soft materials, is a complex matter and will be discussed in detail in Chapter 4. Here, for brevity, analytical expressions derived from Persson's theory on rough contacts are used to calculate solid pressure.

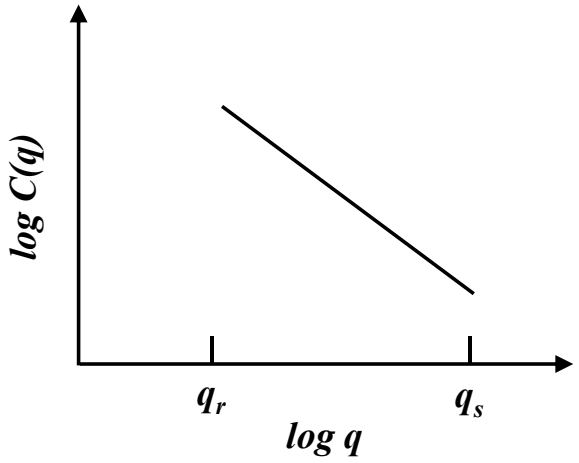

Figure 3-3 The surface roughness power spectrum of a self-affine surface. The lower wavevector q_r and the higher wavevector q_s depend on the system considered. The slope of the log C(q) - log q for $q_r<q<q_s$ is determined by the fractal dimension D_f. More information of self-affine surfaces and roughness power spectrum can be referred to Chapter 4.

The self-affine fractal surface of the cylinder was characterised by the roughness power spectrum $C(q)$, shown in Figure 3-3, where q_r and q_s are the lowest and highest wavevectors, and the fractal dimension is D_f = 2.2. For this kind of rough surface, Persson's theory predicts that the contact pressure p_s and the interfacial separation u follow the relation [77]:

$$p_s \approx 0.375 E_r q_r h_{rms} e^{(-u(x)/h_{rms})} \qquad \textit{Equation 3-11}$$

where $E^{'}$ is the reduced elastic modulus $E_r = E/(1-\upsilon^2)$, and h_{rms} is the RMS roughness value. Note that the above equation is derived for very small pressures and purely self-affine surfaces as mentioned in Chapter 2, leaving the asymptotic behaviour between logarithm of solid pressure and the mean gap only rigorously valid for large separation ($u > h_{rms}$). In Chapter 4, a complete derivation of Persson's theory regarding the load-separation relations will be demonstrated, and the difference between the approximated solution and a more accurate one will be discussed.

3.3.3 Elastic deformation

Another important quantity to consider in the modelling of fluid-solid interactions is the

separation between interacting bodies, also known as the film thickness in full film lubrication conditions, particularly for applications such as windscreen wipers or seals, where the film thickness is directly related to the wiping quality or sealing performance.

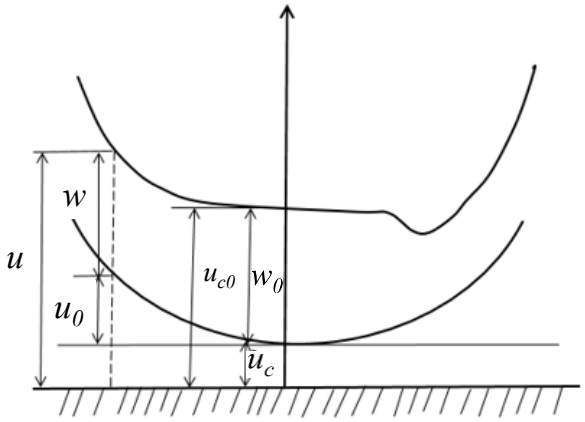

Figure 3-4 An original configuration and the deformed profile between two surfaces.

Referring to Figure 3-4, the separation between two surfaces usually takes the form:

$$u(x) = u_0(x) + u_c + w(x) \qquad \textit{Equation 3-12}$$

where u_0 is the undeformed profile, and in this case, can be approximated as:

$$u_0(x) = \frac{x^2}{2R} \qquad \textit{Equation 3-13}$$

u_c defines the rigid approach between the undeformed bodies, and w is the elastic deformation from its original shape.

In the framework of theory of elasticity [159], where deforming bodies can be considered as elastic half-spaces and the elastic deflection is solely determined by the external load and elastic property, w can be calculated by:

$$w(x) = \frac{-2}{\pi E_r} \int_{s1}^{s2} p(x) ln(s-x)^2 \, ds \qquad \textit{Equation 3-14}$$

or in its discrete form on uniform grids:

$$w_i = -\frac{2}{\pi E_r}\sum_{j=1}^{n} K_{ij} p_j. \qquad \textit{Equation 3-15}$$

The term K_{ij} is denoted as the influence coefficient referring to the elastic deformation at point i caused by the pressure applied on point j:

$$K_{ij} = (i-j+0.5)\Delta x[(ln|i-j+0.5|\Delta x)-1] - (i-j-0.5)\Delta x[(ln|i-j-0.5|\Delta x)-1] \qquad \textit{Equation 3-16}$$

The traditional way of solving Equation 3-15 is to derive the influence coefficient matrix K_{ij} beforehand and directly sum up the calculated displacement for each node. An alternative is to take advantage of the convolution theorem and FFT to perform calculations in the frequency domain [37, 97]. The latter is particularly beneficial for three-dimensional problems and will be described in detail in Chapter 4. In this chapter, the direct summation was employed for simplicity.

Hence, by substituting Equation 3-13 and 3-15, Equation 3-12 can be rewritten as:

$$u_i = u_c + \frac{x_i^2}{2R} - \frac{2}{E_r}\sum_{j=1}^{n} K_{ij} p_j \qquad \textit{Equation 3-17}$$

3.3.4 Load conservation

The load conservation is important in balancing the system with the applied force and predict the rigid approach between surfaces. The load carrying capacity can be determined by integrating the hydrodynamic pressure and the asperity pressure in the entire domain, which is:

$$W = \int_{x_{in}}^{x_{end}} (p_f + p_s) dx \qquad \textit{Equation 3-18}$$

Equations mentioned above, particularly Equation 3-7, 3-11, 3-17, and 3-18 constitutes the governing equation system to describe the fluid-solid interaction in the nominal contact area and can be solved by the algorithms presented in the next section.

3.4 Basic FSI algorithms

Generally, in the context of modelling FSI in rough contacts, there are three types of methods, namely the stochastic approach, the deterministic approach and the two-scale approach. The comprehensive overview of these approaches has been provided in Chapter 2. Briefly, the stochastic solution gives overall estimation but strongly depends on the flow factor. The deterministic one offers detailed information of each asperities but can be computationally expensive. Thus, in this thesis, a two-scale approach is adopted to obtain locally averaged results within reasonable time.

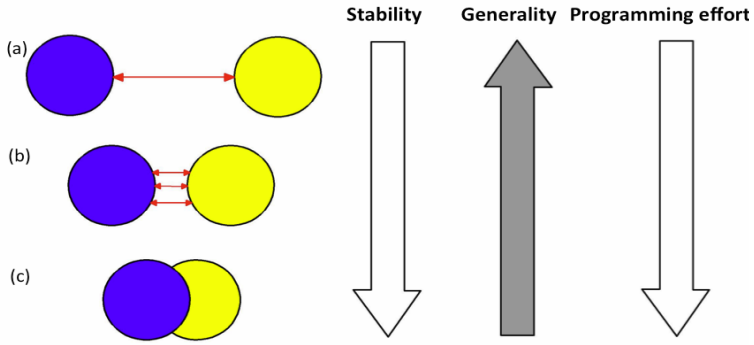

Figure 3-5 Coupling approaches for FSI solver (a) weak (b) strong (c) one system of equations.[160]

Common algorithms implemented in FSI models can be categorised as monolithic or partitioned [160]. The balance between stability, generality and programming effort is shown in Figure 3-5. The monolithic algorithm involves the simultaneous solution of fluid and solid behaviours in a single solver. This approach is suitable for strongly coupled fluid-solid interactions given the stability requirement. However, the employment of a single equation system may result in ill-conditioned matrices of coefficients with zero entries on the diagonal and cause convergence issues. The partitioned method solves the governing equations separately and requires the communication between different solvers. In practice it is easier to handle an individual solver and then use an additional iteration loop to improve the coupling stability. In this thesis, depending on the lubrication regimes, both

strategies are considered.

The proposed FSI model includes three modules accommodating for all lubrication regimes. Each module has a specific algorithm to tackle the strong coupling between fluid flow and elastic deflection and is described in the following order. The EHL algorithm is first introduced as it is rather easier without considering the effect of roughness. The solid pressure from asperity contacts is subsequently incorporated to account for the solid-solid interaction in a boundary-mixed lubrication (BML) algorithm. For the transition from mixed lubrication to EHL, a novel approach introduced by Persson and Scaraggi [2] is employed and adapted for the mixed-EHL (MEHL) module.

3.4.1 EHL module

In EHL problems, as contacting bodies are fully separated by fluid flow, the most important interaction is between the lubricant and the solid body. A typical algorithm to solve EHL problems involves nested loops, as shown in Figure 3-6. After initialization, the innermost loop is a fluid solver which is essentially to solve the hydrodynamic pressure from the Reynolds equation by using FDM and a GS iterative approach, as illustrated in section 3.3. The relaxation factor α_l used in this loop is usually in the range of 0.6 ~ 0.8.

The updated pressure is consequently used to derive the elastic deflection which determines separation and the new pressure. This process forms the intermediate loop and is repeated until separation is converged.

The load balance is enforced in the outer loop where central separation is adjusted by Δu_c based on the difference between the current load F_n and the target load W:

$$\Delta u_c = -\alpha_c (W - F_n) \qquad \textit{Equation 3-19}$$

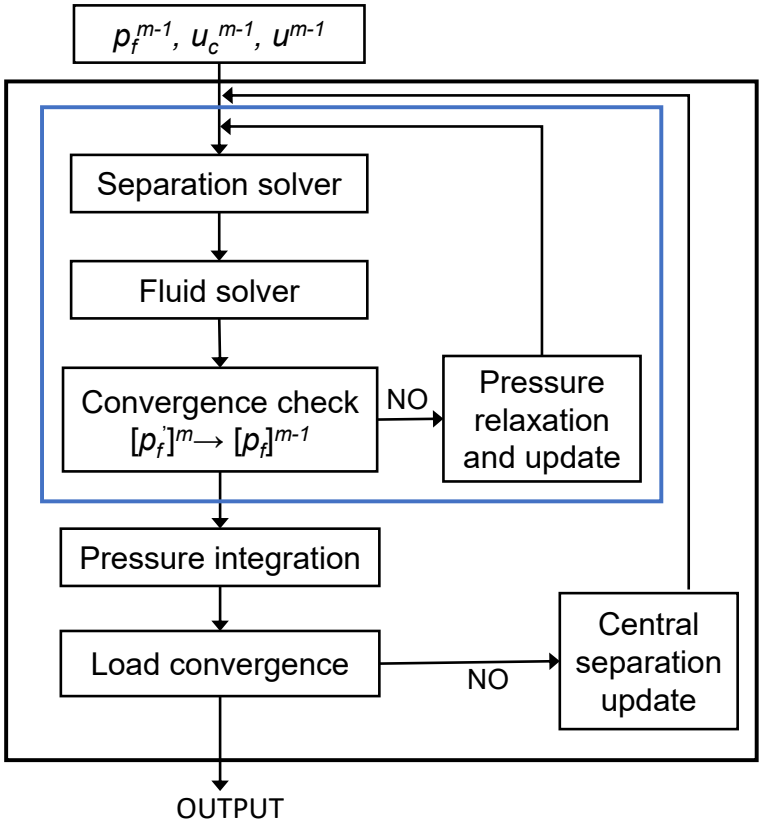

Figure 3-6 The EHL algorithm.

The current load, which is entirely carried by the fluid film, is calculated through the integral form of pressure distribution acting on the deformed surface via Simpson's rule. The criterion for load balance is calculated using load residuals by:

$$\frac{|W - F_n|}{W} < \varepsilon_W \qquad \textit{Equation 3-20}$$

3.4.2 Boundary-mixed lubrication module

When a system operates at very low sliding velocity so that the fluid layer is too thin to form a film between contacting bodies. In this transition regime from boundary lubrication to early mixed lubrication, pressure arising from prevailing asperity contacts can no longer be neglected but becomes rather dominant. Thus, in the BML module, fluid pressure, solid pressure and separation are calculated in individual solvers and periodically updated in an iterative fashion. The load balance is enforced during the iteration that updates the solid

pressure and which determines the central separation.

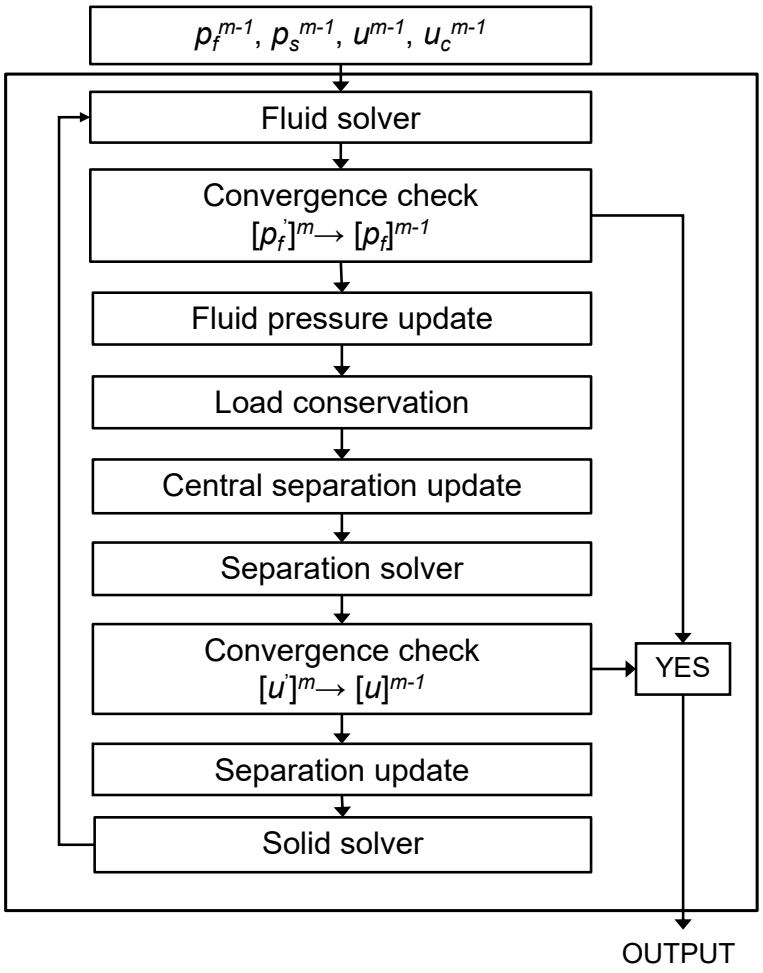

Figure 3-7 The BML algorithm.

The general procedure of the BML algorithm shown in Figure 3-7 is described as follows:

To initialize the iteration, a Hertzian-like pressure or a solution from a different velocity run is adopted. The hydrodynamic pressure is then calculated in the same manner as in the EHL module, followed by a convergence check and under-relaxation update using relaxation factor α_f:

$$[p_f]^m = [p_f]^{m-1} + \alpha_f([p_f']^m - [p_f]^{m-1}), \qquad \textit{Equation 3-21}$$

where superscript m indicates the iteration time.

The load conservation is subsequently performed to derive a renormalized solid pressure $p_s^{temp} = k_1 p_s$, where k_1 is given by:

$$k_1 = \frac{W - \int p_f^m(x')\,dx'}{\int p_s^{m-1}(x')dx'} \qquad \textit{Equation 3-22}$$

As in this regime, the solid pressure is the main pressure in the contact region, the central separation is decided to be at $x = 0$ and can be determined by the corresponding solid pressure according to the Persson's contact theory [77]:

$$u_c = h_{rms}\, l\, n\left(\frac{0.375 E_r q_r h_{rms}}{p_s^{temp}(x=0)}\right) \qquad \textit{Equation 3-23}$$

Based on the rescaled pressure $p_{total} = p_s^{temp} + p_f$ and central separation u_c, the separation u is calculated from the elastic integral equation, before another convergence check and update for separation using relaxation factor α_u.

Finally, the solid pressure is calculated by Persson's analytical expression, *i.e.* Equation 3-11, and relaxed by factor α_s. This iteration process is considered converged only when the residuals of fluid pressure and separation both meet the criteria. The convergence of solid pressure is implicitly performed as it is determined solely by the separation.

It should be noted that although the fluid pressure, solid pressure and separation are relaxed in the same manner, corresponding relaxation factors are unique depending on the sliding velocity range. Choosing the relaxation factors rationally is crucial for achieving convergence at a reasonable computing speed. Generally, α_f and α_u are in the range of 0.001 to 0.1, with higher values for higher speed. α_s is relatively larger, between 0.1 to 1, and also increases with speed. Moreover, to improve converging performance, it is recommended to keep α_f smaller than α_u and α_u smaller than α_s.

3.4.3 Mixed-EHL module

As a system gradually enters the mixed lubrication regime, the fluid pressure grows with the increasingly entrained lubricant and becomes of the same order of the solid pressure. As a result, the strong coupling between fluid pressure and separation is difficult to handle with the previous algorithm and may easily lead to convergence issues. Hence, another approach used to capture the transition from the mixed lubrication regime to EHL regime is presented.

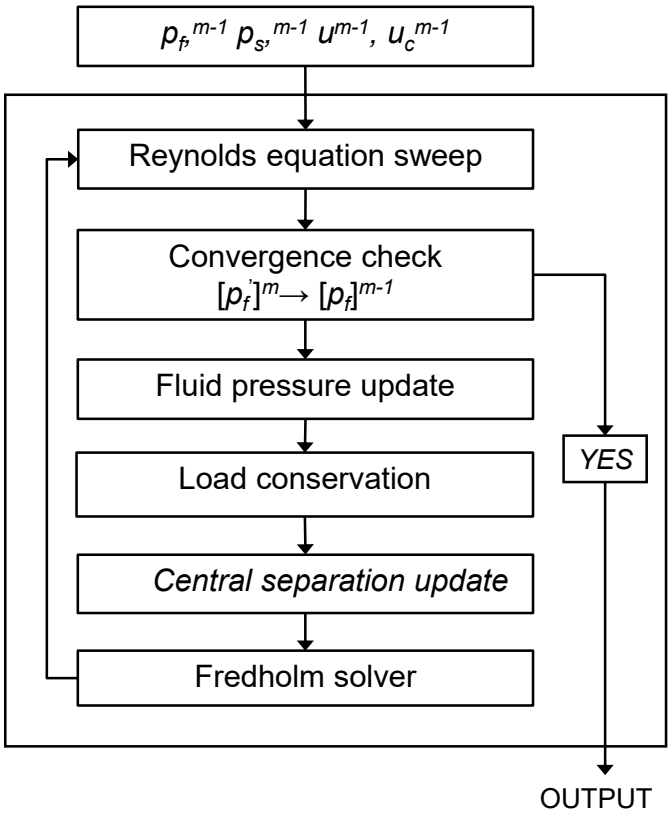

Figure 3-8 The MEHL algorithm.

The iterative algorithm in the MEHL module features the Reynolds equation sweep (RES) to update the fluid pressure and the Fredholm Solver (FS) to calculate the separation and the solid pressure. In addition, the central separation updater (CSU) is employed to update the central separation based on the total pressure. Shown in Figure 3-8, the general process and mathematical implementation are described as follows:

1. Initialisation utilises simulation results from a lower speed test, including pressure, separation and central separation, for the sake of convergence.

2. The RES is firstly evoked to update the fluid pressure. However, unlike the fluid solver in the BML module where the output is the pressure solution of Reynolds equation for a given separation profile, the RES only updates the fluid pressure by a one-time sweeping. In the original study [2], this was achieved by a Newton-Raphson (NR) step. The Reynolds equation and elasticity equation were organized in one discrete form:

$$L_i^m = u_{0\,i+1} - u_{0\,i-1} + \sum_j \left(K_{i+1,j} - K_{i-1,j}\right)\left(\left[p_f\right]^m + \left[p_s\right]^m\right)_j - \frac{1}{\Delta x}\left[\varepsilon_{i-1/2}\left[p_f\right]_{i-1}^m + \varepsilon_{i+1/2}\left[p_f\right]_{i+1}^m + \left(\varepsilon_{i-1/2}+\varepsilon_{i+1/2)}\right)\left[p_f\right]_i^m\right] \qquad \textit{Equation 3-24}$$

Then based on the Newton-Raphson method, the fluid pressure was updated by:

$$\sum_C \left[\frac{\partial L_i}{\partial \left[p_f\right]_C}\right]_{m-1} \left(\left[p_f\right]^m - \left[p_f\right]^{m-1}\right)_C = -L_i^{m-1} \qquad \textit{Equation 3-25}$$

To capture the cavitation condition, the contact domain C was divided into three different computational zones (high pressure zone $C1$, low pressure zone $C2$ and cavitation zone $C3$) and in each zone the NR method can be rewritten as:

$$\begin{aligned} -L_i^{m-1} = &\left[\frac{\partial L_i}{\partial \left[p_f\right]_{i-2}}\right]^{m-1}\left(\left[p_f\right]^m - \left[p_f\right]^{m-1}\right)_{i-2} \\ &+\left[\frac{\partial L_i}{\partial \left[p_f\right]_{i-1}}\right]^{m-1}\left(\left[p_f\right]^m - \left[p_f\right]^{m-1}\right)_{i-1} \\ &+\left[\frac{\partial L_i}{\partial \left[p_f\right]_{i+2}}\right]^{m-1}\left(\left[p_f\right]^m - \left[p_f\right]^{m-1}\right)_{i+2} \\ &+\left[\frac{\partial L_i}{\partial \left[p_f\right]_{i+1}}\right]^{m-1}\left(\left[p_f\right]^m - \left[p_f\right]^{m-1}\right)_{i+1} \\ &+\left[\frac{\partial L_i}{\partial \left[p_f\right]_{i}}\right]^{m-1}\left(\left[p_f\right]^m - \left[p_f\right]^{m-1}\right)_{i} \end{aligned} \qquad \text{in C1,}$$

$$-L_i^{m-1} = \left[\frac{\partial L_i}{\partial [p_f]_{i-1}}\right]^{m-1} \left([p_f]^m - [p_f]^{m-1}\right)_{i-1} + \left[\frac{\partial L_i}{\partial [p_f]_{i+1}}\right]^{m-1} \left([p_f]^m - [p_f]^{m-1}\right)_{i+1} + \left[\frac{\partial L_i}{\partial [p_f]_i}\right]^{m-1} \left([p_f]^m - [p_f]^{m-1}\right)_i \quad \text{in C2,}$$

$$-L_i^{m-1} = \left[\frac{\partial L_i}{\partial [p_f]_i}\right]^{m-1} \left([p_f]^m - [p_f]^{m-1}\right)_i \quad \text{in C3.}$$

Alternatively, a Gauss Seidel (GS) iterative scheme as in Equation 3-8 can be applied, *i.e.* the pressure p_i updated by the newly modified pressure p_{i-1}. Both methods can lead to the same result, which will be shown in the next section. Usually, the NR method is favoured for its computational efficiency. Nevertheless, in occasions where separation is very small, the inversion of matrix may fail due to numerical singularity. Moreover, defining cavitation domains in a Newton-Raphson step is rather arbitrary, resulting in abrupt stops in pressure. Therefore, the GS method is employed in this thesis.

3. A convergence check is consequently carried out before the fluid pressure is relaxed by a factor α_f. Then, the central separation is updated in the CSU by Δu_c which is calculated as:

$$\Delta {u_c}^m = -\alpha_c \Delta F^m \qquad if\ \Delta F_c^m \cdot \Delta F^m \leq 0$$

$$\Delta {u_c}^m = 0 \qquad otherwise$$

$$\Delta F^m = [W - \Delta x \Delta y([p_f]^m + [p_s]^m)]_i \qquad \textit{Equation 3-26}$$

$$\Delta F_c^m = \sum_i([p_f]^m + [p_s]^m)_i + \sum_i([p_f]^{m-1} + [p_s]^{m-1})_i \qquad \textit{Equation 3-27}$$

Normally, Equation 3-26 is used to adjust central separation in the EHL community. However, in the present algorithm, the convergence history is not monotonic, thus, an additional logical condition Equation 3-27 is introduced to find the solution. The intuitive interpretation is that the central separation is only updated if the pressure field is converging towards the target load.

4. Subsequently, the separation and the solid pressure are solved in a separate iterative solver (the FS solver) where a Fredholm type of integral equation is formulated. Given the fluid pressure and the central separation, Equation 3-17 can be rewritten as:

$$g_i = -1 + \frac{u_c + u_{0i} + \sum_j K_{ij}[p_f + p_s(u)]_j}{u_i} \qquad \textit{Equation 3-28}$$

Since the solid pressure p_s is a function of separation u, the above equation can be calculated by a Newton-Raphson iterative method using:

$$u_i^l = u_i^{l-1} - \frac{g_i}{g'(u)_i} \qquad \textit{Equation 3-29}$$

Thus, the new separation profile is obtained by:

$$u_i^l = u_i^{l-1}\left[1 + \alpha_{fs}\frac{g_i^{l-1}}{1 + g_i^{l-1} - K_{ij}\left[\frac{\partial p_s}{\partial u}\right]_{u_i^{l-1}}}\right] \qquad \textit{Equation 3-30}$$

where α_{fs} is the relaxation factor.

5. This new separation is thereafter checked for convergence. If both residuals of fluid pressure and separation meet the criteria, the MEHL module is completed, otherwise, the calculation restarts from the RES.

Similar to the BML module, relaxation factors are very important for computing efficiency. Small values certainly encourage convergence but may cause more than 10,000 times of iterations in some cases, therefore, it is suggested to make decisions depending on specific

problems. Generally, stronger hydrodynamic effect requires larger values. While α_f and α_{fs} are in the same range between 0.001 and 1, α_c is usually higher between 0.01 to 1.

3.5 Validation

The developed FSI model was validated by comparing with the study of Persson and Scaraggi [2], where a different algorithm for line contact problems was adopted. The physical model described in section 3.2 with parameters listed in Table 3-1 is used. Details of the numerical setups in each module are shown in Table 3-2.

For the sake of numerical convenience and converging efficiency, it is practical to start with the BML module and carry out simulation at sliding velocities in an ascending order. The BML module can be easily initialised using the Hertzian solution (Hertzian pressure as solid pressure and zero pressure as fluid pressure), followed by the MEHL module taking the results from a lower speed run as inputs and, eventually, the EHL module.

Table 3-1 Properties of the contacting system in Figure 3-1.

Parameter	Value
Young's modulus E	10 MPa
Poisson ratio υ	0.4999
Cylinder radius R	1 cm
Applied load W	100 N/m
Lubricant viscosity η	0.1 Pa s
Sliding velocity v	1×10^{-5} ~ 100 m/s
Surface fractal dimension D_f	2.2
Root-mean-square roughness h_{rms}	1 μm
Roughness low cut-off wave vector q_r	1×10^{4} m^{-1}
Roughness high cut-off wave vector q_1	0.78×10^{10} m^{-1}

Table 3-2 Numerical settings of the FSI solver.

	Parameter	**Value**
General	Nodes	1025
	Computational domain	-1 mm ~ 1mm
BML module	Fluid relaxation factor α_f	0.001 ~ 0.1
	Separation relaxation factor α_u	0.01 ~ 0.1
	Solid relaxation factor α_s	0.1 ~ 1
	Fluid convergence error ε_f	1e-5
	Separation convergence error ε_u	1e-5
MEHL module	Fluid sweep relaxation factor α_f	0.001 ~ 1
	Central separation relaxation factor α_c	0.1 ~ 1
	Fredholm solver relaxation factor α_{fs}	0.001 ~ 1
	Fluid convergence error ε_f	1e-5
	Central separation convergence error ε_u	1e-5
	Fredholm solver convergence error ε_{fs}	1e-5
EHL module	Fluid relaxation factor in the innermost loop α_l	0.6 ~ 0.8
	Central separation update factor α_c	0.1
	Fluid convergence error for the innermost loop ε_f^l	1e-5
	Separation convergence error for the intermediate loop ε_f^m	1e-5
	Load convergence error ε_W	0.001

Figure 3-9, Figure 3-10 and Figure 3-11 depict the pressure distribution (on the left scale) and separation (on the right scale) between the half cylinder and the substrate at sliding speed 1e-5 m/s, 1.5e-3 m/s and 0.12 m/s. It should be noted that, in all results, the effect of the roughness has been locally averaged according to the mean field theory, thus the solid (contact) pressure and the nominal separation are presented as smooth lines. It was found that results obtained by the current model (dotted line) were very close with those by Persson's model (solid line). The evolution of pressure field and lubricant film were evident. At low speeds, solid pressure was predominant and similar to Hertzian pressure with a small broadening resulted from the surface roughness, while at relatively high speeds, the influence of fluid pressure became more significant.

The trivial deviation between Persson's model and the present one, as shown in Figure 3-9 and Figure 3-10, was mainly due to the calculation of the solid pressure. In the current study, the analytical expression in Equation 3-11 $p_s \approx 0.375 E_r q_r h_{rms} e^{(-u(x)/h_{rms})}$ Equation 3-11was used to approximate the solid pressure, whereas in Persson's model, a full integral equation was employed to evaluate the solid contact behaviour [2]. When the speed was high enough such that the effect of the solid pressure can be ignored, Persson's model and the present work made identical predictions of the fluid pressure and the separation. In Figure 3-11, the solid pressure was amplified by 10^5 times to be visible in Persson's results [2], whereas in the current study, the EHL module was used for such high speed and the solid pressure was assumed to be zero.

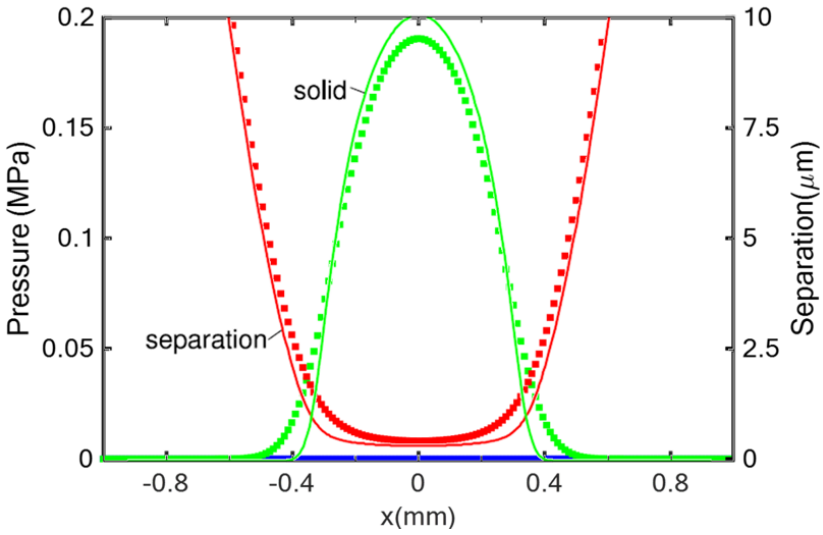

Figure 3-9 The fluid pressure (blue), the solid pressure (green), and the interfacial separation (red) in the contact system of Figure 3-1 at the sliding velocity 1e-5 m/s. The dotted lines are obtained by the current study, whereas the solid lines are taken from [2]

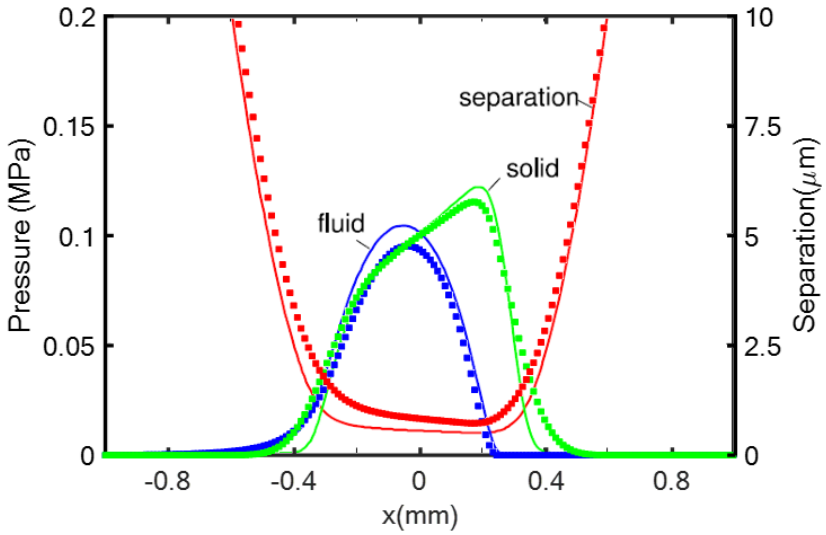

Figure 3-10 The same as in Figure 3-9 but for the sliding velocity 1.5e-3 m/s.

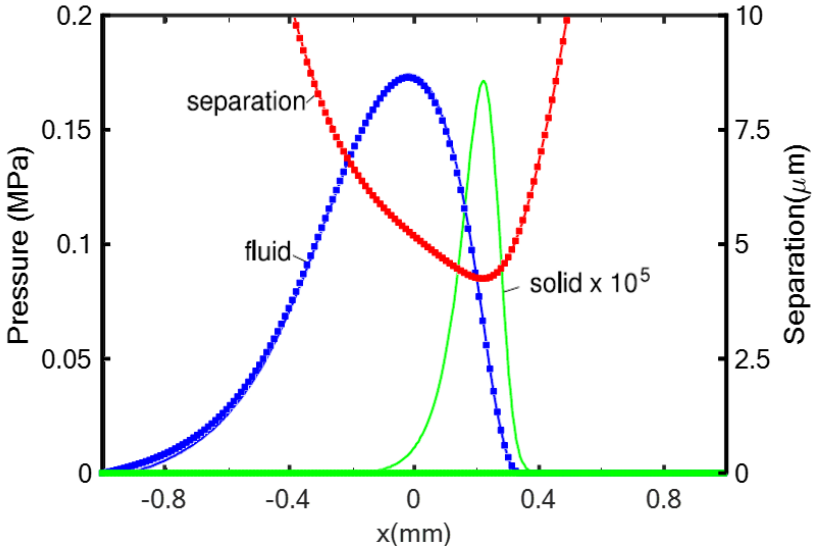

Figure 3-11 The same as in Figure 3-9 but for the sliding velocity 0.12 m/s.

Figure 3-12 shows the pressure distribution and separation calculated by the MEHL module using Newton-Raphson and Gauss-Seidel sweep. Results were in good agreement except that the NR method forced the fluid pressure into cavitation zone abruptly while the GS scheme captured it more naturally. Considering this effect and the numerical flexibility, GS was used for all fluid pressure update throughout the thesis.

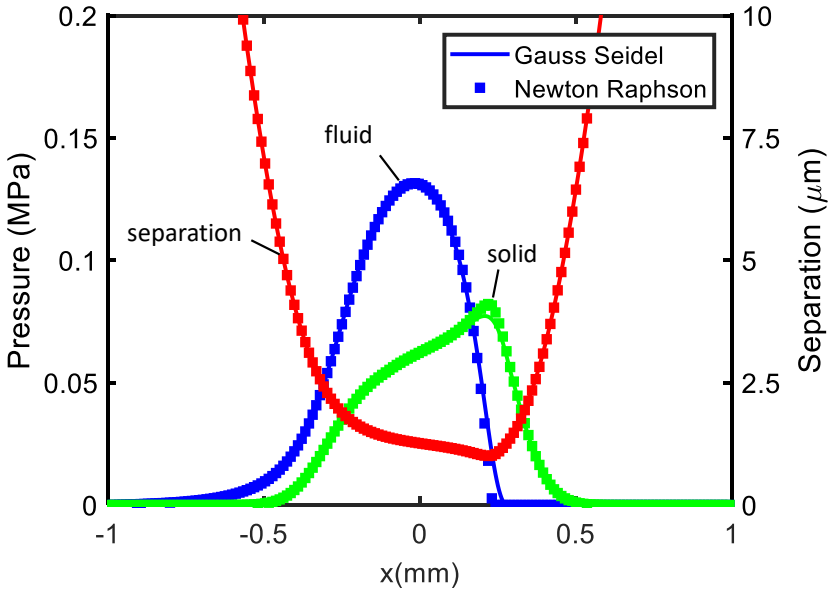

Figure 3-12 Pressure distribution and interfacial separation obtained by the MEHL module with Gauss Seidel and Newton Raphson iterative scheme at sliding speed 0.03 m/s.

To ensure that the evolution of the tribological behaviour from the boundary lubrication regime to the EHL regime was well described without being influenced by the algorithm, simulations were carried out for two transition speeds. At 1.5e-3 m/s, both the BML and the MEHL module were employed, and nearly identical results were produced, as shown in Figure 3-13. Similar comparison was performed between the MEHL with the traditional EHL solver (no solid pressure) for sliding velocity 0.12 m/s, and the same fluid pressure and separation were found, as shown in Figure 3-14. The solid pressure obtained by the MEHL module (green line) was so small that, as expected in this regime, can easily be neglected. Therefore, the presented algorithms proved sufficient to describe all three lubrication regimes.

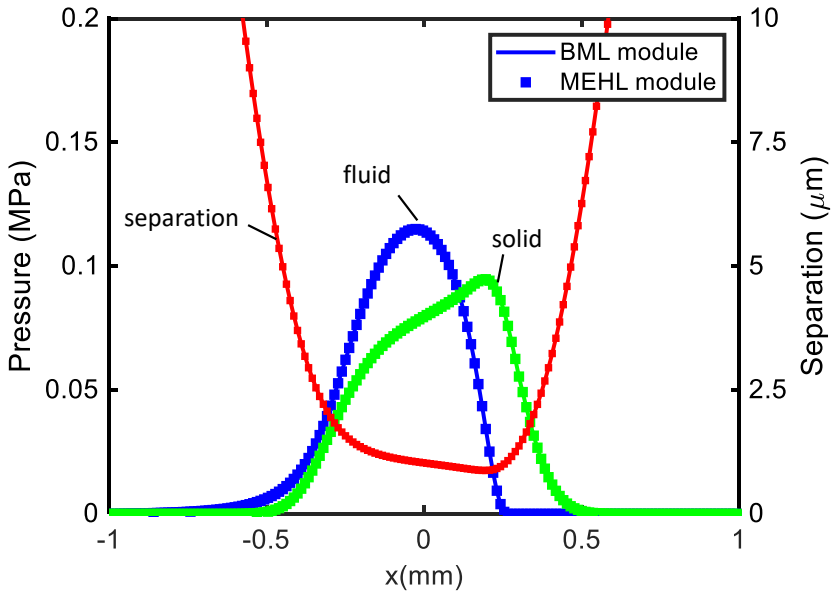

Figure 3-13 Pressure distribution and interfacial separation obtained by the BML module and the MEHL module at the same sliding velocity 1.5e-3 m/s.

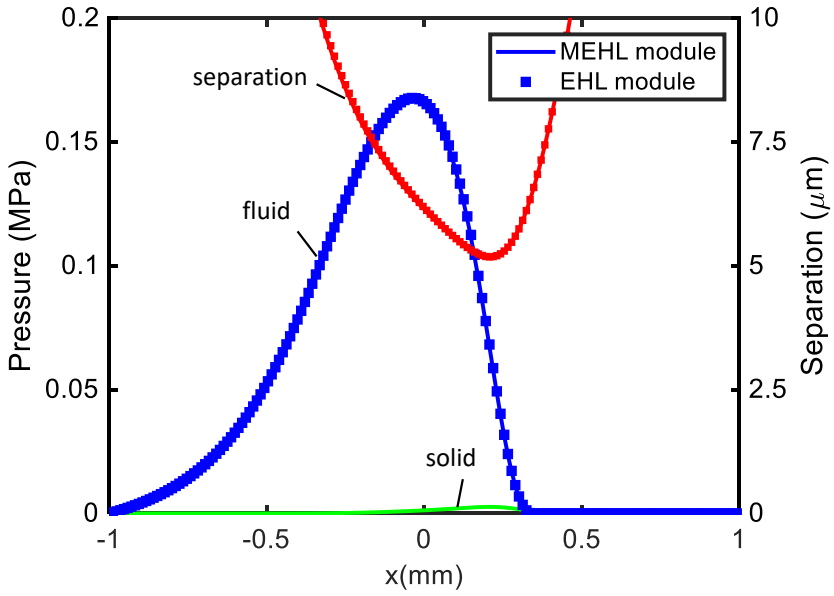

Figure 3-14 Pressure distribution and interfacial separation obtained by the MEHL module and the EHL module at the same sliding velocity 0.12 m/s.

3.6 Friction calculation

The pressure distribution and separation results shown in the previous section enable one to predict the frictional behaviours in each lubrication regime and consequently full

Stribeck curves. The frictional stress is derived from the solid-solid shearing and the fluid-solid interactions:

$$\sigma_{total} = \sigma_s + \sigma_f \qquad \textit{Equation 3-31}$$

The first term, σ_s, is related to shear strength σ_1 and the ratio of real contact area over the nominal contact A/A_0 through [2]:

$$\sigma_s = \sigma_1 \frac{A}{A_0} \approx \chi \sigma_1 p_s / E_r \qquad \textit{Equation 3-32}$$

σ_1 represents the friction from van De Waals interaction and is assumed to be a constant value of $0.1 \times E$ *[2],* where E is the elastic modulus of the soft body, but experiments showed that it may change with the sliding velocity, which will be discussed in Chapter 6. The real contact area A, when adhesion is neglected, is considered only dependent on a surface roughness related parameter χ and the contact pressure as long as the contact area is very small. χ can be calculated from the surface roughness power spectrum through:

$$\chi = \frac{1}{(\pi G')^{1/2}} \qquad \textit{Equation 3-33}$$

where $G' = \frac{\pi}{4} \int_{q_r}^{q_s} dq\, q^3 C(q)$.

The second term, σ_f, is the stress component from fluid shearing which, for iso-viscous lubricant, depends on the velocity profile:

$$\sigma_f = \eta \frac{\partial v}{\partial z} \qquad \textit{Equation 3-34}$$

Since the velocity profile v can be expressed as:

$$v = \frac{v}{u(x)} z + \frac{1}{2\eta} \frac{\partial p_f}{\partial x} (z^2 - z u(x)) \qquad \textit{Equation 3-35}$$

Equation 3-34 is equivalent to:

$$\sigma_f = \eta \frac{v}{u(x)} + \frac{u(x)}{2} \frac{\partial p_f}{\partial x} \qquad \textit{Equation 3-36}$$

The friction force, therefore, can be calculated by integrating the total shear stress:

$$F_f = \int (\sigma_f + \sigma_s) dx \qquad \textit{Equation 3-37}$$

and the friction coefficient is:

$$\mu = \frac{F_f}{F_n} = \frac{\int \sigma_{total} dx}{\int p_{total} dx} \qquad \textit{Equation 3-38}$$

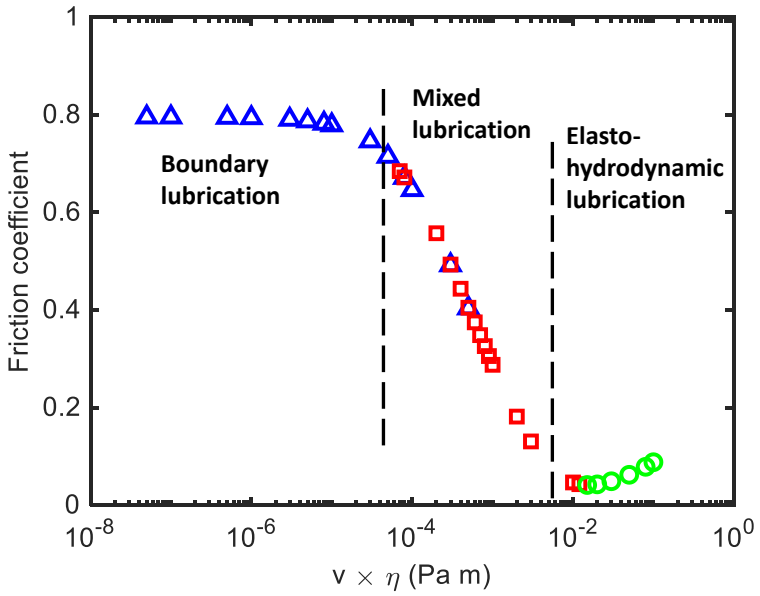

Figure 3-15 Friction coefficient as a function of Hersey number, obtained by the BML module, MEHL module and EHL module.

Using Equation 3-38, friction coefficient of the system described in Figure 3-1 was calculated and plotted versus the Hersey number (the product of sliding velocity and lubricant viscosity) in Figure 3-15. Different markers stand for the usage of different modules. This curve clearly resembles a Stribeck curve and nicely captures the transition from the boundary lubrication regime to the EHL regime, spanning more than 6 orders of magnitude in speed.

Figure 3-16 shows the loading force carried by the fluid and the asperity contacts as a function of the sliding velocity. The vertical dashed line indicates the velocity where the friction force was minimal. It should be noted that at this velocity, the load carried by

asperities was only 0.3% of the total force. The variation of central separation was also given in Figure 3-17, where a remarkable increase of fluid attributed to the friction plunge.

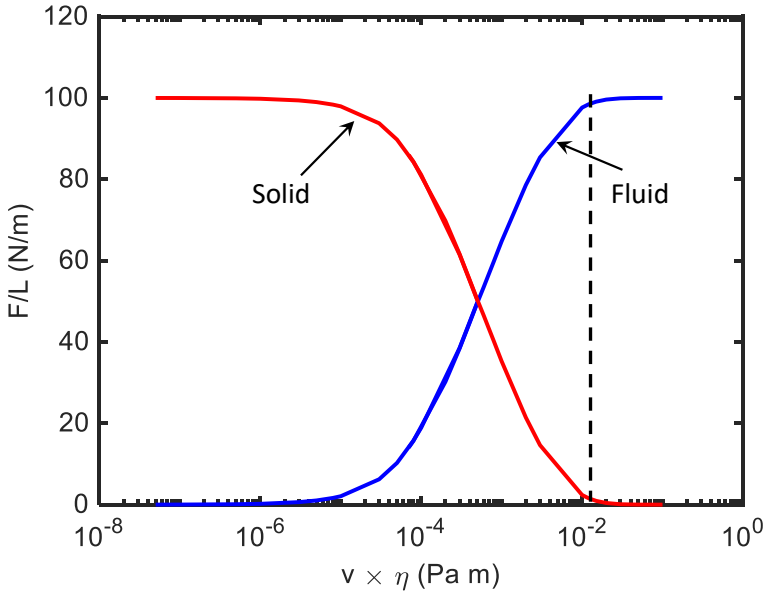

Figure 3-16 The load force carried by the fluid and the solid contact as a function of Hersey number.

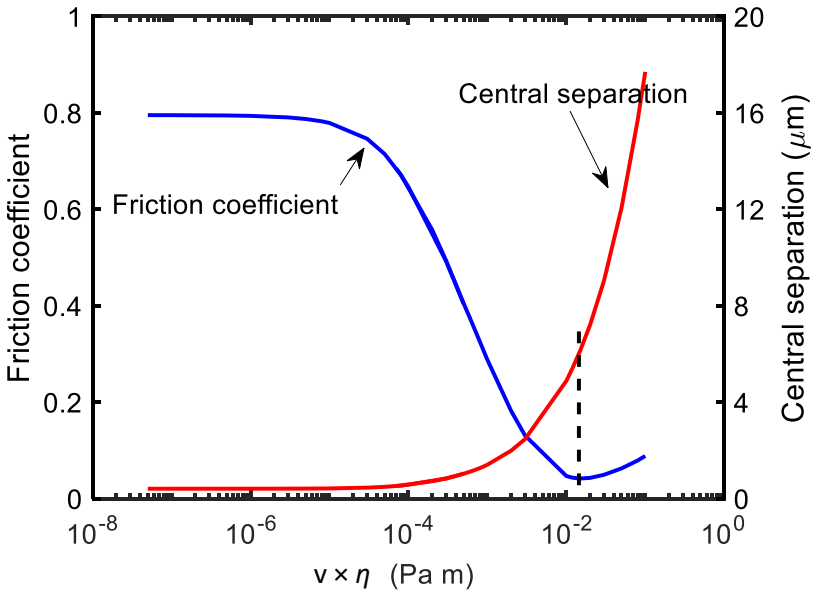

Figure 3-17 The friction coefficient and the minimum surface separation as a function of Hersey number.

3.7 Parametric tests

In this section, the effect of elastic modulus and RMS roughness on Stribeck curves and minimum separation are evaluated. All results are obtained for the contact system shown in Figure 3-1 with parameters listed in Table 3-1.

3.7.1 The effect of elastic modulus

Elastic properties are crucial in describing the solid deformation and influencing frictional behaviours. Elastic moduli of the cylinder specimen varying from 10 MPa to 50 MPa were examined, shown in Figure 3-18. Despite the small range of elasticity, these three systems show distinct difference in friction, particularly in the mixed lubrication regime, where the more compliant body are found to deform more significantly and to entrain fluid faster, entering the mixed lubrication regime at a lower speed. The effect on boundary friction and hydrodynamic friction are less noticeable, with nearly the same friction predicted for all elastic systems.

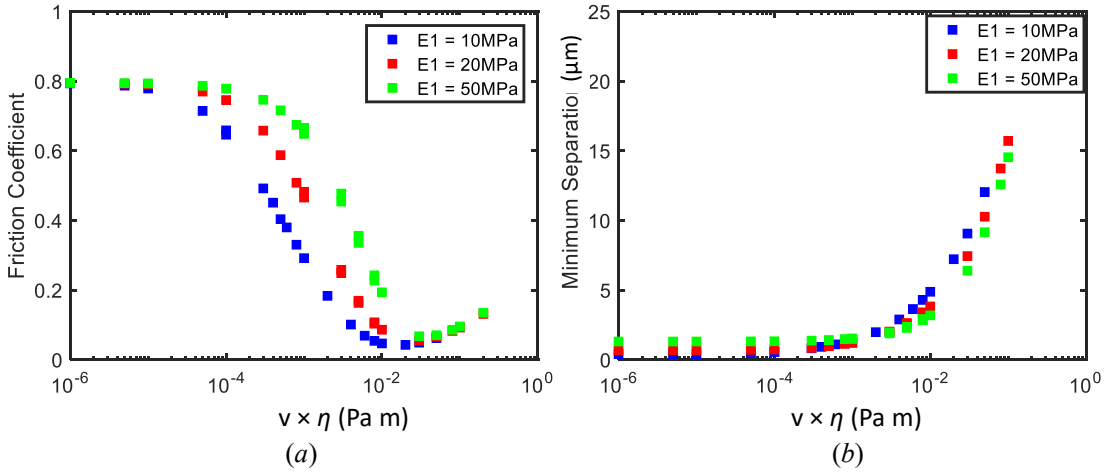

Figure 3-18 The friction coefficient (a) and the minimum separation (b) as a function of Hersey number for the same system as in Figure 3-9 but with three different elastic properties,.

3.7.2 The effect of RMS roughness

It is well known that roughness can affect the boundary and mixed friction intrinsically due to the asperity interaction. Normally, the RMS roughness is the value referred to when roughness is discussed. This is not always accurate as it only reflects the amplitude of the surface profile and not the spatial information. Details of the characterization of roughness and its impact on contact mechanics will be discussed in the next chapter. Here, it is assumed that rough surfaces have the same properties except the RMS value of 1 μm, 3 μm, 6 μm.

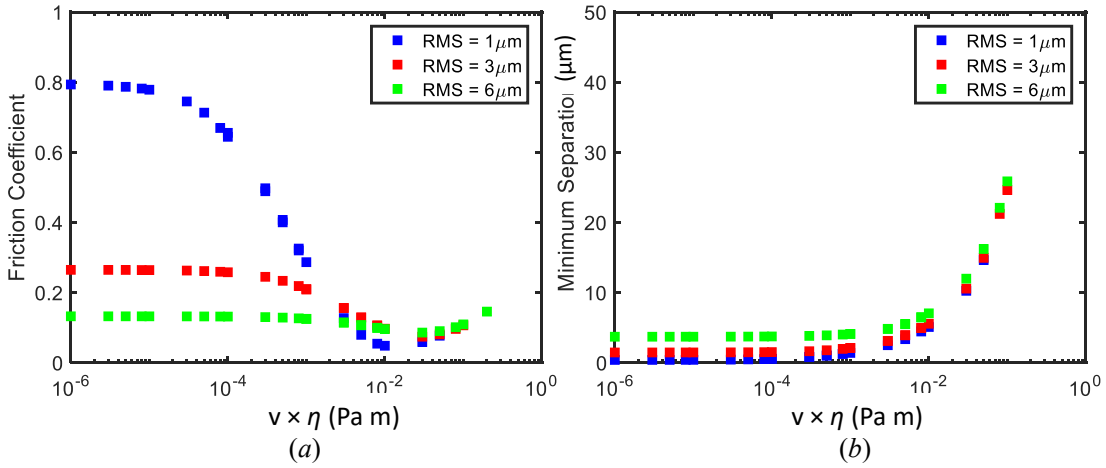

Figure 3-19 The friction coefficient (a) and the minimum separation (b) as a function of Hersey number for the same system as in Figure 3-9 but with three different RMS roughness.

As shown in Figure 3-19, friction and separation results were expected to be barely affected by the roughness in the EHL regime. In the boundary lubrication regime, however, the RMS value has a strong impact, with lower friction for higher RMS roughness. This is in good agreement with experimental tests [121, 123, 124], where sliding friction was measured between PDMS balls and rigid flat discs, and other numerical analysis [2], and can be attributed to the reduction in the real contact area for rougher surfaces. Another interesting observation was that the minimum of friction coefficient shifts to a larger $v \times \eta$ and this minimum value increases as the RMS roughness grows, since the rougher interface

requires more fluid to achieve full film lubrication.

3.8 Summary

In this chapter, a basic FSI model developed for rough compliant systems in line contacts is presented. The governing equation as well as numerical strategies to solve fluid flow, asperity contact, elastic deformation and load balance are described in detail. Three algorithms accommodating to all lubrication regimes are introduced and adapted based on a similar study in [2]. This model is validated by comparing the pressure and separation results obtained with other numerical solutions. It was shown that the current model is perfectly capable of predicting the tribological behaviour in the frictional interface considered, and the effect of elastic properties and RMS roughness was qualitatively consistent with experimental finding and other numerical analysis.

4 ROUGH CONTACT MECHANICS: SURFACES AND SOLVERS

4.1 Introduction

Nearly all surfaces have roughness extending over many length scales, from the macroscopic size of the system down to atomic distance. Even the seemingly smooth surfaces have roughness at the nano-scale. As a result, when two solids are in contact, it is in fact the asperities on the surfaces that are in contact and the real contact area is much smaller than the apparent contact area. This effect of roughness is of great importance in nature and technology, and it is directly related to many physical phenomena, such as contact mechanics, adhesion, friction and sealing. For instance, roughness is the main reason why adhesion is usually not observed in most macroscopic phenomena. Therefore, understanding contact mechanics between rough surfaces is crucial and fundamental for solving surface related problems.

Contact area, interfacial separation, contact stiffness, elastic deformation, probability distribution of stress are all quantities of interest in the study of rough contact mechanics. For the purpose of developing a reliable and efficient solid solver for the FSI, the thesis focuses on the contact area evolution with force and the load-separation relations between rough surfaces.

This chapter starts with an accurate characterization of roughness, followed by a numerical approach to generate representative rough surfaces. In section 4.4 and 4.5, a stochastic method and a deterministic method for solving contact problems are presented, respectively. In terms of the former, Persson's theory is adopted given its mathematical advantage for self-affine fractal surfaces, while regarding the latter, a Conjugated Gradient iterative method combined with the Fast Fourier Transform technique is employed to solve contact problems for any given rough surface. The effect of surface properties on the contact mechanics, particularly the real contact area and the mean interfacial separation, is then discussed in section 4.6. Finally, a brief summary is provided in section 4.7.

4.2 Roughness

The term “roughness” and “rough surfaces” are often used interchangeably. However, studies on the multiscale nature of the roughness have shown that it is important to obtain an accurate quantitative description of the surface of interest, as the metrology of roughness measurement and the processing of the topography can have significant impacts on the surface properties. For example, most measurement technologies are limited in a small area or may introduce artefacts due to the stylus tip geometry[59], which is why a combination of different methods is advised to provide extensive information of the roughness [56, 58]. Furthermore, a raw rough surface measured, either by stylus methods, optical methods or atomic force microscopy, consists of not only roughness but also form and waviness, and should be treated carefully for the extraction of useful information. Usually, the raw measurement data should be fitted in a least-square sense to remove the mean height and tilt (or curvature in some cases). Depending on the situation, waviness which contains wavelengths too long for the contact needs to be discarded as well. Figure 4-1 shows the process of subtracting tilt and waviness from a one-dimensional rough profile to acquire roughness. It should be noted that many surface measurement instruments already provide the option automatically, but the cut-off wavelength for the filtering is rather arbitrary. Thus, it is practical to assess or define this value considering the contact problems under investigation.

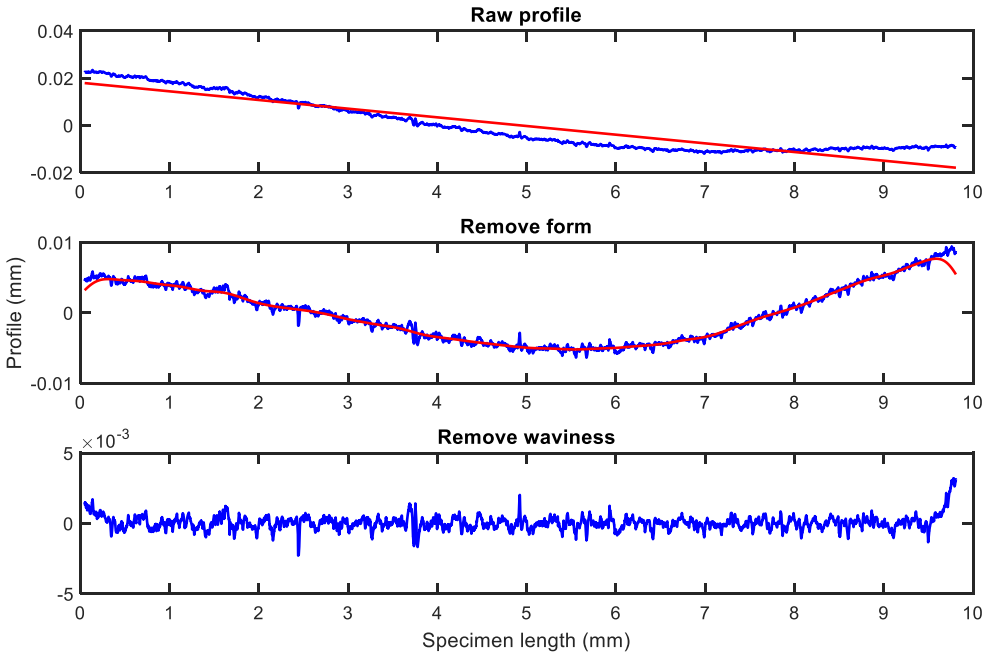

Figure 4-1 One-dimensional rough profile measured using a Talysurf profiler. From top to bottom, blue lines are profiles of the raw measurement, after removing the form, and after removing the waviness, while red lines are the filter plane/wave.

After pre-processing, statistical properties of roughness can be obtained from two perspectives. The amplitude related parameters such as the average roughness h_a, the RMS roughness h_{rms} and the root-mean-square gradient h'_{rms}, which are used to characterise the height of asperities can be calculated by the following equations:

$$h_a = \frac{1}{L}\int_0^L |z(x)|dx \qquad \textit{Equation 4-1}$$

$$h_{rms} = \sqrt{\frac{1}{L}\int_0^L (z(x))^2 dx} \qquad \textit{Equation 4-2}$$

$$h'_{rms} = \sqrt{\frac{1}{L}\int_0^L (\frac{dz(x)}{dx})^2 dx} \qquad \textit{Equation 4-3}$$

where $z = f(\boldsymbol{x})$ represents the rough profile over length L at point $\boldsymbol{x}$. Probability density function of height distribution is another important index in providing roughness amplitude information. It has been found that surfaces that are formed by cumulative processes (such as peeling, electropolishing, and lapping) are usually governed by a Gaussian form, as a result of the central limit theorem of statistical theory [161]. An example of Gaussian

distributed rough surface (Gaussian surface for short) measured from a rubber specimen is shown in Figure 4-2 (a) with its height distribution calculated and fitted by the Gaussian distribution in Figure 4-2(b).

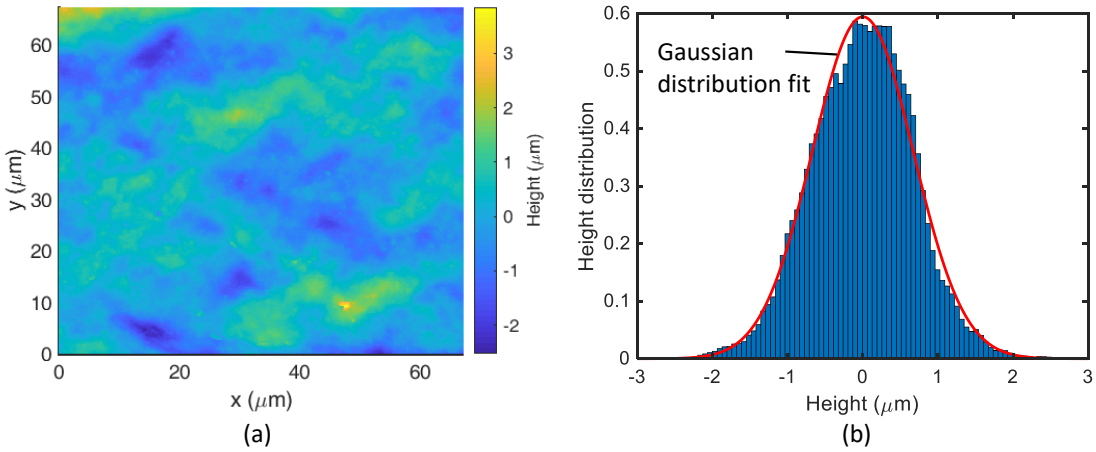

Figure 4-2 (a) Rough surface of a rubber specimen measured by AFM; (b) Height distribution of asperities calculated from rough surface.

In addition to asperity heights, spatial information of roughness is also essential and commonly described by power spectral density (PSD). Mathematically, PSD is the Fourier transform of the autocorrelation function (ACF) of a signal over a range of frequency. In the case of rough surfaces, the correlation information between different wavelengths in the ACF is then transformed to the frequency domain as wavevectors, denoted as q. By definition, calculating roughness PSD uses the following equation:

$$C_{2D}(\boldsymbol{q}) = \frac{1}{(2\pi)^2}\int d^2x < z(\boldsymbol{x})z(\boldsymbol{0}) > e^{-i\boldsymbol{q}\boldsymbol{x}} \qquad \textit{Equation 4-4}$$

where z is the height of surface at the point $\boldsymbol{x}$ above a flat reference plane chosen so that $<z(\boldsymbol{x})> = 0$. The angular bracket $<>$ stands for ensemble average, and $\boldsymbol{q}$ is the wavevector with magnitude $q = |\boldsymbol{q}| = 2\times\pi/\lambda$, λ being the wavelength.

Note that the power spectrum given by Equation 4-4 is in two-dimensional frequency space. If the rough surface is isotropic, $C_{2D}(\boldsymbol{q})$ should be radially symmetric. It is then possible to

take a radial average of $C_{2D}(\boldsymbol{q})$ to yield a one-dimensional function $C(q)$ depending solely on the magnitude of the wavevector $q = |\boldsymbol{q}|$, with units of m^4.

Many rough surfaces in engineering applications exhibit a self-affine fractal feature, i.e. the statistical properties remain unchanged if a scale change is made. In the diagram of $C(q)$, this presents a straight line, as shown in Figure 4-3, where the surface is self-affine fractal for a finite wavevector regime $q_r < q < q_s$. In this case, $C(q)$ can be written as:

$$C(q) = \begin{cases} \frac{H}{\pi} \frac{{h_{rms}}^2}{q_r^2} \left(\frac{q}{q_r}\right)^{-2(H+1)} & q_r < q < q_s \\ C_0 & q_L < q < q_r \end{cases} \qquad \textit{Equation 4-5}$$

where q_r is the roll-off wavevector below which the PSD is constant and H is the Hurst exponent related to the fractal dimension D_f via $H = 3 - D_f$, and $C_0 = C(q=q_r)$. The largest wavevector q_s is $q_s = 2\times\pi/a$, with a being atomic distance or lattice constant, and the smallest wavevector is $q_L = 2\times\pi/L$, with L being the linear size of the surface.

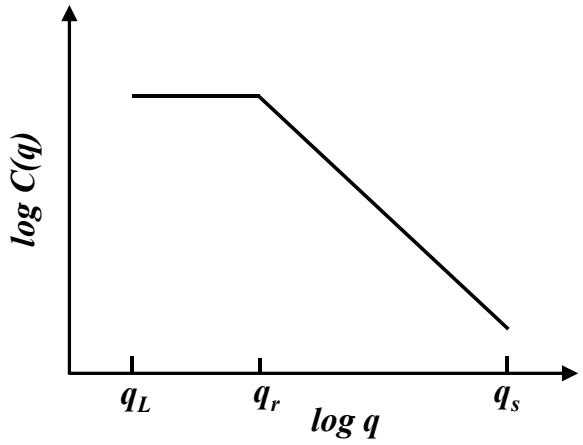

Figure 4-3 The surface roughness power spectrum of a self-affine surface. The roll-off wavevector q_r and the cut-off wavevector q_s depend on the system considered. The slope of the log C(q) - log q for $q_r<q<q_s$ is determined by the fractal dimension D_f. The smallest wavevector q_L is determined by the lateral size of the available surface region.

It is common to use PSD to characterize roughness, also given that many commercial packages already provide it for spectral information along with topography when rough surfaces are measured. Normally, one-dimensional (1D) PSD are reported instead of two-

dimensional (2D) PSD because they are easier to present and compare. However, some software takes the 1D PSD of each line of the roughness data and calculates an average over all lines, denoted as $C_{1D+}(q)$, which is different from the radially averaged 2D PSD $C(q)$. Thus, caution must be taken when quantitative values are computed. If the surface is isotropic and well described by a self-affine fractal, the $C_{1D+}(q)$ and $C(q)$ can be related in an empirical equation [69]:

$$C_{1D+}(q) = C(q) \times \pi \times q \qquad \textit{Equation 4-6}$$

Figure 4-4 shows the radial ACF and the radially averaged 2D PSD $C(q)$ and the 1D PSD $C_{1D+}(q)$ performed on the rough surface given in Figure 4-2. Note the unit is in m^3 for $C_{1D+}(q)$.

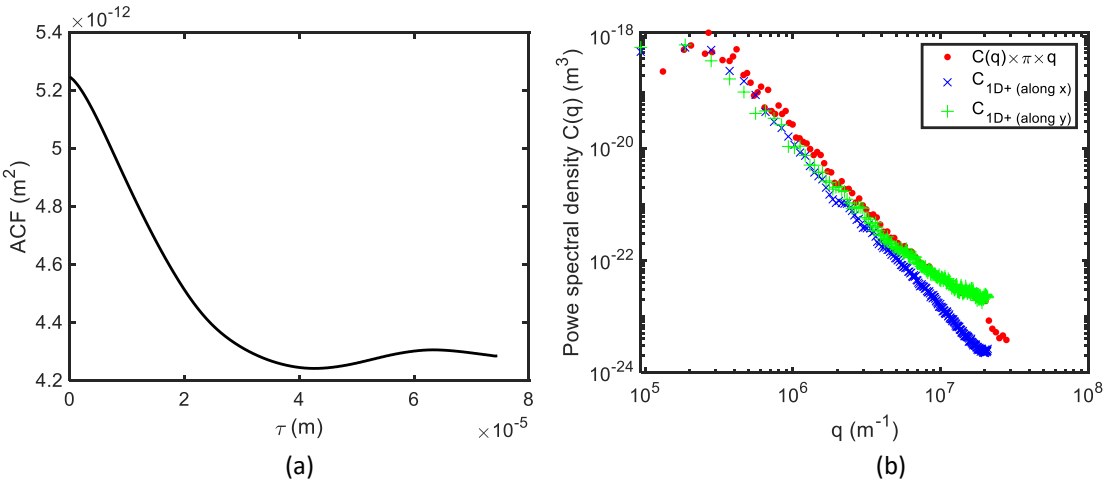

Figure 4-4 (a) The radial Auto-correlation function and the radially averaged two-dimensional power spectrum C(q) and equivalent one-dimensional power spectrum $C_{1D+}(q)$ for the rough surface shown in Figure 4-2.

4.3 Generation of surface roughness

Synthetic rough surfaces are usually needed for systematic studies of contact mechanics so that a large range of statistical properties can be analysed in a controlled manner. There are several means available of generating rough surfaces, such as methods based on the moving average model [96, 162], methods based on spectral analysis [163], fractal models [164],

etc. In this thesis, random process model of topography is employed to create synthetic rough surfaces which are isotropic, Gaussian and self-affine fractals. For a given power spectrum $C(q)$, the rough surface is obtained by [69]:

$$h(x) = \sum_q B(q) e^{i[q \cdot x + \varphi(q)]} \qquad \textit{Equation 4-7}$$

where $B(q)$ determines the amplitude of the roughness and is given by $(2\pi/L) \times C(q)^{(1/2)}$ with $L = A_0^{(1/2)}$ (A_0 being the area of the square rough surface under investigation); φ is an independent random variable, uniformly distributed between in the interval $[0,2\pi]$.

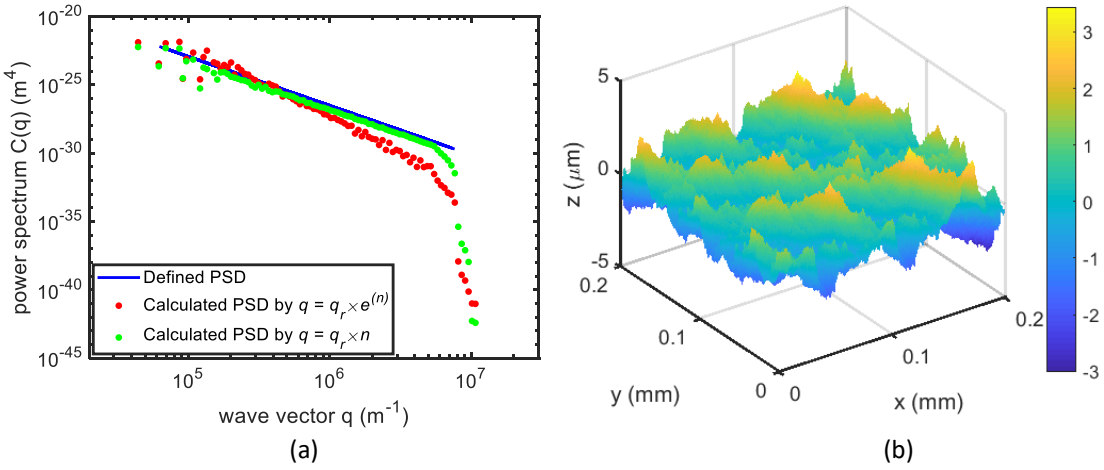

Figure 4-5 (a) Defined PSD and calculated PSD of surfaces generated by different discretization in wavevectors; (b) Generated rough surface using $q = q_r \times n$.

Despite the wide employment of this method in the study of contact mechanics, there is no universal means of selecting the wavelength components. For example, Pohrt and Popov [99] defined the roughness of different scales over exponentially increased intervals, *i.e.* $q = q_r \times e^n$, whereas Putignano *et al.* [71] utilized linearly increasing wavevectors, *i.e.* $q = q_r \times n$. Although both have demonstrated satisfying representations of rough surfaces in their own research, in this thesis, it was found that the discretization of wavevectors might have a strong impact on resultant properties of the synthetic surfaces. More specifically, in the process of generating a rough surface with the PSD (blue line) shown in Figure 4-5(a), it was found that choosing exponential discretization implicitly introduced more long-

wavelength component and less short-wavelength ones, which ultimately changes the surface property. Thus, $q = q_r \times n$ was adopted here to accurately reproduce the rough surface (shown in Figure 4-5(b)) with the desired PSD.

4.4 Stochastic methods

Contact mechanics between rough surfaces are fundamental in many areas, as it provides crucial information related to friction, wear, interfacial separation, heat transfer between surfaces and so on. There are many studies on developing analytical models to predict the rough contact mechanics; however, a full understanding of the exact nature of the interactions between two solids with randomly rough surfaces has not yet been achieved. The reason is that surfaces usually exhibit roughness over many decades of length scales. Up to now, two mainstream approaches, namely the multi-asperity theories [61-63, 65] and Persson's theory [67, 69, 77, 165], are commonly used.

As mentioned in Chapter 2, multi-asperity theories, including the traditional Greenwood and Williamson (GW) model [61], the modified GW model [62, 63] and the theory by Bush, Gibson and Thomas (BGT theory) [65], model the roughness as an ensemble of spherical asperities with randomly distributed heights and applies Hertzian theory on every asperity to account for deformation. Mathematically simple as it is, this approach is limited in two aspects. First, the "bumps" or hemispheres used to describe the asperities do not capture the self-affine fractal features that seem to typically characterise real rough surfaces. Additionally, the long-range elastic deformation or the interaction between asperity deflections is neglected, which would lead to smaller contact areas, especially for contacts between soft solids.

Therefore, in this work, the theory of Persson for rough contact mechanics is considered. As the aim is to incorporate the effect of roughness into the FSI model, the Persson's theory on the real contact area, which is vital in calculating friction, and the interfacial separation,

which in turn has great significance in determining the solid pressure, are described as follows. More details about Persson's theory, readers refer to [67, 69, 77, 165].

4.4.1 Persson's theory on contact area evolution

Assuming an elastic solid with flat surface and Young's modulus E and Poisson's ratio v is in contact with a rigid solid with rough profile $z(x)$ under the pressure σ_0, Persson's theory [67, 69]considers the rough profile at many different magnifications ζ, from small $\zeta = \lambda/\lambda_r$ with λ_r being a reference wavelength, *e.g.* the roll-off wavelength, to large ζ, where the shortest wavelength roughness that can be resolved. At low magnification, $\zeta = 1$, a complete contact at macroscales occurs, while with the increase of ζ, roughness with smaller wavelength will be detected, and contacts only occur partially between some asperities.

If the real contact area at magnification ζ is denoted as $A(\zeta)$, and the nominal contact area (when $\zeta = 1$) is denoted as A_0, then the contact area ratio $A(\zeta)/A_0$ and the stress distribution in the contact area $P(\sigma, \zeta)$ are related by [69]:

$$\frac{A(\zeta)}{A_0} = \int d\sigma\, P(\sigma, \zeta). \qquad \textit{Equation 4-8}$$

When $\zeta = 1$, solids are in contact everywhere and the stress at the interface is everywhere equal to the applied pressure, so the distribution will be delta function-like:

$$P(\sigma, 1) = \delta(\sigma - \sigma_0). \qquad \textit{Equation 4-9}$$

When the magnification increases, in order to continuously spread between the contact region and the non-contact region, stress distributes with a tail extending to zero as shown in Figure 4-6, which, according to Persson [69], satisfies a diffusion-like equation where time is replaced by magnification ζ and the spatial coordinate by the stress σ as in:

$$\frac{\partial P}{\partial \zeta} = f(\zeta)\frac{\partial^2 P}{\partial \sigma^2} \qquad \textit{Equation 4-10}$$

where

$$f(\zeta) = \frac{\pi}{4}\left(\frac{E}{1-\nu^2}\right)^2 q_L q^3 C(q) \qquad \textit{Equation 4-11}$$

and $q_L = 2\pi/L$.

Equation 4-8 is established for complete contacts. For partial contacts, a boundary condition (with no adhesion) was introduced [69]:

$$P(0,\zeta) = 0, \qquad \textit{Equation 4-12}$$

such that the fraction of actual contact area can be calculated by:

$$\frac{A(\zeta)}{A_0} = \frac{1}{\sqrt{\pi}}\int_0^G dx\, e^{-x^2/4} = erf(1/2\sqrt{G}) \qquad \textit{Equation 4-13}$$

where

$$G(\zeta) = \frac{\pi}{4}\left(\frac{E}{(1-\nu^2)\sigma_0}\right)\left(\frac{E}{1-\nu^2}\right)\int_{q_L}^{\zeta q_L} dq\, q^3\, C(q) \qquad \textit{Equation 4-14}$$

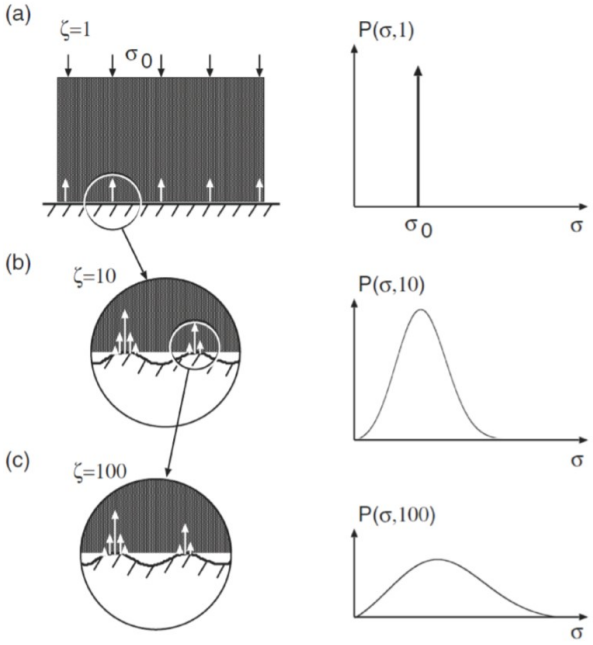

Figure 4-6 The stress distribution P(σ, ζ) in the contact region between a (rigid) block and an elastic substrate at increasing magnification ζ. At the lowest (engineering) magnification ζ = 1 the substrate surface looks smooth and the block makes (apparent) contact with the substrate in the whole nominal contact area. As the magnification increases, we observe that the area of (apparent) contact decreases, while the stress distribution becomes broader and broader. Copyright with permission from Ref. [166].

As mentioned previously, the proportionality coefficient κ is a variable correlating the contact area ratio A/A_0 to the applied pressure, σ_0, the elastic modulus, E_r, and the second spectral moment of the rough surface, m_2, as:

$$\frac{A}{A_0} = \kappa \frac{\sigma_0}{E_r\sqrt{2m_2}} \qquad \textit{Equation 4-15}$$

with $E_r = E/(1-\nu^2)$ and $m_2 = \langle h'^2_{rms} \rangle/2$. This is often used to quantify the linear evolution of contact areas for relatively small loads. In Persson's theory, this value is approximately $(8/\pi)^{1/2}$, smaller than the prediction of the BGT model $\kappa = (2\pi)^{1/2}$ [65]. Persson argued that the origin of this $2/\pi$ difference may be from the independent contact regions assumed in the BGT model, which is confirmed by many numerical analysis, with κ values repeatedly reported in between this range [82, 93, 167].

4.4.2 Persson's theory on load-separation relations

Another important quantity in contacting interfaces is the separation. Since interacting bodies are only partially in contact between some asperities, there are gaps randomly distributed in the apparent contact area. Unlike the analysis of the contact area evolution which is derived from full contacts, Persson's theory for interfacial separation starts from small loads [77]. In a contact system shown in Figure 4-7, if the mean gap between the elastic block and the average surface plane of the substrate is denoted as u ($u > 0$), then u will certainly decrease with increasing pressure p. The work done by the external pressure p in the squeezing process is equal to the elastic energy stored in the vicinity of the asperity contact regions:

$$\int_u^\infty du' A_0 p(u') = U_{el}(u) \qquad \textit{Equation 4-16}$$

or

$$p(u) = -\frac{1}{A_0}\frac{dU_{el}}{du} \qquad \textit{Equation 4-17}$$

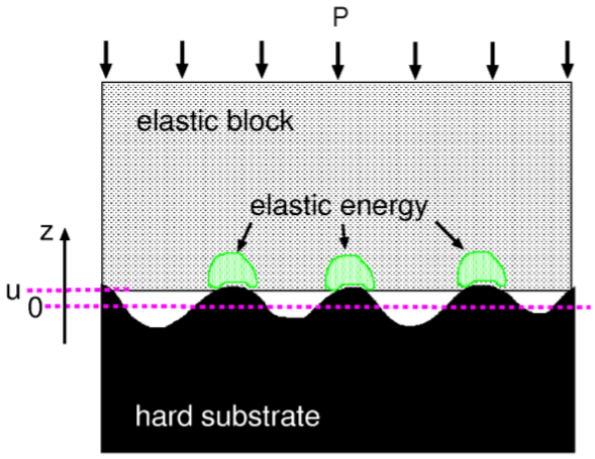

Figure 4-7 An elastic block squeezed against a rigid rough substrate. The separation between the average plane of the substrate and the average plane of the low surface of the block is denoted by u. Elastic energy is stored in the block in the vicinity of the asperity contact region.[77]

The elastic energy U_{el} in the simplest approximation takes the form:

$$U_{el} \approx A_0 E_r \frac{\pi}{2} \int_{q_L}^{q_s} dq q^2 P(q,p) C(q) \qquad \textit{Equation 4-18}$$

Since $P(q,p)$ and $C(q)$ are known from Equation 4-8 and Equation 4-5 respectively, substituting them into Equation 4-17 gives:

$$p(u) = -\sqrt{\pi}\gamma \int_{q_L}^{q_s} dq\, q^2\, C(q) s(q) e^{-\left[\frac{s(q)p}{E_r}\right]^2} \frac{dp}{du} \qquad \textit{Equation 4-19}$$

or

$$du = -\sqrt{\pi}\gamma \int_{q_L}^{q_s} dq\, q^2\, C(q) s(q) e^{-\left[\frac{s(q)p}{E_r}\right]^2} \frac{dp}{p} \qquad \textit{Equation 4-20}$$

where w is

$$s(q) = \left(\pi \int_{q_L}^{q} dq' q'^3 C(q')\right)^{-1/2} \qquad \textit{Equation 4-21}$$

At small loads, integrating Equation 4-20 from $u = 0$ to u gives the exact form of the interfacial separation [73]:

$$u = \sqrt{\pi}\gamma \int_{q_L}^{q_s} dq q^2 C(q) s(q) \int_p^{\infty} dp' \frac{1}{p'} P_p(q) exp(-[s(q)p'/E_r]^2) \quad \textit{Equation 4-22}$$

For purely self-affine fractal surfaces and very small pressures, Equation 4-22 can be further reduced to an approximated equation [77]:

$$u = \beta_1^{-1} h_{rms} log(\beta_2 \epsilon q_r h_{rms} E_r / p) \quad \textit{Equation 4-23}$$

where ε is around 0.75. β_1 and β_2 can be calculated from the roughness power spectrum. For surfaces with fractal dimension $D_f = 2.2$, $\beta_1 = 1$ and $\beta_2 = 0.5$ [77].

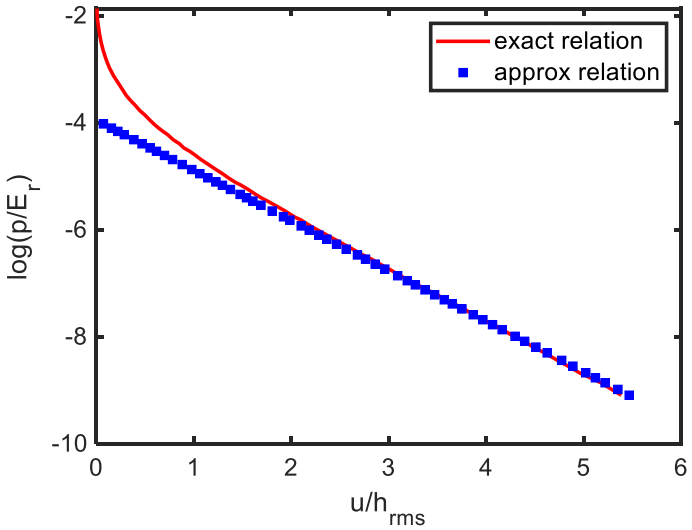

Figure 4-8 The relation between the applied pressure and the average interfacial separation for an elastic solid squeezed against a rigid, self-affine fractal surface given in Figure 4.5(b) calculated by a full numerical analysis(Equation 4-22) and its approximated form(Equation 4-23).

Figure 4-8 shows both the exact and approximated relations between the squeezing pressure p and interfacial separation u between an elastic solid and a hard, self-affine fractal rough surface with $C(q)$ given by Figure 4-5(b). Notice that the approximated solution only captures the asymptotic behaviour predicted by Equation 4-23 and starts to deviate when the interfacial separation is relatively small ($u < h_{rms}$); a similar trend was also shown in Persson's study [77]. This difference explains the small discrepancy found in the validation section in Chapter 3 (shown in Figure 3-9 and Figure 3-10), where the solid pressure was slightly underestimated in this thesis using the approximated Equation 4-23 compared with

those predicted by Persson and Scaraggi [2] where the full analytical solution using Equation 4-22 was adopted.

4.5 Deterministic method

In addition to theoretical studies, deterministic approaches are also powerful in investigating contact mechanics between rough surfaces. Comparing to theoretical models which can only make predictions based on surface properties, numerical simulations excels in providing details such as pressure distribution and actual separation for any given surface topography. This is particularly useful when local tribological behaviour are pursued. Chapter 2 listed and compared several common deterministic approaches, including the finite element method (FEM), the boundary element method (BEM), the molecular dynamics (MD) based method, *etc*. In this section, a BEM-based approach is employed to solve frictionless contact problems between elastic solids with rough surfaces, focusing on obtaining the real contact area and the interfacial separation.

As described in the previous section, such contact problems can be represented by an elastic solid with isotropic random rough surface in contact with a rigid flat half space. The rough surface can be either obtained from experimental measurements (1D or 2D) or generated artificially.

Solving contact problems as such comprises two parts. One is to determine the deformation of the elastic solids. The one-dimensional calculation has been presented in Chapter 3. For two-dimensional rough surfaces, based on the elasticity theory, the deformation of an elastic solid at a random point due to a distributed pressure p can be computed by:

$$w(x,y) = \frac{2}{\pi E_r} \iint \frac{p(\xi,\eta)}{\sqrt{(x-\xi)^2+(y-\eta)^2}} d\xi d\eta \qquad \textit{Equation 4-24}$$

where $\frac{1}{\sqrt{(x-\xi)^2+(y-\eta)^2}}$ is denoted as Green's functions and frequently used in the calculation of macroscopic deformation in the EHL community, and E_r is the reduced

elastic modulus.

It is convenient to use discrete from in numerical analysis as discussed in the previous chapter. If the computational domain is discretized on uniform grids, then the integral part of Equation 4-24 can be expressed as

$$w_{ij} = \frac{2}{\pi E_r} \sum_k^{Nx} \sum_l^{Ny} D_{ij}^{kl} p_{kl} \qquad \textit{Equation 4-25}$$

where D_{ij}^{kl} is the influence coefficient matrix relating the normal deformation at (i,j) with acting loads at (k,l) through:

$$\begin{aligned} D_{i,j,k,l} = & \left| x_i - x_k + \frac{\Delta x}{2} \right| ln \left(\frac{f\left(y_j - y_l + \frac{\Delta y}{2}, x_i - x_k + \frac{\Delta x}{2}\right)}{f\left(y_j - y_l - \frac{\Delta y}{2}, x_i - x_k + \frac{\Delta x}{2}\right)} \right) \\ & + \left| x_i - x_k - \frac{\Delta x}{2} \right| ln \left(\frac{f(y_j - y_l - \frac{\Delta y}{2}, x_i - x_k - \frac{\Delta x}{2})}{f(y_j - y_l + \frac{\Delta y}{2}, x_i - x_k - \frac{\Delta x}{2})} \right) \\ & + \left| y_j - y_l + \frac{\Delta y}{2} \right| ln \left(\frac{f(x_i - x_k + \frac{\Delta x}{2}, y_j - y_l + \frac{\Delta y}{2})}{f\left(x_i - x_k - \frac{\Delta x}{2}, y_j - y_l + \frac{\Delta y}{2}\right)} \right) \\ & + \left| y_j - y_l - \frac{\Delta y}{2} \right| ln \left(\frac{f(x_i - x_k - \frac{\Delta x}{2}, y_j - y_l - \frac{\Delta y}{2})}{f(x_i - x_k + \frac{\Delta x}{2}, y_j - y_l - \frac{\Delta y}{2})} \right) \end{aligned} \qquad \textit{Equation 4-26}$$

where $f(x,y) = x+(x^2+y^2)^{1/2}$,and Δx and Δy are distances between two neighbouring nodes.

Traditionally, using Equation 4-25 to solve normal surface deformation requires two steps. First is to determine D_{ij}^{kl} depending on the nodal positions in a predefined mesh. The second step is to calculate the multi-summation, *i.e.* to calculate the deformation at one node due to the pressure field using D_{ij}^{kl} and subsequently sum them up. This procedure usually involves many iteration loops or huge matrices in MATLAB, resulting in rather high computational cost, especially in two-dimensional contacts.

To address this issue, the FFT technique [37, 97] and discrete convolution were proposed.

Note that Equation 4-25 appear in the form of continuous linear convolution:

$$c_k = \sum_{n=0}^{N-1} h_{k-n} a_n \,, \qquad k = 0,1,\dots,2N-2 \qquad \textit{Equation 4-27}$$

Based on the convolution theorem, *i.e.* the Fourier transform of a convolution of two functions equals the product of the Fourier transform of these two functions, it is convenient to have:

$$c_n = IDFT(DFT(h_n) \times DFT(a_n)) \qquad \textit{Equation 4-28}$$

However, the convolution theorem does not apply to the discrete linear convolution but to the cyclic convolution, which is introduced as:

$$c_k = \sum_{n=0}^{N-1} h_{\langle k-n \rangle} a_n \,, \qquad k = 0,1,\dots,N-1 \qquad \textit{Equation 4-29}$$

Thus, the linear convolution for contact problems should be converted into the cyclic convolution that can be efficiently and accurately handled by the discrete convolution and Fast Fourier Transform method (DC-FFT). It should be borne in mind that, in order to calculate the linear convolution using circular convolution, the dimensions of h_n and a_n must be extended so that the circular convolution will give the same length output as obtained from the linear convolution. The most common way is by adding an appropriate number of zeros to the arrays h_n and a_n, known as zero-padding. Secondly, h_n has to be circulated or wrapped around according to the definition of circular convolution [37, 168].

The employment of FFT and convolution theorem can accelerate the computation significantly. Figure 4-9 compares the central-line deformation of a half-sphere under Hertzian pressure calculated by both multi-summation method and the DC-FFT method. Same results were obtained but DC-FFT achieved the solution (in 0.06s) 10 times faster than the traditional multi-summation method (in 7.1s) using Intel Core i5 CPU.

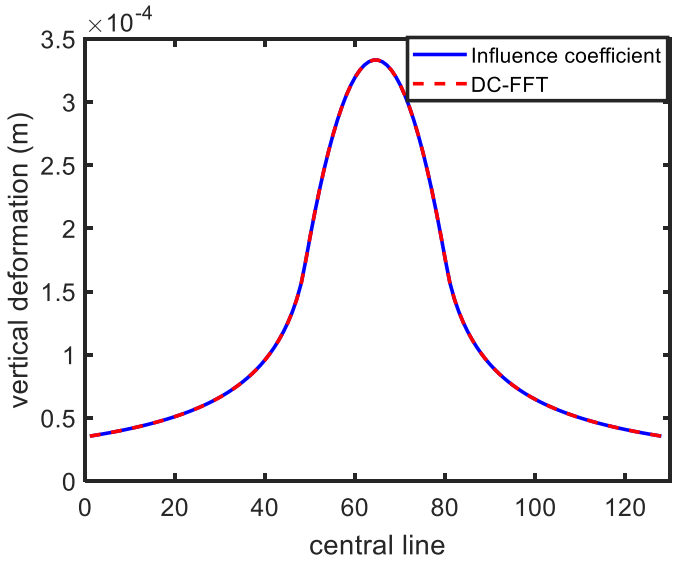

Figure 4-9 Deformation of a semi-sphere under Hertzian pressure along central line. The applied load is 1.3 N. Radius of the sphere is 1 cm. Blue line represents the results calculated using an influence coefficient matrix and red dash line represents the one calculated using DC-FFT method.

Another important part of solving rough contact problems is to find the contact area. When a rough surface is squeezed by a certain load W and gets into contact with a flat space, there will be pressure arising in contact regions where no separation can be observed and the opposite, *i.e.* zero pressure and positive separation, in the non-contact regions. The total resultant pressure in the contact area should be balanced with the applied load. Such problems can be mathematically described using the following system of equations and inequalities:

$$u_0 + u_{ij} + \sum_{(h,k)\in I_g} D_{ij}^{kl}\, p_{hk} > 0 \qquad (i,j) \in I_c \qquad \textit{Equation 4-30}$$

$$p_{ij} > 0 \qquad (i,j) \in I_c \qquad \textit{Equation 4-31}$$

$$u_0 + u_{ij} + \sum_{(h,k)\in I_g} D_{ij}^{kl}\, p_{hk} > 0 \qquad (i,j) \notin I_c \qquad \textit{Equation 4-32}$$

$$p_{ij} = 0 \qquad (i,j) \notin I_c \qquad \textit{Equation 4-33}$$

$$a_x a_y \sum_{(k,l)\in Ig} p_{ij} = W \qquad \textit{Equation 4-34}$$

Here, u_0 is the rigid-body approach and u_{ij} is the surface roughness height. I_c stands for

nodes in contact and I_g for all the nodes in the calculation domain.

According to the theory of optimization, Equation 4-30 ~ 4-34 compose a quadratic complementary problem with linear inequality constraints, for which a Conjugate Gradient (CG) iterative method can be particularly suitable with some modification. This was first applied by Polonsky and Keer [89] to non-periodic rough surface contact problems and can be adapted to either a load-control or distance-control situation. In this thesis, a load-control scheme was employed, featuring enforcing the load balance in a single level of iteration, which is not only advantageous for convergence but also permits great compatibility with other numerical techniques such as DC-FFT.

Specifically, the CG iterative method follows these steps:

1. To start with, the non-zero pressure p_{ij}, contact area I_c, applied load W and the influence coefficient matrix D_{ij}^{kl} are used to initialise the iteration.
2. Then the interfacial separation is computed and adjusted by its mean value:

$$u_{ij} = w_{ij} + u_{ij} \qquad \textit{Equation 4-35}$$

$$u_{ij} = u_{ij} - N_c^{-1} \sum_{k,l \in I_c} u_{kl} \qquad \textit{Equation 4-36}$$

   with nodal deformation w_{ij} calculated by DC-FFT and N_c being the number of nodes in contact region I_c, which is the set of (i,j) where $p(i,j) > 0$.

3. For the new gap u_{ij}, a variable G is introduced as:

$$G = \sum_{(i,j) \in I_c} u_{ij}^2 \qquad \textit{Equation 4-37}$$

4. The conjugate direction t can subsequently be obtained by:

$$t_{ij} = \begin{cases} u_{ij} + \delta(G/G_{old}) t_{ij} & (i,j) \in I_c \\ 0 & (i,j) \notin I_c \end{cases} \qquad \textit{Equation 4-38}$$

   where δ here is initialized as 0. Note that if $\delta = 0$, t_{ij} will coincide with the steepest decent direction.

5. The convolution of D_{ij}^{kl} and t_{ij} is computed and adjusted by its mean value:

$$r_{ij} = \sum_{(k,l)\in I_g} D_{ij}^{kl}\, t_{kl} \qquad \textit{Equation 4-39}$$

$$r_{ij} = r_{ij} - N_c^{-1} \sum_{k,l\in I_c} r_{kl} \qquad \textit{Equation 4-40}$$

which is subsequently used to calculate the step size in the conjugate direction

$$\tau = \frac{\sum_{(i,j)\in I_c} u_{ij} t_{ij}}{\sum_{(i,j)\in I_c} r_{ij} t_{ij}} \qquad \textit{Equation 4-41}$$

6. After being stored to $p^{old} = p$, the pressure at contact can be updated by:

$$p_{ij} = p_{ij} - \tau\, t_{ij} \qquad (i,j) \in I_c \qquad \textit{Equation 4-42}$$

7. To enforce inequalities, the negative pressures are first set to be zeros. It is necessary to identify those points where zero pressure and negative separation are found. This indicates an overlap of node, *i.e.* contact, and thus the pressure should be corrected to positive. The overlapping domain is determined by:

$$I_{ol} = \{(i,j) \in I_g: \quad p_{ij} = 0, u_{ij} < 0\} \qquad \textit{Equation 4-43}$$

If $I_{ol} = \emptyset$, δ is set to 1 otherwise remains 0. The pressure in the new contact area is corrected by:

$$p_{ij} = p_{ij} - \tau u_{ij} \qquad (i,j) \in I_{ol} \qquad \textit{Equation 4-44}$$

8. Load balance is finally performed, and the new pressure is adjusted based on the current load F_n and the applied load W:

$$F_n = \Delta x \Delta y \sum_{(i,j)\in I_g} p_{ij} \qquad \textit{Equation 4-45}$$

$$p_{ij} = p_{ij}(F_n/W) \qquad (i,j) \in I_g \qquad \textit{Equation 4-46}$$

Convergence check for pressure to exit the iteration uses the following criterion:

$$\frac{\Delta x \Delta y \sum_{(i,j)\in I_g} |p_{ij} - p_{ij}^{old}|}{W} \leq 1e-10 \qquad \textit{Equation 4-47}$$

The deterministic method described above is referred to as the CG+FFT method in this

thesis. It was applied to the synthetic rough surface in Figure 4-5(b) under various loads. Generally, a full convergence for one load test can be achieved within 200 iterations given a mesh density of 513×513. Periodicity errors are intrinsically introduced when FFT-based solution is considered and are commonly handled by extending the grid much larger than the contact area. In this thesis, the two-fold extension of the grid though zero-padding and wrap-up made the non-periodic calculations possible. In addition, the dimension of the rough surfaces used for calculation are already much larger than the contact area (see discussion of the thermodynamic correction in section 4.5), thus the impact the periodic error can be neglected here. Figure 4-10 shows the reduced separation and the associated increased contact pressure on the central line of the surface in two columns.

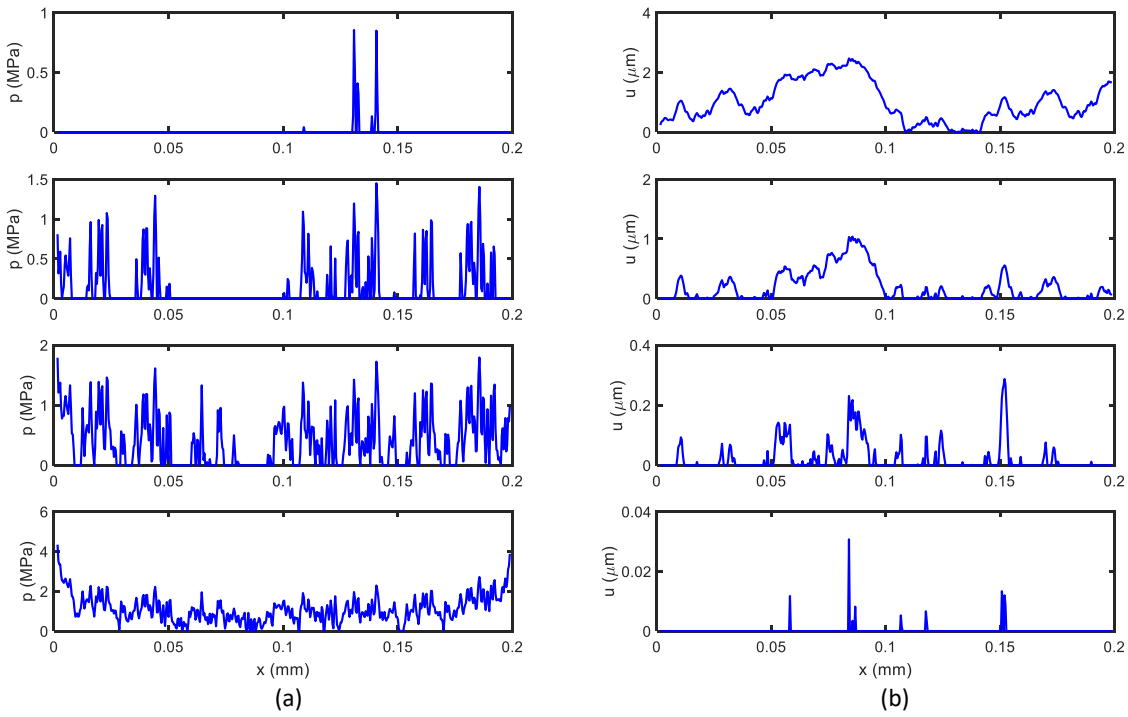

Figure 4-10 Contact pressure (a) and separation field (b) of an elastic solid with rough surface shown in Figure 4-2 along the central line. The Young's modulus and Poisson's ratio of the solid are 3.3 MPa and 0.499. Applied loads for these four cases are 0.03 MPa, 0.23 MPa, 0.6 MPa and1.6 MPa.

Based on these results, the contact area evolution curve and the load-separation curve were generated and validated against those obtained from an MD simulation solver developed by Pastewka *et al.* [101, 169, 170]. It is shown in Figure 4-11 that both contact area and

interfacial separation by CG+FFT agree well with the other solver, especially in highly loaded conditions, where the stochastic method lacks in accuracy. The small deviation is due to the different choice of defining the contact. In the current study, the contact occurs when the interfacial separation is less than 1e-9 m, while in their work, this threshold is decided to be 1e-20 m.

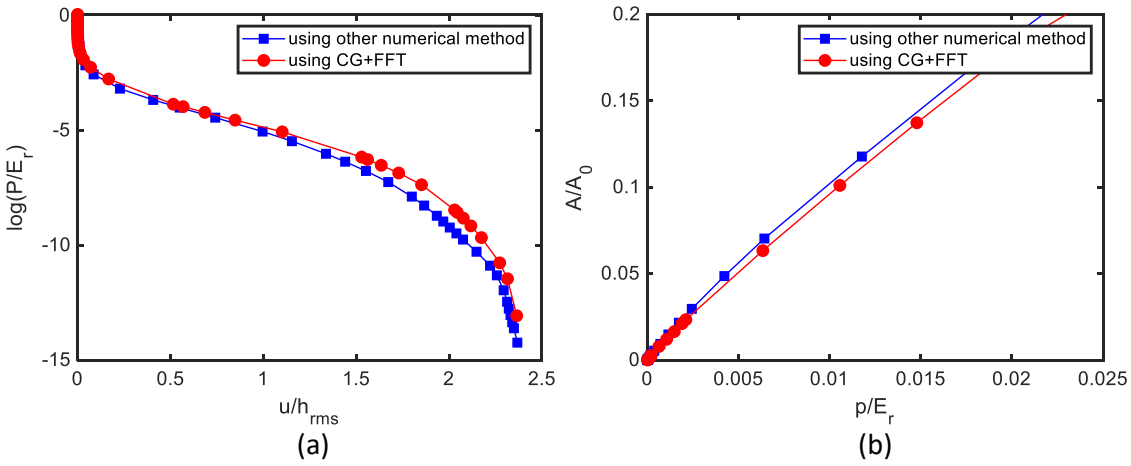

Figure 4-11 Load-separation relation (a) and contact area evolution (b) obtained by the described CG+FFT and another numerical method [169].

4.6 Parametric tests

In analytical theories, the contact mechanism is determined by the stochastic properties of the surfaces, such as the Hurst exponent H, the low cut-off wavevector q_L, the high cut-off wavevector q_s, the roll-off wavevector q_r (if exists), and the roughness power spectrum $C(q)$, whereas in numerical calculations, additional information of the given rough surface, whether measured or synthetic, including the finite system size L and the resolution of the lattice Δx, are also important quantities in affecting the results.

Ideally, the contacting system size L should be much larger than the largest roughness wavelength λ_L, *i.e.* L/λ_L to infinity. The grid spacing Δs should be sufficiently small to resolve the smallest roughness wavelength λ_s so that the sampled roughness surface is continuous, *i.e.* $\Delta x/\lambda_s$ to infinity. Moreover, the rough surface should be considered

expanding over (nearly) the entire frequency domain, *i.e.* q_s/q_L to infinity. These three limits are introduced by Prodanov *et al.* [78] as the thermodynamic limit, the continuum limit and the fractal limit, with L/λ_L, $\Delta x/\lambda_s$ and q_s/q_L denoted as the thermodynamic correction, the continuum correction and the fractal correction. When all of them are satisfied, it is referred to as the "TFC" limit.

However, when solving a rough contact problem using a discrete system, it is almost impossible to reach the TFC limit. In this section, the effect of aforementioned factors on the contact area evolution and the load-separation relation is investigated. First, a reference system was generated, with all relevant parameters and properties listed in Table 4-1. All length related parameters were in the unit of meters and wavevectors q are calculated from wavelength λ accordingly. Then, TFC corrections were systematically controlled by varying each value while keeping the other two constant. For each combination of the parameters, three different realizations of the synthetic rough surfaces were employed, and the average results were taken. While TFC corrections are tested for self-affine fractal surfaces with Hurst exponent 0.8, which is mostly common in real applications, the effect of fractal dimension is examined at the end of this section.

Table 4-1 Statistical parameters of the reference rough surface system

Ref	λ_L	λ_r	λ_s	H	L	N	Δx	h_{rms}	h'_{rms}
	2e-4	1e-4	7.81e-7	0.8	4e-4	1025	3.9e-7	9.58e-7	0.2066

4.6.1 Effect of the continuum correction

Most synthetic or experimental surfaces are represented in discrete forms and limited by the numerical resolution or the measurement technique. To remain in the continuum framework and to capture the mechanics accurately, the continuum corrections should be very small to ensure the smoothness of the rough surface. In some studies [86, 87], this value was inherently set to one and resulted in "one node one asperity", which did not allow

for correctly reproducing the local change of contact force with separation or estimating a realistic growth of localized contact zones. To investigate how this could affect the contact solutions, simulations were carried out on the reference system discretized at different levels. All system parameters are referred to in Table 4-2.

Table 4-2 Statistical parameters of rough surface systems for continuum correction test

Surf	λ_L	λ_r	λ_s	H	L	N	Δx	h_{rms}	h'_{rms}
1	2e-4	1e-4	7.81e-7	0.8	4e-4	1025	3.9e-7	9.58e-7	0.2066
2	2e-4	1e-4	7.81e-7	0.8	4e-4	2049	1.9e-7	9.64e-7	0.2071
3	2e-4	1e-4	7.81e-7	0.8	4e-4	4097	9.7e-8	9.63e-7	0.2079
4	2e-4	1e-4	7.81e-7	0.8	4e-4	8193	4.8e-8	9.70e-7	0.2085

Figure 4-12(a) depicts the evolution of contact area with load when small contacts (A/A_0 up to 20%) occur. As suggested in [82], in the following study of contact area, the applied load takes the normalized form $p/(E_r \times h'_{rms})$, which considers effect of the RMS gradient. Consequently, the proportionality coefficient κ, estimated at approximately 2.1, fell between the Persson's prediction 1.6 and BGT model's 2.5 and agreed well with some other numerical studies [93].

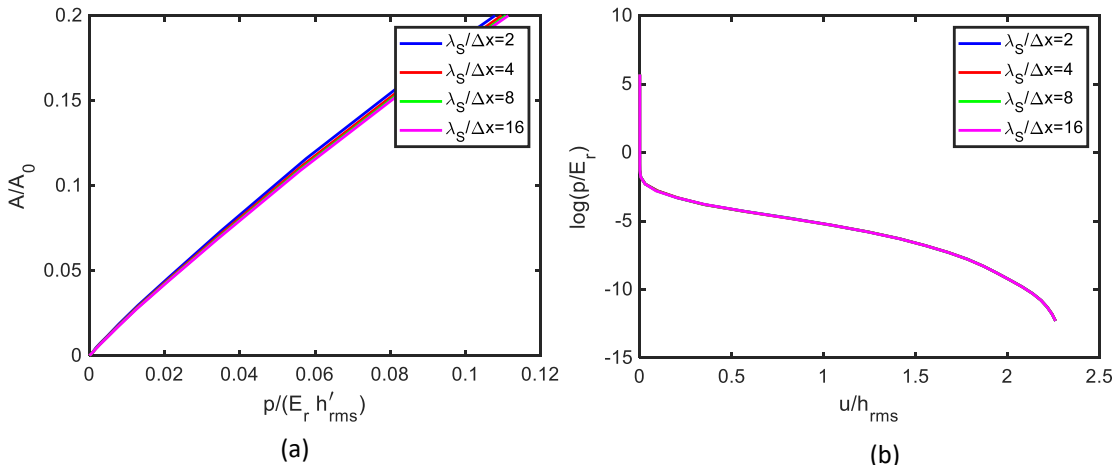

Figure 4-12 (a) Contact area evolution of four rough surface systems in Table 4-2 under low load, i.e. contact ratio below 20%; (b) load-separation curve of the same contact systems from infinitesimal to full contact.

It also appears that, in the present work, the relation between contact area and load is marginally affected by the discretization choice. The same conclusion was drawn by Prodanov *et al.* [78] and by Yastrebov *et al*. [82], where very fine meshes were employed. However, given that the largest grid size considered in the present work is $\lambda_s/2$, it is suggested to use at least half of λ_s to include all small wavelength roughness.

The continuum correction does not seem to affect load-separation relations either, seen in Figure 4-12(b), suggesting again that $\lambda_s/2$ is already capable of resolving the smallest wavelength, at least for the present combination of parameters. Although there are very little studies to be found regarding this, the work presented in Ref. [78] showed that for fractal surfaces with $H = 0.8$, the effect of discretization was moderate.

4.6.2 Effect of thermodynamic correction

When solving rough contact problems numerically, the size of rough surface is usually finite, which has been proved to have significant effect on contact behaviour [83, 93, 98]. This is known as the thermodynamic effect, or the finite size effect. In many early studies [83, 86, 87, 93, 98], the edge length of a square surface was set equal to the longest wavelength in the surface spectrum. In such cases, the rough surface only had a few large "macro" asperities and did not exhibit Gaussian behaviour. Consequently, pronounced clustering of contact zones close to peaks of "macro" asperities would occur. The most common way to overcome the finite size effect is to increase the ratio between the system size L and the longest wavelength λ_L, in other words, to include more long-wavelength components.

From the analytical results, it is argued that the Gaussianity of heights of surfaces is independent of the spectral content itself but relies on the system size. This was verified by Yastrebov *et al.* in [82] where they demonstrated that the distribution was affected by L/λ_L and larger L/λ_L would render more Gaussian-like surfaces. However, in order to obtain different L/λ_L, rough surfaces were generated by varying the lower cut-off wavevector q_L,

which changed the fractal width of the roughness spectrum as well. Moreover, the long wavelength plays a very important role in characterizing the surface properties and determining the elastic response. Although their approach guaranteed the variation of L/λ_L, it is hard to deduce whether the change of contact behaviour is due to L/λ_L or simply λ_L. Other studies [78, 80] used fixed q_r and q_s to generate pure self-affine rough surfaces, *i.e.* $q_L = q_r$, and investigated the finite size effect by varying the system size L. Nevertheless, in this work, it is found that simply increasing system size cannot guarantee the Gaussianity of the surface. In fact, a rough surface is more prone to Gaussian when it has wider plateau in its power spectrum. This can be seen in Figure 4-13, where the roughness power spectrum and the height distribution of synthetic surfaces are presented. While keeping q_r and q_s constant, surfaces with smaller q_L are more Gaussian-like. Note that the system size L was always chosen 2 times of the longest wavelength, $L = 2\times\lambda_L$, thus the thermodynamic correction was changed implicitly as in other studies. Therefore, the main cause of the Gaussianity of the surface is the roll-off wavevector and this was not explicitly explained before. All the relevant parameters are listed in Table 4-3.

Table 4-3 Statistical parameters of rough surface systems for thermodynamic correction test

Surf	λ_L	λ_r	λ_s	H	L	N	Δx	h_{rms}	h'_{rms}
1	1e-4	1e-4	7.81e-7	0.8	2e-4	513	3.9e-7	1.01e-6	0.2120
2	2e-4	1e-4	7.81e-7	0.8	4e-4	1025	3.9e-7	9.58e-7	0.2066
3	4e-4	1e-4	7.81e-7	0.8	8e-4	2049	3.9e-7	9.63e-6	0.2069
4	8e-4	1e-4	7.81e-7	0.8	1.6e-3	4097	3.9e-7	1.02e-6	0.2139

These rough surfaces were used to investigate the effect of thermodynamic correction on the contact area. The numerical procedure adopted here was the same as the one used in the continuum correction study using CG+FFT. Figure 4-14(a) shows that in the evolution of contact area with pressure, the dependence of κ (approximately 2.1) on the thermodynamic correction is weak.

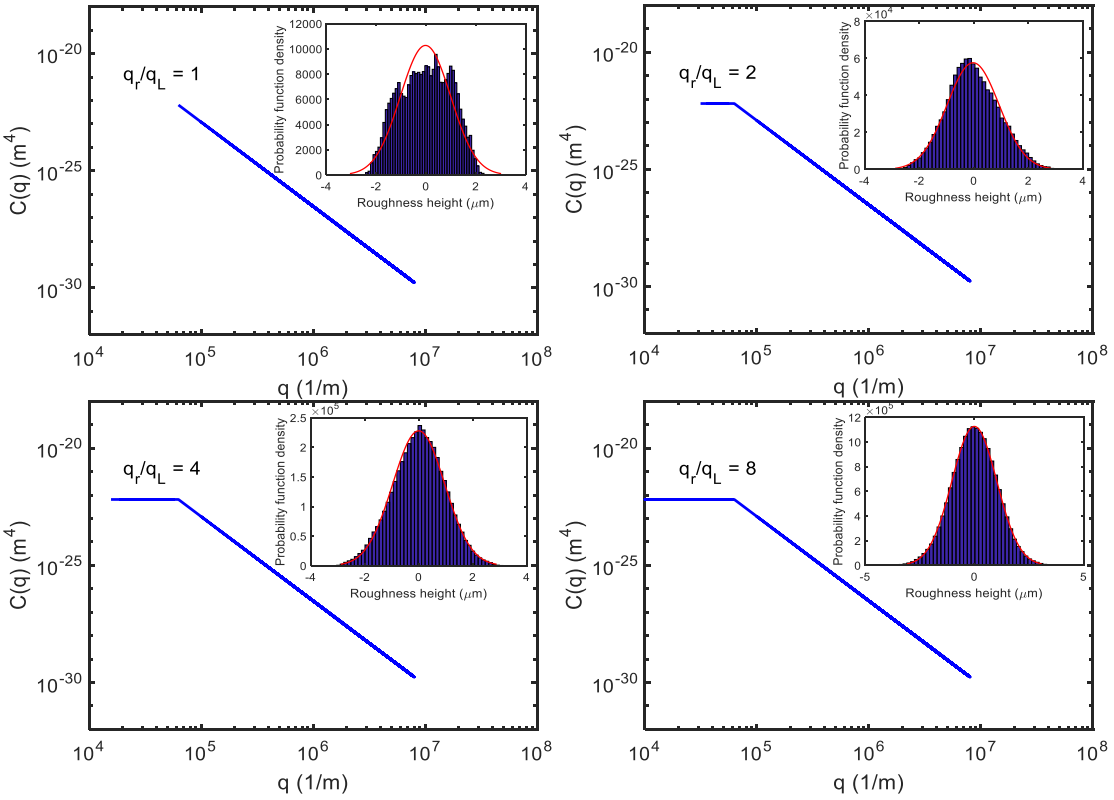

Figure 4-13 Power spectra of surfaces 1-4 in Table 4-3 and their corresponding height distribution.

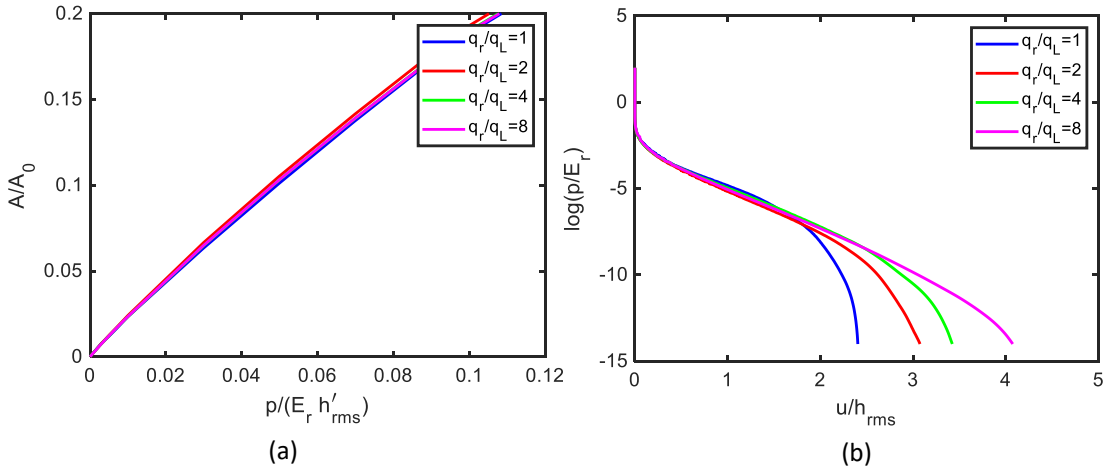

Figure 4-14 (a) Contact area evolution of four rough surface systems in Table 4.3 under low load, i.e. contact ratio below 20%; (b) load-separation curve of the same contact systems from infinitesimal to full contact.

On the contrary, when the applied load is low, the Gaussianity of the rough surfaces strongly influences the load-separation curve, especially in the high separation regime, seen in Figure 4-14(b). This result not only confirms what many studies showed as the "finite

size effect", *i.e.* data start to deviate from the logarithmic relation under low loads, but also reveals that this effect can be improved by introducing higher q_r/q_L rather than blindly increasing L/q_L.

4.6.3 Effect of fractal correction

In the investigation of fractal correction effect, synthetic rough surfaces with same q_L, q_r and varying q_s were used. Details are referred to Table 4-4. Figure 4-15(a) presents the contact area evolution against normalized load for different fractal corrections. The contact proportionality κ appeared to decrease from 2.5 and converged to 2, which is similar with what Prodanov *et al*. found for the low load test in their study [78]. Interestingly, Yastrebov *et al.* who focused on the continuum limit and used a small fractal correction also found 2.5 for the prediction of this coefficient [82], agreeing with the BGT theory. This may suggest that systems with small fractal correction do not always behave like self-affine randomly rough surfaces but more like a collection of elastic bumps.

Table 4-4 Statistical parameters of rough surface systems for fractal correction test

Surf	λ_L	λ_r	λ_s	H	L	N	Δx	h_{rms}	h'_{rms}
1	4e-4	1e-4	6.25e-7	0.8	8e-4	257	3.1e-6	9.57e-7	0.1165
2	4e-4	1e-4	3.13e-7	0.8	8e-4	513	1.5e-6	9.67e-7	0.1445
3	4e-4	1e-4	1.56e-7	0.8	8e-4	1025	7.8e-7	9.57e-7	0.1738
4	4e-4	1e-4	7.81e-7	0.8	8e-4	2049	3.9e-7	9.62e-7	0.2069
5	4e-4	1e-4	3.90e-7	0.8	8e-4	4097	1.9e-7	9.54e-7	0.2444

The load-separation relation was marginally affected by the short wavelength included in the rough surface, as shown in Figure 4-15(b). This is consistent with theoretical predictions [67], numerical simulations [73] and some experimental findings [85]. The reason is possibly because the strain energy stored at the interface is more related to the mid-low frequency components of the rough surface PSD and does not significantly change

with the high frequency terms. This could also explain the strong dependence of separation on h_{rms} as the latter is influenced by the long wavelength components. Such finding seems to contradict the results shown by Prodanov and co-workers [78], where a power-law increase of separation with respect to the fractal correction (q_s/q_L) was found. However, Prodanov *et al.* [78] used rough surfaces with a much large range of wavelength components and no roll-off terms in the corresponding PSD, which made the short wavelength play a more important role in determining the RMS roughness and hence the separation. In reality, rough surfaces are more prone to have the roll-off plateau in their PSD and observing the smallest possible asperities is nearly impossible due to limitations of resolution in experimental apparatus. Therefore, it is safe to state that for most practical cases, fractal correction does not influence the mean gap as long as λ_s does not significantly affect h_{rms}.

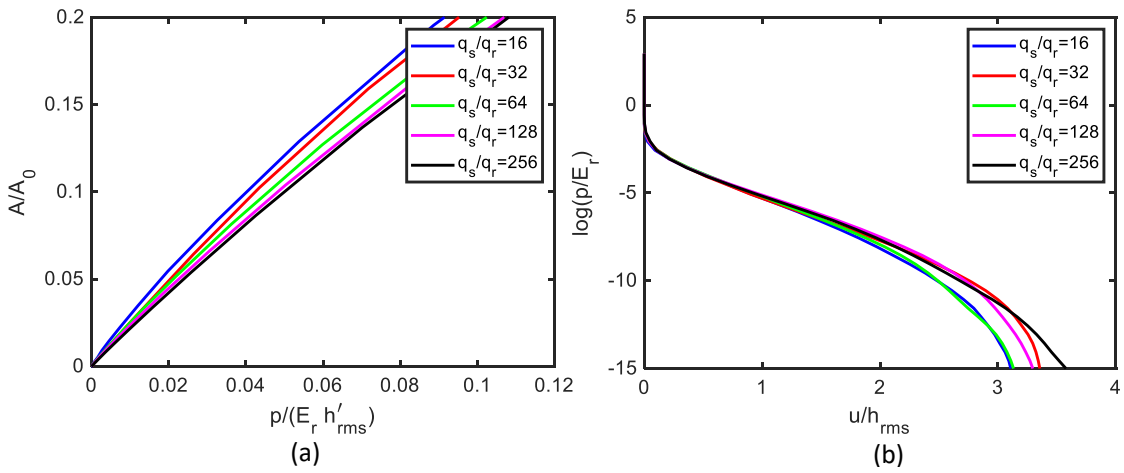

Figure 4-15 (a) Contact area evolution of four rough surface systems in Table 4.4 under low load, i.e. contact ratio below 20%; (b) load-separation curve of the same contact systems from infinitesimal to full contact.

4.6.4 Effect of the Hurst exponent

Up to now, there has been no consensus on how Hurst exponent affects contact behaviour between rough surfaces. Some found that κ decreases with an increasing Hurst exponent [167] while others suggested negligible dependence of κ on the Hurst exponent [71]. This

ambiguity can be related to various reasons, for example, some of them employed the non-Gaussian rough surface due to the finite size effect, or they may estimate the proportionality coefficient κ from non-linear relation between contact fraction and load. To rule out any other potential influential factors, well-resolved Gaussian surfaces were generated based on the study of TFC correction, with details listed in Table 4-5.

Table 4-5 Statistical parameters of rough surface systems with different Hurst exponents

Surf	λ_L	λ_r	λ_s	H	L	N	Δx	h_{rms}	h'_{rms}
1	4e-4	1e-4	7.81e-7	0.1	8e-4	2049	3.9e-7	9.83e-7	1.5406
2	4e-4	1e-4	7.81e-7	0.3	8e-4	2049	3.9e-7	9.99e-7	0.9660
3	4e-4	1e-4	7.81e-7	0.5	8e-4	2049	3.9e-7	1.02e-6	0.5881
4	4e-4	1e-4	7.81e-7	0.8	8e-4	2049	3.9e-7	9.62e-7	0.2069

Figure 4-16(a) demonstrates the contact area evolution against normalized load for interacting systems with these surfaces, and a distinct dependence of proportion coefficient κ on the Hurst exponent was observed. Generally, increasing H caused a decline of κ significantly. Different conclusions were drawn by Putignano *et al.* in [94] where these lines were overlapped if the load was normalized by h'_{rms}. Nevertheless, Yastrebov *et al.* [82] explained that the Hurst exponent may not have an independent impact but rather influence the contact through the Nayak's parameter, which can be derived from the cut-off wavevectors and the Hurst exponent. It is possible that with roll-off component considered in the current study, the variation of Nayak's parameters was not the same as that in [94].

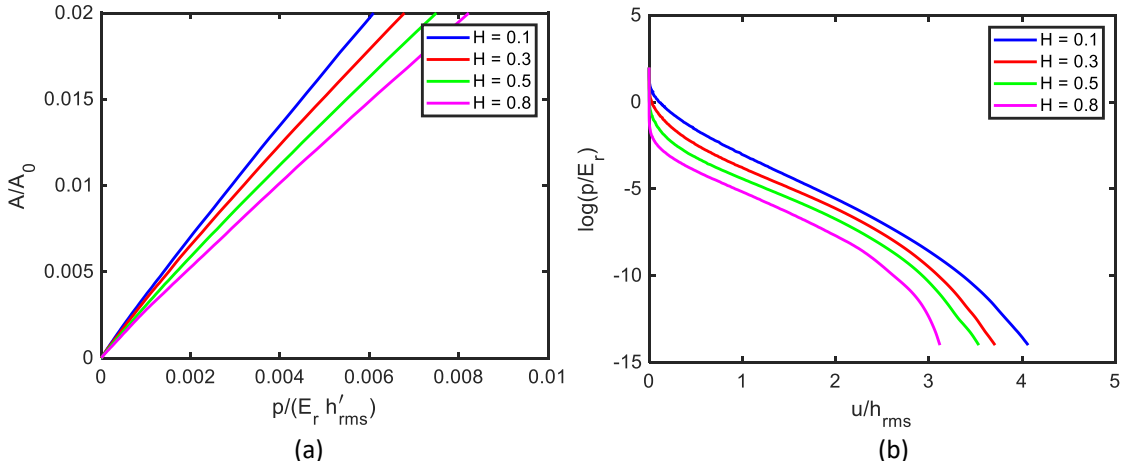

Figure 4-16 (a) Contact area evolution of four rough surface systems in Table 4.5 under low load, i.e. contact ratio below 20%; (b) load-separation curve of the same contact systems from infinitesimal to full contact.

Regarding the relation between the mean gap and the normalized load, the impact of Hurst exponent was more remarkable, shown in Figure 4-16(b). It can be observed that for a given load, an increase of Hurst exponent almost always led to a decreased separation. This agreed with what Putignano *et al.* found in [93] and most of Prodanov *et al.*'s results in [78]. Differences occurring in the low load condition was mostly likely due to the finite size effect.

To briefly conclude this section, the effect of thermodynamic correction, fractal correction and continuum correction on the contact area and the average separation have been thoroughly and systematically discussed. For self-affine rough surfaces with fractal dimension D_f= 2.2, the fractal correction plays a more substantial role in influencing the contact area than continuum and thermodynamic corrections. With regards to the mean gap, choosing $\Delta x/\lambda_s$ as large as 0.5 does not seem to introduce any artefacts. Small bandwidth in surface PSD q_s/q_r also does not lead to considerable errors. Separation at low load are more sensitive to the finite size, in other words, the Gaussianity of the surface. It is noticeable that the current study shows large q_r/q_L can significantly increase the Gaussianity of the asperity height distribution, generating more representative rough surfaces, which was simply related to the growing system size in the previous literatures.

In addition, the current study and previous research show rather different results in the evolution of contact area when surfaces with different Hurst exponent are concerned, making it rather difficult to qualitatively describe the relation. However, it is very likely that the Hurst exponent does not affect the system independently, as suggested by Yastrebov *et al.* [82].

4.7 Summary

This chapter describes in detail the rough contact mechanics between elastic solids. Statistical properties used to accurately characterize roughness are presented, as well as means of generating synthetic rough surfaces. The study focused on two aspects which are most relevant to the development of FSI model, *i.e.* how the contact area grows with the applied pressure and the nonlinear relation between separation and load. For self-affine fractal surfaces which can be described by statistical parameters, Persson's theory provides convenient equations to derive the contact area and interfacial separation. In more general cases, numerical approaches are preferable thanks to the increasing computing power and the advanced techniques. Here, a boundary element method combined with the conjugate gradient iterative scheme is elaborated and proved to give detailed information in the contact region. Finally, the effect of thermodynamic-fractal-continuum correction as well as the Hurst exponent are evaluated, and some guidelines are suggested.

5 FINITE DEFORMATION OF RUBBER-LIKE MATERIALS

5.1 Introduction

Accurate calculation of elastic deformation of solids is indispensable for reliable FSI predictions. It directly affects the lubrication film thickness hence the lubrication behaviour of the overall system. In the previous chapters, the classical theory of elasticity is used to determine the deflection of solids. Despite its widespread application, this approach is limited for linearly elastic and half-space cases, which may hold true for hard contacts but does not apply to compliant ones, where the deflection can be affected by the finite geometry of the system, and nonlinear and rate-dependent material properties. Therefore, in this chapter, a novel approach of computing the structural deformation is introduced to provide more flexibility in accounting for geometric and material nonlinearities.

To this end, the current chapter is organized as follows. First, the limitation of the elasticity theory is revealed by comparing with the FEM where the significance of finite domain deformations is presented. Afterwards, in section 5.3, a new approach, namely the reduced stiffness method (RSM), is proposed, with theoretical background and procedure explained, and validated by FEM for different types of soft materials. Specifically, section 5.4 assesses this method for linear elastic materials subjected to both static loading and sliding motion. Section 5.5 focuses on the hyper-elastic materials and the employment of RSM to approximate deformation. Finally, the rate-dependent behaviour of viscoelastic material is characterised and strategies for applying RSM are illustrated in detail in section 5.6, before conclusions are given in section 5.7.

5.2 Elasticity theory and finite element method

In the use of classical linear elasticity theory, two fundamental assumptions are made. First, the deformation has to be very small comparing to the overall dimension so that it solely

depends on the external load rather than other boundary conditions. Second, the material behaviour needs to be linearly elastic, homogenous and isotropic. However, for compliant systems, especially the wiper/windscreen problem pursed in this thesis, these assumptions are usually not valid due to the existence of strong nonlinearities.

In practical applications, nonlinear behaviour of solids takes two forms: material nonlinearity and geometric nonlinearity. For the former, the simplest form corresponds to situations in which the strain does not respond to the stress linearly, *e.g.* hyper-elasticity. More complicated situations are those where the material behaviour is also rate-dependent, *e.g.* viscoelasticity. In terms of the latter, it occurs when the deformation of a solid reaches a state for which the undeformed and deformed shape are substantially different, in which case it is no longer possible to write and solve linear strain-displacement or equilibrium equations using the undeformed geometry.

The finite element method is by far the most widely used and versatile technique for simulating deformable solids. By subdividing a structure into several elements and connecting them at nodes, FEM reformulates the problem into a system of simultaneous algebraic equations and then uses variational method to approximate a solution based on the philosophy of energy minimization, which allows it to handle very complex geometry, materials and constraints for static and dynamic analysis. Specifically, in the framework of finite element analysis (FEA), the numerical solution of a solid problem is accomplished by solving the following equations:

$$M_g\ddot{\boldsymbol{u}} + C_g\dot{\boldsymbol{u}} + K_g\boldsymbol{u} = \boldsymbol{F} \qquad \textit{Equation 5-1}$$

where M_g, C_g and K_g are the mass, damping and stiffness matrices of the full finite element (FE) model. $\ddot{\boldsymbol{u}}$, $\dot{\boldsymbol{u}}$, $\boldsymbol{u}$ are the nodal acceleration, velocity and displacement vectors, respectively. $\boldsymbol{F}$ is the nodal force vector. Note that $\ddot{\boldsymbol{u}}$, $\dot{\boldsymbol{u}}$, $\boldsymbol{u}$ and $\boldsymbol{F}$ include all the degree of freedoms (DOFs) of all the nodes in the entire FE model, and so do the global matrices M_g, C_g and K_g.

There are several commercial software packages designed to perform FEA, among which ABAQUS provides a powerful tool to solve structural problems and is used in this work. In ABAQUS, the required inputs are: geometric definition, material properties, mesh properties, boundary conditions, loading conditions, analysis types and output requests. These inputs can be either controlled interactively though a graphically-aided ABAQUS/CAE interface or provided by a tabular text file, denoted as INP file, listing detailed information. In addition, ABAQUS offers an application programming interface to models and data which can be scripted by Python. This is particularly helpful because users can access and modify the model and results while communicating with other software such as MATLAB.

Generally, in ABAQUS, a basic analysis includes the following process:

1. Create part instances.
2. Define material properties and assign them to part instances.
3. Create an assembly consisting of one or several part instances.
4. Mesh a part instance or several instances depending on requirement.
5. Define interaction and interaction properties such as normal contact and frictional contact if more than one instances are involved.
6. Generate steps based on the purpose of analysis. ABAQUS offers a variety of analysis techniques to simulate various static or dynamic loading configurations. Different analysis methods utilize specific algorithms to solve the problem. This thesis will exploit static analysis, dynamic implicit and linear perturbation. Usually during step generation, field output or history output, such as nodal forces, nodal displacement, stress, strain and so on, can be requested.
7. Define boundary conditions including loading conditions and rigid body movement.
8. Create a job for submission.

Considering the structural and material impact on all nodes, and the capability to handle various nonlinearities, FEM estimate deformations more accurately compared with the

classical elasticity theory. Figure 5-1 depicts a FE model (undeformed and deformed) of the half-cylinder shown in Chapter 3 and the comparison of deformation under Hertzian pressure obtained from FEA and the elasticity theory. As can be seen, when the deformation in the contact is comparable with the radius of the elastic body (as shown in Figure 5-1(a) and (b)), the elasticity theory tends to underestimate the deformation in the contact as the half-space assumption is no longer valid.

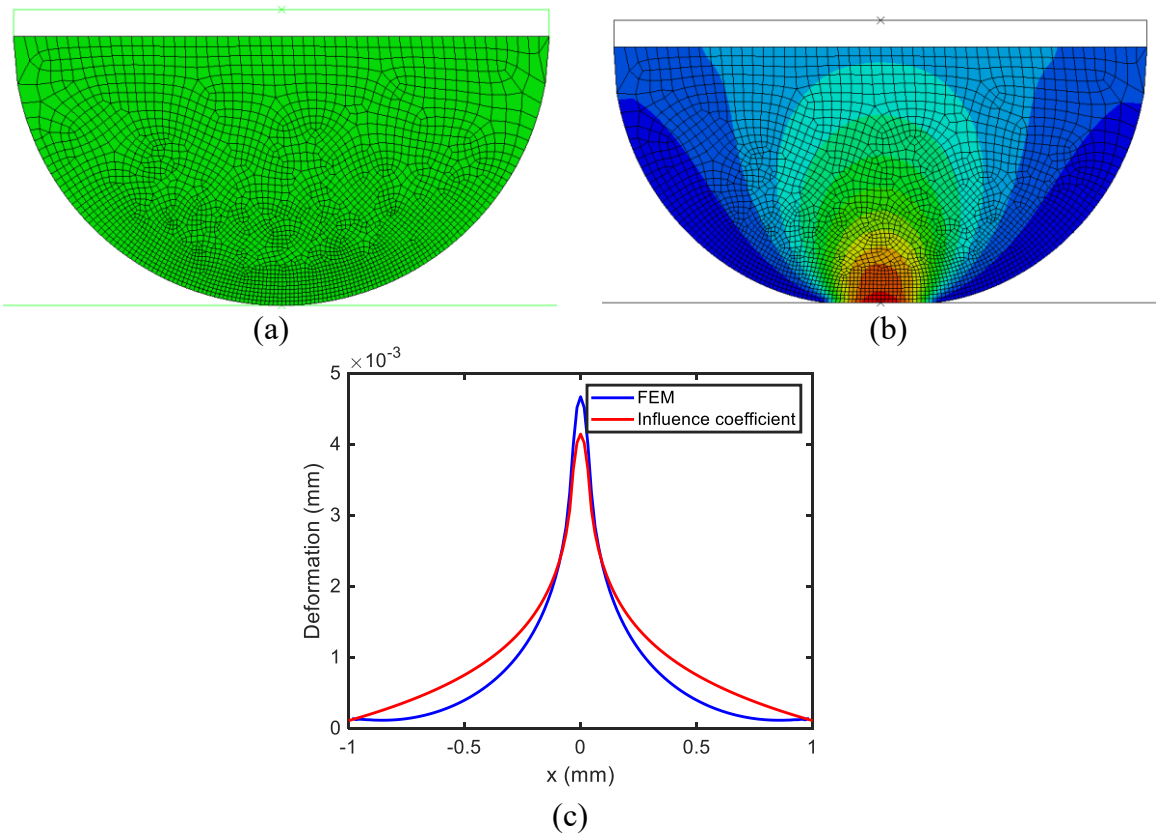

Figure 5-1 (a) A two-dimensional finite element model of the half-cylinder with mesh information; (b) The deformed configuration of the FE model shown in (a); (c) Displacement of the surface nodes obtained from finite element method and the classical elastic theory under the same load.

5.3 The reduced stiffness method

By employing a large number of equations to represent the model, the FEM is able to calculate the deformation of all nodes in the system. However, as the model complexity increases with the number of elements, the computational cost rises accordingly, which disqualifies it as the best candidate for the deformation solver in the FSI model. Since only

the deformed profiles are important, it is convenient to use substructure techniques to reduce the entire FE model to an equivalent system that retains the DOFs of nodes placed on the contact surfaces. The reduced form of the equation of motion is:

$$M_r\ddot{\boldsymbol{u}}_{\boldsymbol{r}} + C_r\dot{\boldsymbol{u}}_{\boldsymbol{r}} + K_r\boldsymbol{u}_{\boldsymbol{r}} = \boldsymbol{F}_{\boldsymbol{r}} \qquad \textit{Equation 5-2}$$

where subscript r denotes quantities of the reduced model. If considering a quasi-static state and neglecting the inertial and damping terms, the governing equation can further be simplified to:

$$K_r\boldsymbol{u}_{\boldsymbol{r}} = \boldsymbol{F}_{\boldsymbol{r}} \qquad \textit{Equation 5-3}$$

This concept of reducing DOFs in a large and complex model is often known as model reduction (or model condensation) and has the following advantages [171]. As the reduced stiffness matrix K_r only contains information of retained DOFs of selected nodes, it is much smaller and easier to handle than the global stiffness matrix K_g. Furthermore, the global matrices are sparse, while the reduced matrices are fully populated due to the inherent coupling of the DOFs in substructure systems. In addition, boundary conditions are automatically transferred from the full FE model to the reduced model as part of the condensation.

In this work, using K_r to compute deformation is denoted as the reduced stiffness method (RSM). The extraction of K_r utilizes the substructure generation step in ABAQUS, which is based on the Guyan and modal condensation methods. Substructure is a valuable feature in FEA and referred to as a collection of elements from which the internal degrees of freedom have been eliminated [171]. Retained nodes and DOFs are those that will be recognized externally at the usage level. Not only can the substructure provide computational advantages by using much smaller matrices, it also shows organizational advantages in terms of providing a systematic approach to complex analysis. To preserve ease of readability and take into consideration the fact that more complex stress strain states are treated by the software, mathematical derivations are not detailed here and can be referred to ABAQUS documentation [171, 172]. The main aim in this chapter is to exploit

this feature and develop a practical approach to calculate deformation outside ABAQUS. Hence, in the following, only the procedure of extracting K_r is described.

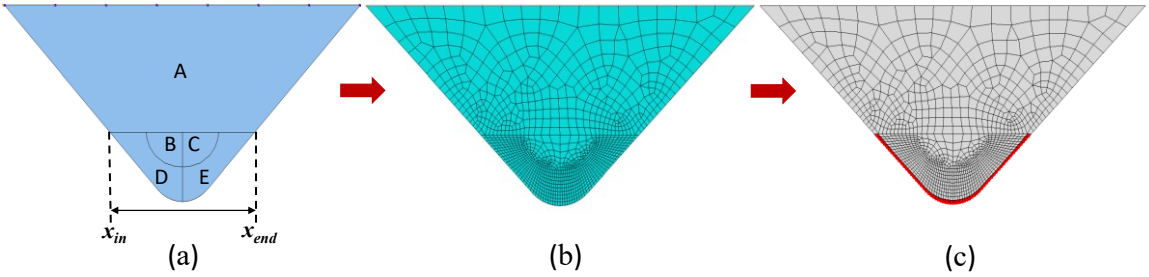

Figure 5-2 Illustration of model reduction in ABAQUS. From left to right are: the continuum model, the finite element model with mesh details and the retained nodes (substructure) highlighted in red.

Figure 5-2 shows an example of the reduction of a two-dimensional continuum model. This particular configuration is also used in the rest of this chapter as it resembles the profile of an elastomeric specimen used in our experimental set up (note that the "triangular shape" is a simplified version of the wiper blade configuration that will be discussed in Chapter 7). More details related to the experiments will be illustrated in Chapter 6.

First, a two-dimensional shell model of an elastic solid was created and partitioned into several regions, as shown in Figure 5-2(a). The reason for partition was to allow different mesh densities to be more effectively implemented in various regions of the model. The shape and size of the partition region can be arbitrary except that $[x_{in}, x_{end}]$ should be large enough to capture the most distinct deformation (*i.e.* to extend far beyond the contact area).

After assigning material properties to the solid, elements were defined and meshes were generated. In the regions which were adjacent to the contact surface, *e.g.* regions D and E, fine meshes with equally distributed nodes on the contact edges were preferred. In addition, the structural meshing technique was used to guarantee the transformation function to be consistent. In other regions, the quad-dominated element was chosen, and the mesh density can be gradually relaxed as the mesh discretisation moves further from the contact area to improve computing efficiency, as shown in Figure 5-2(b).

Boundary conditions are crucial for any type of finite element analysis, including the substructure generation. All boundary conditions to be built into the substructure matrices must be specified using a boundary condition definition. In this example, the top edge of the model was fixed in DOF 1, 2 and 6, meaning the substructure to be created were subjected to the same constraint and cannot be seen as a free body.

Finally, substructures were defined using the substructure generation step which can be invoked in a linear perturbation analysis in ABAQUS. It is suggested that in two-dimensional analysis, retaining two nodes with all translational degreed of freedom is sufficient to compute an equivalent rigid body motion of the substructure [171]. Thus, in this thesis, the 1st and 2nd degrees of freedom of nodes on the contact surface (highlighted in Figure 5-2(c)) were retained as external degrees of freedoms. The reduced stiffness matrix on these DOFs can consequently be extracted and written into a text file as an output request, which can be only defined in the INP file. By default, ABAQUS handles the node set by node labels in an ascending order, including writing output information. In practice, it is necessary to have them ordered along the x axis so that the matrix can be used directly based on the location of the surface nodes. To achieve that, a python script was programmed to reorder all the node label of the retained node and modify the INP file accordingly.

In addition to the basic procedure and general techniques mentioned above, another important property affecting K_r is the material. In a linear perturbation step, the response of a mode is defined by the linear elastic stiffness at the base state. The base state is the current state of the model at the end of the last general analysis step prior to the linear perturbation step. If the first step of an analysis is a perturbation step, the base state is determined from the initial conditions [171]. In this thesis, the reduced stiffness matrix extracted in such situation is referred as the “initial stiffness matrix”, using the notation of K_r^0. The following sections elaborates the extraction of K_r^0 from three common materials and takes the reader through the necessary validation steps.

5.4 RSM for linearly elastic material

5.4.1 RSM in static loading

Linearly elastic materials, or sometimes simply referred to as elastic materials, are probably the most commonly used for deformable solids. The stress strain curve of such material usually exhibits a linear behaviour, with the slope representing the stiffness, denoted as the elastic modulus. Given its simplicity, this material has been widely employed to simulate behaviours of a large variety of solids, from soft to hard with the elastic modulus ranging from MPa to GPa.

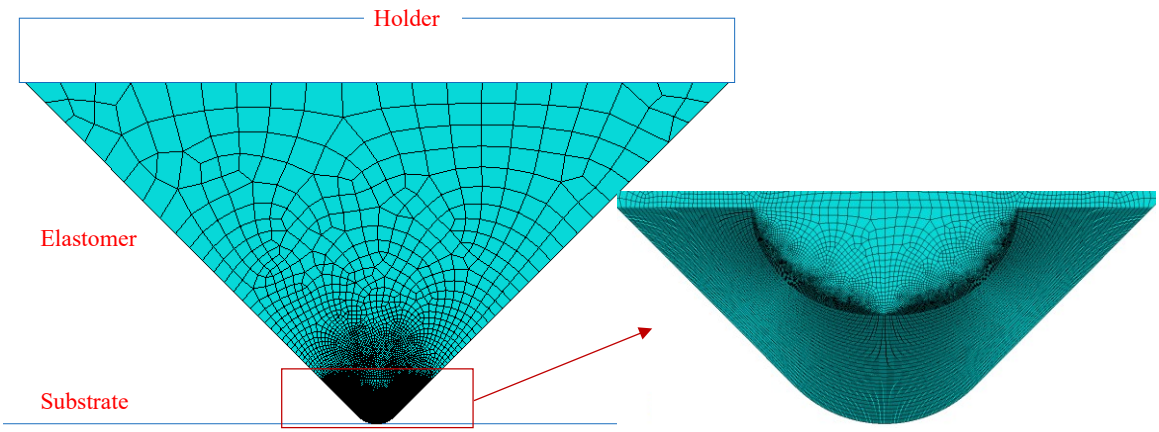

Figure 5-3 A FE contact model consisting of a rigid holder, an elastic solid and a rigid substrate, with meshing details.

To validate the RSM for linearly elastic materials, a FEA was initially performed as a benchmark. The contact model consists of three parts, a holder, an elastomer and a substrate, as shown in Figure 5-3. Given the large difference in stiffness with respect to the deformable blade (elastomer), both the holder and the plate were modelled as two-dimensional rigid parts and the elastomer was modelled as a two-dimensional elastic shell with Young's modulus 3.5 MPa and Poisson ratio 0.5 (incompressible). The geometric dimension of the elastomer is in accordance with an experimental specimen, which will be discussed in detail in Chapter 6. For the sake of efficiency, partition rules described in the

previous section were applied to the elastomer. The total width of the elastomer is 7.5 mm and the calculation domain between x_{in} and x_{end} was chosen to be 1 mm wide. 513 nodes are distributed uniformly on the contact edge (calculation domain) and bias algorithms are used everywhere else to increase the element size remotely from the contact surface. Structured mesh is employed the contact region as shown in the magnified view in Figure 5-3. Linear quadrilateral plane strain elements (CPE4) were strictly used in contact region and a small number of compatible linear triangular elements (CPE3) were used in other regions.

Interactions defined between part instances are crucial for contact models. In this case, the holder, which is always tied (or glued) to the top surface of the elastomer, was primarily used to define the loading and boundary conditions given the simplicity of the system under investigation. The substrate, on the other hand, was assumed to be in contact with the elastomer. ABAQUS documentation recommends that the stiffer body be defined as the master surface and the softer one as the slave surface [171]. Thus, the substrate and the elastomer were defined as such respectively. The tangential behaviour at the contact interface was initially defined as frictionless, while the normal contact definition used the default method, "hard" contact.

For the initial modelling attempt, the elastomer and the plate were brought into contact by applying a displacement in the z-direction to the holder in a static analysis. The nonlinear algorithm was switched on to include any possible nonlinear effect due to the large deformation. Once the analysis was completed, pre-requested outputs, *e.g.* the deformed configuration, stress field and so on, were saved automatically. A python script was then used to read selective information from the output ODB file.

The extraction of K_r^0 followed the same procedure described in section 5.3 and is not going to be repeated here. Given K_r^0 and $\boldsymbol{F}$, deformation of retained nodes can therefore be calculated. It is worth mentioning that $\boldsymbol{F}$ from the FEA results were specifically used so

that the retained nodes were under the same loading condition, leaving K_r^0 to be the only quantity to be evaluated. Results are shown in Figure 5-4, where a comparison with the full FEM solution is also shown. Notice that the rigid displacements were removed from the FEA result, whereby only elastic deflections were considered. In both vertical and lateral directions, perfectly identical deflections are observed, proving the validity of the RSM at least in this configuration and for simple material characteristics.

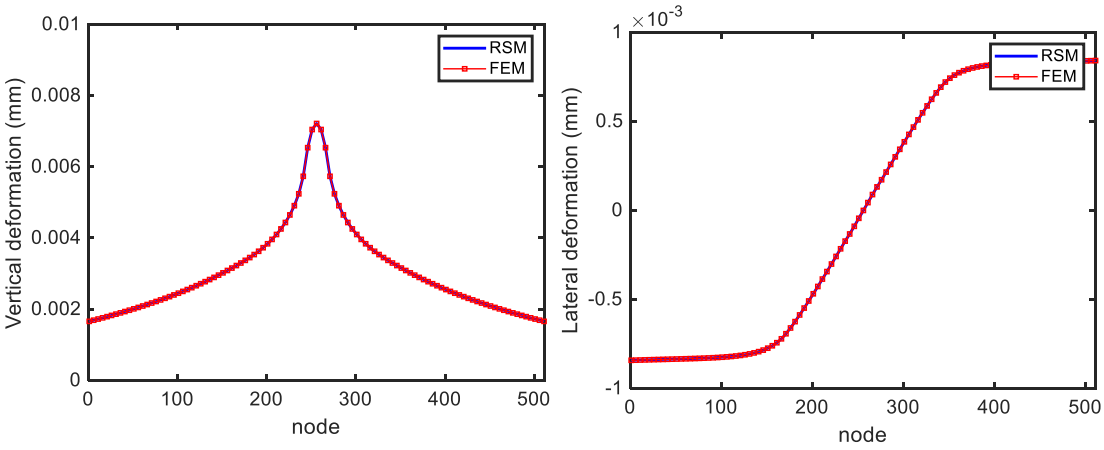

Figure 5-4 Nodal deformation of a linearly elastic solid obtained by the reduced stiffness method and the standard finite element static analysis for the vertical (left) and lateral (right) directions.

5.4.2 RSM in sliding analysis

In many engineering applications, the elastomer undergoes sliding motion, thus, it is also necessary to investigate the performance of RSM in these conditions. To this end, the previous model was modified to simulate the contact system where the elastomer slid against the plate steadily.

While material properties and meshing strategies were maintained, interaction between surfaces were considered frictional with friction coefficient 0.4 to mimic the actual sliding more closely. This should not affect the evaluation of RSM since both DOF 1 and 2 have been retained. The normal contact was defined 'hard' as in the static analysis.

The sliding motion was achieved in ABAQUS through three quasi-static steps. In the first

step, “inContact”, a small displacement was initially applied to the holder to establish the contact so that the following “loading” step can be carried out without encountering numerical difficulties. A concentrated force of 17 N/m was subsequently used to replace this displacement, rendering the elastomer to be fully in contact with the substrate, and kept the same in the final step, the “sliding” step, to maintain the contact. Whilst the external force was applied to the holder, the sliding motion was controlled by moving the substrate horizontally at a given speed. Depending on the step time, initial and minimum increment size were adjusted accordingly to achieve numerical convergence of the iterative solution process embodied in the software for solving the nonlinear problems.

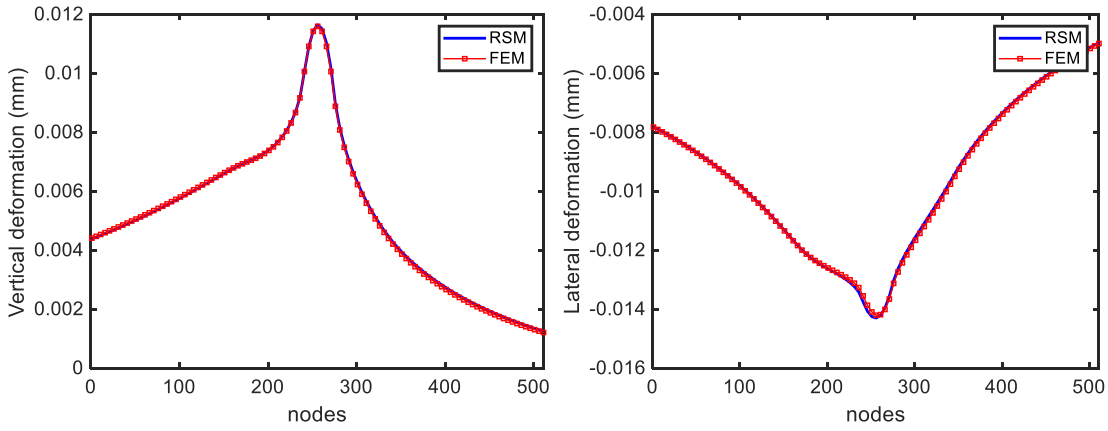

Figure 5-5 Nodal deformation of a linearly elastic solid obtained by the reduced stiffness method and the standard finite element sliding analysis in the vertical (left) and the lateral (right) directions.

Figure 5-5 shows the deformation calculated from RSM and FEM after removing the rigid displacement. Results obtained using the reduced and full numerical solution are found again to be identical, suggesting that the RSM can also be applied to sliding scenarios.

5.5 RSM for hyper-elastic material

5.5.1 Characterization of hyper-elastic materials

For rubber-like materials, the elastic stress-strain behaviour can extend to large strain (more than 200%) and exhibits strong nonlinearity, as *e.g.* shown in Figure 5-6; this is referred to as hyper-elasticity. Although the response of the material is not directly proportional to the applied load, it exhibits a Cauchy-elastic property which means that the stress at each point is determined only by the current state of deformation with respect to an arbitrary reference configuration and not the path or history of deformation.

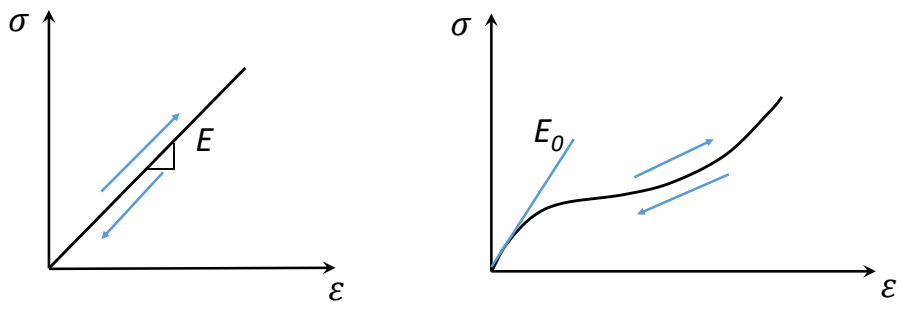

Figure 5-6 The stress strain curve of linearly elastic materials (on the left) and of hyper-elastic materials (on the right). The elastic modulus of a linearly elastic material is the gradient of the stress strain curve, while the tangent modulus of a hyper-elastic material varies with the strain state. E_0 is the initial tangent modulus and can be determined by strain energy potentials.

To model such constitutive behaviour, the strain energy potential, which defines the strain energy stored in the material per unit of reference volume (volume in the initial configuration) as a function of the strain at that point in the material, can be written in polynomial form as [171, 173] :

$$W = \sum_{i+j-1}^{N} C_{ij}(I_1 - 3)^i (I_2 - 3)^j + \sum_{i=1}^{N} \frac{1}{D_i}(J-1)^{2i}, \qquad \textit{Equation 5-4}$$

Where W is the strain energy potential, J is the elastic volume ratio, I_1 and I_2 are stretch invariants, and C_{ij} and D_i are material constants describing the shear behaviour and

compressibility of the material respectively;

Other common forms such as the Mooney-Rivlin form [174, 175], the neo-Hookean form [174] and the Yeoh form [176] are special cases of the polynomial forms and can be all defined in ABAQUS. In this thesis, a neo-Hookean model was employed based on the suggestion of our industrial collaborator, Bosch, based on their experience in characterising the behaviour of different types of rubber compounds used for wiper blades production. In this case the strain potential energy can be expressed as:

$$W = C_{10}(I_1 - 3) + \frac{1}{D_1}(J-1)^2 \qquad \textit{Equation 5-5}$$

where C_{10} and D_1 are material parameters related to the initial shear modulus G_0 and bulk modulus K_0 respectively as:

$$G_0 = 2C_{10}, \qquad \textit{Equation 5-6}$$

$$K_0 = \frac{2}{D_1}. \qquad \textit{Equation 5-7}$$

Table 5-1 lists the property coefficients of hyper-elastic models used in this study. For clarity, models which are only defined as hyper-elastic are denoted by "HE" model in this thesis. The two material selected here are those closest to the application (see Chapter 7).

Table 5-1 Hyper-elastic material properties defined by neo-Hookean model

Hyperelastic material	C_{10}	D_1
L_H material	0.5932	0.001
Y_H material	0.5767	0.001

5.5.2 RSM for hyper-elastic models

Validating the RSM for hyper-elastic materials in sliding motion followed the same procedures described in section 5.4.2 except the material of the elastomer was hyper-elastic, *e.g.* L_H material in Table 5-1 was used. Correspondingly, mesh elements needed to be

modified as hybrid, *i.e.* CPE4H, as requested for incompressible bodies in ABAQUS. With the same definition of interaction properties, boundary conditions and loading conditions, deformation were calculated and comparisons between the full FEM and the RSM were performed, as shown in Figure 5-7. Not only good agreement between the two solutions was found but results also show great similarity with those obtained for elastic materials with elastic modulus E_0. This can be explained by the fact that, given the smaller load, the elastomer was only slightly deformed from its original configuration, and the stress-strain behaviour for the case under investigation can be approximated as linear and accounted for by K_r^0, which here is simply related to the initial linear response given by E_0 in Figure 5-6.

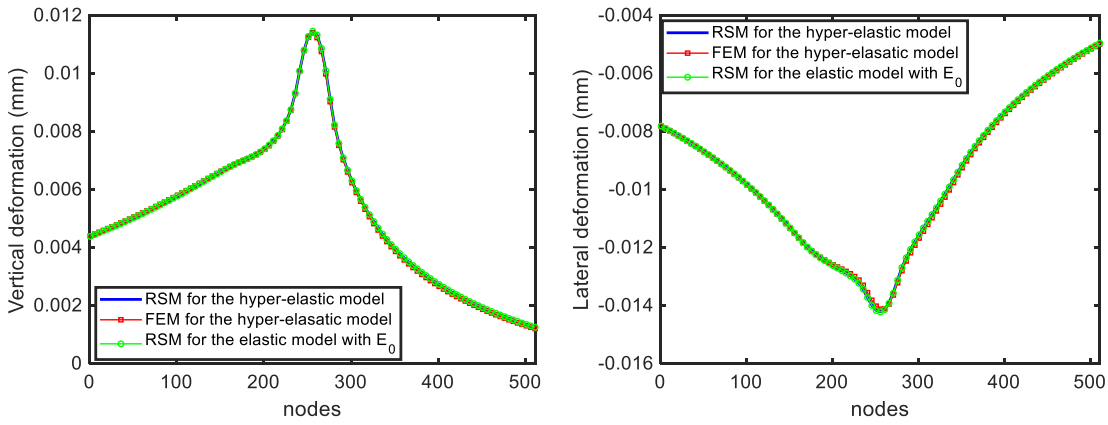

Figure 5-7 Nodal deformation of a hyper-elastic solid obtained by the reduced stiffness method and the standard finite element sliding analysis, in comparison with that of an elastic model defined by the initial tangential modulus E_0, in the vertical (left) and the lateral (right) directions.

One may argue that the RSM is only valid in this particular case given the extremely low load and the small deformation. However, the applied load is in fact quite common in wiper blade applications, and the allegedly "small" deformation still produces large contact areas which in turn invalidates the half-space assumption. Thus, the RSM can still be considered as an alternative to FEM and is more accurate than the classical elasticity theory based on the half-space approximation. In cases where large strains are expected, different reduced stiffness matrices are extracted from loaded states, which will be discussed in Chapter 7.

5.5.3 More advanced techniques

During the study of RSM, it was found that some definitions in the FE model may potentially affect the quality of the extracted stiffness matrix, *e.g.* the structural meshing and the hybrid element type. Very few studies are available in the literature that consider this issue, therefore, it is therefore worth making a full investigation to identify these factors and provide guidelines. As K_r is condensed from K_g, which reflects the response of each element, element type, mesh density, and constraint posed on elements were examined.

Element type: ABAQUS offers various element types to characterise element behaviour by its family, degree of freedom, number of nodes, formulation and integration. In this case, plane strain elements were chosen as strains in a loaded domain were considered to be function of planar coordinates alone. In addition, hybrid (mixed formulation) element were used due to the incompressibility of the material. The remaining feature was the integration method, which was why element type CEP4H and CEP4RH were employed in the RSM and compared with the FEM. Results show that both integration method obtained the same deformations, with no influence found on K_r^0, seen in Figure 5-8.

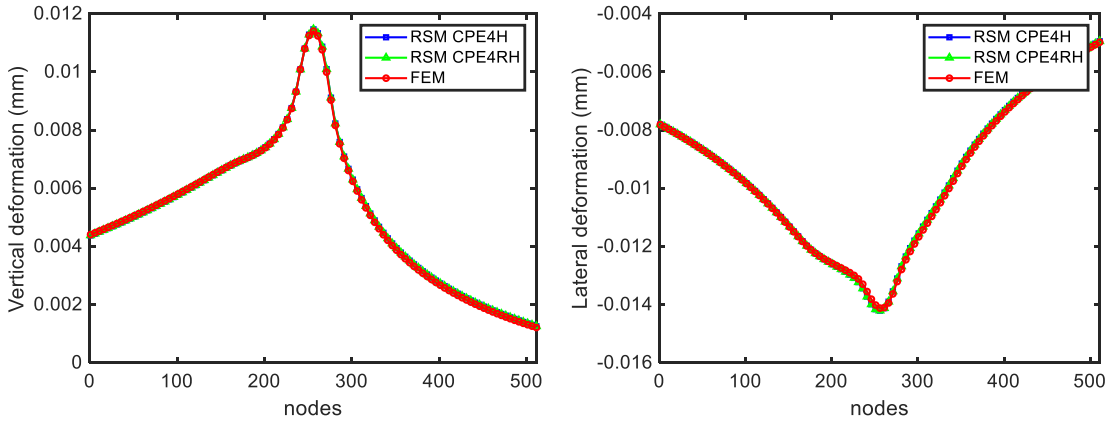

Figure 5-8 Nodal deformation of a hyper-elastic solid obtained by the reduced stiffness method and the standard finite element sliding analysis in the vertical (left) and the lateral (right) directions. Two types of elements used in RSM are CPE4H and CPE4RH.

Mesh density: The second property tested was the mesh density, where two models

containing 512 and 1024 surface elements were employed for the stiffness extraction. Although the extraction for the refined model is more time-consuming and the corresponding matrix values are generally lower, resultant deformation are the same and agreed with the FEM very well (as shown in Figure 5-9), suggesting that mesh density is somewhat irrelevant with regards to the quality of K_r^0 provided that the number of elements of the region selected for the reduction is sufficient to capture the local deformation.

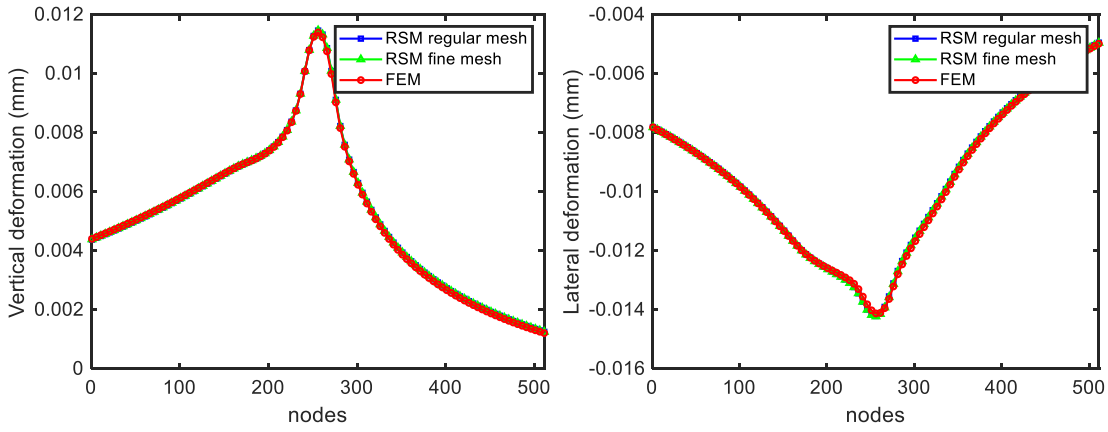

Figure 5-9 Nodal deformation of a hyper-elastic solid obtained by the reduced stiffness method and the standard finite element dynamic analysis in the vertical (left) and the lateral (right) directions. A regular fine and a very fine mesh were used in the RSM method.

Constraint: In the present model, it is possible to extract K_r with or without a defined interaction between the elastomer and the plate. Figure 5-10 shows the nodal displacement calculated from both methods and a comparison with the full FEM solution. It is worth noting that even though there was no load applied during the stiffness extraction, the reduced stiffness extracted in the presence of contact constraint takes the interaction definition as an additional boundary condition as a result of the perturbation method, which further influence the deflection significantly. This is an important step for RSM, especially the extraction of K_r^0 and should not be overlooked.

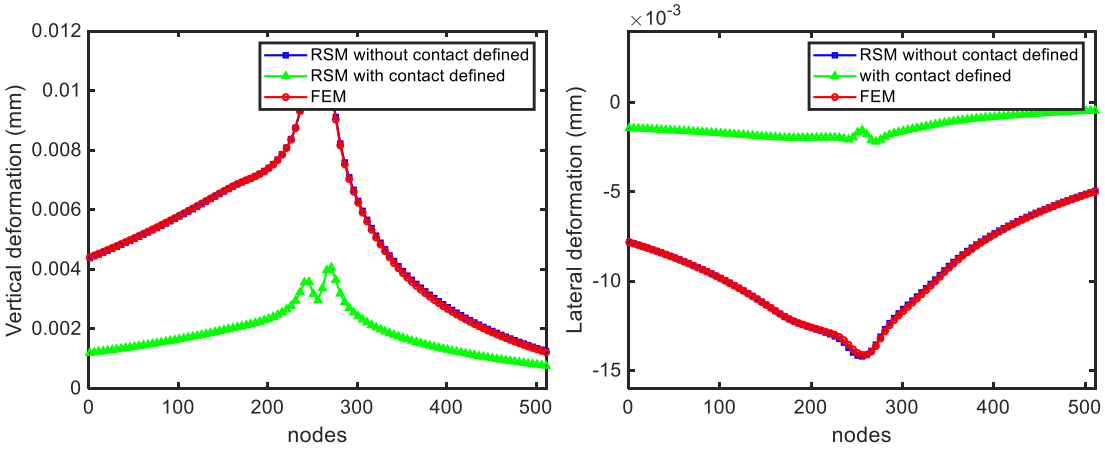

Figure 5-10 Nodal deformation of a hyper-elastic solid obtained by the reduced stiffness method and the standard finite element sliding analysis in the vertical (left) and the lateral (right) directions. Reduced stiffness matrices were extracted from models with and without interaction constraints.

5.6 RSM for viscoelastic materials

5.6.1 Characterization of viscoelastic materials

In addition to strain dependency, behaviours of elastomers are also found to be rate-dependent due to viscoelasticity. While elastic materials deform instantly with the stress and return to their original state once the stress is removed, viscous materials resist against shear flow with time in the presence of applied stresses. Viscoelastic materials possess both features and exhibit particular relations between stresses and strains when undergoing deformation. Three phenomena are usually caused by the viscoelastic behaviour, and are commonly known as the creep, the stress relaxation and the hysteresis.

Creep: is the tendency of a solid material to increase strain over time with a decreasing rate under constant stress.

Relaxation: Stress relaxation is observed as the stress decreases when the material is held at a constant strain. This is due to a re-arrangement of the material at the molecular scale.

Hysteresis: refers to the loss of energy during the loading and unloading process of the material under investigation. When viscoelastic materials have a force applied to them and then removed, it takes more energy to displace the material than it does to return the material to its original configuration. This energy difference is related to heat dissipation or molecular rearrangement within the material and is often recognized as the main source of mechanical loss and friction.

These phenomena reveal that the mechanical response of viscoelastic materials not only depend on the magnitude of the stress but also on how fast the stress is applied to or removed from the material. In the following, the mechanical description of the material behaviour is presented.

5.6.1.1 Mechanical response in time domain

The mechanical behaviour of ideally elastic solid, *e.g.* a spring, can be mathematically expressed as:

$$\sigma = E\varepsilon \qquad \textit{Equation 5-8}$$

where σ and ε are stress and strain, respectively, and E is the stiffness of the spring.

On the other hand, the behaviour of fluid obeys Newton's viscosity law and can be represented by a dashpot:

$$\sigma = \eta \cdot \frac{\partial \varepsilon}{\partial t} = \eta \cdot \dot{\varepsilon} \qquad \textit{Equation 5-9}$$

where η is the dynamic viscosity of the liquid, and $\dot{\varepsilon}$ is the strain rate.

Based on the above equations, it is possible to construct the constitutive models for linear viscoelastic material (the stress-strain behaviour at any given time is linear). In this thesis, all viscoelastic material discussed are linear unless otherwise stated.

There are two basic forms to combine the above equations to model linear viscoelastic behaviour. One is called Maxwell model [174, 177-179]where the spring and the dashpot are connected in series; this model is often used to describe creep. The other, the Kelvin-Voigt model [174, 177-179], consists of a linear spring and a viscous element in parallel, which is used to describe relaxation. In more common cases, a generalized Maxwell model, which is several Maxwell elements added by a spring in parallel, is used, seen in Figure 5-11. Since the mechanical response of the dashpot is time dependent, the viscoelastic model also predicts time-dependent behaviours. With more than one dashpot components, the generalized Maxwell model takes into account the relaxation not just at a single time, but at distribution of times.

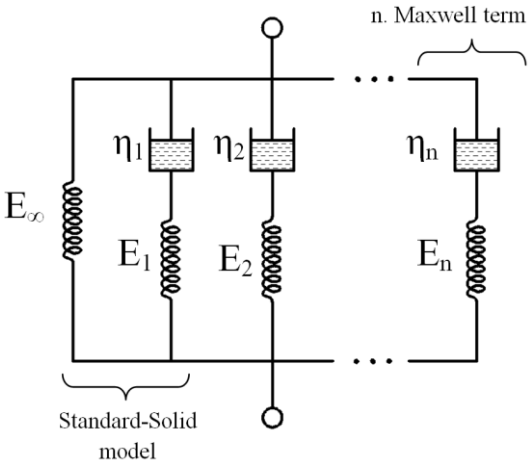

Figure 5-11 A Generalized Maxwell model.

A mathematical formulation to describe the strain behaviour of the above model is the so-called Prony series [171], by which the shear and bulk moduli can be calculated in:

$$G(t) = G_0\left(1 - \sum_{i=1}^{N} g_i\left(1 - e^{-\frac{t}{\tau_i}}\right)\right) \qquad \textit{Equation 5-10}$$

$$K(t) = K_0\left(1 - \sum_{i=1}^{N} k_i\left(1 - e^{-\frac{t}{\tau_i}}\right)\right) \qquad \textit{Equation 5-11}$$

where g_i,k_i being the i-th modulus and τ_i being the i-th relaxation time of the n-term generalized Maxwell model. Instantaneous moduli G_0 and K_0 can be also related to the instantaneous elastic moduli E_0 and υ_0:

$$G_0 = \frac{E_0}{2(1+\nu_0)} \qquad \textit{Equation 5-12}$$

$$K_0 = \frac{E_0}{3(1-2\nu_0)} \qquad \textit{Equation 5-13}$$

5.6.1.2 Mechanical response in frequency domain

The above models describe the viscoelastic behaviour in the time domain, however, it is also necessary to introduce the dynamic mechanical modulus in the frequency domain when short-term response is important.

If an elastomer is subject to cyclic load, the strain lags somewhat behind the stress due to the viscous property of the material, which can be characterised by a complex modulus E^* defined as:

$$E^* = E' + i \cdot E'' \qquad \textit{Equation 5-14}$$

where E' is the in-phase response, denoted as the storage modulus, and E'' is the out-of-phase component, denoted as loss modulus. While the storage modulus relates to the elastic behaviour of the material and defines the stiffness, the loss modulus represents the viscous part of the material and is a measure of the energy dissipated through heat. Equation 5-14 can also be expressed by the loss factor $tan(\varphi)$ a measure of the internal friction or damping of material:

$$E^* = |E^*| \cdot e^{i \cdot \varphi} \qquad \textit{Equation 5-15}$$

where $|E^*| = \sqrt{(E')^2 + (E'')^2}$ and $\tan(\varphi) = \frac{E''}{E'}$

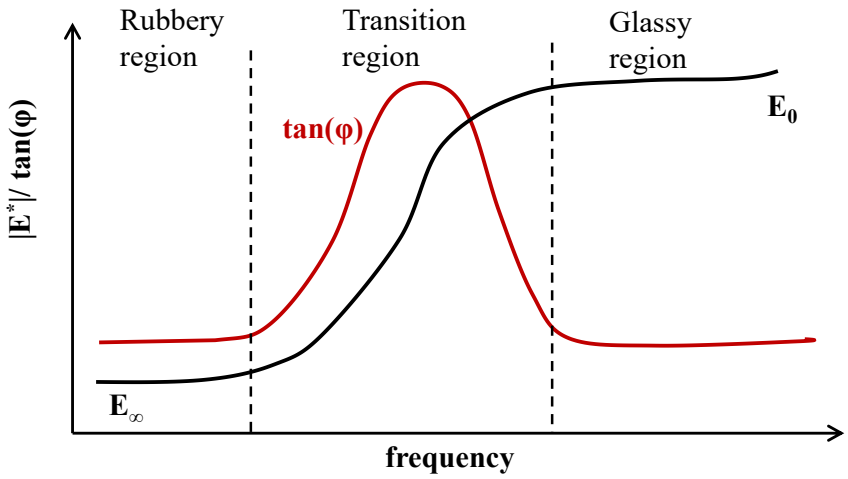

Figure 5-12 Complex modulus and loss factor vs the loading frequency.

A typical plot of the complex moduli is shown in Figure 5-12. At low frequencies, the storage modulus is small and approximately constant with $|E^*(\omega)| = E_\infty$, whereas the loss modulus is relatively lower but inclined to increase rapidly. This is referred as the "rubbery" region where material behaves elastically since the modulus varies slightly with the frequency and the viscoelastic dissipation can be neglected. At very high frequency, the material is again elastic but very stiff (brittle-like) with $|E^*(\omega)| = E_0$. This is referred as the "glassy" region where polymer chains are rigidly ordered and crystalline in nature, possessing glass-like behaviour. At intermediate frequencies, the "transition" region, the material undergoes tremendous change in stiffness and achieve its highest level of damping performance. This is depicted by the large value of loss tangent, resulting in frictional effect through energy dissipation. For more studies on the complex modulus and contact behaviours of viscoelastic materials, readers can refer to [70, 155, 180-182].

5.6.1.3 Temperature dependent behaviours

For many rubber-like materials, the mechanical behaviour is also temperature dependent. A temperature variation produces a shift of the viscoelastic frequency response along the frequency axis. Basically, increasing the temperature entails shifting to the right the viscoelastic modulus since, thanks to the thermal energy, the material tends to relax [183, 184]. For the majority of linear viscoelastic material, a simple logarithmic relation between

temperature and time can be assumed. A time-temperature shift factor can be introduced such that [185]:

$$loga_T = \frac{-K_1 \cdot (T - T_{ref})}{K_2 + (T - T_{ref})}$$

Where T is the test temperature and T_{ref} is the reference temperature. K_1 and K_2 are constants depending on the material and the temperature. The introduction of shift factors allows the modulus at one temperature to be shifted to overlap with adjacent curves at another temperature, which are particularly useful when load frequency range are limited for testing. This theory is termed as time-temperature superposition theory, or WLF theory named after Williams, Landel and Ferry [185]. In this thesis, the effect of the temperature is not considered for simplicity.

5.6.1.4 Dynamical mechanical thermal analysis

The most common way to analyse the dynamic behaviour and obtain extensive description of the material is through the dynamical-mechanical-thermal-analysis (DMTA). This is a technique to study the material response when a sample is subjected to a small deformation, either controlled by stress or strain, in a sinusoidal manner. Thanks to the time-temperature superposition effect, the viscoelastic modulus in a very broad frequency range can be gained by measuring strain and stress in a narrow frequency window at different temperatures, which is normally presented as a fitted Prony series.

5.6.2 Model viscoelastic materials in ABAQUS

Defining viscoelasticity in ABAQUS/CAE can be achieved in either time domain or frequency domain. Despite using different characterising parameters, both domains allow to use Prony series to describe the rate-dependent behaviour of viscoelastic materials. It is worth mentioning, however, the extraction of the reduced stiffness matrix directly from a

viscoelastic model requires the material to be defined in the frequency domain with frequency value specified.

Importantly, the viscoelastic model must be combined with another elastic model which prescribes the rate-independent elastic response. For small-strain applications, linear elasticity can be assigned, and for large-strain applications, a hyper-elastic material model must be employed. In addition, whether this rate-independent property is an instantaneous or a long-term response should be specified in order to determine the effective elastic moduli.

In this thesis, elastomer specimens were provided by Bosch with calibrated material properties given. Two materials, material L and material Y, were particularly considered for the present FSI model. Neo-Hookean model was adopted to describe the hyper-elastic response, as demonstrated in section 5.5.2, and Prony series of multiple terms in time domain is used to capture the viscoelastic behaviour. It is worth mentioning that although the time-independent response of material L is characterised by the same model and parameters as for material L_H, it should be distinguished from the latter which only considers the hyper-elastic property; this also applies to material Y and Y_H.

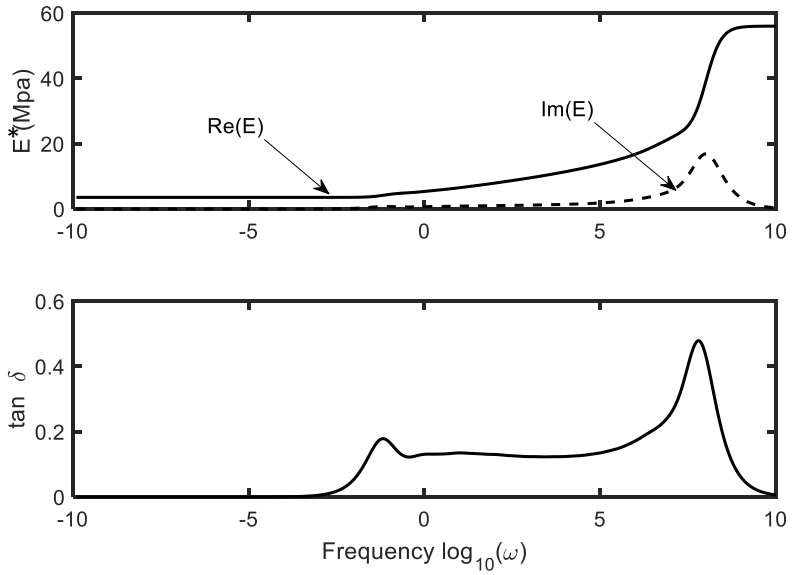

Figure 5-13 Complex modulus and loss factor of material L used in the field.

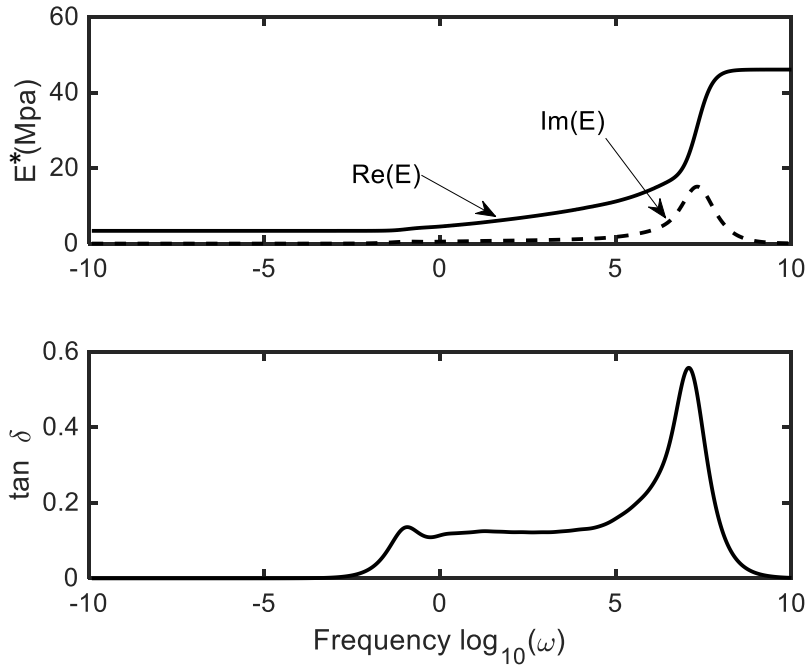

Figure 5-14 Complex modulus and loss factor of material Y used in the field.

Figure 5-13 and Figure 5-14 depict the dynamic elastic modulus and loss factor of material L and Y, respectively. Interestingly, for both materials, the transition region extends over an extremely large range of frequencies, of 10 orders of magnitude. The significant stiffening effect does not take place until the loading frequency ω is as high as 10^7 s^{-1}. A moderate energy loss occurs at $\omega=10^4$ s^{-1}, which is still much higher than the operational speed of a wiper blade. For frequencies below 10^3 s^{-1}, the elastic stiffness remains the same value of the long-term modulus E_∞, around 3~4 MPa. In the rest of this thesis, models with viscoelastic response defined are denoted as VE models.

5.6.3 RSM for VE model

By default, ABAQUS allows users to extract the initial reduced stiffness matrix of viscoelastic materials for a given frequency. It can be implemented by specifying the frequency at which the properties are evaluated for use in the substructure generation step. If no frequency is chosen, ABAQUS evaluates the stiffness at zero frequency and does not consider the stiffness contribution from frequency-domain viscoelasticity. If a frequency is

specified, only the real part of the stiffness, *i.e.* the storage modulus, is considered [171, 172]. However, there is no consensus on a specific frequency in the sliding system as it varies with many factors, such as the sliding speed, the contact area and so on. In the study of a rough contact between a rubber block and a steel plate, Carbone and Putignano [180] used a dimensionless quantity $\xi = v\tau_0/L$, where v, τ_0 and L were the actual sliding speed, the relaxation time and the length of the block, to indicate the loading speed. Nevertheless, relations between this quantity with the actual frequency have not been rigorously proven.

In this thesis, an alternative approach is proposed to bypass this ambiguity. It is suggested that the deformation of a VE model during sliding can be roughly approximated by that of a HE model under the same motion. In other words, it is possible to find an equivalent HE model of which the mechanical response gives the same deflection of a VE model. Taking the system described in section 5.4.2 as an example, two similar contact models were created for investigation. One is viscoelastic, assigned with L material, the other is hyper-elastic, with prescribed neo-Hookean coefficients C_{10}=0.8898 and D_1=0.0015. Sliding analyses were performed on both models in the same fashion as shown in section 5.4.2. Deformed configurations were conveniently read and are shown in Figure 5-15. Apparently, the HE model perfectly captures the deflection of the original VE model, indicating the possibility of using the equivalent model to reach the same state. A difference error ε_g is further introduced as:

$$\varepsilon_g = \frac{\sum_N (x_V - x_H)^2 + (y_V - y_H)^2}{N} \qquad \textit{Equation 5-16}$$

where (x_V, y_V) and (x_H, y_H) are the nodal position of the VE model and the equivalent HE model, respectively. In the present example, this value is so small (< 2e-4), confirming that identical geometries are found.

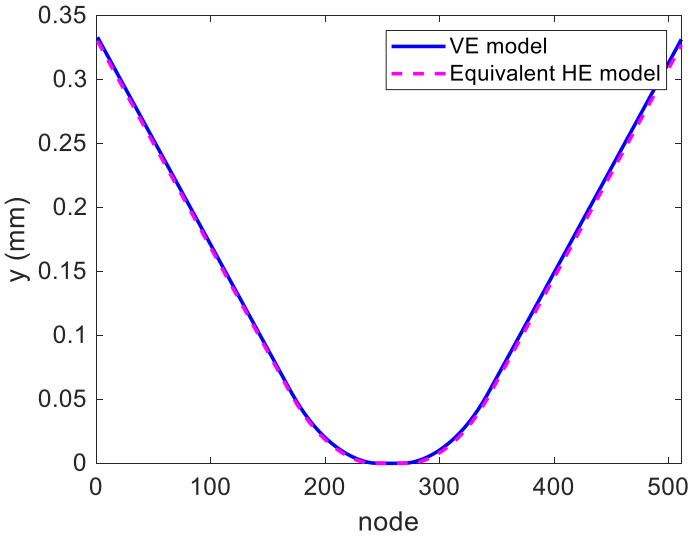

Figure 5-15 Deformed profile of a VE model and that of a HE model under the same sliding conditions.

It needs to be point out that the equivalent HE model was not randomly chosen. The material coefficients C_{10} and D_1 are actually two times of those used in the VE model. This relation is generalized as:

$$C_{10}^{eqv\ HE} = \alpha_{eqv} \cdot C_{10}^{VE} \qquad \textit{Equation 5-17}$$

$$D_{1}^{eqv\ HE} = \alpha_{eqv} \cdot D_{1}^{VE} \qquad \textit{Equation 5-18}$$

where α_{eqv} is denoted as the equivalence coefficient and employed to indicate the stiffening effect of the material due to its viscoelastic response in a sliding motion. The use of α_{eqv} depends on various conditions, including the material property, the contact mechanics, the sliding motion, *etc.*, and should be considered based on circumstances. Regardless, for contact systems under investigation in this thesis, it is almost always possible to find an equivalent HE model in the context of steady-state sliding. More details of identifying the equivalent model will be discussed in Chapter 6 and Chapter 7.

Once the equivalent HE model is determined, the initial stiffness matrix of the HE model is extracted and validated following the description in previous sections. Figure 5-16 shows

the deformation calculated from the RSM and standard FEM on both directions.

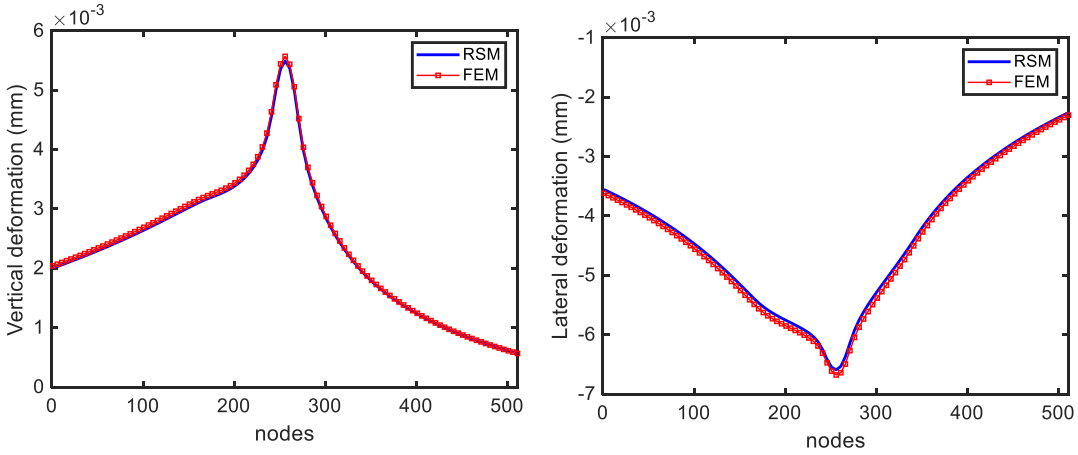

Figure 5-16 Nodal deformation of the elastomer shown in Figure 5-3 obtained by the reduced stiffness method and the standard finite element sliding analysis in the vertical (left) and the lateral (right) directions. Reduced stiffness matrix extracted from the equivalent HE model was used in RSM, and the VE model is used in FEM.

The given example reveals that the main impact of the viscoelastic property is to stiffen the material, and the possibility of replacing the VE model with an equivalent HE model is confirmed. However, it should be noted this approach is particularly suitable for the present study because that the employed material did not experience significant energy loss for the sliding speed considered and remains in the rubbery region. If different viscoelastic properties or transient motions are expected, it is likely that the strain behaviour is too complicated to be captured by an equivalent HE model, in which case other methods should be resorted.

5.7 Summary

In this chapter, the reduced stiffness method is proposed to overcome the limitation of classical elasticity theory. This new method not only accounts for the finite deformation resulted from geometric nonlinearity but can also be implemented much more efficiently than the FEM. By interacting with ABAQUS, a reduced stiffness matrix extracted from undeformed configuration of a solid is used to describe the strain behaviour in cases where

small deformation takes place. Having tested on linearly elastic and hyper-elastic materials, this approach shows great capability of calculating the deformation with a high level of accuracy compared with FEM. For viscoelastic materials, although an equivalent hyper-elastic model is required to approximate the stiffening effect and used for stiffness extraction, the resultant deformation is still in good agreement with the FEM, implying a wide application of RSM. Introducing initial stiffness matrices into FSI model for small strain problems is going to be explained in the next chapter. For more severely distorted cases such as wiper blade systems, Chapter 7 will extend the approach by extracting the reduced stiffness from a loaded state.

6 FLUID SOLID INTERACTION MODEL FOR SMALL DEFORMATIONS

6.1 Introduction

In FSI models for soft lubricated contacts, while the fluid is routinely solved by the Reynolds equation, the multi-scale asperity contacts and the nonlinear solid deformation, which are essential for the quality of the model, are more difficult to describe comprehensively and usually involve considerable computing efforts. The majority of studies in the literature focuses on one of the issues by either incorporating rough contacts under the assumption of half-space theory [2] or capturing the bulk deformation using FEM [4]. In this chapter, the FSI model described in Chapter 3 is improved considering both the study of rough contact mechanics and the RSM. Chapter 4 has shown that the contact area evolution and load-separation relations can be obtained deterministically and expressed as fitted functions, which enables the accurate calculation of asperity pressure. With regards to the finite deformation, the RSM has been proved to be effective and efficient for soft materials, as demonstrated in Chapter 5, and is going to be employed for the deformation solver.

In order to verify the new FSI model, experiments were carried out in this study. As mentioned, the current project is a continuance of a previous experiment-based project in which the actual wiper blade specimens were mainly used in the measurement of friction and film thickness. Those results will be briefly mentioned in the next chapter where the configuration of the real windscreen wipers are considered for the FSI model. In this chapter, the experiments conducted in the current project where a different type of elastomer was employed are discussed. The elastomers possess triangular cross-sections, as shown in Figure 6-1; this test configuration was designed to initially avoid the complexity of the deformations (including large rotations and changes in contact configurations, which depend on the complex shape) observed in the wiper blade system. The deformations are however large enough for the half-space approximation to fail and the test is designed to mimic the line contact experienced by a portion of the wiper blade.

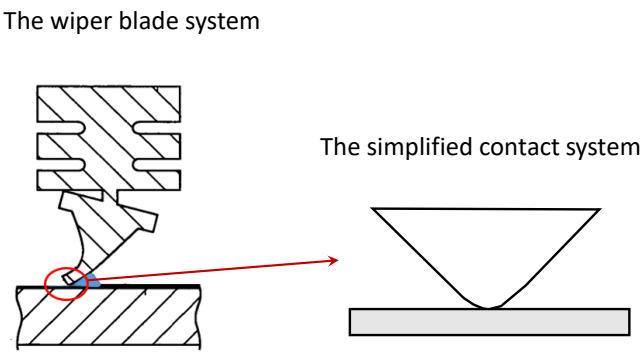

Figure 6-1 The real wiper blade system and the simplified contact system with a triangular specimen

This chapter illustrates the development of the model as well as the experimental tests carried out to validate the simulations. Starting with the description of the experimental setup and the testing conditions, the necessary pre-processing of the experimental data is performed to provide more reliable inputs for the model. Specifically, rough surfaces measured from the elastomer specimens were analysed and the contact problem is solved using the measured surfaces and a deterministic model to prepare the fitted functions in section 6.3. A FE model of the contact system is then created to identify the reduced stiffness matrix in section 6.4. After modifying the solid solver and the deformation solver based on section 6.3 and 6.4, the FSI algorithms are updated to incorporate the new solvers and tested for the experimental operation conditions. Results and comparisons with experimental findings are presented in section 6.6 before a brief summary is provided.

6.2 Experimental setup

In order to validate the proposed FSI model, experiments were carried out to measure the friction in a soft contact system by loading and sliding an elastomer against a glass plate, using a commercially available tribometer UMT2 (Universal Materials Tester) manufactured by CETR, Campbell, USA. The particular rubber specimens with triangular cross section used for the experimental part of this project were provided by the industrial partner Bosch to mimic the wiper blade system, as shown in Figure 6-2; this allows the

experiments to be carried out without dealing with issues associated with the complex deformations often observed for real wiper blades. The radius of the round tip of the elastomer is about 0.2 mm, much larger than that of a real wiper blade, which is approximately 0.01 mm. However, in the previous experiment-based project collaborated with Bosch [1], researchers have shown that the difference of geometries between a commercial wiper blade and a triangular specimen does not seem to affect the sliding friction results in lubricated conditions, although the deformations of the elastomers are quite distinct [1]. This is most likely because the actual contacts for the real wiper blades do not occur exactly at the tips but rather on the edges, which will be further discussed in Chapter 8. The material properties of the rubber were characterised and provided by our collaborator, which includes the density and the elastic properties. In this chapter, the elastomers employed were manufactured with L material as described in Chapter 5, of which the hyper-elastic property is defined by a neo-Hookean model with $C_{10} = 0.5932$, and $D_1 = 0.001$, and the viscoelastic property characterised by Prony series though fitting the DMT data (performed by Bosch). The complex modulus is already given in Figure 5-13 and will not be further discussed here. For each test, a new section of elastomer of 10 mm was used by cutting with a surgical blade. The undeformed profile of the cross section was also measured by the digital microscope manufactured by Hirox to provide a more accurate geometry input for the FSI model. The rough surface of the specimens was measured using scanning probe method which will be discussed in detail in the next section.

Glass microscope slides were used to simulate the windscreen surface in the friction measurements due to its uniformity and ease of cleaning. They also possess similar roughness to that of the windscreen of cars, making them reliable for representing the real contact system. The measurement of the glass surface was carried out using the White Light Interferometry (WLI) and the topography is shown in section 6.3. These glass slides are made of soda-lime glass (Corning Inc., USA) and are naturally hydrophilic. The dimension of the glass is 75×50 mm^2 and its thickness ranges from 0.90 to 1.10 mm.

Before starting the test, it is necessary to prepare and clean the specimens thoroughly. While the elastomer was used shortly after manufacture without any cleaning and retained their natural, hydrophobic surface characteristics, the glass was submersed in an ultrasonic bath of toluene for 20 mins followed by the same treatment with isopropanol (to remove residual of toluene), before being dried in a warm air stream.

The experimental setup is shown as in Figure 6-2. In order to realistically replicate the windscreen wiper system, all the friction measurements were operated in the pin-on-disc mode with the glass specimen attached to the rotating bed of the tribometer and a stationary elastomer located 17 mm away from the centre of the disc. During the test, the rubber specimen was fixed in its horizontal position and loaded from the above, in the meantime, the glass specimen was rotated at a series of speeds beginning from a low value and increasing in stages. It is worth pointing out that the actual speed is not uniform along the specimen and varies from inner radius to outer radius given the small radius at which the sample is held, however, this effect is less significant in the real application and not investigated in this thesis. Lubricant was fed into the contact constantly to avoid starvation by using a pump. The friction force and normal load were acquired by means of force transducers located above the elastomer holder, whereby the friction coefficients can be calculated subsequently. Similar setups were also used in the study of effect of surface hydrophobicity and the measurement of film thickness using fluorescence carried out in the previous experiment-based project [1].

Due to the limited rotating speed of the lower drive, it is difficult to obtain a full Stribeck curve using just one lubricant. To address this issue, fluids with different viscosities were utilised to span a wide range of Hersey number; similar techniques were also adopted in [122-124] where friction and lubrication were studied for compliant contacts. Table 6-1 lists the main lubricants employed in this work and their viscosities measured using a Stabinger Viscometer (Anton Paar, UK) at the test temperature 21 ˚C. Solutions are produced in distilled water and all fluids are Newtonian in the range of shear rates between

1 to 1000 s^{-1}, which satisfies the test parameters. For each lubricant, a specific speed range was chosen for the sliding test to ensure continuously increased Hersey numbers, as shown in Table 6-1, and for each lubricant-speed combination, measurements were carried out at least three times for the same pair of the elastomer and the glass slide. In order to avoid contamination, the specimens (both the elastomer and the glass) are changed when a different lubricant-speed combination is tested. After finishing all the combinations, the friction coefficients can be plotted as a function of Hersey number (the product of the viscosity and velocity), and a full Stribeck curve can be obtained. Three applied loads are considered, *i.e.* 0.10 N, 0.17 N and 0.3 N, which corresponds to the pressure averaged over the blade in the real application. The repeatability of friction results is shown and discussed in section 6.6.2, where comparisons between the experiments and numerical analyses are presented.

Table 6-1 Lubricant used in experiments with their viscosities and testing speed range.

lubricant	composition	Viscosity at 21 °C （Pa·s）	Velocity range (m/s)
Water	Demineralised water	0.000979	1.78e-5 ~ 0.178
GLY60	60 wt.% Glycerol in water	0.0108	1.78e-4 ~ 0.0534
GLY	Glycerol	0.306	0.0018 ~ 0.1780

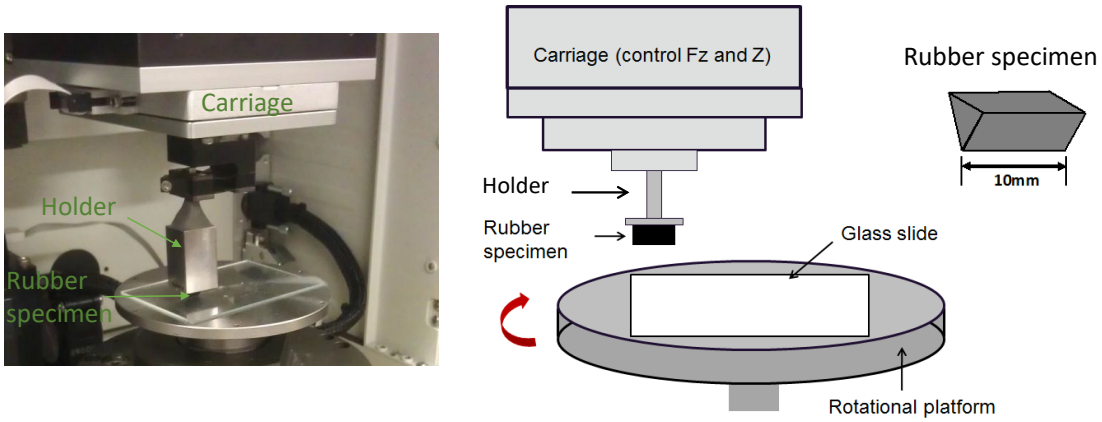

Figure 6-2 The experimental setup and the rubber specimen

6.3 Process experimental roughness data

In order to determine the contact behaviour between the elastomer and the glass using a deterministic approach, it is necessary to measure the surface topography of both specimens. Common measuring techniques that are available today generally fall into two categories, optical methods (*e.g.* optical profilometry) and scanning probing methods (*e.g.* atomic force microscopy (AFM) and stylus profilometry).

The Optical method uses either phase shifts of monochromatic light or optical coherence of white light to determine the vertical position of each pixel in an analysis region. As a non-contact method, it is preferred where materials are highly deformable, fragile (prove to damage when scanned by a probe), or chemically sensitive. Moreover, this technique is able to provide optimal topography information with nanoscale resolution achieved in both vertical and lateral directions [56]. However, the optical feature requires the surface to be reflective or at least coated with reflective materials, which is not the case for the rubber. For this reason, only the surface of an apparently smooth glass plate was measured using this method. Figure 6-3 shows the topography of the glass specimen obtained by Wyko NT9100 optical profiler, with RMS roughness around 0.5 nm.

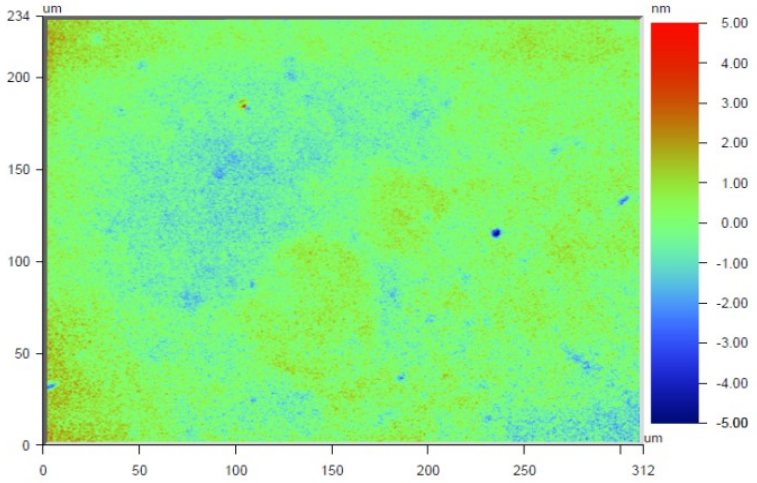

Figure 6-3 A roughness topography of the glass specimen measured by Wyko

The scanning profilometry is a technique where the measuring apparatus drags a stylus

across the surface and records its movement. Normally the stylus is designed to have a very small tip radius (typically in the order of 2~10 μm for conventional roughness measurements or at nanoscales for AFM) to keep a fine resolution, but limitation and artefacts resulting from the tip is still unavoidable and should be considered. Despite that, this procedure is extremely robust and versatile. In this study, rough surface of the elastomer specimens has been measured by both a Talysurf profiler and AFM, however, in this chapter, only the AFM measurement was used as the Talysurf profiler was found to deform the rough surface and result in inaccurate results, which will be discussed in Chapter 7.

The measurement was performed in a 450 × 450 grid with resolution 0.15 μm in the x and y directions at three different locations using contact mode. An opensource software, Gwydion, was subsequently used to process raw data, including removing the tilt and filtering out the long wavelength roughness. The average roughness h_a, the RMS roughness h_{rms} and the RMS gradient h'_{rms} are 0.55 μm, 0.68 μm and 0.5547, respectively. Figure 6-4 shows the processed roughness profile and the corresponding PSD. A fitted $C(q)$ for self-affine fractal surfaces using Equation 4.5 can be also found with q_r, q_s approximately 2e5, 3e7, respectively, and an estimated Hurst exponent $H = 0.8$.

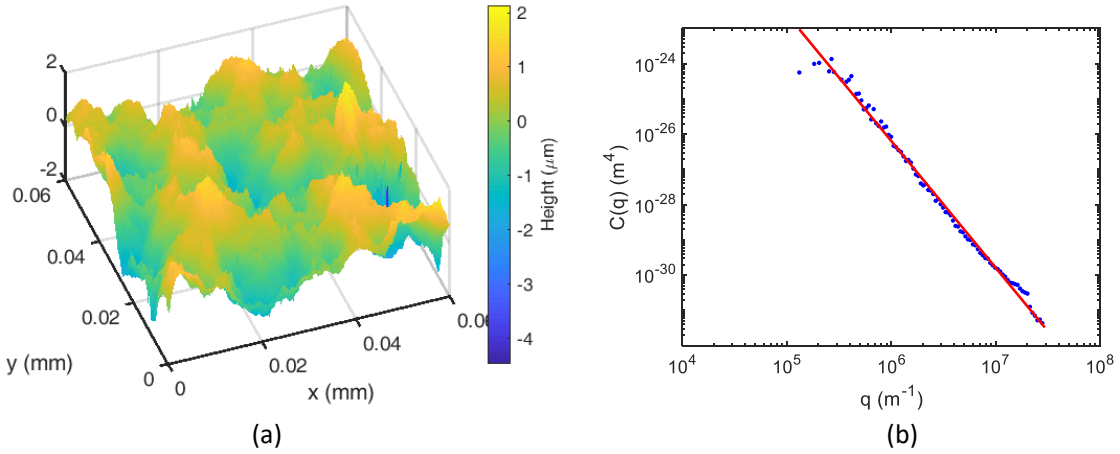

Figure 6-4 (a). Rough surface topography of the elastomer obtained from AFM after processing. (b). Power spectral density of the rough surface in (a). Red line shows a fitted C(q) with H = 0.8.

Once the rough surface is determined, the numerical method based on CG+FFT described in Chapter 3 can be applied to describe the load-separation relations and the contact area evolution. Although it is also possible to derive the statistic properties of the rough surface and apply Persson's theory, this is not considered in the present study given that the correction factors used in Persson's theory is still unclear. The deterministic method (CG+FFT) was carried out for three measured roughness profiles before an average was taken to represent the contact behaviour, as shown in Figure 6-5. The relations between the applied pressure (in its dimensionless form p/E_r) and the separation (also in its dimensionless form u/h_{rms}), and the relations between the contact area ratio A/A_0 and the pressure (p/E_r), are fitted into interpolation functions, denoted as $f_{p\text{-}u}$ (or $f_{u\text{-}p}$) and $f_{AA0\text{-}p}$, respectively, which are subsequently used for two different purposes. One is to redefine the solid solver of the FSI model such that a contact pressure can be calculated for a given separation or vice versa. The other is to prescribe the normal interaction properties in the FE model which will be discussed in section 6.4.

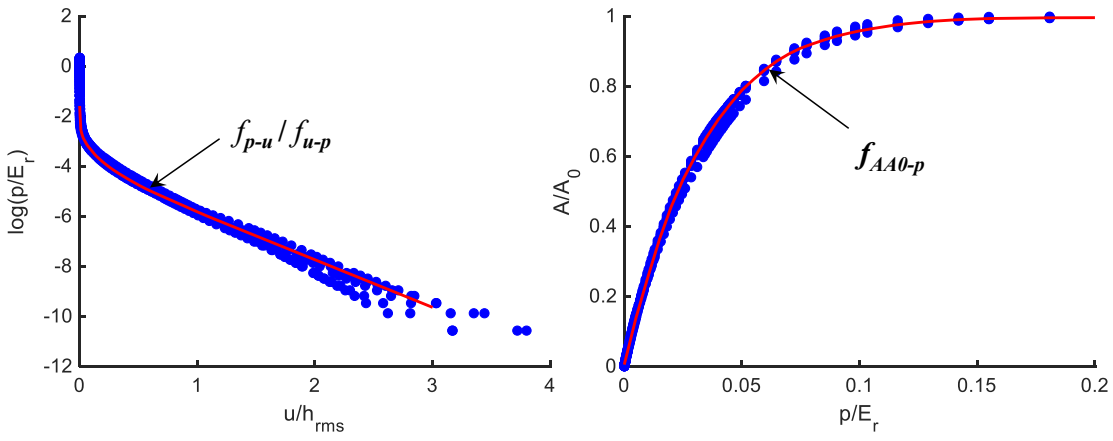

Figure 6-5 The load-separation curve (on the left) and the contact area evolution curve (on the right).

6.4 Stiffness matrix extraction

As demonstrated in Chapter 5, when a VE model undergoes small deformation, an equivalent HE model can be found to approximate the stress-strain behaviour, represented

by the initial stiffness matrix. Following this strategy, the FE model described in section 5.4.1 is re-employed here with some modifications. Firstly, based on the measurement of the geometry of the elastomer, a Python script was used to create an identical two-dimensional part and mesh it with nodes uniformly distributed along the sliding directions. This ensures a perfect match of node locations between the structural model and the fluid solver so that the same coordinate system can be introduced for applying the reduced stiffness matrix and solving the Reynolds equation. While maintaining the same partition rule and meshing strategies, the use of Python scripts allows for better control of the geometry information which is difficult to achieve through ABAQUS/CAE.

While the elastomer was assigned with material L, the interaction properties between the elastomer and the glass needs to be modified to simulate the rough contacts. ABAQUS offers several ways to define normal contact behaviour. "Hard" contacts used in the previous chapter indicates no pressure occurs unless the contact is established, with pressure-clearance (ABAQUS uses clearance to indicate separation) illustrated in Figure 6-6. However, it is known from Chapter 4 that the pressure and the separation actually follows a different relation, as shown in Figure 6-5(a). Thus, in this example, the normal contact behaviour was redefined in a tabular form where the pressure and the separation were given based on the rough contact analysis in section 6.3. The tangential behaviour was initially set to be frictional with friction coefficient 0.4.

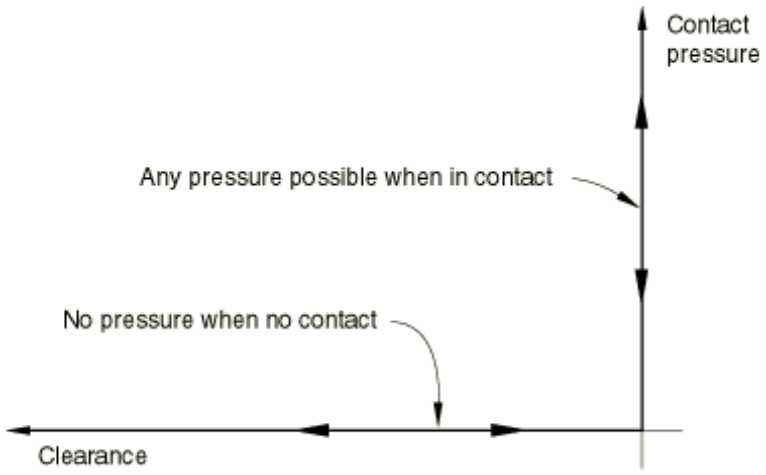

Figure 6-6 Relations between pressure and separation (clearance) for the "hard" contacts definition in ABAQUS [171].

A sliding analysis was subsequently performed to this VE model to find the equivalent HE model. Step definitions, boundary conditions and output request used the same definition as described in Chapter 5. For the example considered here the applied load is 0.017 N, and the sliding speed is 1e-3 m/s. The equivalence coefficient α_{eqv} defined in Chapter 5 was found to be 1.5 and the deformed configuration obtained from both models are presented in Figure 6-7 with the difference error ε_g calculated from Equation 5-16 being 5.6e-5.

Before rushing into the extraction of the reduced stiffness matrix, it was decided to investigate the potential variation of α_{eqv}. If α_{eqv} is a measure of the stiffening effect, then presumably it could be affected by the material property, the contact definition and the operational conditions in the FE model. As the material properties and the normal contact behaviour are determined by experiments, the influence of the friction coefficient and the speed on α_{eqv} were examined in the following.

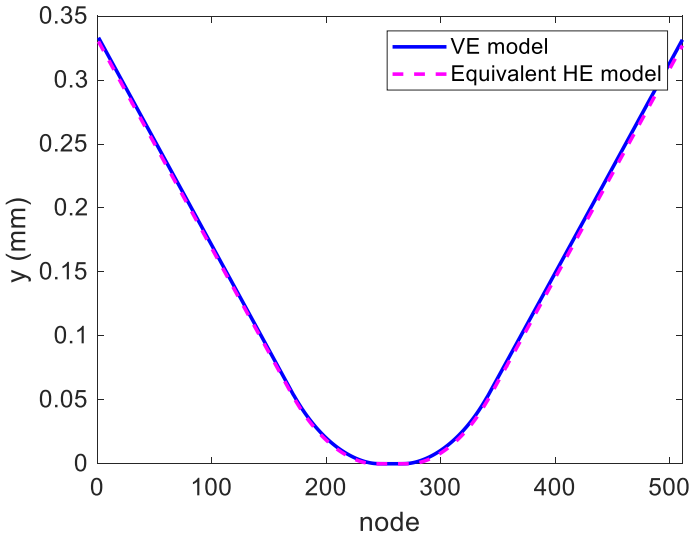

Figure 6-7 Comparison of deformed configuration between the VE+HE modal and the equivalent HE model with α_{eqv} = 1.5.

A series of finite element analysis was performed to find the equivalent HE model for three different frictional contacts and three sliding velocities (these values were defined within the range of values observed and measured for the prototypical application). Obtained α_{eqv}

values are listed in Table 6-2. Apparently, for the same contact system, *i.e.* the friction coefficient is the same, the sliding speed causes a slight increase in α_{eqv} because it is directly related the loading frequency, as discussed by Carbone and Putignano [180]. However, as the viscoelastic response of the employed material spans over a wide range of rubbery regime, as shown in Figure 5-13 in Chapter 5, it is very likely that the sliding speed is not high enough to cause significant energy loss and the stiffening effect is trivial. Additionally, the friction coefficient does not seem to change α_{eqv} at all, suggesting that the frictional force has a very minor impact on the overall deformation. This is also understandable as in the presented case the deformation mainly occurs in the vertical direction; this is similar to ball-on-disc systems, where only the perpendicular deflection is usually considered. In fact, in such cases, even if the tangential behaviour is defined as frictionless, the difference with the response obtained for various values of friction coefficients would be negligible. Nevertheless, in large strain cases, a more accurate estimate of the friction coefficient must be provided to capture the deformation more accurately, which will be shown in the next chapter.

Table 6-2 α_{eqv} values obtained for different frictional contacts and different sliding velocities.

		Sliding velocity		
		0.001 m/s	1 m/s	10 m/s
Friction coefficient	0.1	1.5	1.5	1.6
	0.4	1.5	1.5	1.6
	0.8	1.5	1.5	1.6

To further simplify the problem, the deformed profile of HE model with α_{eqv} = 1.5 was compared to that of the VE model at different frictional contact and in different sliding speed condition. The difference errors ε_g were calculated and listed in Table 6-3; nearly all values are below 0.001, implying that HE model with α_{eqv} = 1.5 can be used to approximate the original VE model very well for all test conditions considered. Therefore, the initial stiffness matrix was extracted from this equivalent HE model and prepared for future use.

Table 6-3 The difference error of the deformed profile calculated from VE+HE and the equivalent HE model with α_{eqv} = 1.5 for different frictional contacts and different sliding velocities.

		Sliding velocity		
		0.001 m/s	1 m/s	10 m/s
Friction coefficient	0.1	9.4e-5	9.4e-5	7.7e-4
	0.4	5.6e-5	5.6e-5	9.3e-4
	0.8	8.8e-5	8.8e-5	1.3e-3

6.5 The modified FSI algorithm

The overall workflow of conducting a full FSI analysis is illustrated in Figure 6-8. First, the measured rough surfaces should be processed and used to solve contact problems using the deterministic method (CG+FFT). Based on the normal contact defined by the fitting functions, $f_{p\text{-}u}$ ($f_{u\text{-}p}$), finite element analyses are performed to simulate the sliding motion (*e.g.* at 10 mm/s) of the elastomer on the glass and identify the equivalent HE model from which the initial stiffness matrix, K_r^0, is extracted (along with the calculation of the equivalent matrix, EK_{ij}^0, which will be explained in section 6.5.2). The contact definition, $f_{p\text{-}u}$ ($f_{u\text{-}p}$), the reduced stiffness matrix, K_r^0, and the undeformed configuration of the elastomer, u_0, are subsequently employed to initialise the main FSI solver in MATLAB to predict the tribological behaviour of the system.

In this section, algorithms in BML module and MEHL module are updated to incorporate $f_{p\text{-}u}$ ($f_{u\text{-}p}$) and K_r^0 (EK_{ij}^0) into the FSI model. In the EHL module, only the deformation solver needs to be modified following the same procedure discussed here for the BML module, thus will not be repeated.

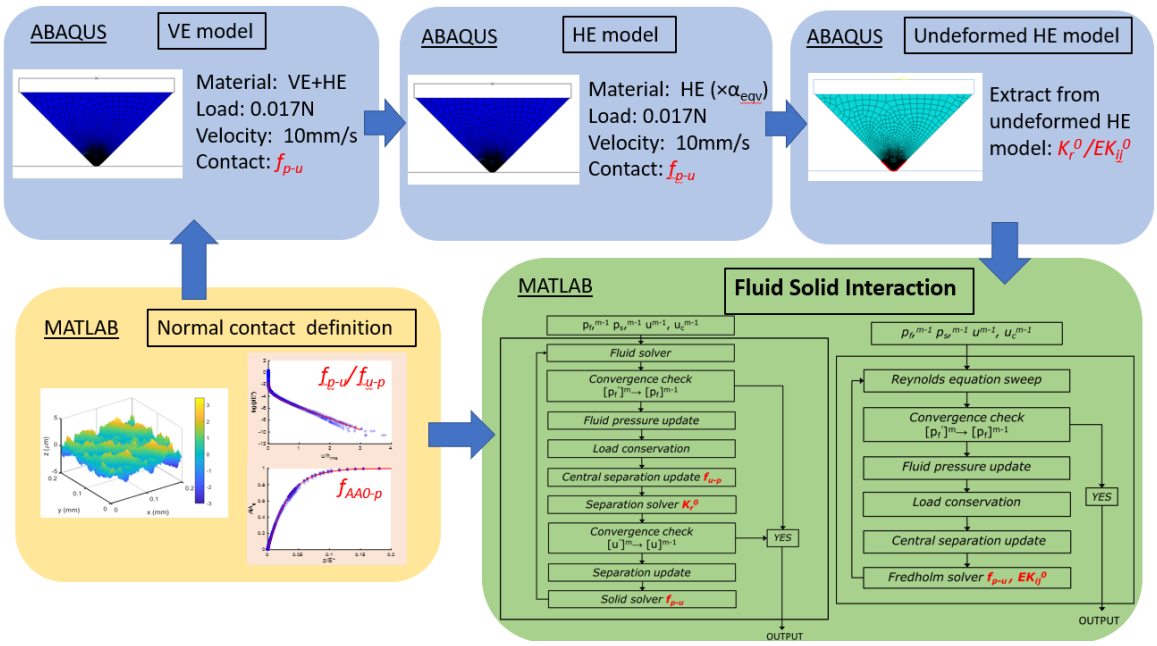

Figure 6-8 The general workflow of a full FSI analysis for small strain problems.

6.5.1 Updating the BML module

In the BML module, the fluid solver remains the same, and solvers related to the asperity contact and the deformation require to be updated. To begin with, the solid pressure solver uses the fitting function f_{p-u} instead of an analytical expression to calculate the contact pressure. For consistency, the central separation determined by the solid pressure uses the inverse version of the function f_{u-p}. Most importantly, the separation solver adopts K_r^0 to compute deformation.

To apply the RSM, the pressure field should first be converted into force vectors. Mathematically, forces on each mesh node can be acquired by integrating pressure acting on the element. In the context of the two-dimensional model, if the pressure is assumed to be uniformly distributed around the node and the linear interpolation function is adopted, the line load at node i can be obtained by:

$$\boldsymbol{F_i} = p_i \times (0.5\Delta s_1 + 0.5\Delta s_2) \cdot \boldsymbol{n_e} \qquad \textit{Equation 6-1}$$

with Δs_1 and Δs_2 being the distance between x_{i-1} and x_i and between x_i and x_{i+1} respectively, as shown in Figure 6-9.

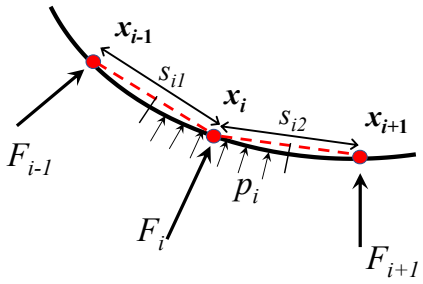

Figure 6-9 Illustration of the nodal force and external load field (pressure) of a reduced model.

By using the initial stiffness matrix K_r^0 extracted from the HE model and the force vectors $\boldsymbol{F_i}$ integrated from the total pressure, the nodal displacement can then be calculated using Equation 5-1. It should be noted that result obtained directly from the equation includes displacement in two directions and only the vertical deformation is retained.

6.5.2 Updating the MEHL module

Updating the MEHL module is not as straightforward as the BML module. While RES and CSU remain the same, the Fredholm solver, where the separation and the solid pressure are derived, has to be reorganized. The reduced stiffness matrix cannot be directly applied to calculate deformation as the separation and the solid pressure are solved iteratively in the integration equation. Recall that in Chapter 3, using the influence coefficient matrix K_{ij} to calculate the deformation involves a matrix multiplication:

$$w_i = \sum_j^n K_{ij} * p_j \qquad \textit{Equation 6-2}$$

or in the matrix form:

$$\begin{bmatrix} w_1 \\ w_2 \\ \vdots \\ w_{n-1} \\ w_n \end{bmatrix} = \begin{bmatrix} K_{11} & K_{12} & \cdots & K_{1,n-1} & K_{1n} \\ K_{21} & & & & K_{2\,n} \\ \vdots & & \ddots & & \vdots \\ K_{n-1,1} & & & & K_{n-1,n} \\ K_{n,1} & K_{n,2} & \cdots & K_{n,\,n-1} & K_{n,n} \end{bmatrix} \times \begin{bmatrix} p_1 \\ p_2 \\ \vdots \\ p_{n-1} \\ p_n \end{bmatrix} \qquad \textit{Equation 6-3}$$

Similarly, the RSM also involves a matrix multiplication, *i.e.*:

$$w'_{2n} = {K_r}^{-1}{}_{2n} \times F_{2n} \qquad \textit{Equation 6-4}$$

or in the matrix form:

$$\begin{bmatrix} w'_{1x} \\ w'_{1y} \\ \vdots \\ w'_{nx} \\ w'_{ny} \end{bmatrix} = \begin{bmatrix} K_{r_{11}} & K_{r_{12}} & \cdots & K_{r_{1,n-1}} & K_{r_{1n}} \\ K_{r_{21}} & & & & K_{r_{2n}} \\ \vdots & & \ddots & & \vdots \\ K_{r_{n-1,1}} & & & & K_{r_{n-1,n}} \\ K_{r_{n,1}} & K_{r_{n,2}} & \cdots & K_{r_{n,n-1}} & K_{r_{n,n}} \end{bmatrix} \times \begin{bmatrix} F_{1x} \\ F_{1y} \\ \vdots \\ F_{nx} \\ F_{ny} \end{bmatrix} \quad \textit{Equation 6-5}$$

If only the vertical deformation is concerned as in:

$$w_i = w'_{2i} \quad \textit{Equation 6-6}$$

then it is possible to have a matrix in an equivalent form of the influence coefficient matrix, but derived from the reduced stiffness matrix for a given geometry:

$$EK_{ij} = \frac{1}{2}(\Delta s_{j1} + \Delta s_{j2})[K_{r_{2i,2j-1}} cos(\theta_j) + K_{r_{2i,2j}} sin(\theta_j)] \quad \textit{Equation 6-7}$$

where s and θ are respectively the distance and angle between two adjacent nodes.

In the present case, EK_{ij}^0 (corresponding to K_r^0) can be obtained straight after the extraction of K_r^0 and employed in the Fredholm solver repeatedly. This also explains the importance of keeping the same coordinate system in the FE model and the main numerical model. Note that although in the same format, K_{ij} only applies for half-space cases whereas EK_{ij}^0 accounts for the stiffness of a finite body.

It is also suggested to run the FSI model from low speed to high speed in order to improve convergence. The most important variables for initialization are the fluid pressure p_f, the solid pressure p_s, the initial separation profile (or undeformed profile), u_0, and the central separation, u_c. In general, p_f can be zero and p_s can be the Hertzian pressure (expected to be a close approximation for very low values of sliding speed), although it is also possible to use the contact pressure obtained from ABAQUS as p_s. u_0 corresponds to the coordinates of all retained nodes at the undeformed state and u_c should be a reasonable guess depending on the operating conditions.

6.6 Results

6.6.1 Pressure and separation results

The improved FSI model was used to simulate the experimental system described in section 6.2. The applied load is 17N/m, and the lubricant is assumed to be iso-viscous with viscosity 1 mPa·s. The sliding speed range is from 1e-5 m/s to 5 m/s, covering all velocities used in the experiments. 513 nodes were used in the calculation, which is specifically chosen after a few mesh convergence trials, so that a relatively fine mesh can be achieved to capture the pressure smoothly while minimising computation time.

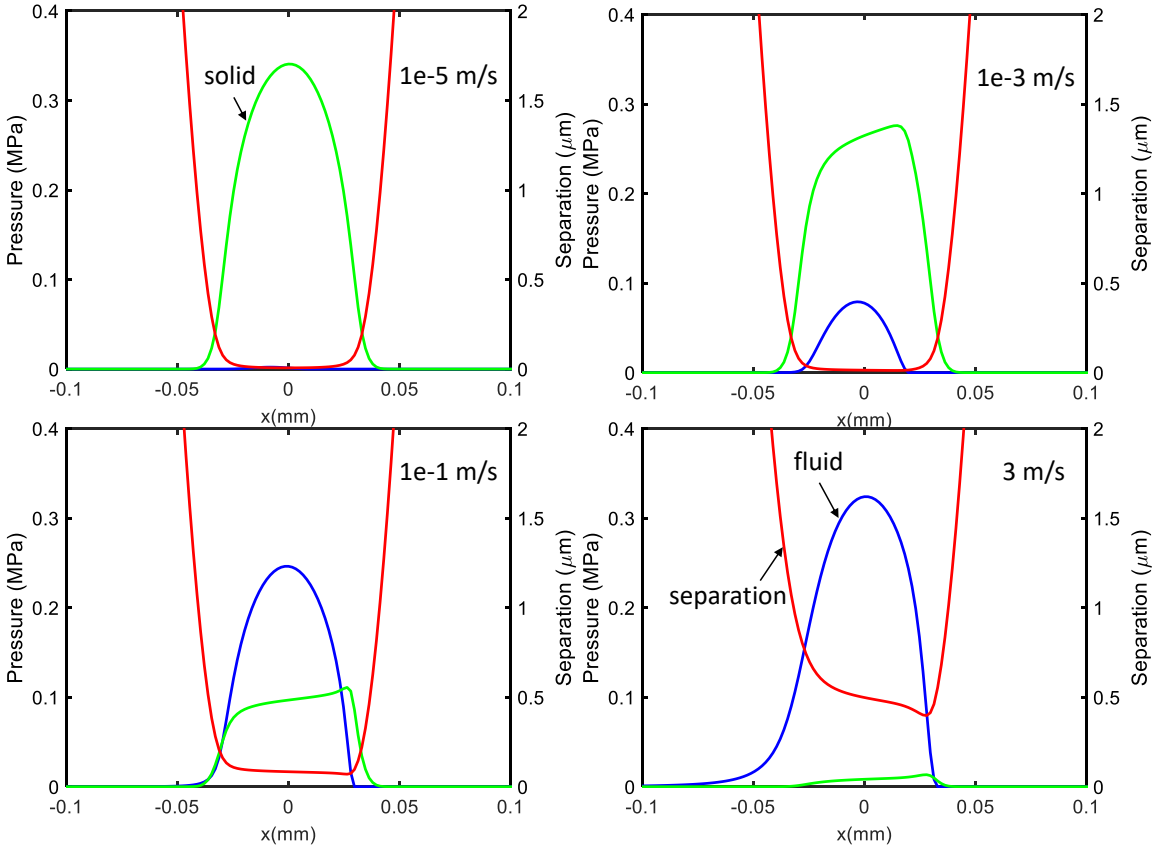

Figure 6-10 Pressure field and separation obtained from the FSI model simulating the contact system in section 6.2 at sliding speed 1e-5 m/s, 1e-3 m/s, 1e-2 m/s, 3 m/s.

Pressure distribution and separation results at four different speeds are presented in Figure 6-10. The blue line and the green line stand for fluid pressure and solid pressure,

respectively, and separation is represented by the red line. It is clear to see the build-up of fluid pressure with the increasing entrainment of lubricant. At 3 m/s, the effect of roughness on the solid pressure become insignificant and the majority of load is carried by the fluid. In addition, the overall film thickness is expected to be between 0.1 μm and 0.5 μm for the speed range from 0.1 m/s to 5 m/s, similar to what Dobre estimated in the previous experiment-based project [1].

6.6.2 Friction results

The friction calculation was also performed in a similar manner as in Chapter 3 but with some distinct differences. While the fluid shear stress, σ_f, was calculated based on separation:

$$\sigma_f = \eta \frac{v}{u(x)} + \frac{u(x)}{2} \frac{\partial p_f}{\partial x} \qquad \textit{Equation 6-8}$$

the solid shear stress, σ_s, was acquired by considering the solid pressure and the real contact area in:

$$\sigma_s = \sigma_1 \frac{A}{A_0} \qquad \textit{Equation 6-9}$$

which is different from Chapter 3 where an approximated formula was used. The real contact area ratio A/A_0, can be obtained from the solid pressure through the fitting function $f_{AA0\text{-}p}$ derived in section 6.3.

While the fluid shear stress plays a more important role in the mixed lubrication and EHL regime, boundary friction is mostly determined by the solid shear stress, *i.e.* shear strength of the boundary layer σ_1 and the real contact area A/A_0. In the previous friction calculations in Chapter 3, σ_1 was assumed to be constant. As the ratio A/A_0 did not change much at low speeds, friction appeared to plateau in the boundary lubrication regime.

However, in the experiments, a clear increase in boundary friction was observed, as shown in Figure 6-11, where the friction measurements of the repeatable tests are presented as grey dots. This indicates that the shear strength may not be always independent of sliding velocity or pressure. Supporting evidence can be found in [186] which stated that σ_1 would vary with speed, molecular weight and so on, and should be only determined by experiments (this is unless much more detailed molecular dynamics and multi-scale methods are invoked to produce a better estimation [54]). In this chapter, the adhesion is neglected for simplicity, thus σ_1 ought to be varied in order to capture the growth of friction. This was conducted by fitting numerical results to the friction measurement for the estimation of σ_1.

In the present case, for example, a constant σ_1 was found to give the best prediction based on the experimental results in the mixed lubrication and EHL regime. Then, it was gradually reduced with respect to the decreasing speed so that the predicted friction follows the general trend of measured ones. The resultant σ_1 and the corresponding friction coefficients (including solid friction component and the fluid friction component) are given in Table 6-4. The Stribeck curves obtained experimentally and numerically are plotted in Figure 6-11 where a good agreement was observed between the experimental friction and the numerical prediction in the mixed lubrication and EHL regimes with σ_1 equal to $0.1\times E$. On the contrary, determining σ_1 for the boundary friction was more difficult as experimental measurement results are less repeatable and spread from 0.4 to 0.8 at low speeds. However, this is not surprising as the contact behaviour in this regimes can be sensitive to a variety of factors, including the change of surface properties, the amount of water, the stability of the testing rig, and most importantly, the local interaction between asperities. To give the best practice, manual adjustment was performed carefully for each speed test to assess σ_1. The exact nature of the variation of this value with speed remains to be investigated and requires more in-depth studies, and this will be discussed in Chapter 8. Figure 6-12 shows the predicted friction and the contact ratio A/A_0 as functions of the Hersey number. When the friction is minimal at around 5 m/s, the relative contact area is reduced from 0.75 in the boundary lubrication regime to only 0.001.

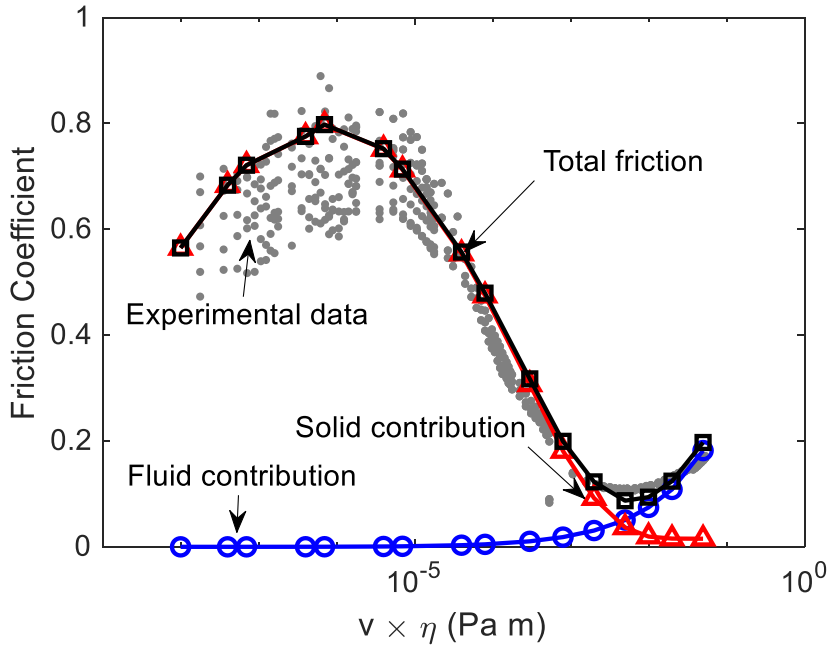

Figure 6-11 Stribeck curves obtained from experimental measurement (scattered) and the numerical estimation from the FSI model for the contact system in section 6.2 under load 17 N/m.

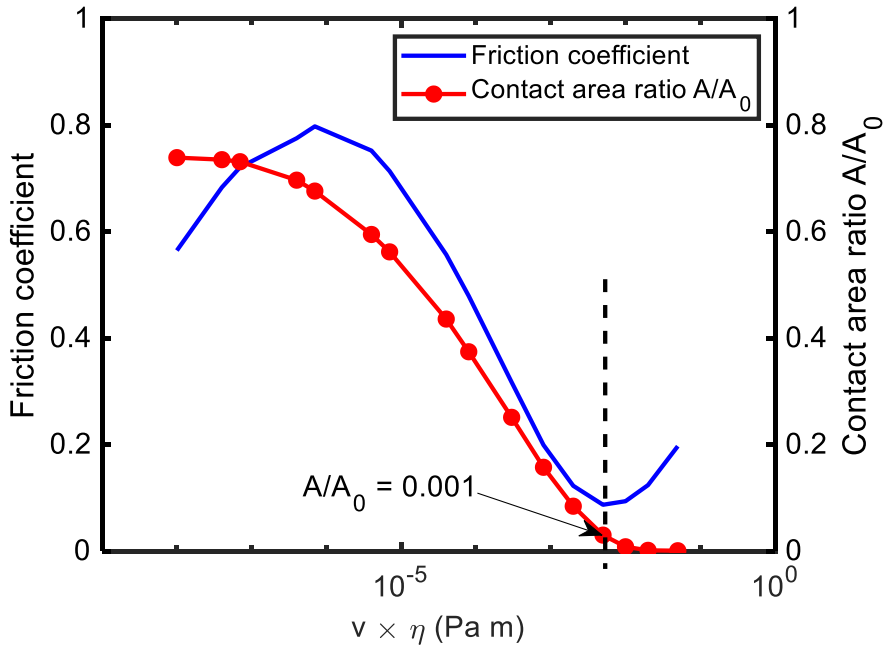

Figure 6-12 The friction coefficient and the contact area ratio A/A0 as functions of the Hersey number for the same system as Figure 6-11.

Table 6-4 Variation of σ_1 with respect to Hersey number and calculated friction coefficient including fluid and solid components.

v×η (m×mPa)	σ_1	μ_{fluid}	μ_{solid}	μ_{total}
1e-5	0.07×E	3.89e-6	0.5648	0.5648
4e-5	0.085×E	1.52e-5	0.6834	0.6834
7e-5	0.09×E	2.60e-5	0.7211	0.7211
4e-4	0.1×E	1.19e-4	0.7755	0.7756
7e-4	0.105×E	1.86e-4	0.7977	0.7979
4e-3	0.11×E	6.63e-4	0.7518	0.7524
7e-3	0.11×E	9.74e-4	0.7128	0.7138
4e-2	0.11×E	0.0031	0.5541	0.5571
8e-2	0.11×E	0.0047	0.4747	0.4794
0.3	0.11×E	0.0104	0.3070	0.3174
0.8	0.11×E	0.0184	0.1810	0.1994
2	0.11×E	0.0309	0.0921	0.1228
5	0.11×E	0.0506	0.0367	0.0872
10	0.11×E	0.0745	0.0194	0.0939
20	0.11×E	0.1085	0.0156	0.1241
50	0.11×E	0.1819	0.0153	0.1972

6.6.3 Effect of load

Other load conditions, *i.e.* 10 N/m and 30 N/m, were also tested in experiments and simulation. Accordingly, σ_1 was evaluated to obtain the best performance, as presented in Figure 6-13 and Figure 6-14. For all load considered, constant σ_1 was found to be perfectly capable of predicting the friction in the mixed lubrication and EHL regimes. This confirms that when the system enters the mixed lubrication regime, the contribution of asperity contact to friction mainly depends on the contact area, rather than the interfacial bonds between asperities.

Figure 6-15 depicts the variation of σ_1 at three loading conditions. It appears that in the mixed lubrication and EHL regimes, σ_1 rises slightly with the increase of load, with values around $0.1\times E$. This could be linked to the increased resistance to flow between asperities,

which involves the calculation the flow factors and is not included in the present model. The quantitative relation between the increasing σ_1 and the growing boundary friction still remains unclear and requires more test conditions and better control of the repeatability.

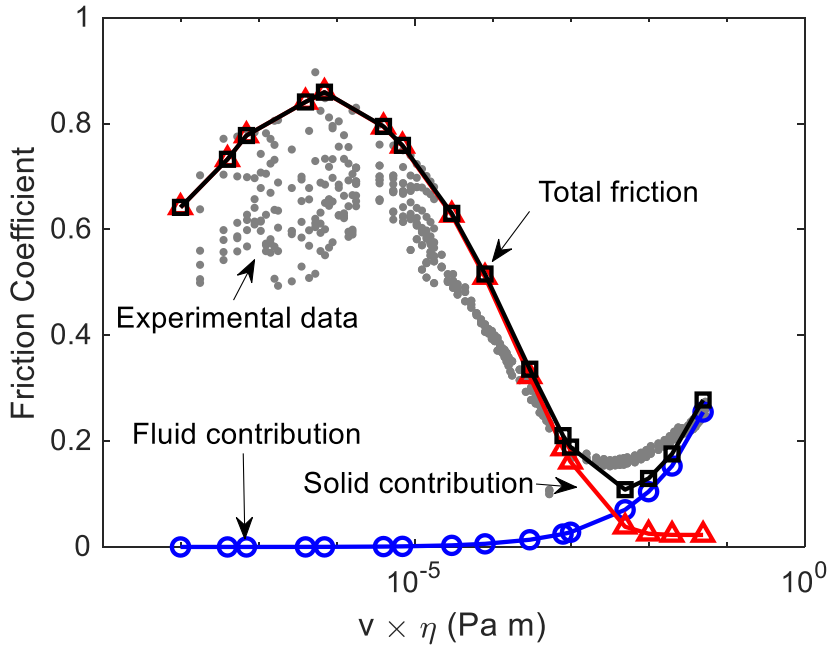

Figure 6-13 Stribeck curves obtained from experimental measurement (scattered) and the numerical estimation from the FSI model for the contact system in section 6.2 under load 10 N/m.

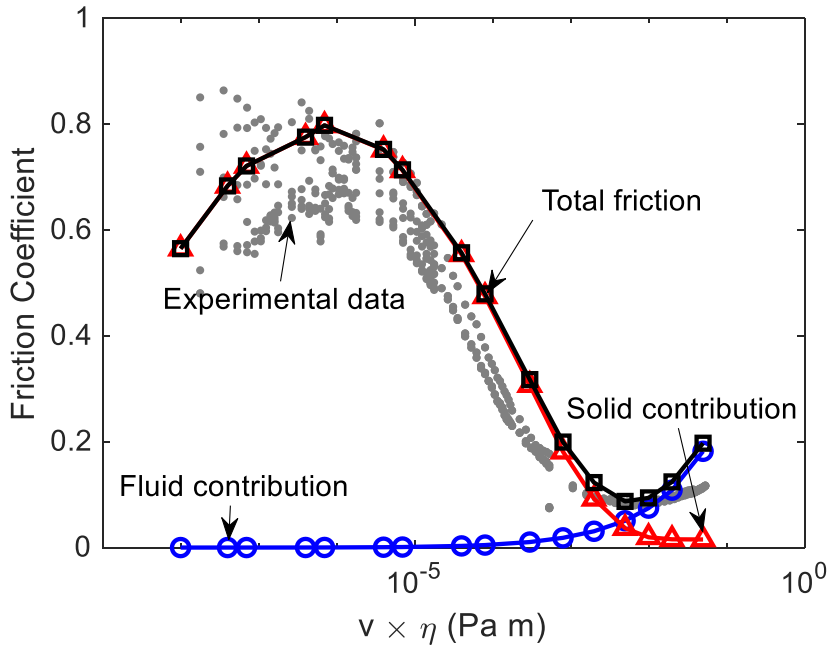

Figure 6-14 Stribeck curves obtained from experimental measurement (scattered) and the numerical estimation from the FSI model for the contact system in section 6.2 under load 30 N/m.

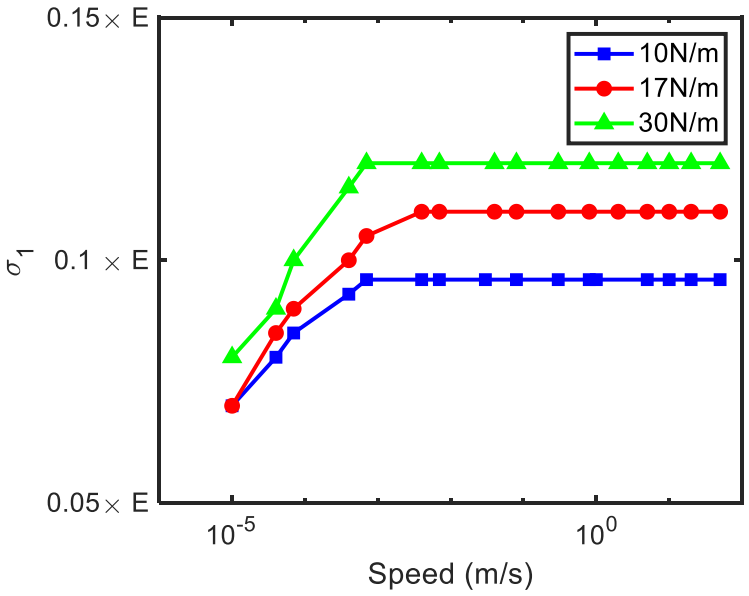

Figure 6-15 Variation of σ_1 with sliding velocity and load.

6.7 Summary

To briefly summarize, this chapter describes a modified FSI model which considers both the contact behaviour between rough surfaces and the finite deformation of viscoelastic materials in small strain situations. Based on the investigation in Chapter 4 and Chapter 5, fitted functions $f_{p\text{-}u}$ (or $f_{u\text{-}p}$) and initial stiffness matrices K_r^0 are used to determine the solid pressure and the elastic deflection. Specifically, measured rough surfaces are processed and employed to solve contact problems by adopting the CG+FFT method. FEA is performed to simulate the contact systems and find the equivalent HE model from which the reduced stiffness matrix is extracted and used to calculate deformation.

Experiments were carried out to obtain the Stribeck curves between an elastomer and a glass plate. The measured friction was used to calibrate the shear strength σ_1. It is found that the modified FSI model can predict the friction in mixed lubrication and EHL regime quite well with a constant σ_1 equal to $0.1\times E$. Given the poor repeatability in the boundary friction measurement and the limited number of tests, it was difficult to correlate the shear strength with the operating conditions in a systematic way. However, the growth of

boundary friction was observed for all tests, indicating that σ_1 is expected to experience an increase as well.

7 FLUID SOLID INTERACTION MODEL FOR LARGE DEFORMATIONS

7.1 Introduction

In Chapter 6, a modified FSI model was described to solve lubricated problems in compliant contacts when localized deformations occur in the contacting regions. The initial stiffness matrix was employed to calculate the elastic deformation of solids from its original configuration. If a viscoelastic model is considered, the equivalent hyper-elastic model is to be found and used to extract the tangent stiffness. This method is suitable for common contact systems, such as the typical cylinder-on-disc, ball-on-disc, door seals and so on. However, in many engineering applications, windscreen wipers in particular, the rubber experiences a more complex loading process in the operational conditions, with the overall geometry of the component being severely affected and distorted from its original undeformed shape. In this case, the initial tangent modulus becomes insufficient to describe the nonlinear strain behaviour. Therefore, in this chapter, the RSM is extended to account for large and complex deformations by using the reduced stiffness matrix of a deformed configuration instead. Correspondingly, a more advanced FSI model based on the modification of the deformation solver is developed and discussed. The approach was specifically developed for targeting FSI problems in wiper/glass contacts, but it can be adapted to other mechanical systems.

It is worth mentioning that due to the limited time and resources, experiments on real wiper blade systems were not carried out in this study. As the main goal is to develop and improve the FSI model, experimental data used for comparison, *e.g.* the friction and film thickness, are obtained from the previous experiment-based project [1]. Important inputs for the model, such as the material properties of the wiper blade, the geometry of the specimen and the rough surface properties, are consistent with those used in the experiments and discussed in this chapter, however, the details of the setup and procedures will not be elaborated here and can be referred to [1].

This chapter is organized in the following way. First, the strategy of applying RSM to large

strain and deformation cases is explained and validated using a simple model, followed by a more general implementation on a wiper blade model to which the actual sliding motion is simulated. Subsequently, in section 7.3, the FSI algorithm described in Chapter 6 is further updated with the BML and MEHL modules modified to incorporate the new RSM into the deformation solver. Pressure and separation results are presented in section 7.4 as well as the predicted friction and film thickness, which leads to the discussion and evaluation of various quantities that may affect the performance of the proposed model. Finally, a complete summary is given section 7.6.

7.2 Reduced stiffness method for large and complex deformations

7.2.1 Validation of the reduced stiffness method for large and complex deformations

Recall the contact model in Chapter 6, if the triangular specimen is replaced by a windscreen wiper in the same sliding analysis, significant deflections can be clearly visualised, especially in the lower part of the wiper (usually named as the wiper lip), as shown in Figure 7-1. Such a strong nonlinear behavior is due to a combination of rough surface interaction, the material property and the unique geometry of the system and cannot be simply characterised by an initial stiffness matrix.

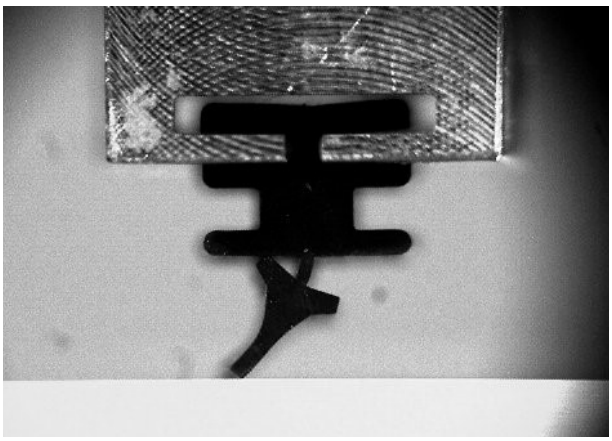

Figure 7-1 A deformed profile of a sliding wiper blade

From the description of the implicit dynamic analysis from ABAQUS documentation [171], a deformed state such as in Figure 7-2(c) is determined by adjusting the increment size and load as the response is gradually developed in the step. Following this idea, it is possible to view the deforming history as a sequence of linear reactions until a convergent solution is achieved. Figure 7-2(d-f) schematically shows the deforming processing of the wiper lip. Evidently, it would be impractical to use the stiffness at the undeformed stage A to capture the solid behaviour during the whole time as the response is nonlinear. However, it could be hypothesized that the material behaves somewhat linearly from stage B to stage C if the two configurations are indeed similar in terms of part of the blade interacting with the glass and overall contact region. Thus, the nodal displacement from stage B to stage C (ignoring the rigid movement), Δw, can be obtained from the reduced stiffness matrix extracted at the deformed stage B, K_r^d, and the load increment between the stages, ΔF, by:

$$\Delta w = {K_r^d}^{-1} \times \Delta F \qquad \textit{Equation 7-1}$$

In this thesis, K_r^d, the reduced stiffness matrix extracted at a deformed state, is referred to as the deformed stiffness matrix, and this notion of linearization using Equation 7-1 forms the basis of RSM for large deformation.

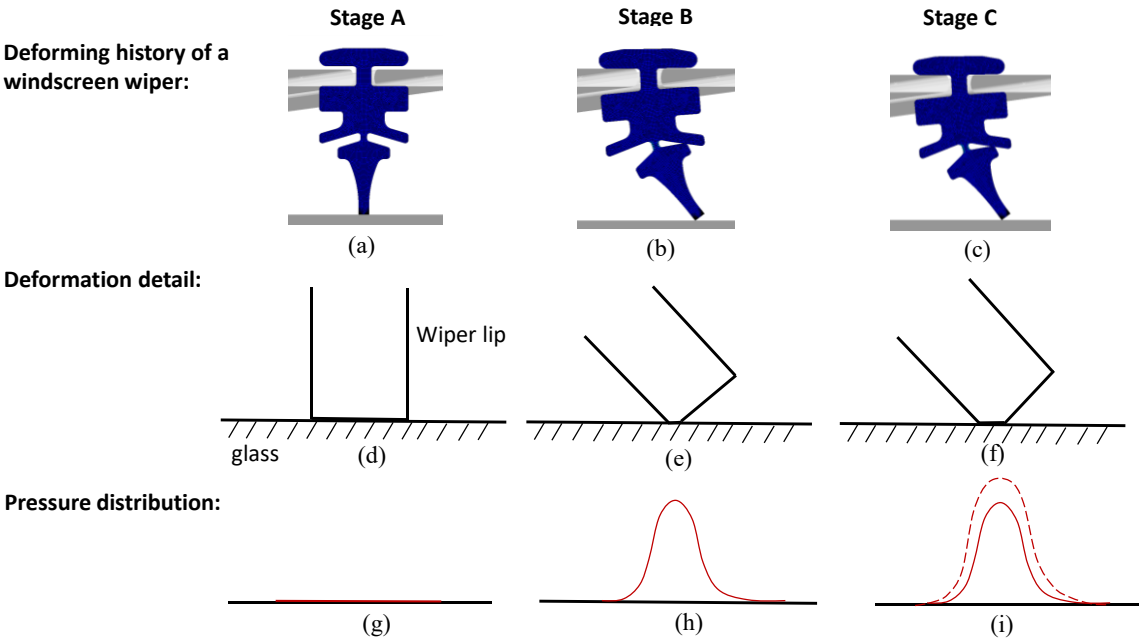

Figure 7-2 Illustration of the simulation strategy for large strain problems

In the early attempts to verify this hypothesis, a wiper lip model was employed for simplicity, as shown in Figure 7-3. The lip was assumed to slide toward the positive x direction for a small distance under the applied load W. In addition to the wiper lip/glass contact pair, a small rigid block was attached to the top of the lip and acted as a holder to simplify the description of the system linked to the application of the load.

The wiper lip was assigned with material L_H, *i.e.* hyper-elastic with the neo-Hookean parameters $C_{10} = 0.5932$ and $D_1 = 0.001$. The contact between the lip and the glass was defined as "hard" with friction coefficient 0.4. In the contact region, *i.e.* the right bottom corner of the wiper lip, a very fine mesh with 100 nodes uniformly distributed on the edge and quadrilateral hybrid plain strain elements (CPE4H) were prescribed, while in others the mesh density was relaxed for computational efficiency. Unlike the triangular model of which the geometry was strictly controlled by the python script, creation of the wiper blade model (or the wiper lip model) was solely completed in ABAQUS/CAE. The Python script was only used to define the retained node set based on their labels, which is difficult to perform in the CAE interface.

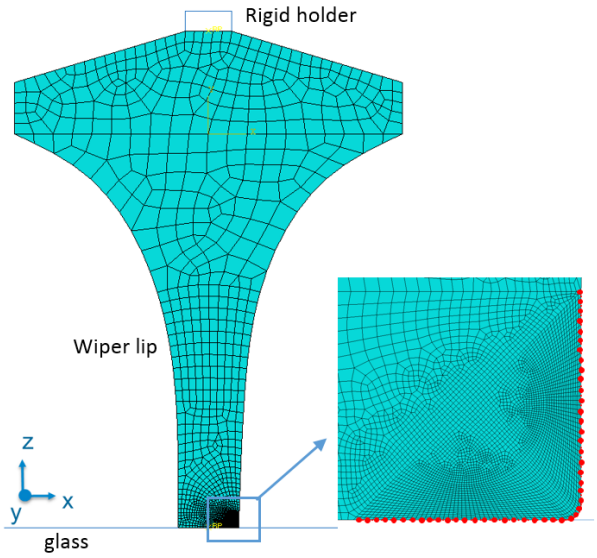

Figure 7-3 A wiper lip model with mesh details

The validation of the deformed stiffness matrix was carried out sliding in three quasi-static steps. The first step (Step 1) was to initialise the contact by moving the wiper lip towards the glass by a small distance. Then in Step 2, while keeping the same vertical position, a positive horizontal displacement was imposed to the holder as if to "drag" the wiper lip. Due to the existence of friction, the elastomer deforms and only interacts with the glass on a small area. This peculiar behaviour does not occur if the interface is assumed to be frictionless, which further shows the importance of the definition of the tangential behaviour. The following step (Step 3) was designed to deform the lip even further by replacing the vertical displacement with a concentrated force of 0.02 N applied to the top of the holder. Although the general procedure is similar to the previous sliding motion, this validation process was specifically used to explore whether the deformed stiffness matrix is effective in accounting for the displacement from Step 2 to Step 3. Finally, outputs including configuration, nodal forces etc. at each step (or each increment in one step) were read for future analysis.

Extracting K_r^d is not as straightforward as K_r^0. In addition to many rules that must be complied with the definition of linear perturbation step, one difficulty of the direct extraction is that interactions defined between the lip and the glass prevent an accurate

calculation of the reduced matrix, as mentioned in Chapter 5. Originally, this problem was handled by deforming the solid to the same state with equivalent external forces. Later, it came to the author's attention that a restart analysis can be employed for the same purpose.

Restart analysis is a powerful feature in ABAQUS that allows users to continue an interrupted run, append more steps the load history or restart the analysis from an intermediate point and change the remaining loading history data [171, 172]. If a restart analysis is needed, a restart output must be requested in the original analysis by specifying a step or increment. In the present case, for example, if the deformation state after Step 2 is of interest, it can be used as the starting point of the extraction process, followed by a static step and a substructure generation step. The static step is a "dummy step" and must be placed prior to the linear perturbation step to bring the system to the equilibrium state. In the static step, the interaction definition can be removed while the wiper lip is maintained at its deformed state by boundary conditions. Without constraints, the subsequent linear perturbation step can be executed to generate the substructure and calculate the deformed stiffness matrix in the same manner as described in Chapter 6.

Let the deformed configuration at Step 2, denoted as $[u]_2$, be the base state and the force increment between Step 2 and Step 3, ΔF be the load increment; following Equation 7.1, it is possible to calculate the displacement using different K_r^d and compare them with the standard FEA output, which was derived by $\Delta u = [u]_3 - [u]_2$. Four deformed stiffness matrices were tested, namely $[K_r^d]_2$, $[K_r^d]_{3\text{-}10}$, $[K_r^d]_{3\text{-}13}$ and $[K_r^d]_3$, which refers to the matrix extracted at Step 2, increment 12 of Step 3, increment 13 of Step 3, and Step 3, respectively. It can be seen in Figure 7-4(a) and (b) that all displacements calculated are in good agreement with the FEA in the contact area but with some deviation further away. This is because the deformation from Step 2 to Step 3 is still large and nonlinear due to the step design and K_r^d can only give the best approximation of a linear response. Nevertheless, all the resultant profiles do not differ much from the FEA output, as shown in Figure 7-4(c), which verifies the possibility of using the deformed stiffness matrices as defined above.

It should be noted that during the validation, given the frictional contact, the total force increment vectors ΔF consists of the lateral component ΔF_1 and the vertical component ΔF_2 contributed by the normal contact pressure and the tangential shear stress, *i.e.*

$$\Delta \mathrm{F}_1 = \Delta F_{NORM_1} + \Delta F_{SHEAR_1}$$
$$\Delta \mathrm{F}_2 = \Delta F_{NORM_2} + \Delta F_{SHEAR_2}$$

where ΔF_{NORM} and ΔF_{SHEAR} represent the force increment given by the normal contact pressure component and the shear stress component, respectively, with the subscript 1 and 2 indicating the lateral and the vertical direction, respectively.

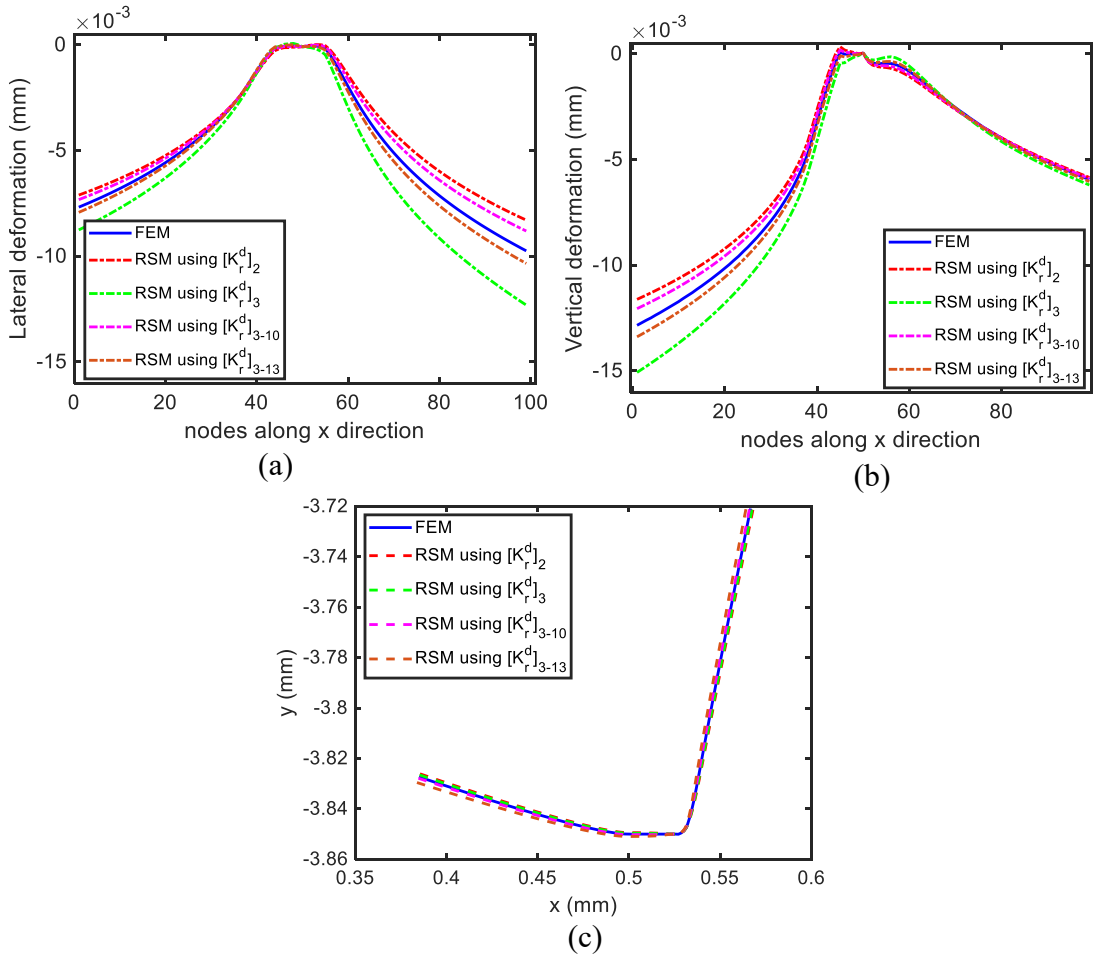

Figure 7-4 Vertical deformation (a), lateral deformation (b) and the deformed profile obtained by FEM and RSM using different K_r^d

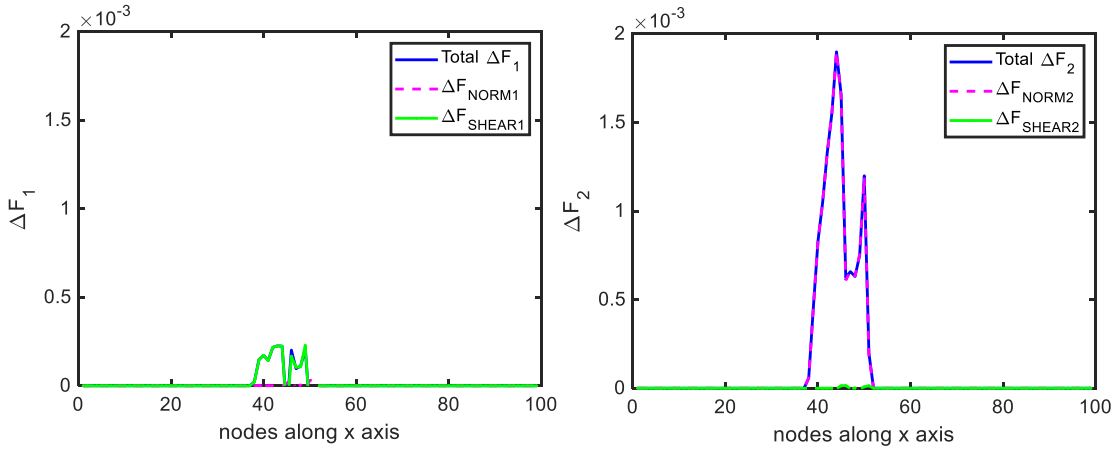

Figure 7-5 Force increment and its components plotted long the lateral direction (a) and the vertical direction (b).

As shown in Figure 7-5, the increase of nodal forces from Step 2 to Step 3 is more significant on the vertical direction than on the lateral direction. Moreover, the majority of the vertical force increment originates from the increased normal pressure and not the shear stress. This suggests that once the wiper is loaded and starts to slide, the pressure variation plays a more important role than the shear stress. This is very helpful as it allows the FSI model to mainly consider the pressure component (hydrodynamic or structural) in the iteration.

7.2.2 Sliding analysis

Having proved the validity of the deformed stiffness matrix, it is time to apply the above method to the FSI model. For this purpose, a full FE model was employed which comprises a wiper blade, a windscreen plate and a pair of holders, as shown in Figure 7-6. While the windscreen and holders were rigid bodies, the wiper blade was modelled as a two-dimensional deformable object. The profile of the windscreen wiper, provided by Bosch, is usually divided into two sections where different materials are used during manufacturing. In the upper region is the viscoelastic material Y and the lower is the viscoelastic material L. Partitions were also applied to optimize meshing. Particularly, fine structural meshes were utilised at the corner of the wiper lip for the generation of

substructure, as demonstrated in the previous subsection.

The rigid motion of the wiper blade was controlled by the holder which was in coupled constraints (*i.e.* all the reference nodes are subjected to the same motion) with a reference node designated at the neck of the wiper. Interactions between the wiper lip and the windscreen were defined by the tabular form for the consideration of rough contacts. The rough surface used to determine the pressure separation relation was measured by AFM. Frictional coefficient was also used and prescribed to be 0.4, which represents values of friction usually encountered in the wiper blade system.

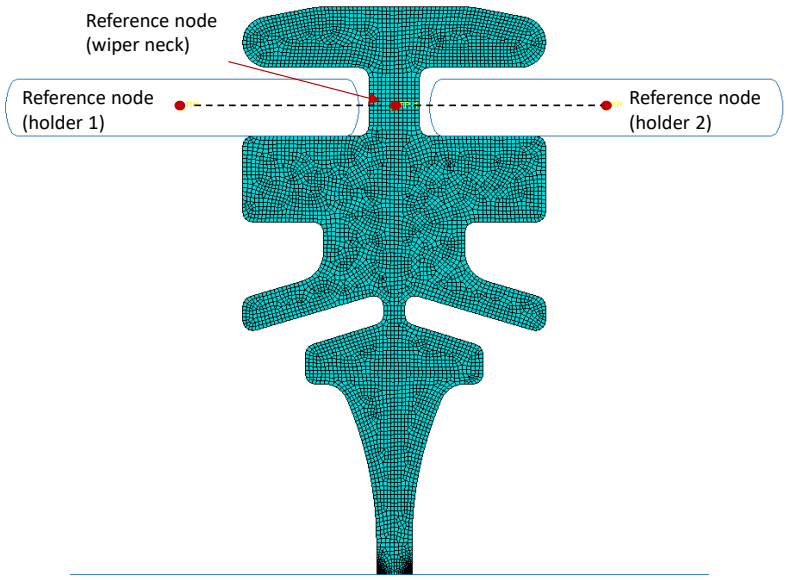

Figure 7-6 A FE model of a wiper blade system

The analysis of the interactions between wiper and glass surface when they undergo sliding and relative motion in the contact model is of crucial importance for solving FSI problems. As explained in Chapter 6, it is essential to find the equivalent HE model where K_r^d is obtained. In the framework of large strain problems, an additional purpose of the finite element analysis is to determine the intermediate state which will be used as inputs for the FSI model. Taking the wiper blade system as an example, it is reasonable to assume that the deformed configuration in a dry sliding case is similar to one in a lubricated case, at

least in the macroscopic scale. In other words, the dry sliding case can be considered as the stage B in Figure 7-2, whereas stage C represents a lubricated one. Here, a dry sliding motion at speed 10 mm/s was simulated in ABAQUS as follows.

The overall realisation is the same as that for the triangular specimen. First, a small rigid displacement was applied to the wiper to initialise the contact. This is referred to as the "inContact" step. Then in the "loading" step, a concentrated force, was applied in replacement of the displacement to press the wiper blade against the glass. The applied load was 0.017 N given the thickness of the model is 1 mm, equivalent to 17N/m in the real application. Finally, the wiper blade was maintained under this load throughout the last step, the "wiping" step. Note that during the whole analysis, the windscreen was static, while the wiper was moved at a certain speed. Given the relatively fine mesh density, convergence was usually achieved with 40 increments for each step.

Finding an equivalent HE model for viscoelastic materials is the first step towards solving FSI problems as the reduced stiffness matrix cannot be directly extracted from the frequency dependent materials. In the present study where the wiper blade was modelled by two materials, two options are available for handling this. One is to replace only the lower section with equivalent hyper-elastic property and keep the upper section viscoelastic, as shown in Figure 7-7(a). The other is to replace each section with appropriate hyper-elastic materials. It is found that the difference of resultant profile using both methods is trivial (Figure 7-7(b)), thus for simplicity, the former one is adopted here.

After identifying the equivalent HE model, a restart analysis as described in section 7.2.1 can then be applied to extract the deformed stiffness. It was decided to use the final deformation state, *i.e.* the last increment of the "wiping" step, as the starting point of the restart analysis for the reason that it resembles the steady state wiping motion most closely.

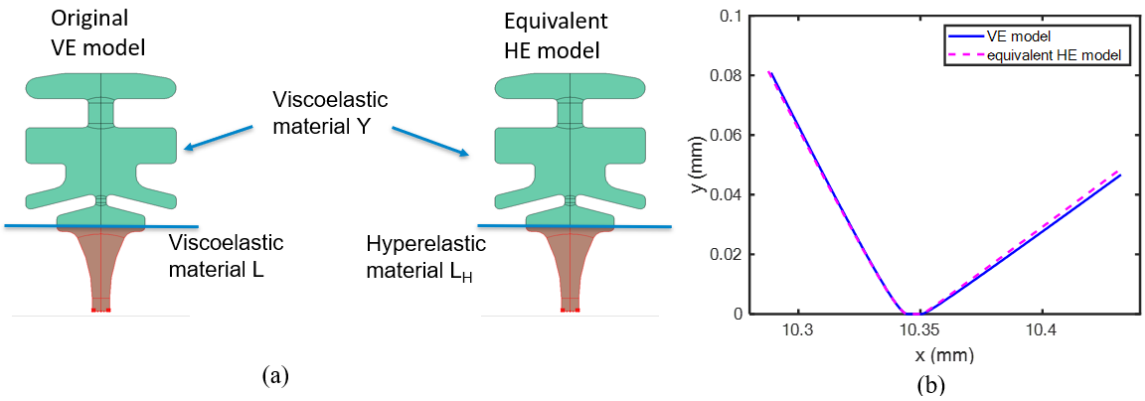

Figure 7-7 (a) Material property of a viscoelastic model and its equivalent HE model; (b) Deformed configuration of a viscoelastic model and its equivalent HE model.

7.3 Updating the FSI algorithms

The algorithms of the FSI model must be modified to accommodate the use of deformed stiffness matrix K_r^d. In contrast to Chapter 6, where the undeformed profile u_0 and the initial stiffness matrix K_r^0 are used as inputs, in the case of wiper blade (or any large strain and deformation problems to be tackled), the deformed profile u_0^d where K_r^d is extracted, and the pressure field p_{s0}^d associated with such deformation are imported to initialise the calculation. During the iteration, they are also used repeatedly as a base state whenever the separation is computed. More specifically, the deformation solver in the FSI model determines the current separation profile according to the base profile and the load difference between the current pressure and the base state pressure. This enables the approximation of a deformed configuration without going through the whole nonlinear deformation history, and therefore increases the computational efficiency significantly. The aforementioned inputs, including the base state pressure p_{s0}^d, the deformed configuration u_0^d, as well as the deformed stiffness matrix K_r^d, depend on the sliding analysis results in ABAQUS. Additional initialisations such as the fluid pressure and the central separation can be defined as zero and a reasonable small value as previously shown in Chapter 3.

The general process of the FSI simulation is given in the flowchart in Figure 7-8. In the

following, details of the adapted algorithms in BML module and MEHL module are explained with attentions paid to the deformation solver.

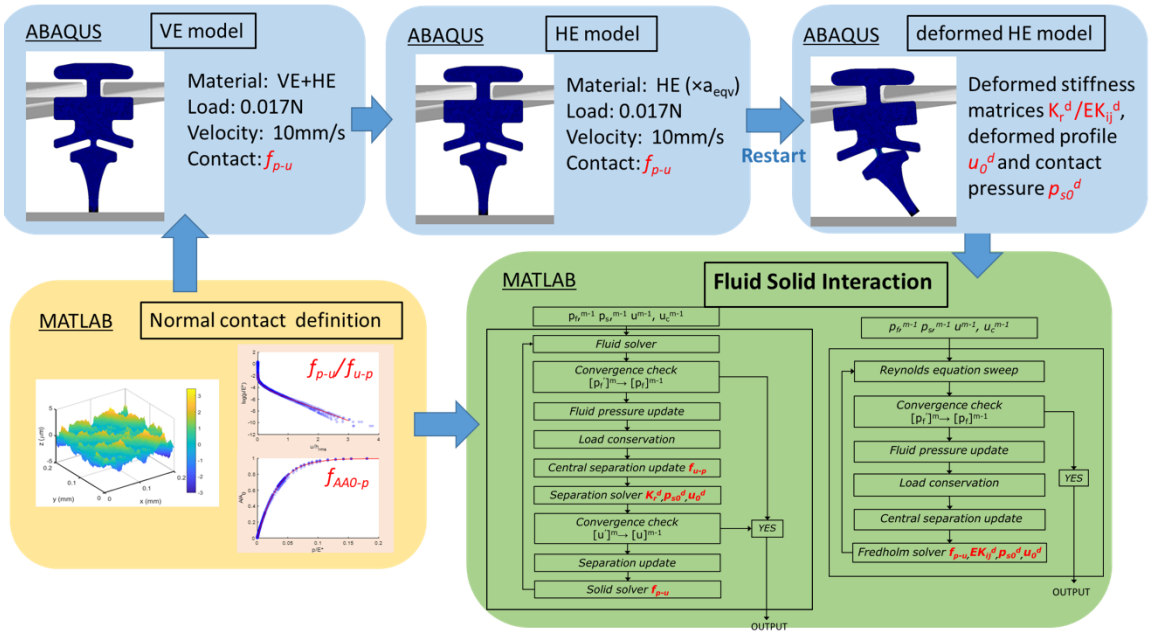

Figure 7-8 The general workflow of a full FSI analysis for large strain and deformation problems.

7.3.1 BML module

In the BML module, calculation starts with solving the Reynolds equation by using the pre-defined initialisation. As nodes of the deformed configuration obtained from FEA are no longer evenly spaced, it is necessary to re-discretise the profile with a uniform grid so that the existing fluid solver can be employed. Such transformation of nodal information is achieved through an interpolation technique and is required often in the following process. For clarity, in this chapter, the uniform mesh required for computing fluid flow is referred to as the fluid coordinate system, and the nonuniform gird corresponding to the deformation calculation is referred to as the structural coordinate system.

After updating the fluid pressure and performing the load conservation step, the central separation is adjusted based on the solid pressure. Here, the central separation is decided to be at the node where the initial gap is minimum, different from the definition in previous

chapters where the middle point along the x axis is chosen. This is due to the fact that the central contact migrates, and it is not as meaningful here as it is in hard contacts. Nevertheless, the principle is the same that this node is somewhere in the contact and gives the general separation between the windscreen and the wiper lip when deformed. The structural coordinate system is utilised during the update to be in accordance with the following deformation calculation.

As discussed, the deformation solver determines the new separation profile relative to the base profile. Here, the fluid pressure and solid pressure are integrated into force vectors, which is used with the deformed stiffness matrix to calculate nodal displacements. Section 7.2 has already shown that the normal pressure undergoes the largest change during the steady state sliding, thus, only the vertical deflection is considered.

Subsequently, the solid pressure is updated based on the new separation, and the iteration restarts from the fluid solver until the desired convergence is reached. Note that the separation field should be transformed back to the fluid coordinate system before solving the Reynolds equation again.

7.3.2 MEHL module

The mixed lubrication module can also be modified to accommodate the use of the deformed stiffness matrix. Concretely, the RES and the CSU are solved in the fluid coordinate system as previously. The Fredholm solver, on the contrary, needs to be reformulated to calculate the separation in the structural coordinate system. Recall that in Chapter 6, an equivalent matrix EK_{ij} is derived from K_r^0 to perform the Newton Raphson method. Analogously, a matrix D_{EK}^d can be obtained from the K_r^d following the same procedure except that the geometry considered is the deformed configuration u_0^d. Afterwards, using the base configuration u_0^d, the base pressure p_{s0}^d, the current pressure p and the matrix D_{EK}^d, the new separation is determined iteratively as well as the

corresponding solid pressure.

Straightforward as it looks, converting K_r^d into D_{EK}^d strongly relies on the geometry and may result in numerical singularities that leads to convergence problems. This issue was encountered in the use of the MEHL module in the current study, however, the results obtained in a certain range matched the BML, which is therefore used here.

7.4 Results

Results of a wiper blade system operating in a steady state condition are presented in this section. Rough surface measured on a wiper blade sample by AFM was processed to define the contact mechanics. Viscoelastic material Y and L characterising the same batch of specimens were considered. Applied load was 17 N/m and the lubricant viscosity was 1 mPa·s, compatible with experimental conditions. For the initialisation, outputs from the sliding analysis carried out in section 7.2.2 were employed.

7.4.1 Pressure and separation results

Figure 7-9 depicts the variation of pressure field and separation profile over a wide range of velocities from 10 mm/s to 5 m/s, which covers the experimental conditions as well as the real windscreen wiper operating situations. As can be seen, fluid pressure gradually rises with the sliding speed due to the increase of entrained fluid, while the contribution of asperity contact is significantly reduced. Central separation (or central film thickness), as an important implication of the wiping quality, was estimated to be around 140 nm at 5 m/s. Although this value seems to be slightly lower than the actual film thickness (>200 nm) measured in the previous project [1], it is still within a reasonable range and can be affected by various factors, which will be discussed in section 7.5.

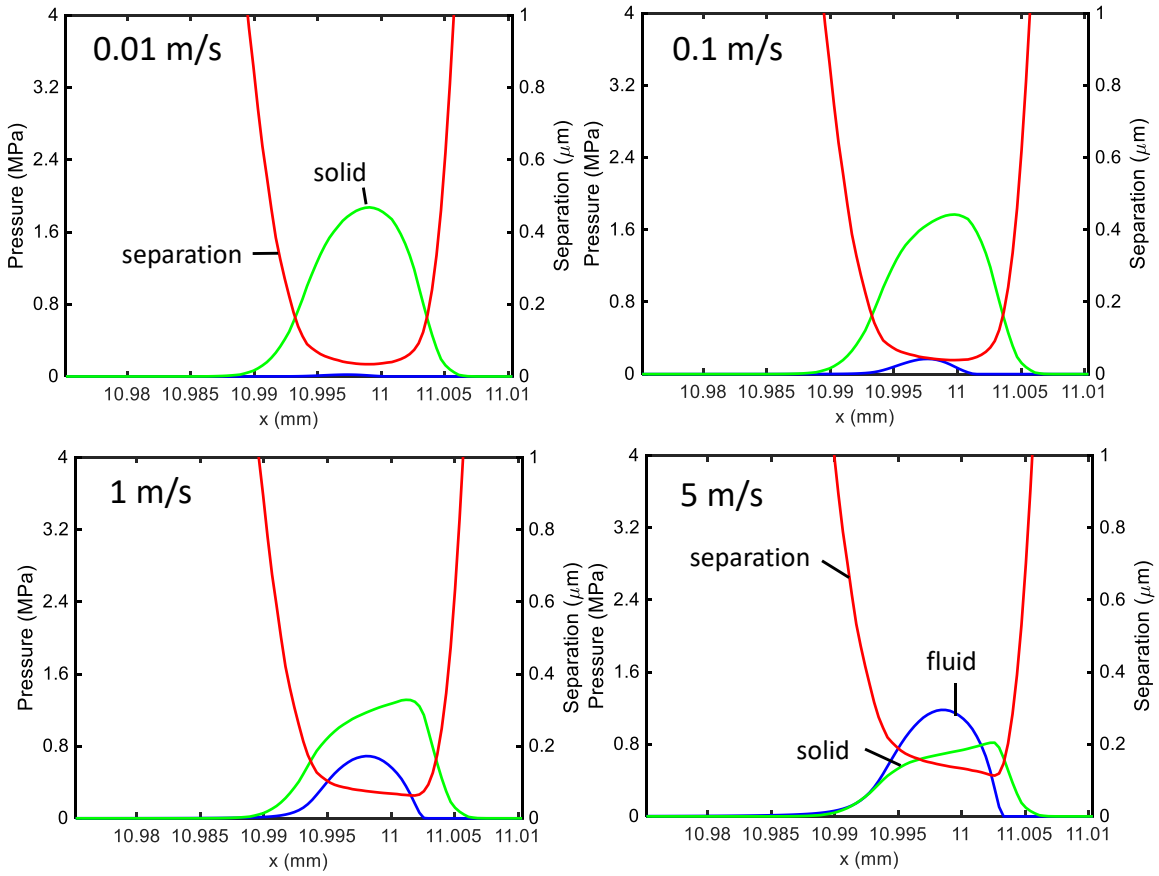

Figure 7-9. Pressure distribution and separation profile of the wiper blade system under load 17 N/m at sliding velocity 0.01, 0.1, 1 and 5 m/s.

7.4.2 Friction prediction

For comparison, the friction measurement of the wiper blade obtained in the previous project by Dobre is presented in Figure 7-10 (a), where the friction coefficient was found to decline quickly from 0.6 to 0.11 in the speed range of 0.01 m/s ~ 1.8 m/s, clearly demonstrating a mixed lubrication regime. However, using the results shown in Figure 7-9, it was almost impossible to fit the calculated friction to the experimental observations with a constant shear strength σ_1. For example, in Figure 7-10 (b), when σ_1 is approximated to be 0.4×E so that the same friction can be obtained at 0.01 m/s, the numerical model predicted the mixed lubrication to occur at a much higher speed, resulting in an overall overestimation of the friction. If a smaller shear strength σ_1 is considered in order to fit at the relatively high speed (*e.g.* 1 m/s), the friction at low speeds is in turn underestimated,

as shown in Figure 7-10(c).

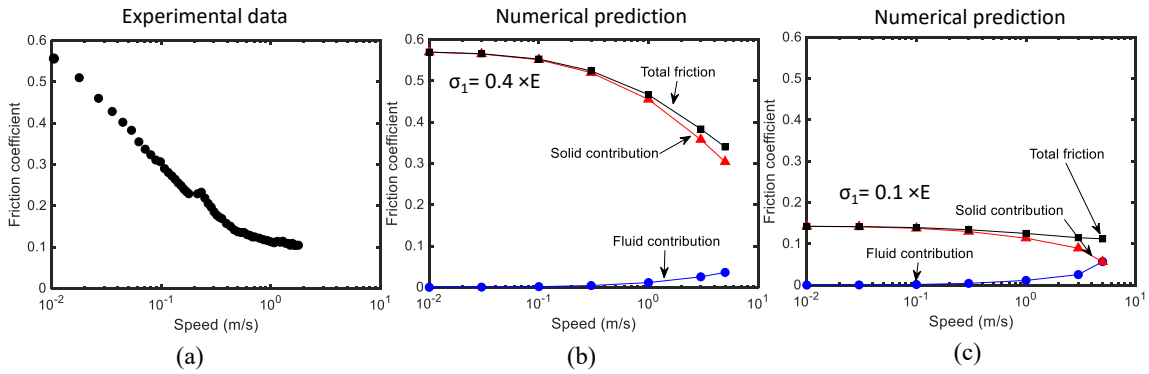

Figure 7-10 Experimentally measured friction for the wiper blade system [1] (a) and the predicted friction when σ_1 = 0.4×E (b) and σ_1 = 0.1×E (c). Figure 7-10(a) is reproduced from [1] with permission.

There are many reasons for this deviation from measurements. First, the system appears to remain in the mixed lubrication at relatively high speed when it is expected to have more hydrodynamic pressure acting on it. Secondly, according to Equation 3-13, the solid friction, which accounts for a large amount of the total friction, strongly depends on the shear strength and the real contact area. The former, although assumed to be constant in the previous chapter and several contributions reported in the literature [2, 186], is still an open discussion and may vary with circumstances. This again implies the importance of choosing an appropriate σ_1 for an accurate description of the frictional behaviour, which requires more experimental work to characterise the interaction between asperities as mentioned in Chapter 6. In terms of the latter (the real contact area), it is a direct result of the deterministic solution and can be affected by various factors such as the surface topography obtained and the material property considered. Furthermore, the friction component contributed by fluid flow may be underestimated here given the relatively low fluid pressure and separation, which are influenced by the roughness, the deformation and the initial profile. In the following studies, 0.4×E are used in order to highlight the difference between different lubrication regimes.

Improvement of the numerical prediction should be addressed for the following two aspects.

On one hand, it is important to gain better understanding of the contact in the experiments. Indeed, the wiper blade system is very complex with sophisticated friction mechanism involved. From experiments it was found that, even for a given sample operating on a certain condition, the actual load may vary due to damping; the roughness and lip shape may differ due to the wear; the contact angle between the lip and the glass constantly changes and causes the contact area to change as well; all of which could affect the input for simulation. On the other hand, it is necessary to mimic the system as closely as possible in the sliding analysis. In the FSI model, deformation state obtained from the FEA is a crucial input and may deviate from the reality for reasons such as approximated interaction definition and structural constraints. This would result in inaccurate initialisations and the reduced stiffness that further affects the pressure field considerably. Therefore, in the following section, several factors that have potential impact on the simulation results and that are most relevant to this thesis are examined carefully in order to improve the prediction.

7.5 Discussion

7.5.1 The effect of roughness

7.5.1.1 Measurement techniques for rough surfaces

Roughness is the first to examine given its intuitive importance of influencing lubrication regime. In order to be consistent with the experiments, rough surfaces of the same batch of specimens were measured in different ways and analysed. They are Talysurf measurement in one dimension and AFM measurement in two dimensions. In principle, if the rough surface is isotropic, both methods should provide representative information of the surface and have no remarked impact on contact mechanism. The only expected difference probably lies in the spectral width which is larger for the one-dimensional measurement since it permits to detect longer wavelength components. In a study by Tevis *et al*. [56], it

was suggested to combine both in the PSD so that a more comprehensive statistical property can be considered. However, in the present study, it was interesting to find that the two measurements exhibited different spectral features and resulted in significant distinctions in the contact behaviour, as shown in Figure 7-11. To investigate this and explore which one is better, contacts defined by both were employed in the FSI simulation. For clarity, the two types of roughness results are referred to as the Talysurf roughness and the AFM roughness.

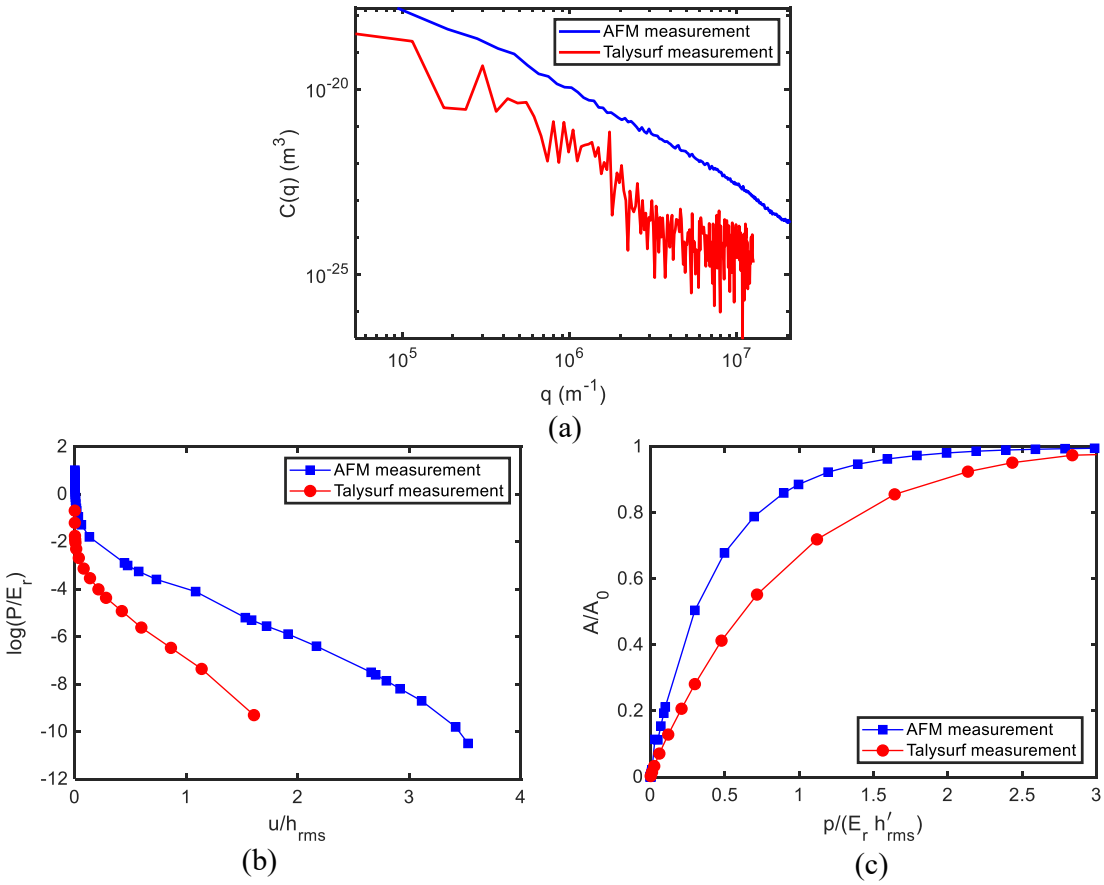

Figure 7-11 (a) PSD, (b) load-separation curve and (c) the contact area evolution of rough surface measured by Talysurf and AFM.

Figure 7-12 shows the calculated friction and central separation over the speed range considered. Although the Talysurf roughness predicts a more evidently reduced friction in the mixed regime, the estimated separation is too low (in the nanometres) to be reliable. A further examination of the roughness data explained this is due to a potential issue with the Talysurf measurement results, which turned out to be not strictly fractal with an

approximated Hurst exponent H = 1. The difference in the two sets of measurements obtained can be attributed to the fact that the stylus of the instrument (Talysurf) may deform the rubber during the measurement and, hence records the wrong profile. This points out the importance of scrutinising the measurement especially for compliant materials. Despite that, the comparisons reveal that the rough topographies (profiles) can significantly affect the predictions obtained for the interactions between the two bodies in terms of friction and separation, especially when they exhibit different spectral properties.

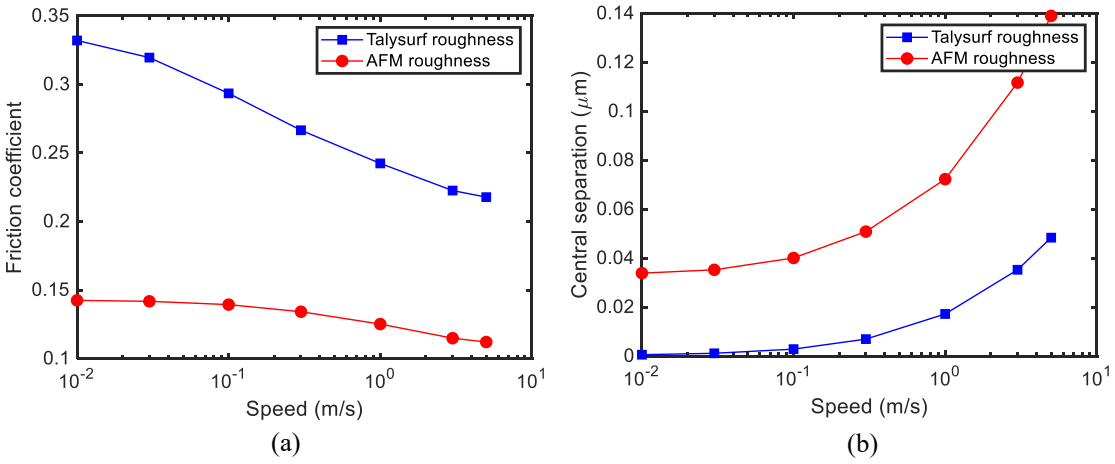

Figure 7-12 (a) Friction prediction and (b) estimated central separation calculated for rough surface measured by Talysurf and AFM.

7.5.1.2 Statistical properties of rough surface

As mentioned in Chapter 4, when rough surfaces are analysed, a pre-processing procedure is often required to remove the waviness and only keep the information of interest. The determination of the cut-off wavelength depends on the contact size and may have significant influence on the contact behaviour. Taking the original AFM measurement as an example, the detected wavelength varies from the measurement dimension 67.5 μm down to the instrumental resolution 0.15 μm. Based on the raw data, three roughness topographies of the rubber were obtained using the open-source image software Gwydion which filtered out different levels of waviness. For simplicity, they are denoted as rough surface, medium rough surface and smooth surface with corresponding h_{rms} value 0.93 μm, 0.67 μm, and 0.32 μm, respectively. Figure 7-13 depicts the spectral information and the

equivalent results obtained from solving the contact mechanics of the problem deterministically. Note that although the load-separation curve and the contact evolution function appear to overlap for all three surfaces, the contact behaviour actually differs due to the different h_{rms} value and h'_{rms}.

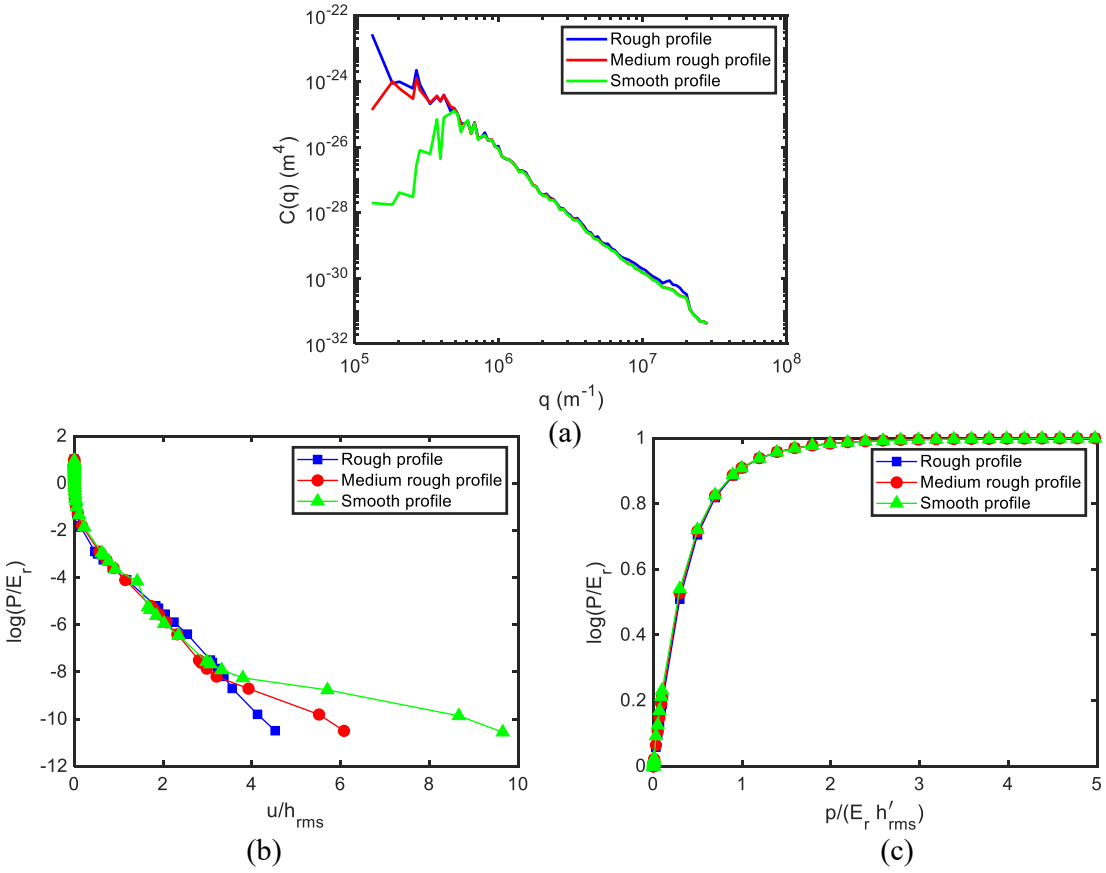

Figure 7-13 (a) PSD, (b) load-separation curve and (c) the contact area evolution of rough surfaces with different h_{rms}.

Friction and central separation predicted by the FSI model using these contact definitions under load 17 N/m are presented in Figure 7-14. The shear strength used here is assumed to be constant and equals 0.4×E. While the boundary friction of all three surfaces are very close, the smooth one enters the mixed regimes at a lower velocity with a lower friction and smaller separation. This is as expected and complies with experiments since it is easier to form a thin film between smooth surfaces than rough ones, although the more important implication here is that the statistical value of the roughness plays a critical role in the proposed FSI model, especially when the mixed lubrication is concerned.

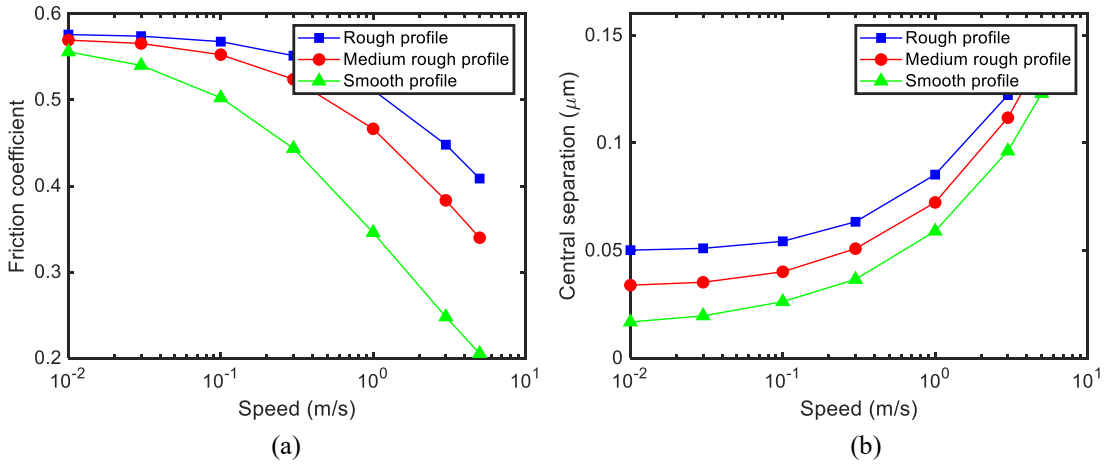

Figure 7-14 (a) Friction prediction and (b) estimated central separation calculated for rough surfaces with different h_{rms}.

7.5.2 The effect of speed

Material properties are essential inputs and particularly important for the proposed FSI model which features solving the nonlinear problems. However, discussing different viscoelastic materials is beyond the scope of this thesis where the focus is to determine the most appropriate reduced stiffness matrix for the given viscoelastic model.

In dry contact problems where the material and the sliding speed is specified, section 7.2.1 shows that all stiffness matrices extracted at deformed states close to the target state approximate the elastic behaviour well. In the simulation of a lubricated system using the presented FSI model, a dry contact solution was the first to mimic, or at least partially reproduce, the solid interaction in the boundary lubrication regime. For example, so far, a sliding FE model at speed 10 mm/s has been employed to identify the equivalent HE model and extract K_r^d. The equivalence coefficient α_{eqv} was found to be 1.4. Alternatively, it is also possible to use a sliding model at 1 mm/s as the dry contact approximation, in which case, the equivalence coefficient became 2.2.

Given the slight difference in the deformed stiffness matrices, investigation was carried out to determine which one produces more realistic results. However, it should be noted that

K_r^d is not the only variable here, but closely associated with the deformed configuration u_0^d shown in Figure 7-15. Thus, a series of tests were conducted with different combination of inputs. Test 1 and Test 2 used u_0^d and the corresponding K_r^d at speed 10 mm/s and 1 mm/s, respectively. For clarity, it was decided to denote the deformed configuration and the corresponding deformed stiffness matrix obtained from sliding model at 10 mm/s as $[u_0^d]_A$, $[K_r^d]_A$ and those from sliding model at 1 mm/s as $[u_0^d]_B$, $[K_r^d]_B$. Test 3 was constructed as a comparison test of which the goal was to simply change the stiffness while keeping everything else the same. All tests were carried out for the AFM medium rough surface under the load 17 N/m and the shear strength were set to be $0.4\times E$.

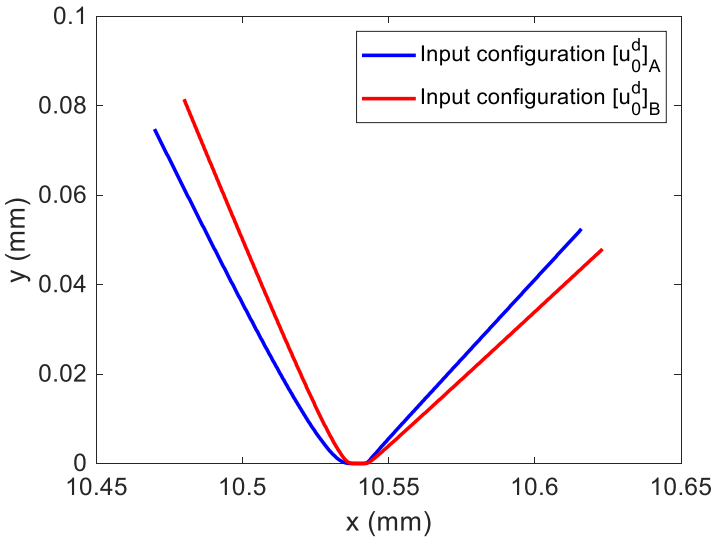

Figure 7-15 Deformed configuration obtained from the FEA at different speed.

Calculated friction and central separation are shown in Figure 7-16, where a small difference was found between Test 1 and Test 2, suggesting that using FE models at different conditions (speed in this case) indeed affects the FSI outcomes. However, the impact is more likely to derive from the deformed geometry rather than the stiffness, which is confirmed by the comparison between Test 2 and Test 3, where nearly identical behaviours are predicted. This implies that in the proposed FSI model, the choice of deformed stiffness matrix is less critical as long as the approximated deformation state does not significantly differ from the true solution, because the contact region is much stiffer

and the displacement in this region is very small. Such phenomenon is similar to what was observed in the validation for dry contacts in Chapter 5 where the stiffness at different increment has negligible influence on the final profile.

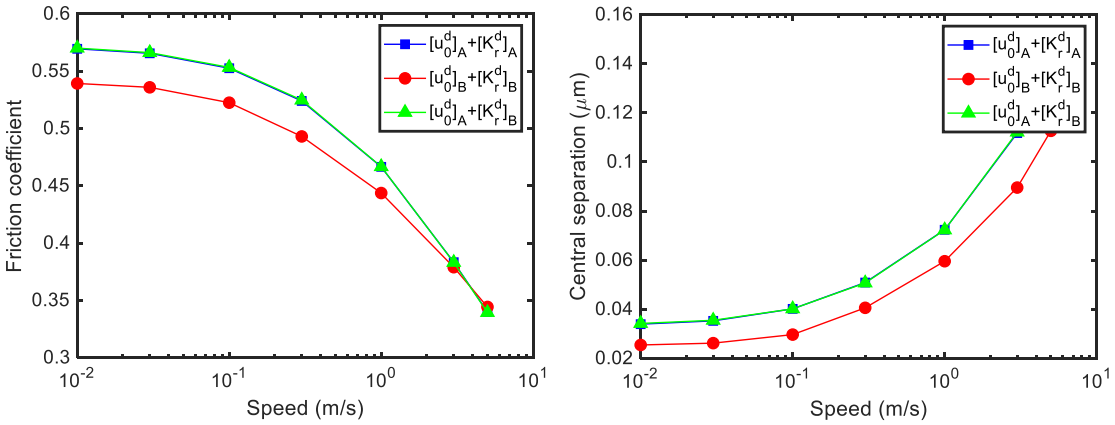

Figure 7-16 (a) Friction prediction and (b) estimated central separation calculated for tests conducted with different combination of u_0^d and K_r^d.

7.5.3 The effect of geometry

The previous section reveals that u_0^d has a strong influence on the frictional behaviour, which is understandable as the configuration directly determines the construction of the pressure field, especially in the contact area. Revisiting results in Figure 7-9, the contact width is only 3~6 μm, much smaller than the experimental observation which is about 50 μm [1]. If the contact area is too small, it will inevitably prevent the fluid pressure from building up, leading to a much lower fluid friction. Thus, in this section, one of the possible reasons for such small contacts, the initial geometry, is examined.

The initial wiper blade profile employed previously is based on the measurement of an unused sample of which the round tip has radius of 0.01 mm. Nevertheless, this may be an unrealistic approximation for the actual wiping phenomenon as the shape of wiper lip will quickly change due to wear, as shown in Figure 7-17, where profiles of a new wiper specimen and a used one were measured by the digital microscope Hirox and the curvature

of a used wiper tip is much larger.

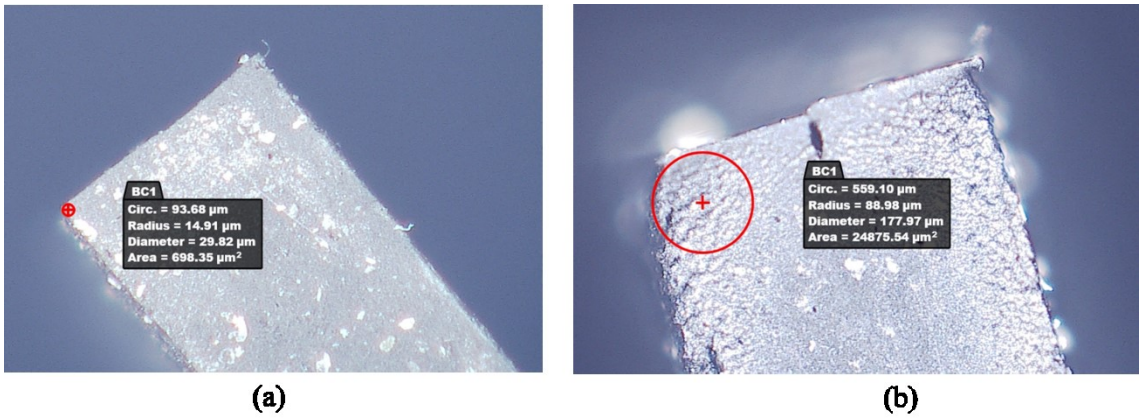

Figure 7-17 Profile measurement of (a) a new wiper blade tip and (b) a used one.

To investigate on this, a similar profile with the tip radius of 0.05 mm was employed to mimic a used wiper. Dry sliding model under 17 N/m at 10 mm/s was chosen to obtain u_0^d and K_r^d, the rough contact was defined by AFM roughness with h_{rms} 6 µm, and the shear strength was decided to be 0.4×E. Pressure field and separation profile calculated at velocity 1 m/s are presented in Figure 7-18, where an evident increase of the contact width can be observed.

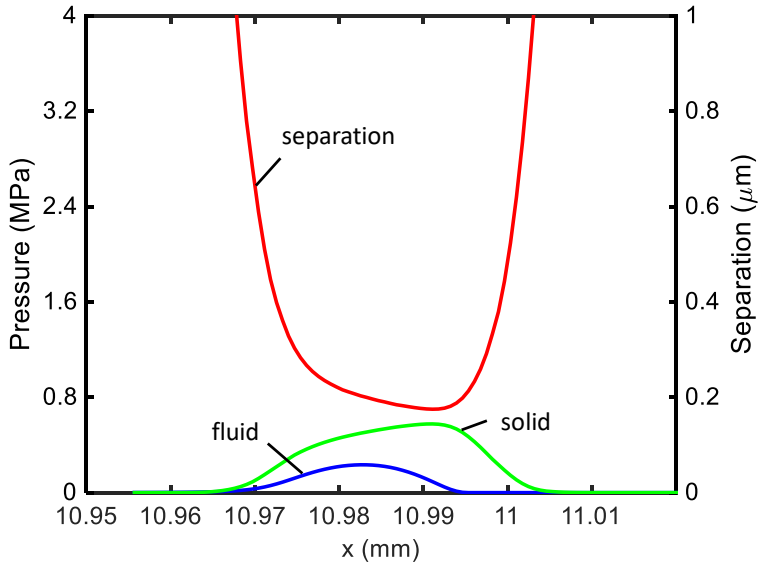

Figure 7-18 Pressure field and separation profile of the wiper blade with lip radius of 0.05 mm under 17 N/m at sliding velocity 1 m/s.

Changes in contact area directly affect the variation of friction and central separation,

which are plotted in Figure 7-19. Due to the rapid build-up of fluid film, friction is expected to experience a marked decline from 0.7 to 0.3, indicating that a simple increase in the model radius can already improve the prediction significantly. Note that the current contact width, 30 μm, is still smaller than the observation in experiments, and the real worn profile does not resemble a circular tip, which means the actual growth of the fluid pressure can be more complicated.

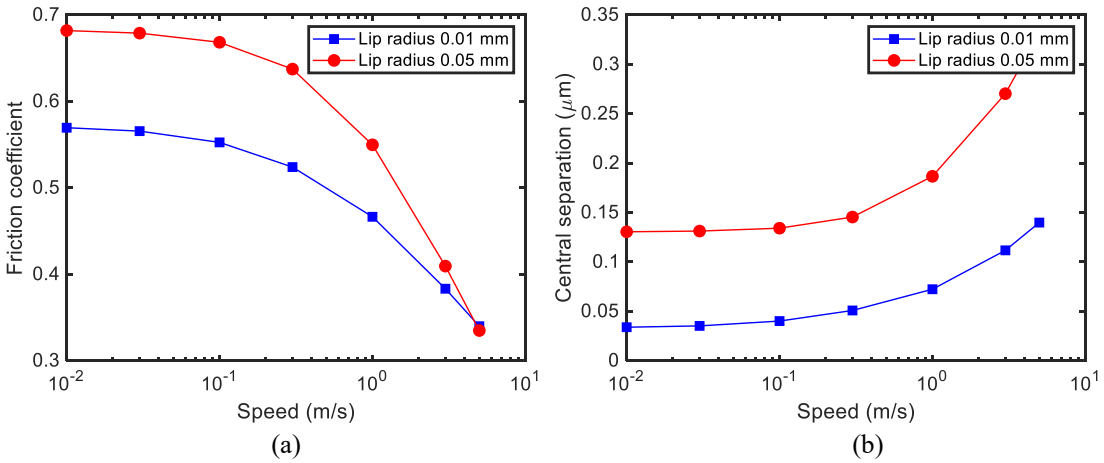

Figure 7-19 (a) Friction prediction and (b) estimated central separation calculated for wiper blade with different tip radius different.

7.5.4 The effect of load

In experiments, when a wiper blade is controlled to slide against the glass plate under a certain load, the real-time normal force is not always constant but varies with time in a pseudo-sinusoidal way. As a result, the deformed profile of the wiper continually changes as if it bounces up and down on the vertical direction. Furthermore, the contact area is different relative to the loading conditions. Under low loads, the contact occurs at the round tip of the lip, while at relatively high loads, it moves to the edge resulting in a larger area and a different shape, as shown in Figure 7-20 where the deformed profile at sliding speed 10 mm/s under load 17 N/m and 30 N/m obtained from FEA are presented.

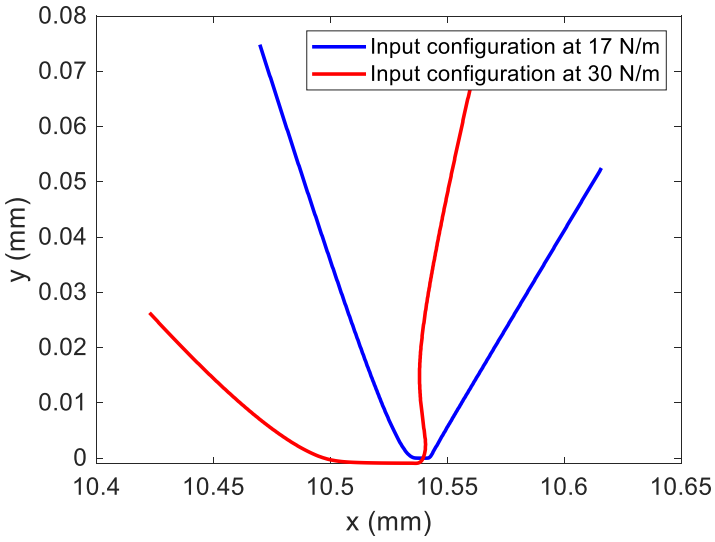

Figure 7-20 Deformed configuration obtained from the FEA under different loads.

From previous sections, it is already known that the different contact profile due to speed and radius can affect the FSI predictions. In this section, in order to replicate the experimental conditions, the effect of load is explored by running the FSI model for the original wiper blade with lip radius 0.01 mm under 17N/m and 30 N/m. Sliding analysis of the dry contact model was carried out at sliding speed 10 mm/s to prepare u_0^d and K_r^d.

Friction and the central separation results are presented in Figure 7-21. It appears that friction experiences a quicker and dramatic decline under 30 N/m, due to the larger contact area and shallow inlet shown in Figure 7-20. In addition, the lubricated system predicts a higher central separation for the applied load 30 N/m, which is somewhat counter-intuitive when relating these results to conventional line and point contact studied in hard and soft, but low deforming, contacts; however, it is worth mentioning that the given results should not be linked to the experiments quantitatively but rather be interpreted as an evaluation of the factors that affect the prediction and further experimental and modelling studies will need to be undertaken to explain the complex behaviour experienced by these systems.

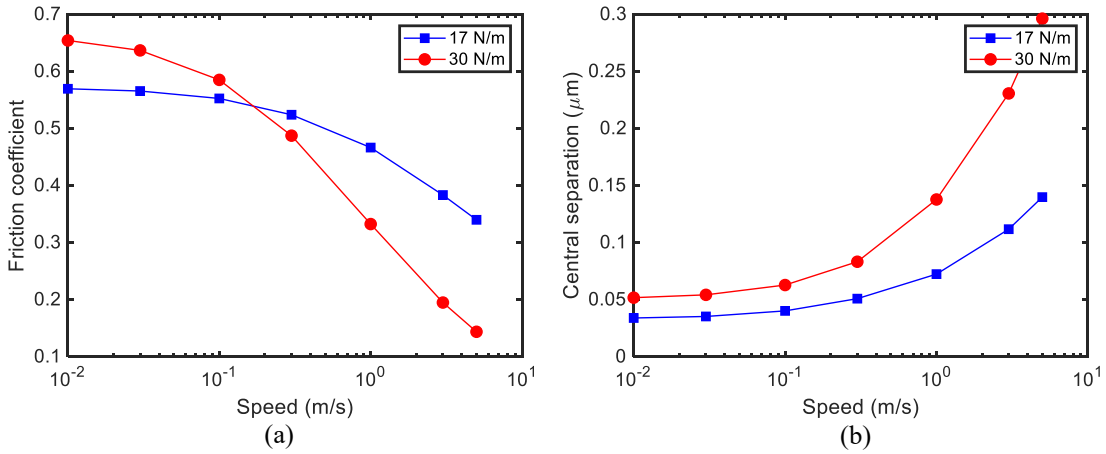

Figure 7-21 (a) Friction prediction and (b) estimated central separation calculated for wiper blade under different loads.

7.5.5 Some guidelines

This chapter has demonstrated how to apply the RSM to large deformation cases and how to improve the proposed FSI model accordingly. Although in principle this model can be applied to any deformation situations, the previous sections show it strongly depends on the inputs, and it is more convenient and efficient to use the model in Chapter 6 if the strain behaviour can be approximated as linear elastic. Thus, in this section, some guidelines will provided in terms of where the linear elastic assumption can be used and when to switch the FSI models for different deformation cases.

Revisiting the previous examples, the first rule is to identify whether there is significant shear strain. For the triangular specimen, the normal strain on the vertical direction is always larger than the shear strain. However, for the wiper blades, the opposite relations were found. As the initial stiffness matrix does not take the shearing into consideration, one should resort to the FEA instead and then employ the deformed stiffness matrix only to calculate the normal strain.

The second rule is to evaluate the response of the solid by observing its hyper-elastic property. For instance, in the stress strain curve of hyper-elastic material HL, as shown in

figure , the tangential stiffness changes dramatically when the nominal compressive strain is larger than 0.2. In the FEA performed in Chapter 6 and section 7.2.2, it has been found that the normal strain of the wiper blade during sliding (on the direction perpendicular to the sliding) is usually larger than 0.2, while that of the triangular specimen is less than 0.05. Therefore, it would be more accurate to use the correct Etan estimated at a deformed state than simply approximating E_0.

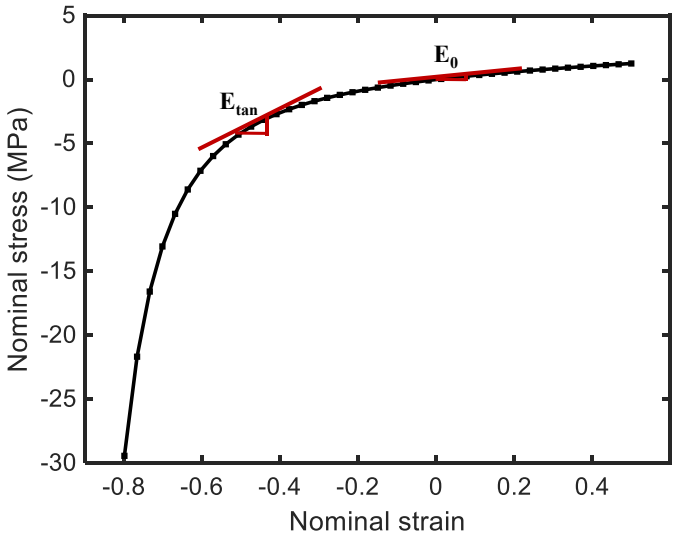

Figure 7-22 The stress strain curve of the hyper-elastic material L_H as shown in Table 5-1

In conclusion, if the elastic solid to be investigated experiences significant level of shear strain and the normal strain in the stress strain curve indicates a tangential modulus much different from the initial modulus, one should consider to use the RSM and the FSI model developed for large deformation cases to obtain a more accurate solution.

7.6 Summary

This chapter extends the FSI model to account for large and complex deformations in the application of windscreen wipers systems. As the large deformation problems often involves nonlinear history originated from material and/or geometry, the simulation strategy is to determine the interaction based on a state that can be obtained with less

computational effort to approximate the actual solution. To achieve this, the concept of deformed stiffness is introduced and validated against the FEM as a linearization approach.

Prior to the main FSI calculation, a rough contact analysis and a dynamic finite element analysis are required to provide not only the contact definitions but also a deformed state which will be used as a base state. Algorithms are modified to accommodate the use of deformed stiffness, and two coordinate systems are used to facilitate the information transfer between the fluid solver and the structural solver.

Results shows that the outcome can be influenced by a variety of quantities encountered in the FSI model, among which the most significant ones are contact definition $f_{p\text{-}u}$, the deformed stiffness matrix K_r^d, and the configuration u_0^d used in the simulation. It should be noted that these quantities do not act separately but in an interlinked manner. For example, the rough contact mechanics will affect the deformed shape as well as the reduced stiffness, the flattened profile and the stiffened material will in turn change the interaction behaviour. Furthermore, the characteristics of the system such as the statistical properties of the rough surface, and the operation conditions such as the applied load, as well as the approximations of the final solution certainly have an impact on aforementioned quantities to different degrees. Investigations in the present study show that for a given topography, the h_{rms} plays a more important role in defining the asperity interaction and directly affect the film formation. Furthermore, an increased contact area attributed to either wear or higher load leads to relatively more fluid contribution to friction. The sliding motion simulated by the FEM also needs to be handled with caution in order to obtain the optimum approximation of the base state. It is difficult to quantitatively describe the influence of the above parameters, but in general, their importance is in order $f_{p\text{-}u} > u_0^d > K_r^d$.

8 CONCLUSIONS AND FUTURE WORK

8.1 Conclusions

The main goal of this project was to develop a Fluid-Solid-Interaction model which can capture the tribological behaviour of a compliant contact systems in lubricated conditions, particularly in the application of the windscreen wiper systems. This was achieved by utilising a two-scale approach where the hydrodynamic flow, the rough contact and the nonlinear deformation are solved in different algorithms depending on the lubrication regimes considered. Given the complexity of problem and the sophisticated friction mechanism, the simulation was divided into five stages.

Firstly, a simple contact between a half cylinder and a flat plate was considered under the assumption of half-space and the approximation of linear elasticity, for which basic algorithms were developed to capture the transition from the boundary lubrication regime to the EHL regime. Secondly, a comprehensive study on rough contact mechanics was performed to gain a better understanding of the asperity interaction and to calculate the contact pressure using a deterministic method. In order to determine the finite deformation of nonlinear materials, this project introduced a novel RSM, where the strain behaviour is described by the reduced stiffness matrix extracted from the deformable body. Based on these improvements, modification was made to relax the previous assumption so that the FSI model can be applied to contact systems where small strains are expected. Finally, by extending the RSM to account for large deformations, the FSI model was further advanced to simulate the interacting behaviour and make friction predictions of a wiper blade system.

8.2 Achievements

The accomplishments of this project have direct industrial implications as the FSI model was handed over to Bosch to make predictions of the frictional behavior and wiping performance of the wiper blades in various operational conditions. This is the first time that a numerical model can be used directly in the industrial field as all the main factors (such

as the material, the geometry, the lubricant, the roughness, etc.) are considered. The most significant achievements of this project are summarised as follows.

- Three algorithms were successfully developed and validated for calculating the fluid flow, the rough contacts and the elastic deformation at the same time. This not only allows the obtainment of a full Stribeck curve from the boundary lubrication to the EHL, but also provides the flexibility to explore the details of a specific regime, such as the contribution of fluid flow and asperity interaction, and the evolution of central or minimum separation at the interface.

- A thorough investigation was conducted to account for the contact behaviour between rough surfaces. The main discoveries can be concluded in three aspects:

    a) It was found that an accurate characterization of the rough surface not only plays an important role in describing the interactions between asperities in dry conditions, but also has a strong impact on the solution of FSI. In addition to the use of power spectral density for more comprehensive information of the roughness, the statistical properties, such as the RMS roughness and RMS gradient, should also be calculated carefully depending on the scale of the contacts under investigation. While RMS value the interfacial separation between rough surfaces, the RMS gradient affects more on the real contact area. Furthermore, when a measured rough surface is considered, it is always necessary to compare and combine different measurement methods to gather complete information and ensure the representativeness of the surface. Characterisation is also important for reconstructing synthetic rough surfaces; wave vectors used for construction should be selected in an exponential interval.

    b) Both Persson's theory and the boundary element method (BEM) have been

employed to derive the contact area evolution and load-separation curves in rough contact problems. Although Persson's theory is more convenient given the analytical formulas available, it is limited for self-affine fractal surfaces, and the results are found to be strongly dependent on the statistical properties and corrective factors. On the contrary, the BEM are less restrict about the surface type and can be directly applied to measured topography efficiently with the assist of FFT and the conjugate gradient method.

c) A parametric study was carried out to investigate the influence of the finite size, the continuum approximation, the spectral breath, and the Hurst exponent on the solutions of rough contact problems using the deterministic method. It was found that the grid spacing has little effect on the results as long as the gird is smaller than the smallest wavelength. While the size of the contact system affects the separation more, the spectral breath is more important for the contact area. The Hurst exponent, which can be derived by fitting the PSD, should be determined carefully as it strongly affects the contact area and interfacial separation under both low and high loads.

- The elastic deformation of the solid body was calculated by the reduced stiffness method (RSM) proposed in this study. This novel approach was found to be more accurate than the traditional theory of elasticity and more computational efficient than a full FEM, which makes it the perfect solver for nonlinear materials with complex configurations. Two different types of reduced stiffness were explored and applied to different deformation cases. For solids which are mainly deformed in the vertical direction and expects the normal strain less than 0.2 ("small deformation"), the initial stiffness matrix was proven to be sufficient in predicting the strain response. For those where large deflection due to shearing is experienced or the normal strain is larger than 0.2, the deformed stiffness matrix is a better choice to linearize the strain behaviour.

- The FSI model for small deformation cases was employed to predict the friction and compare it with the experiments, where an elastomer with triangular cross-sections and a glass were used. Good agreement was observed, especially in the mixed lubrication and EHL regimes. In addition, the results revealed the importance of identifying the shear strength which characterise the interaction between asperities. Comparisons between numerical simulation and the experiments for actual wiper blades were less satisfying, however, the primary reason has been identified as the underestimation of the fluid pressure. Through the investigation of several influential factors, it was found that the roughness plays the most important role.

8.3 Future work

The proposed model has successfully simulated the complex behaviour of windscreen wiper systems in steady-state sliding motions, taking into consideration of the surface roughness, the real configuration and the viscoelastic properties. Future efforts should be devoted to eliminating some approximations made in the model for more practical use and incorporating other significant properties to obtain physically sound results. To achieve this, improvements in the following aspects are suggested.

Rough viscoelastic contacts: As an important component of the proposed FSI, the contact mechanics between rough surfaces were thoroughly studied for elastic materials, as shown in Chapter 4. For hyper-elastic and viscoelastic materials, effective elastic moduli were employed in the main FSI model to approximate their mechanical responses in a linear range, and the nonlinear deformation was captured by the FEA. A more accurate description of the interacting behaviour can be pursued by incorporating the viscoelastic properties in the deterministic method. Specifically, the contact problem between a rigid indenter and a viscoelastic slab can be formulated as [180]:

$$u(\boldsymbol{x},t) = \int_{-\infty}^{t} d\tau \int d^2x' J(t-\tau) G(\boldsymbol{x}-\boldsymbol{x}') \dot{\sigma}(\boldsymbol{x}',\tau) \qquad \textit{Equation 8-1}$$

where $\boldsymbol{x}$ is the in-plane position, t is the time, u ($\boldsymbol{x}$, t) is the normal surface displacement of the viscoelastic solid, σ ($\boldsymbol{x}$, t) is the normal stress, and $G(x)$ and $J(t)$ are the Green's function and the creep function respectively. The numerical solutions can be achieved by employing the adaptive nonuniform mesh as presented by Carbone and Putignano [180], which can be used to generate fitted functions and define normal contacts in the same manner as for elastic materials. This can also be extended to layered materials and reciprocating motion as proposed by Putignano *et al.* [181].

Evaluation of the Shear Strength: One question arose over the course of this research and not addressed due to the time and resource constraint was to identify the shear strength used for friction calculation. As shown in Chapter 4, 6 and 7, this value was assumed to be constant in the mixed lubrication and EHL regimes which is a reasonable estimation as the asperity-asperity interactions in these regimes is less significant due to the presence of lubricant; however, experiments on silicon rubber sliding on flat dry surfaces have shown that this value is closely related the structure of the polymer chain and varies with speed. Comparisons between simulation results and friction measurements carried out in this project also suggested that a small variation of σ_1 is needed when the applied force is increased. Therefore, in order to have a better understanding of the interfacial sliding process especially at low velocities, more tests should be performed in both dry and lubricated conditions to correlate σ_1 with factors such as load, speed, surface properties and material responses. Alternative fundamental modelling studies, which include the use of molecular dynamics and other simulation methods to capture the interactions at the smaller scales [54], can be considered to shed light on the complex mechanisms regulating this very important factor.

Surface Energy: One important property of the system which was omitted in the proposed FSI model is the Surface energy; this is usually categorised as hydrophobic or hydrophilic.

For hydrophobic systems, a dewetting transition may occur in the asperity contact regions, whereas for hydrophilic systems, the asperity contact region tend to be separated by thin fluid layers as illustrated in Figure 8-1(a). A typical result would be a lower sliding friction for the hydrophilic system as compared to the hydrophobic systems in the mixed lubrication regime, with experimental evidence found be Figure 8-1(b).

The presented approach neglected the fluid-asperity interaction, which may be a good approximation for hydrophobic systems, where the asperity contact regions are considered dry. However, in cases of hydrophilic systems which is often observed for glasses without coating, the hydrodynamic pressure should incorporate the effect of the multiscale roughness on the fluid film and be expressed as a function of coordinates and magnification as $p_f(\xi, x)$, which can be solved together with an average mass conservation equation (a Reynolds-like equation with flow factor corrections) as presented in [187] [2].

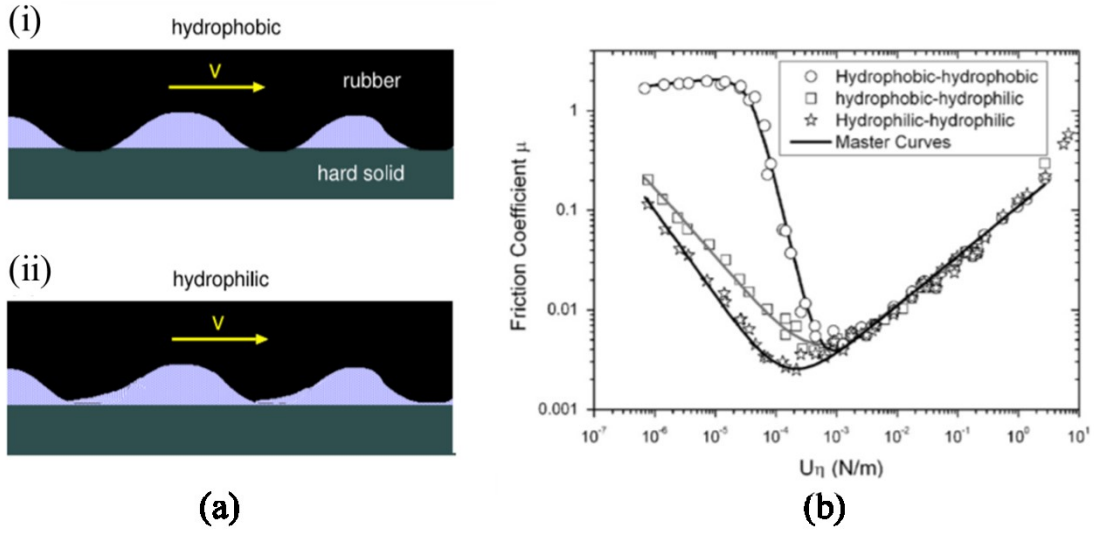

Figure 8-1 (a) Asperity contact for (i) hydrophobic surfaces and (ii) hydrophilic surfaces; (b) Friction coefficient for silicon rubber sliding on hard substrate surfaces in different surface conditions. Copyright with permission from [2, 124].

Study 3D line contacts: The basic FSI described in Chapter 3 was originally developed and applied to both 2D and 3D problems, although only 2D equations and results were shown in this thesis. As the focus is to obtain an accurate and efficient FSI methodology

and approximation of line contacts is not too far from the real contact scenarios, point contacts were not further considered for the development of RSM. However, the extraction of reduced stiffness matrix from a 3D FE model follows the same procedure for the 2D one and can be incorporated to the FSI framework. This would enable to capture the entrainment of lubricant more closely and predict the friction more accurately, but also to deal with edge effects and potential 3D effects (such as blade lip twist) in the real configuration. A nonuniform mesh should also be considered to save computational cost for 3D models.

Experiments: Experiments are critical for understanding the mechanism of friction and lubrication and validating numerical models. For example, as shown in Chapter 6 and Chapter 7, the shear strength, which plays important role in friction prediction, has to be quantified through experiments carried out in a more systematic manner. The effect of surface energy should be also be studied using specimens with a variety of surface properties. In addition, other parameters that strongly affects the performance of the model, such as the roughness and the deformed configuration, should be measured carefully and accurately during the experiments to provide better inputs for the proposed model.

References

1. Dobre, O., *A tribological investigation of windscreen wiper performance.* 2016.
2. Persson, B. and M. Scaraggi, *On the transition from boundary lubrication to hydrodynamic lubrication in soft contacts.* Journal of Physics: Condensed Matter, 2009. **21**(18): p. 185002.
3. Bódai, G. and T.J. Goda, *Sliding friction of wiper blade: Measurement, FE modeling and mixed friction simulation.* Tribology International, 2014. **70**: p. 63-74.
4. Stupkiewicz, S., et al., *Finite deformation effects in soft elastohydrodynamic lubrication problems.* Tribology International, 2016. **93**(Part B): p. 511-522.
5. Herrebrugh, K., *Solving the incompressible and isothermal problem in elastohydrodynamic lubrication through an integral equation.* Journal of Tribology, 1968. **90**(1): p. 262-270.
6. Biswas, S. and R. Snidle, *Elastohydrodynamic lubrication of spherical surfaces of low elastic modulus.* J. Lubr. Technol, 1976. **98**(4): p. 524-529.
7. Baglin, K.P.a.A., J.F, *An analytical solution of the elastohydrodynamic lubrication of materials of low elastic modulus.* In Proceedings of Second IMechE Symposium on Elastohydrodynamic Lubrication, 1972: p. pp. 13-21.
8. Hamrock, B.J. and D. Dowson, *Isothermal Elastohydrodynamic Lubrication of Point Contacts: Part 1—Theoretical Formulation.* Journal of Lubrication Technology, 1976. **98**(2): p. 223-228.
9. Dowson, D. and G.R. Higginson, *CHAPTER 6 - ELASTO-HYDRODYNAMIC THEORY*, in *Elasto-Hydrodynamic Lubrication (SI Edition)*. 1977, Pergamon. p. 65-77.
10. Hamrock, B.J. and D. Dowson, *Elastohydrodynamic Lubrication of Elliptical Contacts for Materials of Low Elastic Modulus I—Fully Flooded Conjunction.* Journal of Lubrication Technology, 1978. **100**(2): p. 236-245.
11. Hooke, C.J., *The Elasto-Hydrodynamic Lubrication of Soft, Highly Deformed Contacts Under Conditions of Nonuniform Motion.* Journal of Tribology, 1986. **108**(4): p. 545-550.
12. Hooke, C., *The calculation of film thicknesses in soft, highly deformed contacts under dynamic conditions.* Proceedings of the Institution of Mechanical Engineers, Part C: Journal of Mechanical Engineering Science, 1987. **201**(3): p. 171-179.
13. Yao, J.Q. and D. Dowson, *Elastohydrodynamic Lubrication of Soft-Layered Solids at Elliptical Contacts: Part 1: Elasticity Analysis.* Proceedings of the Institution of Mechanical Engineers, Part J: Journal of Engineering Tribology, 1994. **208**(1): p. 31-41.
14. Hooke, C.J. and P. Huang, *Elastohydrodynamic lubrication of soft viscoelastic materials in line contact.* Proceedings of the Institution of Mechanical Engineers, Part J: Journal of Engineering Tribology, 1997. **211**(3): p. 185-194.
15. Nikas, G.K., G. Burridge, and R.S. Sayles, *Modelling and optimization of rotary vane seals.* Proceedings of the Institution of Mechanical Engineers, Part J: Journal of Engineering Tribology, 2007. **221**(6): p. 699-715.
16. Christensen, H., *Stochastic models for hydrodynamic lubrication of rough surfaces.* Proceedings of the Institution of Mechanical Engineers, 1969. **184**(1): p. 1013-1026.
17. Lebeck, A., J. Teale, and R. Pierce, *Hydrodynamic lubrication and wear in wavy contacting face seals.* Journal of Tribology, 1978. **100**(1): p. 81-90.
18. Patir, N. and H. Cheng, *An average flow model for determining effects of three-dimensional*

roughness on partial hydrodynamic lubrication. Journal of Tribology, 1978. **100**(1): p. 12-17.

19. Patir, N. and H. Cheng, *Application of average flow model to lubrication between rough sliding surfaces.* Journal of Tribology, 1979. **101**(2): p. 220-229.
20. Elrod, H., *A general theory for laminar lubrication with Reynolds roughness.* Journal of Tribology, 1979. **101**(1): p. 8-14.
21. Tripp, J., *Surface roughness effects in hydrodynamic lubrication: the flow factor method.* Journal of Tribology, 1983. **105**(3): p. 458-463.
22. Letalleur, N., F. Plouraboué, and M. Prat, *Average flow model of rough surface lubrication: flow factors for sinusoidal surfaces.* Journal of tribology, 2002. **124**(3): p. 539-546.
23. Harp, S.R. and R.F. Salant, *An average flow model of rough surface lubrication with inter-asperity cavitation.* Journal of Tribology, 2001. **123**(1): p. 134-143.
24. Harp, S.R. and R.F. Salant, *Inter-asperity cavitation and global cavitation in seals:: an average flow analysis.* Tribology International, 2002. **35**(2): p. 113-121.
25. Kim, T.W. and Y.J. Cho, *The flow factors considering the elastic deformation for the rough surface with a non-Gaussian height distribution.* Tribology Transactions, 2008. **51**(2): p. 213-220.
26. Lubrecht, A.A., W.E. Ten Napel, and R. Bosma, *The Influence of Longitudinal and Transverse Roughness on the Elastohydrodynamic Lubrication of Circular Contacts.* Journal of Tribology, 1988. **110**(3): p. 421-426.
27. Kweh, C.C., H.P. Evans, and R.W. Snidle, *Micro-Elastohydrodynamic Lubrication of an Elliptical Contact With Transverse and Three-Dimensional Sinusoidal Roughness.* Journal of Tribology, 1989. **111**(4): p. 577-584.
28. Ai, X. and H.S. Cheng, *The effects of surface texture on EHL point contacts.* Transaction American society of mechanical engineers journal of tribology, 1996. **118**: p. 59-66.
29. Chang, L., *A deterministic model for line-contact partial elastohydrodynamic lubrication.* Tribology international, 1995. **28**(2): p. 75-84.
30. Jiang, X., et al., *A mixed elastohydrodynamic lubrication model with asperity contact.* Journal of tribology, 1999. **121**(3): p. 481-491.
31. Hu, Y.-Z. and D. Zhu, *A full numerical solution to the mixed lubrication in point contacts.* Journal of Tribology, 2000. **122**(1): p. 1-9.
32. Hu, Y.-z., et al., *A computer model of mixed lubrication in point contacts.* Tribology International, 2001. **34**(1): p. 65-73.
33. Ren, N., et al., *A three-dimensional deterministic model for rough surface line-contact EHL problems.* Journal of Tribology, 2009. **131**(1): p. 011501.
34. Shi, F. and R.F. Salant, *A Mixed Soft Elastohydrodynamic Lubrication Model With Interasperity Cavitation and Surface Shear Deformation.* Journal of Tribology, 1999. **122**(1): p. 308-316.
35. Minet, C., N. Brunetière, and B. Tournerie, *A Deterministic Mixed Lubrication Model for Mechanical Seals.* Journal of Tribology, 2011. **133**(4): p. 042203-042203-11.
36. Brandt, A. and A.A. Lubrecht, *Multilevel matrix multiplication and fast solution of integral equations.* Journal of Computational Physics, 1990. **90**(2): p. 348-370.
37. Liu, S., Q. Wang, and G. Liu, *A versatile method of discrete convolution and FFT (DC-FFT) for contact analyses.* Wear, 2000. **243**(1): p. 101-111.
38. Wang, Q.J., et al., *Mixed Lubrication Analyses by a Macro-Micro Approach and a Full-Scale Mixed EHL Model.* Journal of Tribology, 2004. **126**(1): p. 81-91.

39. Wang, W.-z., et al., *Effect of surface roughness parameters on mixed lubrication characteristics.* Tribology International, 2006. **39**(6): p. 522-527.
40. Scaraggi, M. and G. Carbone, *A Two-Scale Approach for Lubricated Soft-Contact Modeling: An Application to Lip-Seal Geometry.* Advances in Tribology, 2012. **2012**: p. 12.
41. Masjedi, M. and M.M. Khonsari, *Theoretical and experimental investigation of traction coefficient in line-contact EHL of rough surfaces.* Tribology International, 2014. **70**(Supplement C): p. 179-189.
42. Masjedi, M. and M.M. Khonsari, *On the effect of surface roughness in point-contact EHL: Formulas for film thickness and asperity load.* Tribology International, 2015. **82**(Part A): p. 228-244.
43. Masjedi, M. and M.M. Khonsari, *Mixed lubrication of soft contacts: An engineering look.* Proceedings of the Institution of Mechanical Engineers, Part J: Journal of Engineering Tribology, 2016. **231**(2): p. 263-273.
44. Kane, M. and B. Bou-Said, *Comparison of homogenization and direct techniques for the treatment of roughness in incompressible lubrication.* Journal of Tribology, 2004. **126**(4): p. 733-737.
45. Almqvist, A. and J. Dasht, *The homogenization process of the Reynolds equation describing compressible liquid flow.* Tribology international, 2006. **39**(9): p. 994-1002.
46. Sahlin, F., et al., *Rough surface flow factors in full film lubrication based on a homogenization technique.* Tribology international, 2007. **40**(7): p. 1025-1034.
47. Sahlin, F., et al., *A mixed lubrication model incorporating measured surface topography. Part 1: theory of flow factors.* Proceedings of the Institution of Mechanical Engineers, Part J: Journal of Engineering Tribology, 2010. **224**(4): p. 335-351.
48. Meng, F.M., et al., *On elastic deformation, inter-asperity cavitation and lubricant thermal effects on flow factors.* Tribology International, 2009. **42**(2): p. 260-274.
49. Scaraggi, M., et al., *Lubrication in soft rough contacts: A novel homogenized approach. Part I-Theory.* Soft Matter, 2011. **7**(21): p. 10395-10406.
50. Scaraggi, M., G. Carbone, and D. Dini, *Lubrication in soft rough contacts: A novel homogenized approach. Part II - Discussion.* Soft Matter, 2011. **7**(21): p. 10407-10416.
51. Johnson, K.L., *Contact Mechanics*. 1985, Cambridge: Cambridge University Press.
52. Johnson, K.L., K. Kendall, and A.D. Roberts, *Surface Energy and the Contact of Elastic Solids.* Proceedings of the Royal Society of London. A. Mathematical and Physical Sciences, 1971. **324**(1558): p. 301-313.
53. Persson, B.N.J. and M. Scaraggi, *Theory of adhesion: Role of surface roughness.* The Journal of Chemical Physics, 2014. **141**(12): p. 124701.
54. Vakis, A.I., et al., *Modeling and simulation in tribology across scales: An overview.* Tribology International, 2018. **125**: p. 169-199.
55. Ciavarella, M., et al., *The role of adhesion in contact mechanics.* Journal of The Royal Society Interface, 2019. **16**(151): p. 20180738.
56. Tevis, D.B.J., J. Till, and P. Lars, *Quantitative characterization of surface topography using spectral analysis.* Surface Topography: Metrology and Properties, 2017. **5**(1): p. 013001.
57. Lechenault, F., et al., *Effects of Finite Probe Size on Self-Affine Roughness Measurements*. Vol. 104. 2010. 025502.
58. Gujrati, A., et al., *Combining TEM, AFM, and Profilometry for Quantitative Topography Characterization Across All Scales.* ACS Applied Materials & Interfaces, 2018. **10**(34): p. 29169-29178.

59. Poon, C.Y. and B. Bhushan, *Comparison of surface roughness measurements by stylus profiler, AFM and non-contact optical profiler.* Wear, 1995. **190**(1): p. 76-88.
60. Archard, J.F., *Elastic Deformation and the Laws of Friction.* Proceedings of the Royal Society of London. Series A, Mathematical and Physical Sciences, 1957. **243**(1233): p. 190-205.
61. Greenwood, J.A. and J.B.P. Williamson, *Contact of Nominally Flat Surfaces.* Proceedings of the Royal Society of London. Series A. Mathematical and Physical Sciences, 1966. **295**(1442): p. 300-319.
62. Ciavarella, M., V. Delfine, and G. Demelio, *A "re-vitalized" Greenwood and Williamson model of elastic contact between fractal surfaces.* Journal of the Mechanics and Physics of Solids, 2006. **54**(12): p. 2569-2591.
63. Ciavarella, M., J.A. Greenwood, and M. Paggi, *Inclusion of "interaction" in the Greenwood and Williamson contact theory.* Wear, 2008. **265**(5): p. 729-734.
64. Fuller, K.N.G.D.T.F.R.S., *The effect of surface roughness on the adhesion of elastic solids.* Proceedings of the Royal Society of London. A. Mathematical and Physical Sciences, 1975. **345**(1642): p. 327.
65. Bush, A.W., R.D. Gibson, and T.R. Thomas, *The elastic contact of a rough surface.* Wear, 1975. **35**(1): p. 87-111.
66. Carbone, G. and F. Bottiglione, *Asperity contact theories: Do they predict linearity between contact area and load?* Journal of the Mechanics and Physics of Solids, 2008. **56**(8): p. 2555-2572.
67. Persson, B.N.J., *Theory of rubber friction and contact mechanics.* The Journal of Chemical Physics, 2001. **115**(8): p. 3840-3861.
68. Persson, B., F. Bucher, and B. Chiaia, *Elastic contact between randomly rough surfaces: Comparison of theory with numerical results*. Vol. 65. 2002.
69. Persson, B.N.J., *Contact mechanics for randomly rough surfaces.* Surface Science Reports, 2006. **61**(4): p. 201-227.
70. Persson, B.N.J., et al., *Contact area between a viscoelastic solid and a hard, randomly rough, substrate.* The Journal of Chemical Physics, 2004. **120**(18): p. 8779-8793.
71. Putignano, C., et al., *A new efficient numerical method for contact mechanics of rough surfaces.* International Journal of Solids and Structures, 2012. **49**(2): p. 338-343.
72. Campañá, C. and M.H. Müser, *Contact mechanics of real vs. randomly rough surfaces: A Green's function molecular dynamics study.* EPL (Europhysics Letters), 2007. **77**(3): p. 38005.
73. Yang, C. and B.N.J. Persson, *Contact mechanics: contact area and interfacial separation from small contact to full contact.* Journal of Physics: Condensed Matter, 2008. **20**(21): p. 215214.
74. Yastrebov, V.A., G. Anciaux, and J.-F. Molinari, *Contact between representative rough surfaces.* Physical Review E, 2012. **86**(3): p. 035601.
75. Manners, W. and J.A. Greenwood, *Some observations on Persson's diffusion theory of elastic contact.* Wear, 2006. **261**(5): p. 600-610.
76. Wolf , B.D., P. Nikolay, and H.M. Martin *Systematic analysis of Persson's contact mechanics theory of randomly rough elastic surfaces.* Journal of Physics: Condensed Matter, 2014. **26**(35): p. 355002.
77. Persson, B.N.J., *Relation between Interfacial Separation and Load: A General Theory of Contact Mechanics.* Physical Review Letters, 2007. **99**(12): p. 125502.
78. Prodanov, N., W.B. Dapp, and M.H. Müser, *On the Contact Area and Mean Gap of Rough, Elastic Contacts: Dimensional Analysis, Numerical Corrections, and Reference Data.* Tribology Letters, 2014. **53**(2): p. 433-448.
79. Pastewka, L., et al., *Finite-size scaling in the interfacial stiffness of rough elastic contacts.* Physical

Review E, 2013. **87**(6): p. 062809.

80. Papangelo, A., N. Hoffmann, and M. Ciavarella, *Load-separation curves for the contact of self-affine rough surfaces.* Scientific Reports, 2017. **7**(1): p. 6900.
81. Almqvist, A., et al., *Interfacial separation between elastic solids with randomly rough surfaces: Comparison between theory and numerical techniques.* Journal of the Mechanics and Physics of Solids, 2011. **59**(11): p. 2355-2369.
82. Yastrebov, V.A., G. Anciaux, and J.-F. Molinari, *From infinitesimal to full contact between rough surfaces: Evolution of the contact area.* International Journal of Solids and Structures, 2015. **52**(Supplement C): p. 83-102.
83. Yastrebov, V.A., G. Anciaux, and J.-F. Molinari, *On the accurate computation of the true contact-area in mechanical contact of random rough surfaces.* Tribology International, 2017. **114**(Supplement C): p. 161-171.
84. Lorenz, B. and B.N.J. Persson, *Interfacial separation between elastic solids with randomly rough surfaces: comparison of experiment with theory.* Journal of Physics: Condensed Matter, 2009. **21**(1): p. 015003.
85. Lorenz, B., G. Carbone, and C. Schulze, *Average separation between a rough surface and a rubber block: Comparison between theories and experiments.* Wear, 2010. **268**(7): p. 984-990.
86. Hyun, S., et al., *Finite-element analysis of contact between elastic self-affine surfaces.* Physical Review E, 2004. **70**(2): p. 026117.
87. Hyun, S. and M.O. Robbins, *Elastic contact between rough surfaces: Effect of roughness at large and small wavelengths.* Tribology International, 2007. **40**(10): p. 1413-1422.
88. Wriggers, P. and J. Reinelt, *Multi-scale approach for frictional contact of elastomers on rough rigid surfaces.* Computer Methods in Applied Mechanics and Engineering, 2009. **198**(21): p. 1996-2008.
89. Polonsky, I.A. and L.M. Keer, *A numerical method for solving rough contact problems based on the multi-level multi-summation and conjugate gradient techniques.* Wear, 1999. **231**(2): p. 206-219.
90. Polonsky, I.A. and L.M. Keer, *Fast Methods for Solving Rough Contact Problems: A Comparative Study.* Journal of Tribology, 1999. **122**(1): p. 36-41.
91. Webster, M.N. and R.S. Sayles, *A Numerical Model for the Elastic Frictionless Contact of Real Rough Surfaces.* Journal of Tribology, 1986. **108**(3): p. 314-320.
92. Webster, M.N., M.A. West, and R.S. Sayles, *A method of three-dimensional topography measurement and analysis on arcuate surfaces.* Wear, 1986. **109**(1): p. 385-399.
93. Putignano, C., et al., *The influence of the statistical properties of self-affine surfaces in elastic contacts: A numerical investigation.* Journal of the Mechanics and Physics of Solids, 2012. **60**(5): p. 973-982.
94. Putignano, C., et al., *A multiscale analysis of elastic contacts and percolation threshold for numerically generated and real rough surfaces.* Tribology International, 2013. **64**(Supplement C): p. 148-154.
95. Paggi, M. and M. Ciavarella, *The coefficient of proportionality κ between real contact area and load, with new asperity models.* Wear, 2010. **268**(7): p. 1020-1029.
96. Hu, Y.Z. and K. Tonder, *Simulation of 3-D random rough surface by 2-D digital filter and fourier analysis.* International Journal of Machine Tools and Manufacture, 1992. **32**(1): p. 83-90.
97. Stanley, H.M. and T. Kato, *An FFT-Based Method for Rough Surface Contact.* Journal of Tribology, 1997. **119**(3): p. 481-485.

98. Yastrebov, V.A., G. Anciaux, and J.-F. Molinari, *The role of the roughness spectral breadth in elastic contact of rough surfaces.* Journal of the Mechanics and Physics of Solids, 2017. **107**(Supplement C): p. 469-493.
99. Pohrt, R. and V.L. Popov, *Investigation of the dry normal contact between fractal rough surfaces using the reduction method, comparison to 3D simulations.* Physical Mesomechanics, 2012. **15**(5): p. 275-279.
100. Pohrt, R. and V.L. Popov, *Contact stiffness of randomly rough surfaces.* Scientific Reports, 2013. **3**: p. 3293.
101. Campañá, C. and M.H. Müser, *Practical Green's function approach to the simulation of elastic semi-infinite solids.* Physical Review B, 2006. **74**(7): p. 075420.
102. Schallamach, A., *The load dependence of rubber friction.* Proceedings of the Physical Society. Section B, 1952. **65**(9): p. 657.
103. Schallamach, A., *The velocity and temperature dependence of rubber friction.* Proceedings of the Physical Society. Section B, 1953. **66**(5): p. 386.
104. Grosch, K. *The relation between the friction and visco-elastic properties of rubber*. in *Proceedings of the Royal Society of London A: Mathematical, Physical and Engineering Sciences*. 1963. The Royal Society.
105. Barquins, M., *Adherence, friction and wear of rubber-like materials.* Wear, 1992. **158**(1): p. 87-117.
106. Johnson Kenneth, L., et al., *Surface energy and the contact of elastic solids.* Proceedings of the Royal Society of London. A. Mathematical and Physical Sciences, 1971. **324**(1558): p. 301-313.
107. Roberts, A.D. and A.G. Thomas, *The adhesion and friction of smooth rubber surfaces.* Wear, 1975. **33**(1): p. 45-64.
108. Schallamach, A., *How does rubber slide?* Wear, 1971. **17**(4): p. 301-312.
109. Persson, B.N.J. and A.I. Volokitin, *Rubber friction on smooth surfaces.* The European Physical Journal E, 2006. **21**(1): p. 69-80.
110. Fukahori, Y., P. Gabriel, and J.J.C. Busfield, *How does rubber truly slide between Schallamach waves and stick–slip motion?* Wear, 2010. **269**(11): p. 854-866.
111. Klüppel, M. and G. Heinrich, *Rubber Friction on Self-Affine Road Tracks.* Rubber Chemistry and Technology, 2000. **73**(4): p. 578-606.
112. K.N.G. Fuller, D.T.F.R.S., *The effect of surface roughness on the adhesion of elastic solids.* Proceedings of the Royal Society of London. A. Mathematical and Physical Sciences, 1975. **345**(1642): p. 327.
113. Persson, B.N.J., *On the theory of rubber friction.* Surface Science, 1998. **401**(3): p. 445-454.
114. Barquins, M. and A.D. Roberts, *Rubber friction variation with rate and temperature: some new observations.* Journal of Physics D: Applied Physics, 1986. **19**(4): p. 547.
115. Le Gal, A., X. Yang, and M. Klüppel, *Evaluation of sliding friction and contact mechanics of elastomers based on dynamic-mechanical analysis.* The Journal of Chemical Physics, 2005. **123**(1): p. 014704.
116. Lorenz, B., et al., *Rubber friction on road surfaces: Experiment and theory for low sliding speeds.* The Journal of Chemical Physics, 2015. **142**(19): p. 194701.
117. Rowe, K.G., et al., *In situ thermal measurements of sliding contacts.* Tribology International, 2013. **62**: p. 208-214.
118. Denny, D.F., *The Influence of Load and Surface Roughness on the Friction of Rubber-Like Materials.*

Proceedings of the Physical Society. Section B, 1953. **66**(9): p. 721.

119. Greenwood, J. and D. Tabor, *The friction of hard sliders on lubricated rubber: the importance of deformation losses.* Proceedings of the Physical Society, 1958. **71**(6): p. 989.
120. Sabey, B.E., *Pressure distributions beneath spherical and conical shapes pressed into a rubber plane, and their bearing on coefficients of friction under wet conditions.* Proceedings of the Physical Society, 1958. **71**(6): p. 979.
121. De Vicente, J., J. Stokes, and H. Spikes, *The frictional properties of Newtonian fluids in rolling–sliding soft-EHL contact.* Tribology Letters, 2005. **20**(3-4): p. 273-286.
122. De Vicente, J., J. Stokes, and H. Spikes, *Rolling and sliding friction in compliant, lubricated contact.* Proceedings of the Institution of Mechanical Engineers, Part J: Journal of Engineering Tribology, 2006. **220**(2): p. 55-63.
123. Myant, C., H. Spikes, and J. Stokes, *Influence of load and elastic properties on the rolling and sliding friction of lubricated compliant contacts.* Tribology International, 2010. **43**(1): p. 55-63.
124. Bongaerts, J., K. Fourtouni, and J. Stokes, *Soft-tribology: lubrication in a compliant PDMS–PDMS contact.* Tribology International, 2007. **40**(10): p. 1531-1542.
125. Mofidi, M., et al., *Rubber friction on (apparently) smooth lubricated surfaces.* Journal of Physics: Condensed Matter, 2008. **20**(8): p. 085223.
126. Hamrock, B.J. and D. Dowson, *Ball bearing lubrication: the elastohydrodynamics of elliptical contacts.* 1981.
127. Roberts, A. and P. Swales, *The elastohydrodynamic lubrication of a highly elastic cylindrical surface.* Journal of Physics D: Applied Physics, 1969. **2**(9): p. 1317.
128. Kaneta, M. and A. Cameron, *Effects of asperities in elastohydrodynamic lubrication.* Journal of Tribology, 1980. **102**(3): p. 374-378.
129. Guangteng, G., et al., *Lubricant film thickness in rough surface, mixed elastohydrodynamic contact.* Journal of tribology, 2000. **122**(1): p. 65-76.
130. Myant, C., et al., *An investigation of lubricant film thickness in sliding compliant contacts.* Tribology Transactions, 2010. **53**(5): p. 684-694.
131. Bongaerts, J.H.H., et al., *In situ confocal Raman spectroscopy of lubricants in a soft elastohydrodynamic tribological contact.* Journal of Applied Physics, 2008. **104**(1): p. 014913.
132. Myant, C., T. Reddyhoff, and H. Spikes, *Laser-induced fluorescence for film thickness mapping in pure sliding lubricated, compliant, contacts.* Tribology International, 2010. **43**(11): p. 1960-1969.
133. Fowell, M.T., et al., *A study of lubricant film thickness in compliant contacts of elastomeric seal materials using a laser induced fluorescence technique.* Tribology International, 2014. **80**: p. 76-89.
134. Gasni, D., M.W. Ibrahim, and R. Dwyer-Joyce, *Measurements of lubricant film thickness in the iso-viscous elastohydrodynamic regime.* Tribology International, 2011. **44**(7): p. 933-944.
135. Dwyer-Joyce, R.S., B.W. Drinkwater, and C.J. Donohoe, *The measurement of lubricant–film thickness using ultrasound.* Proceedings of the Royal Society of London. Series A: Mathematical, Physical and Engineering Sciences, 2003. **459**(2032): p. 957-976.
136. Dwyer-Joyce, R.S., T. Reddyhoff, and J. Zhu, *Ultrasonic Measurement for Film Thickness and Solid Contact in Elastohydrodynamic Lubrication.* Journal of Tribology, 2011. **133**(3): p. 031501-031501-11.
137. Sterner, O., et al., *Tribological Classification of Contact Lenses: From Coefficient of Friction to Sliding Work.* Tribology Letters, 2016. **63**(1): p. 9.

138. Unsworth, A., *Tribology of Human and Artificial Joints.* Proceedings of the Institution of Mechanical Engineers, Part H: Journal of Engineering in Medicine, 1991. **205**(3): p. 163-172.
139. Bongaerts, J.H.H., D. Rossetti, and J.R. Stokes, *The Lubricating Properties of Human Whole Saliva.* Tribology Letters, 2007. **27**(3): p. 277-287.
140. Stokes, J.R., M.W. Boehm, and S.K. Baier, *Oral processing, texture and mouthfeel: From rheology to tribology and beyond.* Current Opinion in Colloid & Interface Science, 2013. **18**(4): p. 349-359.
141. Moore, D.F., *Friction and wear in rubbers and tyres.* Wear, 1980. **61**(2): p. 273-282.
142. Lorenz, B., et al., *Rubber friction for tire tread compound on road surfaces.* Journal of Physics: Condensed Matter, 2013. **25**(9): p. 095007.
143. Heinrich, G. and M. Klüppel, *Rubber friction, tread deformation and tire traction.* Wear, 2008. **265**(7): p. 1052-1060.
144. Nau, B.S., *An historical review of studies of polymeric seals in reciprocating hydraulic systems.* Proceedings of the Institution of Mechanical Engineers, Part J: Journal of Engineering Tribology, 1999. **213**(3): p. 215-226.
145. Nikas, G.K., *Transient elastohydrodynamic lubrication of rectangular elastomeric seals for linear hydraulic actuators.* Proceedings of the Institution of Mechanical Engineers, Part J: Journal of Engineering Tribology, 2003. **217**(6): p. 461-473.
146. Nikas, G.K., *Eighty years of research on hydraulic reciprocating seals: Review of tribological studies and related topics since the 1930s.* Proceedings of the Institution of Mechanical Engineers, Part J: Journal of Engineering Tribology, 2010. **224**(1): p. 1-23.
147. Roberts, A., *From Wipers to the JKR Equation: Boundary Lubrication and Adhesion of Rubber.* Materials Science Forum, 2011. **662**: p. 27-37.
148. Derler, S., F. Kausch, and R. Huber, *Analysis of factors influencing the friction coefficients of shoe sole materials.* Safety Science, 2008. **46**(5): p. 822-832.
149. Moore, C.T., et al., *Analysis of Shoe Friction During Sliding Against Floor Material: Role of Fluid Contaminant.* Journal of Tribology, 2012. **134**(4): p. 041104-041104-7.
150. Strobel, C.M., et al., *Analysis of the Contribution of Adhesion and Hysteresis to Shoe–Floor Lubricated Friction in the Boundary Lubrication Regime.* Tribology Letters, 2012. **47**(3): p. 341-347.
151. Koenen, A. and A. Sanon, *Tribological and vibroacoustic behavior of a contact between rubber and glass (application to wiper blade).* Tribology International, 2007. **40**(10): p. 1484-1491.
152. Deleau, F., D. Mazuyer, and A. Koenen, *Sliding friction at elastomer/glass contact: influence of the wetting conditions and instability analysis.* Tribology international, 2009. **42**(1): p. 149-159.
153. Le Rouzic, J., et al., *Friction-Induced Vibration by Stribeck's Law: Application to Wiper Blade Squeal Noise.* Tribology Letters, 2013. **49**(3): p. 563-572.
154. Reddyhoff, T., et al., *Friction Induced Vibration in Windscreen Wiper Contacts.* Journal of Vibration and Acoustics, 2015. **137**(4): p. 041009.
155. Putignano, C., *Viscoelastic rough contact mechanics: A multiscale investigation.* Proceedings of the Institution of Mechanical Engineers, Part C: Journal of Mechanical Engineering Science, 2016. **230**(9): p. 1374-1381.
156. Noutary, M.P., C.H. Venner, and A.A. Lubrecht, *Grid generation in hydrodynamic and elastohydrodynamic lubrication using algebraic multigrid method.* Proceedings of the Institution of Mechanical Engineers, Part J: Journal of Engineering Tribology, 2012. **226**(5): p. 343-349.
157. Profito, F.J., et al., *A General Finite Volume Method for the Solution of the Reynolds Lubrication*

Equation with a Mass-Conserving Cavitation Model. Tribology Letters, 2015. **60**(1): p. 18.

158. Giacopini, M., et al., *A Mass-Conserving Complementarity Formulation to Study Lubricant Films in the Presence of Cavitation.* Journal of Tribology, 2010. **132**(4): p. 041702-041702-12.
159. Gohar, R., *Elastohydrodynamics*. 2001: PUBLISHED BY IMPERIAL COLLEGE PRESS AND DISTRIBUTED BY WORLD SCIENTIFIC PUBLISHING CO. 464.
160. Hajishafiee, A., *Finite-volume CFD modelling of fluid-solid interaction in EHL contacts.* PhD thesis, 2014.
161. Persson, B.N.J., *On the Fractal Dimension of Rough Surfaces.* Tribology Letters, 2014. **54**(1): p. 99-106.
162. Medina, S., A.V. Olver, and D. Dini, *The Influence of Surface Topography on Energy Dissipation and Compliance in Tangentially Loaded Elastic Contacts.* Journal of Tribology, 2012. **134**(1): p. 011401-011401-12.
163. Wu, J.-J., *Simulation of rough surfaces with FFT.* Tribology International, 2000. **33**(1): p. 47-58.
164. Majumdar, A. and C.L. Tien, *Fractal characterization and simulation of rough surfaces.* Wear, 1990. **136**(2): p. 313-327.
165. Persson, B.N.J., *Adhesion between an elastic body and a randomly rough hard surface.* The European Physical Journal E, 2002. **8**(4): p. 385-401.
166. Persson, B.N.J., et al., *On the nature of surface roughness with application to contact mechanics, sealing, rubber friction and adhesion.* Journal of Physics: Condensed Matter, 2005. **17**(1): p. R1.
167. Carlos, C., H.M. Martin, and O.R. Mark, *Elastic contact between self-affine surfaces: comparison of numerical stress and contact correlation functions with analytic predictions.* Journal of Physics: Condensed Matter, 2008. **20**(35): p. 354013.
168. Colin, F. and A.A. Lubrecht, *Comparison of FFT-MLMI for Elastic Deformation Calculations.* Journal of Tribology, 2000. **123**(4): p. 884-887.
169. IMTEK, J.H.U., *Surface Topography Analyzer.*
170. Pastewka, L., T.A. Sharp, and M.O. Robbins, *Seamless elastic boundaries for atomistic calculations.* Physical Review B, 2012. **86**(7): p. 075459.
171. *ABAQUS/Standard Analysis Users Guide 6.14.* 2014.
172. *ABAQUS/Standard Example Problems Guide.* 2014.
173. Tobajas, R., E. Ibartz, and L. Gracia, *A comparative study of hyperelastic constitutive models to characterize the behavior of a polymer used in automotive engines*. 2016. A002.
174. Bergström, J., *5 - Elasticity/Hyperelasticity*, in *Mechanics of Solid Polymers*, J. Bergström, Editor. 2015, William Andrew Publishing. p. 209-307.
175. Marckmann, G. and E. Verron, *Comparison of Hyperelastic Models for Rubber-Like Materials.* Rubber Chemistry and Technology, 2006. **79**(5): p. 835-858.
176. Yeoh, O.H., *Some Forms of the Strain Energy Function for Rubber.* Rubber Chemistry and Technology, 1993. **66**(5): p. 754-771.
177. Gutierrez-Lemini, D., *Engineering Viscoelasticity*. 2014.
178. Roylance, D., *Engineering Viscoelasticity.* Cambridge, MA 02139: Massachusetts Institute of Technology, 2001.
179. Tschoegl, N.W., *The Phenomenological Theory of Linear Viscoelastic Behavior.* Book, 1989.
180. Carbone, G. and C. Putignano, *Rough viscoelastic sliding contact: Theory and experiments.* Physical Review E, 2014. **89**(3): p. 032408.

181. Putignano, C., G. Carbone, and D. Dini, *Mechanics of rough contacts in elastic and viscoelastic thin layers.* International Journal of Solids and Structures, 2015. **69-70**: p. 507-517.
182. Scaraggi, M. and B.N.J. Persson, *Friction and universal contact area law for randomly rough viscoelastic contacts.* Journal of Physics: Condensed Matter, 2015. **27**(10): p. 105102.
183. Putignano, C., T. Reddyhoff, and D. Dini, *The influence of temperature on viscoelastic friction properties.* Tribology International, 2016. **100**: p. 338-343.
184. Putignano, C., et al., *A theoretical and experimental study of viscoelastic rolling contacts incorporating thermal effects*. Vol. 228. 2014.
185. Williams, M.L., R.F. Landel, and J.D. Ferry, *The Temperature Dependence of Relaxation Mechanisms in Amorphous Polymers and Other Glass-forming Liquids.* Journal of the American Chemical Society, 1955. **77**(14): p. 3701-3707.
186. Vorvolakos, K. and M.K. Chaudhury, *The Effects of Molecular Weight and Temperature on the Kinetic Friction of Silicone Rubbers.* Langmuir, 2003. **19**(17): p. 6778-6787.
187. Scaraggi, M., et al., *Lubrication in soft rough contacts: A novel homogenized approach. Part I - Theory*. Vol. 7. 2011. 10395-10406.